Phase assemblage and mechanical strength of ultra-high performance concrete under long-term autoclaving

vorgelegt von

M.Sc.
Hongwei Tian

an der Fakultät VI - Planen Bauen Umwelt

der Technischen Universität Berlin

zur Erlangung des akademischen Grades

Doktor der Ingenieurwissenschaften
Dr.-Ing.

genehmigte Dissertation

Promotionsausschuss:

Vorsitzender: Prof. Dr. Sabine Kruschwitz
Gutachter: Prof. Dr. Dietmar Stephan
Gutachter: Prof. Dr. Bernhard Middendorf
Gutachter: Dr. Birgit Meng

Tag der wissenschaftlichen Aussprache: 14. Dezember 2022

Berlin 2023

Abstract

This research studied the behavior of Portland cement-based materials under autoclaving at 200 °C. The cement hydration achieves a higher degree under autoclaving due to the transformation of amorphous C-S-H to more ordered phases, releasing more water for hydration. However, some calcium aluminoferrite phase keeps partially unhydrated after long-term autoclaving, probably due to the retardation by the hydrate layer. A pure cement paste generates the crystalline C-S-H with a high Ca/Si ratio. Quartz powder can effectively decrease the matrix Ca/Si ratio, leading to the crystalline C-S-H with a relatively low Ca/Si ratio. Further increase of quartz powder results in the formation of poorly crystallized C-S-H. The addition of fly ash can increase the effective Al in the matrix, leading to the formation of hydrogarnet. The composition of hydrogarnet depends on the contents of Si and Al in the matrix. High contents of Si and Al favor Si-rich hydrogarnet. A high water/solid ratio can accelerate the dissolution of raw materials, leading to a different hydrate assemblage. Moreover, in the case of a low Ca/Si ratio, a high water/solid ratio favors the transformation of the C-S-H precursor to tobermorite. For the samples with the same contents of fly ash and quartz powder, a low water/solid ratio generates the hydrogarnet with a higher Si content (more anhydrous).

For autoclaved UHPC, the compressive strength can stay robust because a large amount of silica (silica fume and quartz powder) prevents the formation of crystalline hydrates with high densities and leads to tobermorite and poorly crystallized C-S-H as the main hydrates. However, the flexural strength is vulnerable to autoclaving, probably due to the transformation of amorphous C-S-H to more ordered phases. The UHPC performance is improved by partially replacing cement with limestone powder, benefiting from the decreased Ca/Si ratio and the more poorly crystallized C-S-H with a low Ca/Si ratio. However, excessive poorly crystallized C-S-H may magnify the thermal mismatch between matrix and aggregate, leading to low mechanical strength. The addition of fly ash can also mitigate the detrimental effect of long-term autoclaving by increasing the Si and Al contents and inducing tobermorite and poorly crystallized C-S-H as the main hydrates. Meanwhile, the content of fly ash should also be controlled as excessive Al results in the massive formation of hydrogarnet. The mechanical strength is not strictly related to the porosity of UHPC under autoclaving, and the hydrate assemblage overweighs porosity on the mechanical strength. Appropriate incorporation of SCMs in UHPC can decrease the production cost, improve sustainability, and intensify the performance of UHPC under autoclaving.

Zusammenfassung

Diese Arbeit untersucht das Verhalten von portlandzementbasierten Materialien beim Autoklavieren bei 200 °C. Dabei erreicht die Zementhydration ein höheres Niveau, weil durch die Umwandlung von amorpher C-S-H-Phase zu geordneten Phasen mehr Wasser für die Hydratation freigesetzt wird. Allerdings bleibt ein Teil der Calciumaluminatferrit-Phase nach längerem Autoklavieren wahrscheinlich wegen der Verzögerung durch eine Hydratschicht teilweise unhydratisiert. Ein reiner Zementstein erzeugt kristalline C-S-H-Phasen mit hohem Ca/Si-Verhältnis. Aber Quarzpulver kann das Ca/Si-Verhältnis der Matrix verringern, was zu kristallinen C-S-H-Phasen mit niedrigerem Ca/Si-Verhältnis führt. Eine noch größere Zugabe von Quarzpulvers kann jedoch zur Bildung einer schlecht kristallinen C-S-H-Phase führen. Die Zugabe von Flugasche kann den Al-Anteil in der Matrix effektiv erhöhen, was zur Bildung des Hydrogranats führt. Die Zusammensetzung des Hydrogranats ist abhängig von den Gehalten an Si und Al. Ein hohes Wasser/Feststoff-Verhältnis kann die Auflösung der Rohstoffe erhöhen, dadurch wird es zu einer anderen Hydratzusammensetzung geführt. Außerdem begünstigt ein hohes Wasser/Feststoff-Verhältnis bei einem niedrigen Ca/Si-Verhältnis die Umwandlung von C-S-H zum Tobermorit.

Für UHPC kann die Druckfestigkeit auch unter Autoklavierungsbedingungen gleich bleiben, weil eine große Menge von Silika (Silikastaub und Quarzpulver) die Bildung von kristallinen Hydraten mit hoher Dichte verhindert. Es führt dazu, dass Tobermorit und schlecht kristallisierte C-S-H-Phase als Haupthydrate vorliegen. Allerdings ist die Biegezugfestigkeit gefährdet, da amorphe C-S-H-Phase zu mehr geordneten Phasen umgewandelt wird. Die Leistungsfähigkeit des UHPC wird dadurch verbessert, dass Zement durch Kalkstein teilweise ersetzt wird, wobei die Verbesserung auf der Verringerung des Ca/Si-Verhältnisses und einer größeren Menge von schlecht kristallinen C-S-H-Phasen beruht. Übermäßige schlecht kristalline C-S-H-Phase könnte die thermische Fehlanpassung zwischen Matrix und Aggregaten verstärken, was zur niedrigen mechanischen Festigkeit führt. Die Zugabe von Flugasche kann wegen des zunehmenden Si- und Al-Gehalts, des daraus resultierenden Tobermorits und der schlecht kristallinen C-S-H-Phase die nachteiligen Auswirkungen des langfristigen Autoklavierens mildern. Gleichzeitig muss der Gehalt an Flugasche kontrolliert werden, weil übermäßig Al zur massiven Bildung vom Hydrogranat führt. Beim Autoklavieren steht die mechanische Festigkeit nicht in engem Zusammenhang mit der Porosität des UHPC, sondern die Phasenzusammensetzung ist der entscheidende Faktor. Eine geeignete Zugabe von SCMs in UHPC kann die Produktionskosten senken, die Nachhaltigkeit verbessern und die Leistungsfähigkeit des UHPCs beim Autoklavieren erhöhen.

Table of contents

Nomenclature

AAC: Autoclaved aerated concrete

MIP: Mercury intrusion porosimetry

OPC: Ordinary Portland cement

SCM: Supplementary cementitious material

SEM: Scanning electron microscope

TG: Thermogravimetric analysis

UHPC: Ultra-high performance concrete

XRD: X-ray diffraction

Mixtures

C1:   UHPC with typical components silica fume, cement, quartz powder, and quartz sand (plain UHPC)

C2:   Blended UHPC with fly ash (cement : fly ash = 8 : 2, weight proportion)

HB: Pure cement paste with a w/s ratio of 0.29

HF20:   Blended cement paste with fly ash (w/s ratio = 0.29, cement : fly ash = 8 : 2, weight proportion)

HF40:   Blended cement paste with fly ash (w/s ratio = 0.29, cement : fly ash = 6 : 4, weight proportion)

HQ20:   Blended cement paste with quartz powder (w/s ratio = 0.29, cement : quartz powder = 8 : 2, weight proportion)

HQ40:   Blended cement paste with quartz powder (w/s ratio = 0.29, cement : quartz powder = 6 : 4, weight proportion)

HQF20:   Blended cement paste with fly ash and quartz powder (w/s ratio = 0.29, cement : quartz powder : fly ash = 6 : 2 : 2, weight proportion)

LB: Pure cement paste with a w/s ratio of 0.20

LF20:   Blended cement paste with fly ash (w/s ratio = 0.20, cement : fly ash = 8 : 2, weight proportion)

LF40:   Blended cement paste with fly ash (w/s ratio = 0.20, cement : fly ash = 6 : 4, weight proportion)

LQ20:   Blended cement paste with quartz powder (w/s ratio = 0.20, cement : quartz powder = 8 : 2, weight proportion)

LQ40:   Blended cement paste with quartz powder (w/s ratio = 0.20, cement : quartz powder = 6 : 4, weight proportion)

LQF20:   Blended cement paste with fly ash and quartz powder (w/s ratio = 0.20, cement : quartz powder : fly ash = 6 : 2 : 2, weight proportion)

L0:   UHPC with typical components silica fume, cement, quartz powder, and quartz sand (plain UHPC)

L1:   Blended UHPC with limestone powder (cement : limestone powder = 9 : 1, weight proportion)

L2:   Blended UHPC with limestone powder (cement : limestone powder = 7 : 3, weight proportion)

L3:   Blended UHPC with limestone powder (cement : limestone powder = 5 : 5, weight proportion)

w/b ratio: water/binder ratio

w/s ratio: water/solid ratio

Minerals

AFm: $[Ca_4(Al,Fe)_2(OH)_{12}]\cdot SO_4\cdot 6H_2O$

Alite: C_3S, Ca_3SiO_5

Anhydrite: $C\overline{S}$, $CaSO_4$

Belite: C_2S, Ca_2SiO_4

Calcium aluminoferrite: C_4AF, $Ca_4Al_2Fe_2O_{10}$

Calcite: $CaCO_3$

C-S-H: Calcium silicate hydrate

Ettringite: $[[Ca_3Al(OH)_6]\cdot 12H_2O]_2\cdot(SO_4)_3\cdot 2H_2O$

Hillebrandite: $Ca_2(SiO_3)(OH)_2$

Hydrogarnet: $Ca_3Al_2(SiO_4)_x(OH)_{4(3-x)}$; $0\leq x\leq 3$

Hydroxylellestadite: $Ca_{10}(SiO_4)_3(SO_4)_3(OH)_2$

Jaffeite: $Ca_6[Si_2O_7](OH)_6$

Portlandite: $Ca(OH)_2$

Quartz: SiO_2

Reinhardbraunsite: $Ca_5(SiO_4)_2(OH)_2$

Scawtite: $Ca_7(Si_3O_9)_2CO_3\cdot 2H_2O$

Tobermorite: $Ca_5[Si_3O_8(OH)]_2\cdot 4(H_2O)$

Trabzonite: $Ca_4[Si_3O_9(OH)]OH$

Tricalcium aluminate: C_3A, $Ca_3Al_2O_6$

Xonotlite: $Ca_6[Si_6O_{17}](OH)_2$

α-dicalcium silicate hydrate: α-C_2SH, $Ca_2(HSiO_4)\cdot(OH)$

Research outline

This dissertation is structured in four sections, including two published peer-reviewed journal articles, one submitted article in a peer-reviewed journal, and the work which is in preparation for submission.

Chapter 1 contains the research background about hydrothermal conditions (Chapter 1.1) and ultra-high performance concrete (UHPC, Chapter 1.2). Chapter 1.1 introduces the types of hydrothermal conditions and their influence on cement hydration. Chapter 1.2 introduces the main principles for designing UHPC and the typical methods to improve the performance and sustainability of UHPC. Moreover, the research objectives are included.

Chapter 2 involves all the scientific publications and the work in preparation for submission. In order to understand the influence of long-term autoclaving on the hydrates formation in UHPC, the literature review as shown in Chapter 2.1 is carried out. In this article, the influence of the foreign ions Al^{3+}, Na^+, K^+, Mg^{2+}, Fe^{3+}, and SO_4^{2-} dissolved from supplementary cementitious materials (SCMs) and cement clinkers as well as the Ca/Si ratio on the hydration kinetics, including the formation of amorphous C-S-H and its transformation into crystalline phases, and hydrates characteristics under hydrothermal conditions are discussed.

The second publication in a peer-reviewed journal (Chapter 2.2) focuses on the performance of UHPC after long-term autoclaving. Partial cement is replaced by limestone powder to adjust the Ca/Si ratio without introducing interfering ions concerning C-S-H and improve the sustainability of UHPC. The compressive and flexural strength of pure and blended UHPC are tested after normal curing and long-term autoclaving. The hydrates assemblage and microstructure are further analyzed by X-ray diffraction (XRD), thermogravimetric analysis (TG), scanning electron microscope (SEM), and mercury intrusion porosimetry (MIP) to clarify the influence of long-term autoclaving on UHPC.

The third publication in a peer-reviewed journal (Chapter 2.3) studies the properties of steel fiber reinforced UHPC (UHPFRC) after long-term autoclaving. Steel fibers are added in this study, and the compressive and flexural strength of UHPFRC after normal curing and long-term autoclaving are evaluated. Fly ash (rich in Si and Al) is introduced as a partial replacement for cement to mitigate the detrimental effects caused by long-term autoclaving. The hydrates assemblage and microstructure are analyzed by XRD, TG, SEM, and MIP.

The final performance of UHPC after long-term autoclaving is studied in Chapters 2.2 and 2.3. The evolution of hydrates and microstructure with autoclaving is thus further studied in Chapter 2.4. Varied contents of fly ash and quartz powder are introduced to study the influence of mixture compositions on the hydrates assemblage and microstructure after different cycles of autoclaving.

Moreover, a commercial UHPC compound is also studied in Chapter 2.5 to confirm the findings derived from the previous sections.

Chapter 3 collects the main results in this work and presents the general discussion.

Chapter 4 is the conclusion derived from this study.

1 Introduction

1.1 Hydrothermal conditions

Cementitious materials have been widely used in various environments, such as corrosive marine environments, frozen areas, as well as hot oil and geothermal wells. Hydrothermal conditions that cements are subjected to can be divided into two forms: active curing [1,2] and passive resistance [3,4]. The active curing relates to the hydrothermal curing used in concrete technology, including ambient pressure curing and high-pressure steam curing. Normal curing at ambient temperature generally presents slow cement hydration and strength development, while hydrothermal curing accelerates the cement hydration and strength development, which favors the applications where a high early strength is of importance, e.g., precast concrete [5,6]. Furthermore, high-pressure steam curing can lead to the formation of new crystalline phases, such as the application in autoclaved aerated concrete (AAC) [7,8], calcium silicate board (CSB) [9,10], and ultra-high performance concrete (UHPC) [11–13]. AAC is produced by treating a mixture of quartz sand, lime, cement, gypsum, and other additives under saturated steam pressure (typically 0.8-1.4 MPa, 180-200 °C), which is widely used for heat insulation. It is reported that the contents of crystalline 1.1 nm tobermorite and poorly crystalline C-S-H phase formed in AAC are highly related to the product properties [7,8]. CSB is a kind of partition board with excellent properties of moisture resistance, light weight, sound insulation, and flame resistance. It is produced by using ordinary Portland cement (OPC) as calcium supplier, quartz sand as siliceous material, and fibers for reinforcement. After being moulded by compression, the specimens are subject to autoclaving treatment (1.0-2.3 MPa, 180-220 °C) for a certain time [9,10].

The other form of hydrothermal conditions, referred to passive resistance, is caused by high temperatures of the environment in which concrete is used, such as oil and geothermal well cementing [3,14] and the application of constructing water tanks for thermal storage [15]. In these environments, cementitious materials have to resist high temperatures for a long time. In the petroleum and geothermal industry, the strength and anti-permeability of cementing matrix may retrogress due to the hydrothermal reactions induced by high temperatures; amorphous C-S-H transforms to crystalline phases with high density (e.g., α-dicalcium silicate hydrate α-C_2SH, $Ca_2(HSiO_4)\cdot(OH)$), leading to the decrease of solid volume and thus the microstructure degradation. Therefore, to avoid this problem, special cement formulations have been developed that introduce additional silica to reduce the Ca/Si ratio to approx. 1.0,

preventing the formation of α-C_2SH [4,14,16]. Instead, other C-S-H phases are generated, such as tobermorite $Ca_5[Si_3O_8(OH)]_2\cdot4(H_2O)$ and xonotlite $Ca_6[Si_6O_{17}](OH)_2$, depending on the temperature, effective Ca/Si ratio, and the type of added silica [14,17,18].

However, compared with well cementing, the applications like constructing water tanks for thermal storage require a structure with much higher strength and anti-permeability. Such water tanks are usually made of copper, stainless steel, and vitreous enamel-lined carbon steel, but they suffer a short life cycle due to the commonly encountered corrosion and leakage. Concrete has also been explored to construct the water tanks and is commercially affordable for large-scale applications. Furthermore, a concrete water tank can be designed for larger capabilities and buried underground, minimizing the visual impact. However, the temperature of stored water is generally lower than 100 °C, i.e., below the water boiling point at atmospheric pressure, which restricts the energy storage density (the amount of energy per unit of volume or mass) and the applications of stored thermal energy [21–24]. At a constant tank volume, increasing the temperature of stored water is a viable solution, which means that the concrete structure has to withstand a long-term temperature-pressure load. UHPC with superior strength and durability has been used in large-span components, anti-explosive structures, and high-corrosion environments, and it may hold the potential as an alternative material for the construction of hot water pressure accumulators. In general, short-term hydrothermal curing after pre-curing is applied in UHPC production to obtain superior mechanical properties and durability. Such hydrothermal curing is normally with hot water/steam (60/90 °C) for 24-48 h or autoclaving for several hours [1,31–33]. However, the influence of long-term autoclaving on the properties of UHPC is still unclear. This is also the purpose of the present research work to clarify the influence of long-term autoclaving on UHPC and provide guidance for developing an applicable and sustainable UHPC as the construction material for hot water tanks.

Hydrothermal conditions can accelerate cement hydration and change the properties of the hydrates [19]. At high temperatures, the initial hydration proceeds fast with rapid hydrates precipitation during the first hours and days, leading to a fast early strength development [20]. However, this fast hydration in the early stage results in a heterogeneous distribution of hydrates as the products tend to precipitate around clinker particles, building up a dense shell around clinker particles and retarding the subsequent hydration. In contrast, the hydration starts slowly at low temperatures, giving the dissolved ions more time to diffuse before

precipitation. Thus, the gentle environment generates a less dense C-S-H and a more homogeneous microstructure [21,22].

The C-S-H formed at high temperatures has a high packing ratio characterized by an increased apparent C-S-H density from 2.03 kg/m^3 at 20 °C to 2.27 kg/m^3 at 60 °C (a schematic representation is shown in Fig. 1.1) [23]. Meanwhile, the polymerization degree of C-S-H is increased and the Ca/Si ratio of C-S-H is decreased by high temperatures [24,25]. The Ca/Si ratio of C-S-H depends on the available CaO and SiO_2 in the raw materials. At high temperatures, the solubility of SiO_2 increases, while the solubility of $Ca(OH)_2$ decreases, leading to an environment with a low Ca/Si ratio [26]. Besides, the adsorption of SO_4^{2-} and Al^{3+} into C-S-H is accelerated by elevated temperatures [24,25]. The water content of C-S-H decreases with temperatures [27]. Due to the increased C-S-H density, the intrinsic porosity of C-S-H decreases with temperature, leading to the increase of capillary porosity and the decrease of gel porosity (pore coarsening) [23,25,28]. In some cases, this phenomenon is used to explain the lower mechanical properties at later ages of hydrothermally cured samples [22,29–31].
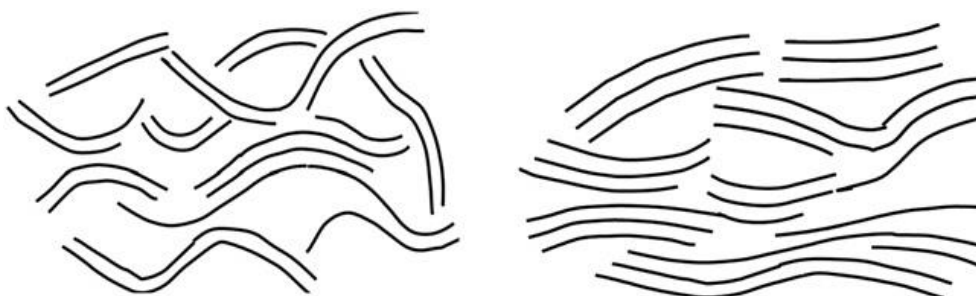

Fig. 1.1 A schematic representation of C-S-H arrangement at low temperatures (left) and high temperatures with denser packing and more nanocrystalline regions (right) [23].

Under autoclaving, amorphous C-S-H ceases to be stable and converts to various crystalline phases depending on the bulk chemical composition and the temperature [3]. The crystallinity of C-S-H increases, and the time required for this process diminishes qualitatively with increasing temperature [32]. Assarsson et al. pointed out that the poorly crystallized C-S-H without a definitive Ca/Si ratio first forms from the rapid reaction of $Ca(OH)_2$ with reactive SiO_2. In the second step, recrystallization under high temperatures transforms unstable and amorphous phases into more stable crystalline phases [32–34], which can be accompanied by leaching Ca^{2+} [35,36]. The structure of C-S-H is rather complex, and more than 30 crystalline hydrates have been identified [37]. The composition of these hydrates varies

significantly, with the Ca/Si ratio ranging from approximately 0.6 to 3.0 [38]. Concerning the thermal stability of these phases, experiments have been carried out over a broad temperature range. The first well-known phase diagram was proposed by Taylor in 1964, where a series of products were synthesized with different Ca/Si ratios in the temperature range of 50 to 1000 °C [39]. Later Hong et al. set up a revised diagram, as shown in Fig. 2 in paper No. 1 (Chapter 2.1), by synthesizing C-S-H with different SiO_2 and $Ca(OH)_2$ contents [38].

In contrast to the research on the CaO-SiO_2-H_2O system, Meller et al. added varying proportions of silica and corundum to oil well cement pastes and characterized the main mineralogical hydrates after 5 d of hydration at 200-350 °C as shown in Fig. 3 in paper No. 1 (Chapter 2.1) [40,41]. Compared with the CaO-SiO_2-H_2O system, there are some apparent deviations in the real cement system. The thermal stability of α-C_2SH is extended to 200 °C and of 11 Å tobermorite (incorporating Al) to 300 °C [40]. It is suggested that the impurities in cement change the phases' boundaries relative to those shown in Fig. 2 (Chapter 2.1). Furthermore, it should be noted that phase equilibrium might not be achieved in all cases as metastable intermediates may persist. Blanc et al. proposed a refined CaO-SiO_2-H_2O phase diagram based on thermodynamic calculations, although the stability field of jaffeite and α-C_2SH should be further refined [42]. Therefore, the influence of foreign ions (Al^{3+}, Na^+, K^+, Mg^{2+}, Fe^{3+} and SO_4^{2-}) and Ca/Si ratio on the hydration kinetics, including the formation of amorphous C-S-H and its transformation into crystalline phases, and hydrates characteristics under hydrothermal conditions are comprehensively reviewed (Chapter 2.1), in order to understand the influence of long-term autoclaving on the hydrates assemblage, microstructure, and mechanical strength of UHPC.

The aluminate hydrates are also sensitive to the curing temperature. At above 40 °C, calcium monosulphoaluminate increases at the expense of ettringite [43]. Besides, the ettringite formed at elevated temperatures (40/50 °C) presents as short needles [19]. Both ettringite and monosulphoaluminate phases become unstable at 80 °C, and hydrogarnet forms [44]. It is reported that only a trace of calcium sulfate is observed after one year in the samples cured at 50/80 °C, indicating that the released sulfate from ettringite may partially dissolve in the pore solution and adsorb into C-(A-)S-H [45]. Correspondingly, after curing at 5, 20, and 50 °C for 150 days, the sulfate concentration in the pore solution increases with the curing temperatures [19]. Besides, the released sulfate may also incorporate into hydrogarnet [44].

Delayed ettringite formation (DEF), which ettringite forms in hardened cementitious materials (the cement paste provides the sulfate), has mainly been observed in hydrothermally cured

concretes (usually above 70 °C) and may damage the concrete structures [46,47]. It is reported that some SCMs, e.g., fly ash and slag, used as the partial replacement of cement may relieve the expansion caused by DEF in hydrothermally cured products. The efficacy of controlling expansion relates to the effective Al_2O_3 content in SCMs. For example, metakaolin with a high amount of reactive Al_2O_3 can reduce the detrimental expansion more effectively than fly ash and slag. Silica fume thus is unlikely to reduce expansion and can only delay the expansion at high levels of replacement [48,49].

Various SCMs are increasingly used in cement-based materials to compensate for the high CO_2 emissions of cement production on the one hand, and improve the products' properties by filler effect and/or pozzolanic reaction on the other hand. In a conventional environment, the influence of SCMs is mainly determined by their physical properties, although in the long term, SCMs can chemically react, changing hydrates composition. However, under hydrothermal conditions, the reactivity of SCMs is significantly increased. In addition to the well-known pozzolanic reaction, the dissolved ions from SCMs, e.g., Al^{3+}, SO_4^{2-}, and Na^+, can also exert significant influence on the formation of C-S-H precursor and its transformation to crystalline phases [31,50,51]. Therefore, when SCMs are used under hydrothermal conditions, their chemical compositions should also be considered in addition to their physical properties.

As for siliceous fly ash, the consumption of portlandite, the formation of additional C-S-H, and the release of Al and Si into the pore solution are accelerated at high temperatures. The effective contents of Ca, Si, and Al in the matrix are thus changed, and the composition of C-S-H is altered accordingly. Parts of Al and alkalis incorporate into C-S-H, and the remaining Al precipitates in AFm phases or hydrogarnet at higher temperatures (50/80 °C) [44]. However, it is reported that the accelerated pozzolanic reaction of fly ash at 50 °C may compete with the cement hydration in consuming water, which suppresses the cement hydration [52]. At 20 °C, the addition of fly ash reduces the compressive strength at an early age, while hydrothermal curing can significantly attenuate this detrimental effect. Furthermore, the phenomenon of high-temperature inversion in compressive strength in the blended samples with fly ash is not apparent after 42 days of high-temperature curing [31].

The reactivity of blast furnace slag as a partial replacement of cement was evaluated using selective chemical dissolution, and it was found that the reactivity of slag increases with the hydration temperatures [50]. For the blended cement paste cured at 10 °C, only a very thin product rim is observed around slag particles, while the product rim of hydration can be clearly observed at 30 °C and 60 °C [20]. However, it is reported that the one-day compressive

strength of blended samples with slag slightly decreases compared with that of a plain sample, which is explained by the decrease of C-S-H as the hydration of slag is not much activated by the high-temperature curing [53]. According to backscattered electron images, high temperature curing at 70 °C leads to a coarser and more continuous pore structure in the neat samples, but the addition of slag is helpful to reduce the pores size and continuity [54].

For metakaolin, a higher compressive strength (one day) can be obtained in blended mortars compared with the plain mortar at hydrothermal curing. The increased compressive strength is explained by the increase of C-(A-)S-H, the decrease of Ca/Si ratio, and the decrease of portlandite [53]. It is also reported that the addition of metakaolin densifies the pore structures at 60 °C [55]. At 20 °C, C-S-H, stratlingite (C_2ASH_8), and tetra calcium aluminate hydrate (C_4AH_{13}) are the most important hydrates in blended samples with metakaolin. However, the stability of C_2ASH_8 and C_4AH_{13} decreases with the increase of temperatures and hydrogarnet instead forms at high temperatures. Such conversion may negatively affect the microstructure and properties of the blended samples due to the solid volume variation [55,56]. Therefore, the use of metakaolin at high temperatures deserves attention as the formation and evolution of hydrates and the reactivity of raw materials can be significantly changed by the hydration temperatures [57,58].

The addition of silica fume can also increase the compressive strength after curing at 50 °C, which enhances with the increase of silica fume. However, the compressive strength of the samples after hydrothermal curing increases slowly, while the samples at 20 °C show a relatively rapid increase of compressive strength, leading to a slightly higher strength after 91 days compared with the hydrothermally cured samples [59]. It is also reported that silica fume can densify the microstructure (70 °C) [54]. Due to the active pozzolanic reaction, the pH of the pore solution can be effectively reduced. In the ternary system of blended cement pastes with slag and silica fume, the reactivity of slag is still low under hydrothermal conditions (125 °C), which is attributed to the reduced pH of pore solution and the dense microstructure [60].

1.2 Ultra-high performance concrete

Compared with conventional normal and high-strength concrete, UHPC has ultra-high mechanical properties and ultra-high durability. The ways to obtain this superior performance include optimizing granulometric distribution, incorporating ultra-fine components, and decreasing the water/binder ratio [61–64]. The grading optimization can be achieved by iterative experimentation and numerical modeling based on the characteristics of the raw

materials. Targeting the high particle packing density, two types of models are developed; Discrete models predict the packing density of UHPC based on mono-sized particle groups, e.g., linear packing density model [65], solid suspension model [66], and compressible packing model [67]. Continuous models use the particle size distributions of raw materials to improve the packing density, represented by Fuller and Thompson curve [68], Andreasen & Andersen (A&A) packing model [69], and modified A&A model [70]. Considering the effect of water and superplasticizer, the wet particle packing method is also proposed to design UHPC mixtures and a higher particle packing density can be achieved [71,72]. However, the high particle packing density does not necessarily lead to the desired performance of UHPC, especially rheological properties. The rheological properties of UHPC are influenced by many factors, e.g., particle characteristics (size, morphology, and volume fraction), fiber content, the type and quantity of the superplasticizer, and water content [73–75]. Thus, performance-based model is proposed for designing UHPC mixtures [72,76,77].

The ingredients of UHPC usually contain cement, ultrafine filler, quartz powder/sand (fine aggregate), water, and superplasticizer. Although the aggregate used in UHPC is usually less than 2 mm, the UHPC with coarse aggregate has also been developed [78–81]. The water/binder (cement + silica fume, w/b) ratio roughly ranges from 0.16 to 0.23. No significant decrease in compressive strength is observed when the w/b ratio increases from 0.18 to 0.23 [82]. However, a high w/b ratio may lead to the formation of capillary pores, resulting in the degradation of impervious microstructure as UHPC has a much denser matrix with virtually no capillary pores [83]. Intensive mixers are needed to homogenize UHPC mixtures due to the high proportions of fine particles compared with normal concrete.

Some examples of UHPC mixtures are shown in Fig. 1.2 [83]. A typical ultrafine filler is silica fume with particle sizes in the sub-micrometer range. The effects of silica fume in UHPC are mainly expressed by pozzolanic reaction and filler effect, controlled by the surface area and reactivity of silica fume. For example, the silica fume with high reactivity dissolves easily and presents a dominantly pozzolanic reaction, while the silica fume with low reactivity and large size tends to favor the filler effect [63,84,85]. The pozzolanic reaction consumes portlandite, generating additional C-S-H. However, due to the low water content in UHPC, the pozzolanic reaction is limited and the filler effect is facilitated. The filler effect of silica fume is twofold: filling the voids among cement particles and serving as nucleation sites for hydrates which accelerates the hydration of clinkers. Silica fume can decrease plastic viscosity at a low content and increase the water demand and plastic viscosity at a high content (particles agglomeration, entrapment of air voids and non-uniform fiber dispersion). The appropriate addition of silica

fume densifies microstructure and improves the matrix-fiber bond, strengthening mechanical properties [86,87]. For hydrothermally cured UHPC, the silica fume with high pozzolanic reactivity accelerates the substitution of Al for Si in the bridging site of C-S-H and densifies microstructure, leading to a high compressive strength during hydrothermal curing; the silica fume with low pozzolanic reactivity favors the precipitation of Al in AFm phases [63]. However, after hydrothermal curing, the UHPC containing silica fume with low pozzolanic reactivity (high filler effect) presents further hydration of silicate clinkers, a higher fraction of Q^1 of C-S-H, a lower porosity in the range of pore diameter below 10 nm, and thus a higher compressive strength [63]. Note that the effective dispersion of silica fume also favors the improvement of mechanical strength [85].
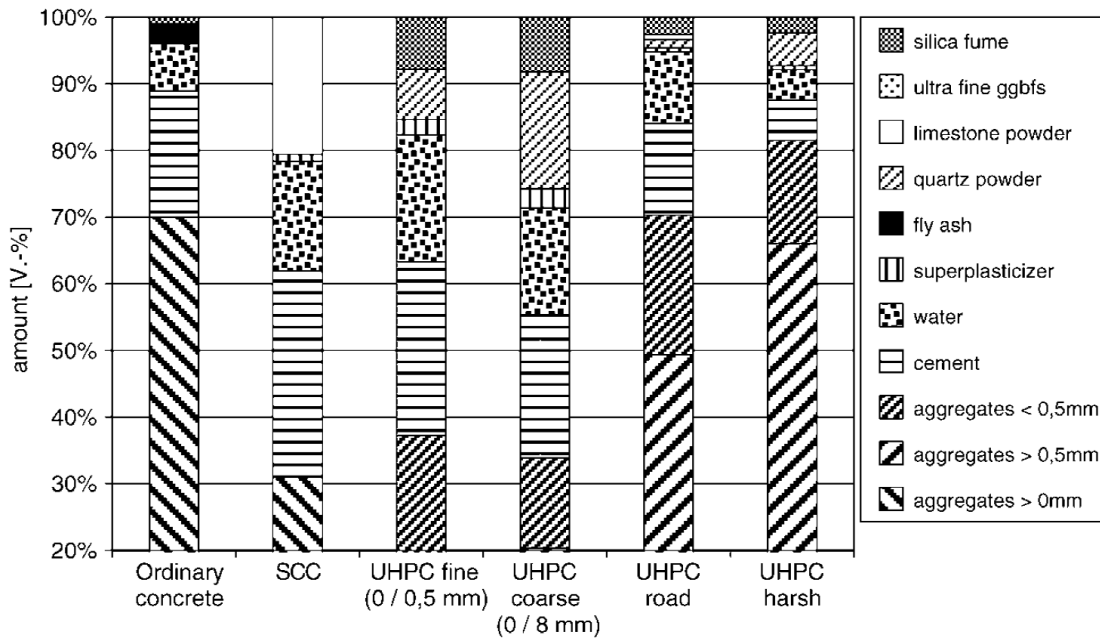

Fig. 1.2 The comparison of mixture compositions between normal concrete and UHPC [83].

However, due to the high cost of raw materials (large amounts of cement, silica fume, and quartz powder/sand), the production of UHPC is usually expensive and environment-unfriendly. To this end, various SCMs have been used to replace cement partially. The flowability of UHPC can be increased by incorporating fly ash mainly due to the lubricating effect by the spherical particles [88,89]. Besides, the addition of fly ash increases the degree of cement hydration at later ages, and the pozzolanic reaction may improve the microstructure, leading to increased mechanical properties and anti-permeability [11,90,91]. However, the blended UHPC with fly ash may suffer a retarded early hydration and a low early age strength due to the dilution effect and the decrease of Ca concentration in the pore solution by fly ash

[92]. The UHPC added with slag also presents increased workability and a poor early age strength, but incorporating slag at an appropriate content can increase the compressive and split tensile strength [88,93,94].

Metakaolin can be used as a partial replacement for silica fume and cement, depending on the particle sizes. In the cement pastes with a w/b ratio of 0.2, the replacement of cement by metakaolin (5 to 15 wt. %) results in a decreased total hydration heat release in the first three days. The UHPC mortars with metakaolin thus present a low early age mechanical strength. However, the blended mixtures achieve stronger compressive and flexural strength after 14 days because, in the blended samples, portlandite increases in the first two days and significantly decreases at later ages by the pozzolanic reaction. The pore structures after 28 days are also densified by metakaolin [95]. The substitution of fine metakaolin for silica fume can also produce the UHPC with equivalent mechanical strength [96]. Besides, limestone powder can partially replace cement and quartz powder without a negative impact on mechanical strength [97]. Limestone particles possess plasticizing effect and induce better workability by partially replacing cement. Appropriate addition of limestone powder can lead to a densified pore structure and enhanced mechanical strength [98]. Furthermore, many other SCMs have also been explored in UHPC to improve sustainability, such as natural pozzolan [99], phosphorous slag [100], iron ore tailing [101], red mud [102], recycled construction waste [103], recycled rock dust [104], and gold tailings [105]. Although the partial replacement of cement by these SCMs with low reactivity induces a low early age mechanical strength, comparable performance of UHPC at later ages can be achieved by their addition with appropriate contents.

A typical substitution of silica fume is rice husk ash (RHA). It is reported that RHA has a mesoporous structure, which can adsorb a certain amount of water. Thus, the addition of RHA in UHPC can decrease the content of free water and release water in the subsequent hydration, leading to enhanced mechanical strength and a decreased autogenous shrinkage (slowing down the reduction of the internal relative humidity in UHPC) [106,107]. However, replacing silica fume with RHA reduces the fluidity of fresh UHPC, and RHA induces a weaker pozzolanic reaction in consuming portlandite compared with silica fume [108,109].

As for the fine aggregate in UHPC, conventional natural and manufactured fine aggregates have also been used to replace quartz sand [110–112]. However, the replacement may decrease the particle packing density, and more silica fume is needed to achieve the equivalent mechanical strength [111]. Besides, the variation of sand gradation may impact the

rheological properties [113]. Glass sand as fine aggregate is also used in UHPC, but the expansion caused by alkali-silica reaction should be considered [114,115]. The UHPC mixtures with coarse aggregate are also developed. It is reported that the incorporation of coarse basalt aggregate results in a slight decrease of mechanical strength, and the mechanical strength decreases with the increase of particle size of basalt aggregate [80]. However, the UHPC mixtures with coarse aggregate perform better in resisting explosive spalling than the UHPC mixtures without coarse aggregate, benefiting from the reduction of inner thermal stress in UHPC by coarse aggregate [79]. Besides, the adoption of coarse aggregate can decrease shrinkage [116]. It is reported that the coarse dolomite aggregate behaves better in maintaining the mechanical properties than coarse basalt aggregate [78,110].

Discrete fibers are usually introduced as reinforcement to improve the ductility of UHPC without sacrificing compressive strength. The texture, aspect ratio, shape, and surface property of fibers significantly affect the behavior of fibers in UHPC. For fiber-reinforced UHPC, the matrix initially sustains the external load and the fiber by transferring stress at the matrix-fiber bond. There are two failure modes of debonding when fibers are pulled out from the matrix. Fiber fracture is not desired for the UHPC reinforcement. The bond strength between matrix and fibers mainly comes from adhesion bond, friction, and mechanical anchorage of fibers [117]. During pulling out, the adhesion bond is first broken, and then friction and/or mechanical anchorage come into effect, accompanied by the fibers' slippage. Steel fiber is most widely used in UHPC. As for straight fibers with different lengths of 6, 13, and 20 mm, longer fibers (2 vol. %) provide a greater pullout strength and ensure the UHPC with higher flexural strength and toughness [118]. The decrease of portlandite can significantly increase the bond strength between matrix and straight fibers [119]. It is reported that deformed steel fibers, such as corrugated and hooked steel fibers, can provide a stronger enhancement in the post-peak response and ductility of UHPC than straight steel fibers [119,120]. However, the enhancing effect on the first crack strength is limited, although the ultimate flexural strength can be markedly increased by incorporating steel fibers [119].

The use of deformed steel fibers and the increase of steel fibers content may decrease the workability of UHPC [120]. Adequate workability of UHPC mixtures is necessary for obtaining a uniform distribution of steel fibers, which contributes to the enhancement of flexural and tensile strength [121]. High plastic viscosity and yield stress of the mixtures during mixing block the dispersion of the fiber, while low plastic viscosity and yield stress may cause segregation during the casting process. It is reported that for the UHPC with 1, 2, and 3 vol. % steel fibers,

the appropriate yield stress of fresh mixtures can range among 900-1000 Pa, 700-900 Pa, and 400-800 Pa, respectively [122]. In addition to adjusting the rheological properties, optimizing the casting method, such as the use of electromagnetic field and optimization of outlet height, can also improve the fibers' distribution. The optimal horizontal outlet height during casting is related to the length of steel fibers, and an enhanced flexural strength and toughness can be obtained when the ratio of fiber length to horizontal outlet height is 1.1 [118]. Note that this value should change with the rheological properties of the mixtures. Compared with the mixtures with randomly oriented steel fibers, the optimization of fibers orientation can lead to the increase of tensile strength by 30%-90%, flexural strength by 10%-80%, and toughness by 20%-100%. Such fibers' alignment corresponding to the direction of principal tensile stress allows using a lower content of steel fibers to achieve the equivalent mechanical strength of UHPC [123,124]. Surface modification of steel fibers is also used to improve the bond strength. The new chemical bond forms between the matrix and the steel fibers modified by silane coupling agent, and the modified steel fibers show an increased surface roughness. Thus, the reinforced UHPC present stronger flexural properties and a larger energy adsorption capacity compared with the UHPC with unmodified steel fibers [125].

Although UHPC possesses superior mechanical strength and durability, some defects still exist in UHPC, such as shrinkage and explosive spalling under fire conditions. Due to the high cement content and low w/b ratio, UHPC usually exhibits a high shrinkage in early ages, which autogenous shrinkage accounts for the most. The autogenous shrinkage is caused by the internal self-desiccation and chemical shrinkage during matrix hardening [126]. Many methods have been proposed to relieve shrinkage, such as shrinkage reducing admixture (SRA), expansive admixture, and internal curing [127]. SRA is a kind of surfactant and composed of a hydrophilic (polar) head and a hydrophobic (non-polar) tail. SRA can function at the water-air interface (pore solution), decreasing the surface tension, capillary stress, and thus shrinkage strain. In addition, the use of SRA can adjust the cement hydration and increase the internal relative humidity, which also accounts for shrinkage mitigation [128–132].

The incorporation of superabsorbent polymer (SAP) as internal curing has been proved to reduce autogenous shrinkage by gradually releasing the pre-adsorbed water and slowing down the decrease of internal relative humidity [133]. The efficiency of SAP is highly dependent on its physical and chemical characteristics. For example, the SAP with a low density of anionic groups has slow liquid adsorption and release kinetics. It releases the stored water at late ages, providing efficient mitigation of autogenous shrinkage [134]. Besides, the rheological properties of UHPC are also affected by the kinetics of water adsorption [135]. Although the

addition of SAP delays the main hydration peak, the degree of hydration after a couple of days is increased [133]. However, if the newly formed hydrates cannot fill the pores left from SAP, the microstructure and mechanical strength may be degraded by the SAP incorporation [133,136]. Appropriate addition of pre-wetted porous aggregate can also effectively reduce autogenous shrinkage without sacrificing mechanical strength [137,138]. Furthermore, replacing cement with less reactive SCMs hinders cement hydration, benefiting the reduction of autogenous shrinkage [139]. The existence of steel fibers can provide internal restraints, resisting shrinkage stress, and deformed fibers performs better than straight fibers in reducing shrinkage [140].

Compared with conventional concrete, UHPC is more susceptible to spalling under fire conditions and elevated temperatures due to the dense microstructure, absence of capillary pores, and low permeability. The compressive strength of UHPC increases after being treated at around 200-400 ºC for several hours, but the flexural strength markedly decreases with the increase of heat duration. As the temperature exceeds around 400 ºC, explosive spalling is observed in UHPC due to the water vaporization, hydrates decomposition, and thermal mismatch of solid phases, accompanied by the degradation of mechanical strength [141]. Three main mechanisms of the clogging effect, thermal gradient, and the combination of the clogging and thermal gradient are proposed to explain the concrete spalling. When the concrete is subjected to elevated temperatures, free water is vaporized and bound water is released by hydrates decomposition, generating internal gas pressure. Once the gas pressure exceeds the tensile strength, the concrete starts to spall. As the temperature increases, the concrete structures usually suffer a thermal gradient, accompanied by thermal stress [142]. Polypropylene (PP) fibers are usually used to reduce the risk of spalling. Due to the thermal mismatch, micro-cracks occur in the matrix-fiber interface under high temperatures. With the further increase of temperature, the fibers melting (melting temperature at ~165 °C) connects the isolated pores and porous matrix-aggregate interface, releasing the steam and thus the internal vapor pressure [143,144]. The addition of PP fibers increases the pore connectivity and permeability of UHPC under elevated temperatures, which relieves the spalling risk [145–147]. Furthermore, the combined use of PP fibers with coarse aggregate presents a synergistic effect in preventing spalling [145,147].

In order to further improve the performance of UHPC, UHPC components are usually cured at hot water/steam (< 100 °C) for 24-48 h or autoclaving for several hours [1,11,83,148]. Once subjected to high temperatures, the heat flow generated from cement hydration and pozzolanic reaction is sharply increased, and a higher temperature exerts a stronger effect, as shown in

Fig. 1.3. However, the heat flow gradually decreases and cumulative heat tends to be steady after the initial 12 h of hydrothermal curing [149]. Due to the accelerated hydration and pozzolanic reaction, the UHPC shows an enhanced microstructure and thus stronger mechanical strength. Furthermore, the enhancing effect increases with the curing temperature by comparing the five types of curing regimes: standard curing at 20 °C for 28 d, steam curing at 60 °C for 48 h, steam curing at 90 °C for 48 h, autoclaving at 200 °C for 8 h, and autoclaving at 250 °C for 8 h [150]. Besides, the nano-mechanical property is also intensified, and the autoclaved samples present higher values than stream cured samples. Hydrothermal curing accelerates the formation of C-S-H with high density, while this effect increases with the curing temperatures [150]. For the fiber-reinforced UHPC, no porous matrix-fiber interface is observed after hydrothermal curing and enhanced interfacial bond strength is obtained [150,151].
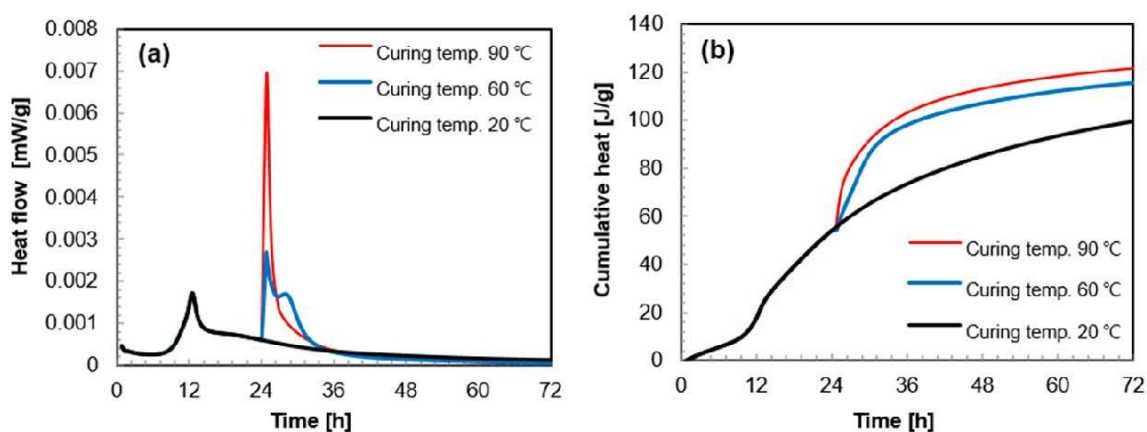

Fig. 1.3 Heat flow (a) and cumulative heat (b) of UHPC cured under 20, 60, and 90 °C (the hydrothermal curing starts from 24 h) [149].

However, after heat curing at 60 °C, the compressive strength slightly increases or maintain until 28 days, and a slight decrease of compressive strength is even observed from 7 to 28 days when the UHPC is cured at 90 °C for longer than 18 h (Fig. 1.4) [149]. Besides, although the matrix-fiber bond is improved, high-temperature curing increases the risk of fiber fracture and thus brittle failure of UHPC, especially for the UHPC reinforced with deformed fibers [152]. Due to heat curing, the UHPC shrinkage is also aggregated, and more serious shrinkage is observed in the UHPC cured at higher temperatures [153,154]. A slight specimen expansion after the curing temperature cooling down is reported in some cases, probably due to the ettringite formation [13]. In addition to the temperature and duration, the UHPC performance

is also affected by the pre-storage time before the heat treatment, and the optimum pre-storage time relates to the curing temperature, duration, and matrix composition [155].
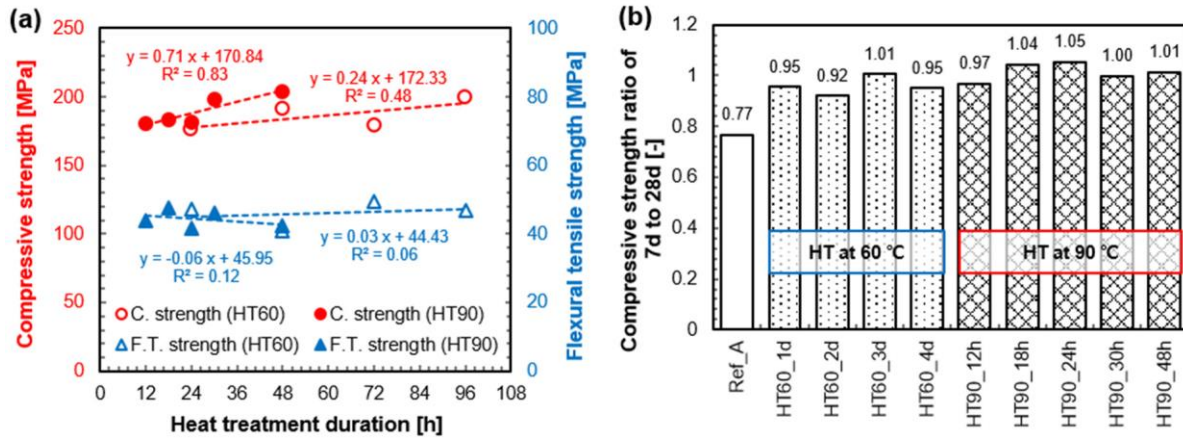

Fig. 1.4 Compressive and flexural strength of UHPC after 28 days as a function of temperature and duration of heat treatment (a); and the compressive strength ratio of 7 to 28 days (b) [149].

As for the blended UHPC, the incorporated SCMs can be activated by heat curing, and more incorporation is allowed in the hydrothermally cured UHPC. The compressive strength of blended UHPC with slag or fly ash is increased by heat curing (90 °C for 48 h), while the compressive strength decreases with the increase of slag or fly ash content [88]. As for autoclaving (156, 183, and 203 °C), the compressive strength of UHPC with fly ash increases as the duration increases from 6 to 8 h, but the compressive strength decreases after longer autoclaving. For the UHPC with 10 wt. % fly ash, autoclaving at 183 °C ensures the UHPC a higher compressive strength. However, for the UHPC with 20 or 30 wt. % fly ash, the samples after autoclaving at 203 °C show higher compressive strengths, indicating that a higher temperature is suitable for the UHPC mixtures with more fly ash and the optimal curing regime relates to the mixture compositions. Compared with plain UHPC, the addition of fly ash also increases the flexural strength of blended UHPC after autoclaving. Besides, overlong autoclaving may degrade the flexural strength of UHPC [11].

1.3 Research objectives

For the applications of UHPC under autoclaving, such as constructing hot water tanks for thermal storage, the UHPC structures are thus loaded by a permanent autoclaving (temperature-pressure) load. However, the published literature about the influence of long-term autoclaving on UHPC is still limited. The present work is based on the research project

of designing UHPC tanks to store the hot water with a temperature up to 200 °C. Therefore, the main objectives of this work are to study the hydrates assemblage, microstructure, and mechanical strength of UHPC under long-term autoclaving, providing guidance for developing an applicable and sustainable UHPC as the construction material for hot water tanks. Fly ash or limestone powder as a partial replacement of cement is introduced to adjust the chemical compositions of the matrix and improve the performance of UHPC under autoclaving. The sustainability of UHPC is also improved by the addition of fly ash or limestone powder.

In addition to the final performance of UHPC after long-term autoclaving, the evolution of hydrates assemblage and pore structures of cement pastes with autoclaving is further studied. The cement pastes include the pure cement paste and the blended cement pastes with varied contents of fly ash and quartz powder. A commercial UHPC compound is later studied to confirm the findings derived from the previous sections.

1.4   References

[1]   T. Zdeb, An analysis of the steam curing and autoclaving process parameters for reactive powder concretes, Construction and Building Materials 131 (2017) 758–766.

[2]   N. Arabi, R. Jauberthie, N. Chelghoum, L. Molez, Formation of C-S-H in calcium hydroxide–blast furnace slag–quartz–water system in autoclaving conditions, Advances in Cement Research 27 (2015) 153–162.

[3]   E.B. Nelson, D. Guillot, Well cementing, 2nd ed., Schlumberger, Sugar Land, Tex., 2006.

[4]   S.L. Colston, P. Barnes, A.C. Jupe, S.D.M. Jacques, C. Hall, P. Livesey, J. Dransfield, N. Meller, G.C. Maitland, An in situ synchrotron energy-dispersive diffraction study of the hydration of oilwell cement systems under high temperature/autoclave conditions up to 130 °C, Cement and Concrete Research 35 (2005) 2223–2232.

[5]   F. Cassagnabère, G. Escadeillas, M. Mouret, Study of the reactivity of cement/metakaolin binders at early age for specific use in steam cured precast concrete, Construction and Building Materials 23 (2009) 775–784.

[6]   J.L. García Calvo, M.C. Alonso, L. Fernández Luco, M. Robles Velasco, Durability performance of sustainable self compacting concretes in precast products due to heat curing, Construction and Building Materials 111 (2016) 379–385.

[7]   L. Cai, B. Ma, X. Li, Y. Lv, Z. Liu, S. Jian, Mechanical and hydration characteristics of autoclaved aerated concrete (AAC) containing iron-tailings: Effect of content and fineness, Construction and Building Materials 128 (2016) 361–372.

[8]   Y.L. Chen, M.S. Ko, J.E. Chang, C.T. Lin, Recycling of desulfurization slag for the production of autoclaved aerated concrete, Construction and Building Materials 158 (2018) 132–140.

[9]   M. Chen, L. Lu, S. Wang, P. Zhao, W. Zhang, S. Zhang, Investigation on the formation of tobermorite in calcium silicate board and its influence factors under autoclaved curing, Construction and Building Materials 143 (2017) 280–288.

[10] Z. Wang, S. Ma, S. Zheng, J. Ding, X. Wang, Flexural strength and thermal conductivity of fiber-reinforced calcium silicate boards prepared from fly ash, Journal of Materials in Civil Engineering 31 (2019) 4019140.

[11] T. Chen, X. Gao, M. Ren, Effects of autoclave curing and fly ash on mechanical properties of ultra-high performance concrete, Construction and Building Materials 158 (2018) 864–872.

[12] S. Kim, N. Lee, H.K. Lee, S. Park, Experimental and theoretical studies of hydration of ultra-high performance concrete cured under various curing conditions, Construction and Building Materials 278 (2021) 122352.

[13] P. Shen, L. Lu, Y. He, M. Rao, Z. Fu, F. Wang, S. Hu, Experimental investigation on the autogenous shrinkage of steam cured ultra-high performance concrete, Construction and Building Materials 162 (2018) 512–522.

[14] E. Grabowski, J.E. Gillott, Effect of replacement of silica flour with silica fume on engineering properties of oilwell cements at normal and elevated temperatures and pressures, Cement and Concrete Research 19 (1989) 333–344.

[15] D. Mangold, Seasonal storage–a German success story, Sun & Wind Energy 1 (2007) 48–58.

[16] G. Le Saoût, E. Lécolier, A. Rivereau, H. Zanni, Chemical structure of cement aged at normal and elevated temperatures and pressures, Part II: Low permeability class G oilwell cement, Cement and Concrete Research 36 (2006) 428–433.

[17] K.J. Krakowiak, J.J. Thomas, S. Musso, S. James, A.-T. Akono, F.-J. Ulm, Nano-chemo-mechanical signature of conventional oil-well cement systems: Effects of elevated temperature and curing time, Cement and Concrete Research 67 (2015) 103–121.

[18] J. Makar, K. Luke, Thermal Stability of the Cement Sheath in Steam Treated Oil Wells, Journal of the American Ceramic Society 94 (2011) 4463–4470.

[19] B. Lothenbach, F. Winnefeld, C. Alder, E. Wieland, P. Lunk, Effect of temperature on the pore solution, microstructure and hydration products of Portland cement pastes, Cement and Concrete Research 37 (2007) 483–491.

[20] J. Escalante-García, J. Sharp, The microstructure and mechanical properties of blended cements hydrated at various temperatures, Cement and Concrete Research 31 (2001) 695–702.

[21] K.O. Kjellsen, R.J. Detwiler, Reaction kinetics of portland cement mortars hydrated at different temperatures, Cement and Concrete Research 22 (1992) 112–120.

[22] J.I. Escalante-García, J.H. Sharp, Effect of temperature on the hydration of the main clinker phases in portland cements: part i, neat cements, Cement and Concrete Research 28 (1998) 1245–1257.

[23] E. Gallucci, X. Zhang, K.L. Scrivener, Effect of temperature on the microstructure of calcium silicate hydrate (C-S-H), Cement and Concrete Research 53 (2013) 185–195.

[24] S. Bahafid, S. Ghabezloo, P. Faure, M. Duc, J. Sulem, Effect of the hydration temperature on the pore structure of cement paste: Experimental investigation and micromechanical modelling, Cement and Concrete Research 111 (2018) 1–14.

[25] S. Bahafid, S. Ghabezloo, M. Duc, P. Faure, J. Sulem, Effect of the hydration temperature on the microstructure of Class G cement: C-S-H composition and density, Cement and Concrete Research 95 (2017) 270–281.

[26] N. Narayanan, K. Ramamurthy, Structure and properties of aerated concrete: a review, Cement and Concrete Composites 22 (2000) 321–329.

[27] F. Avet, K. Scrivener, Effect of temperature on the water content of C-A-S-H in plain Portland and blended cements, Cement and Concrete Research 136 (2020) 106124.

[28] H.M. Jennings, J.J. Thomas, J.S. Gevrenov, G. Constantinides, F.-J. Ulm, A multi-technique investigation of the nanoporosity of cement paste, Cement and Concrete Research 37 (2007) 329–336.

[29] A. Bentur, R. L. Berger, J. H. Kung, N. B. Milestone, J. F. Young, Structural properties of calcium silicate pastes: II, Effect of curing temperature, Journal of the American Ceramic Society 62 (1979) 362–366.

[30] K.O. Kjellsen, R.J. Detwiler, O.E. Gjørv, Pore structure of plain cement pastes hydrated at different temperatures, Cement and Concrete Research 20 (1990) 927–933.

[31] Y. Maltais, J. Marchand, Influence of curing temperature on cement hydration and mechanical strength development of fly ash mortars, Cement and Concrete Research 27 (1997) 1009–1020.

[32] G.O. Assarsson, Hydrothermal reactions between calcium hydroxide and amorphous silica: the reactions between 180 and 220°, The Journal of Physical Chemistry 61 (1957) 473–479.

[33] G.O. Assarsson, E. Rydberg, Hydrothermal reactions between calcium hydroxide and amorphous silica, The Journal of Physical Chemistry 60 (1956) 397–404.

[34] T. Mitsuda, H.F.W. Taylor, Influence of aluminium on the conversion of calcium silicate hydrate gels into 11 Å tobermorite at 90°C and 120°C, Cement and Concrete Research 5 (1975) 203–209.

[35] T. Mitsuda, K. Sasaki, H. Ishida, Phase evolution during autoclaving process of aerated concrete, Journal of the American Ceramic Society 75 (1992) 1858–1863.

[36] F.P. Glasser, S.Y. Hong, Thermal treatment of C–S–H gel at 1 bar H_2O pressure up to 200 C, Cement and Concrete Research 33 (2003) 271–279.

[37] H. F. W. Taylor, Cement Chemistry, 2nd ed, Thomas Telford, London, 1997.

[38] S.Y. Hong, F.P. Glasser, Phase relations in the $CaO\text{-}SiO_2\text{-}H_2O$ system to 200 °C at saturated steam pressure, Cement and Concrete Research 34 (2004) 1529–1534.

[39] H.F.W. Taylor, The Chemistry of Cement. Academic Press, London, 1964.

[40] N. Meller, K. Kyritsis, C. Hall, The mineralogy of the $CaO–Al_2O_3–SiO_2–H_2O$ (CASH) hydroceramic system from 200 to 350 °C, Cement and Concrete Research 39 (2009) 45–53.

[41] N. Meller, C. Hall, J.S. Phipps, A new phase diagram for the $CaO\text{-}Al_2O_3\text{-}SiO_2\text{-}H_2O$ hydroceramic system at 200 °C, Materials Research Bulletin 40 (2005) 715–723.

[42] P. Blanc, X. Bourbon, A. Lassin, E.C. Gaucher, Chemical model for cement-based materials: Temperature dependence of thermodynamic functions for nanocrystalline and crystalline C–S–H phases, Cement and Concrete Research 40 (2010) 851–866.

[43] J.J. Thomas, D. Rothstein, H.M. Jennings, B.J. Christensen, Effect of hydration temperature on the solubility behavior of Ca-, S-, Al-, and Si-bearing solid phases in Portland cement pastes, Cement and Concrete Research 33 (2003) 2037–2047.

[44] F. Deschner, B. Lothenbach, F. Winnefeld, J. Neubauer, Effect of temperature on the hydration of Portland cement blended with siliceous fly ash, Cement and Concrete Research 52 (2013) 169–181.

[45] T.T.H. Bach, C.C.D. Coumes, I. Pochard, C. Mercier, B. Revel, A. Nonat, Influence of temperature on the hydration products of low pH cements, Cement and Concrete Research 42 (2012) 805–817.

[46] R. Barbarulo, H. Peycelon, S. Prené, J. Marchand, Delayed ettringite formation symptoms on mortars induced by high temperature due to cement heat of hydration or late thermal cycle, Cement and Concrete Research 35 (2005) 125–131.

[47] H. Taylor, C. Famy, K. Scrivener, Delayed ettringite formation, Cement and Concrete Research 31 (2001) 683–693.

[48] T. Ramlochan, M.D.A. Thomas, R.D. Hooton, The effect of pozzolans and slag on the expansion of mortars cured at elevated temperature: Part II: Microstructural and microchemical investigations, Cement and Concrete Research 34 (2004) 1341–1356.

[49] T. Ramlochan, P. Zacarias, M. Thomas, R.D. Hooton, The effect of pozzolans and slag on the expansion of mortars cured at elevated temperature: Part I: Expansive behaviour, Cement and Concrete Research 33 (2003) 807–814.

[50] J. Escalante, L. Gómez, K. Johal, G. Mendoza, H. Mancha, J. Méndez, Reactivity of blast-furnace slag in Portland cement blends hydrated under different conditions, Cement and Concrete Research 31 (2001) 1403–1409.

[51] J.I. Escalante-García, J.H. Sharp, Effect of temperature on the hydration of the main clinker phases in portland cements: part II, blended cements, Cement and Concrete Research 28 (1998) 1259–1274.

[52] M. Narmluk, T. Nawa, Effect of fly ash on the kinetics of Portland cement hydration at different curing temperatures, Cement and Concrete Research 41 (2011) 579–589.

[53] F. Cassagnabère, M. Mouret, G. Escadeillas, Early hydration of clinker–slag–metakaolin combination in steam curing conditions, relation with mechanical properties, Cement and Concrete Research 39 (2009) 1164–1173.

[54] Y. Cao, R.J. Detwiler, Backscattered electron imaging of cement pastes cured at elevated temperatures, Cement and Concrete Research 25 (1995) 627–638.

[55] M.F. Rojas, M.I. Sánchez de Rojas, Influence of metastable hydrated phases on the pore size distribution and degree of hydration of MK-blended cements cured at 60 °C, Cement and Concrete Research 35 (2005) 1292–1298.

[56] P.S. de Silva, F.P. Glasser, Phase relations in the system CaO-Al2O$_3$-SiO$_2$-H$_2$O relevant to metakaolin - calcium hydroxide hydration, Cement and Concrete Research 23 (1993) 627–639.

[57] D.S. Klimesch, A. Ray, Hydrogarnet formation during autoclaving at 180°C in unstirred metakaolin-lime-quartz slurries, Cement and Concrete Research 28 (1998) 1109–1117.

[58] M.S. Morsy, A.F. Galal, S.A. Abo-El-Enein, Effect of temperature on phase composition and microstructure of artificial pozzolana-cement pastes containing burnt kaolinite clay, Cement and Concrete Research 28 (1998) 1157–1163.

[59] S. Wild, B.B. Sabir, J.M. Khatib, Factors influencing strength development of concrete containing silica fume, Cement and Concrete Research 25 (1995) 1567–1580.

[60] Y. Xi, D.D. Siemer, B.E. Scheetz, Strength development, hydration reaction and pore structure of autoclaved slag cement with added silica fume, Cement and Concrete Research 27 (1997) 75–82.

[61] A. Arora, M. Aguayo, H. Hansen, C. Castro, E. Federspiel, B. Mobasher, N. Neithalath, Microstructural packing- and rheology-based binder selection and characterization for Ultra-high Performance Concrete (UHPC), Cement and Concrete Research 103 (2018) 179–190.

[62] A. Arora, A. Almujaddidi, F. Kianmofrad, B. Mobasher, N. Neithalath, Material design of economical ultra-high performance concrete (UHPC) and evaluation of their properties, Cement and Concrete Composites 104 (2019) 103346.

[63] N.K. Lee, K.T. Koh, M.O. Kim, G.S. Ryu, Uncovering the role of micro silica in hydration of ultra-high performance concrete (UHPC), Cement and Concrete Research 104 (2018) 68–79.

[64] P. Richard, M. Cheyrezy, Composition of reactive powder concretes, Cement and Concrete Research 25 (1995) 1501–1511.

[65] T. Stovall, F. de Larrard, M. Buil, Linear packing density model of grain mixtures, Powder Technology 48 (1986) 1–12.

[66] F. de Larrard, T. Sedran, Optimization of ultra-high-performance concrete by the use of a packing model, Cement and Concrete Research 24 (1994) 997–1009.

[67] F. de Larrard, T. Sedran, Mixture-proportioning of high-performance concrete, Cement and Concrete Research 32 (2002) 1699–1704.

[68] W.B. Fuller, S.E. Thompson, The laws of proportioning concrete (1907).

[69] A.H.M. Andreasen, Ueber die Beziehung zwischen Kornabstufung und Zwischenraum in Produkten aus losen Körnern (mit einigen Experimenten), Kolloid-Zeitschrift 50 (1930) 217–228.

[70] J.E. Funk, D. Dinger, Predictive process control of crowded particulate suspensions: Applied to ceramic manufacturing, Springer Science & Business Media, 1993.

[71] X. Wang, R. Yu, Q. Song, Z. Shui, Z. Liu, S. Wu, D. Hou, Optimized design of ultra-high performance concrete (UHPC) with a high wet packing density, Cement and Concrete Research 126 (2019) 105921.

[72] F. Dingqiang, Y. Rui, S. Zhonghe, W. Chunfeng, W. Jinnan, S. Qiqi, A novel approach for developing a green Ultra-High Performance Concrete (UHPC) with advanced particles packing meso-structure, Construction and Building Materials 265 (2020) 120339.

[73] K.H. Khayat, W. Meng, K. Vallurupalli, Le Teng, Rheological properties of ultra-high-performance concrete — An overview, Cement and Concrete Research 124 (2019) 105828.

[74] K.G. Kuder, N. Ozyurt, E.B. Mu, S.P. Shah, Rheology of fiber-reinforced cementitious materials, Cement and Concrete Research 37 (2007) 191–199.

[75] S.H. Lee, H.J. Kim, E. Sakai, M. Daimon, Effect of particle size distribution of fly ash–cement system on the fluidity of cement pastes, Cement and Concrete Research 33 (2003) 763–768.

[76] W. Meng, M. Valipour, K.H. Khayat, Optimization and performance of cost-effective ultra-high performance concrete, Mater Struct 50 (2017) 1–16.

[77] R. Yu, F. Zhou, T. Yin, Z. Wang, M. Ding, Z. Liu, Y. Leng, X. Gao, Z. Shui, Uncovering the approach to develop ultra-high performance concrete (UHPC) with dense meso-structure based on rheological point of view: Experiments and modeling, Construction and Building Materials 271 (2021) 121500.

[78] S. Pyo, H.-K. Kim, B.Y. Lee, Effects of coarser fine aggregate on tensile properties of ultra high performance concrete, Cement and Concrete Composites 84 (2017) 28–35.

[79] J. Yang, G.F. Peng, J. Zhao, G.S. Shui, On the explosive spalling behavior of ultra-high performance concrete with and without coarse aggregate exposed to high temperature, Construction and Building Materials 226 (2019) 932–944.

[80] P.P. Li, Q.L. Yu, H. Brouwers, Effect of coarse basalt aggregates on the properties of Ultra-high Performance Concrete (UHPC), Construction and Building Materials 170 (2018) 649–659.

[81] L. Yujing, Z. Wenhua, W. Fan, W. Peipei, Z. Weizhao, Y. Fenghao, Static mechanical properties and mechanism of C200 ultra-high performance concrete (UHPC) containing coarse aggregates, Science and Engineering of Composite Materials 27 (2020) 186–195.

[82] Weina Meng, Design and performance of cost-effective ultra-high performance concrete for prefabricated elements. Dissertation, United States, 2017.

[83] E. Fehling, M. Schmidt, J.C. Walraven, T. Leutbecher, S. Fröhlich, Ultra-high performance concrete UHPC: Fundamentals - design - examples, Ernst & Sohn, Berlin, 2014.

[84] T. Oertel, F. Hutter, U. Helbig, G. Sextl, Amorphous silica in ultra-high performance concrete: First hour of hydration, Cement and Concrete Research 58 (2014) 131–142.

[85] T. Oertel, F. Hutter, R. Tänzer, U. Helbig, G. Sextl, Primary particle size and agglomerate size effects of amorphous silica in ultra-high performance concrete, Cement and Concrete Composites 37 (2013) 61–67.

[86] Z. Wu, K.H. Khayat, C. Shi, Changes in rheology and mechanical properties of ultra-high performance concrete with silica fume content, Cement and Concrete Research 123 (2019) 105786.

[87] Y. Lin, J. Yan, Z. Wang, F. Fan, C. Zou, Effect of silica fumes on fluidity of UHPC: Experiments, influence mechanism and evaluation methods, Construction and Building Materials 210 (2019) 451–460.

[88] Z. Wu, C. Shi, W. He, Comparative study on flexural properties of ultra-high performance concrete with supplementary cementitious materials under different curing regimes, Construction and Building Materials 136 (2017) 307–313.

[89] W. Sun, H. Yan, B. Zhan, Analysis of mechanism on water-reducing effect of fine ground slag, high-calcium fly ash, and low-calcium fly ash, Cement and Concrete Research 33 (2003) 1119–1125.

[90] E. Ghafari, S.A. Ghahari, H. Costa, E. Júlio, A. Portugal, L. Durães, Effect of supplementary cementitious materials on autogenous shrinkage of ultra-high performance concrete, Construction and Building Materials 127 (2016) 43–48.

[91] A.M. Tahwia, G.M. Elgendy, M. Amin, Durability and microstructure of eco-efficient ultra-high-performance concrete, Construction and Building Materials 303 (2021) 124491.

[92] W. Fajun, M.W. Grutzeck, M. Della Roy, The retarding effects of fly ash upon the hydration of cement pastes: The first 24 hours, Cement and Concrete Research 15 (1985) 174–184.

[93] P. Ganesh, A.R. Murthy, Tensile behaviour and durability aspects of sustainable ultra-high performance concrete incorporated with GGBS as cementitious material, Construction and Building Materials 197 (2019) 667–680.

[94] D. Fan, R. Yu, Z. Shui, K. Liu, Y. Feng, S. Wang, K. Li, J. Tan, Y. He, A new development of eco-friendly Ultra-High performance concrete (UHPC): Towards efficient steel slag application and multi-objective optimization, Construction and Building Materials 306 (2021) 124913.

[95] Z. Mo, R. Wang, X. Gao, Hydration and mechanical properties of UHPC matrix containing limestone and different levels of metakaolin, Construction and Building Materials 256 (2020) 119454.

[96] A. Tafraoui, G. Escadeillas, S. Lebaili, T. Vidal, Metakaolin in the formulation of UHPC, Construction and Building Materials 23 (2009) 669–674.

[97] W. Huang, H. Kazemi-Kamyab, W. Sun, K. Scrivener, Effect of cement substitution by limestone on the hydration and microstructural development of ultra-high performance concrete (UHPC), Cement and Concrete Composites 77 (2017) 86–101.

[98] P.P. Li, H. Brouwers, W. Chen, Q. Yu, Optimization and characterization of high-volume limestone powder in sustainable ultra-high performance concrete, Construction and Building Materials 242 (2020) 118112.

[99] S. Ahmad, K.O. Mohaisen, S.K. Adekunle, S.U. Al-Dulaijan, M. Maslehuddin, Influence of admixing natural pozzolan as partial replacement of cement and microsilica in UHPC mixtures, Construction and Building Materials 198 (2019) 437–444.

[100] R. Yang, R. Yu, Z. Shui, X. Gao, X. Xiao, X. Zhang, Y. Wang, Y. He, Low carbon design of an ultra-high performance concrete (UHPC) incorporating phosphorous slag, Journal of Cleaner Production 240 (2019) 118157.

[101] G. Ling, Z. Shui, X. Gao, T. Sun, R. Yu, X. Li, Utilizing iron ore tailing as cementitious material for eco-friendly design of ultra-high performance concrete (UHPC), Materials (Basel, Switzerland) 14 (2021) 1829.

[102] D. Hou, Di Wu, X. Wang, S. Gao, R. Yu, M. Li, P. Wang, Y. Wang, Sustainable use of red mud in ultra-high performance concrete (UHPC): Design and performance evaluation, Cement and Concrete Composites 115 (2021) 103862.

[103] D. Qian, R. Yu, Z. Shui, Y. Sun, C. Jiang, F. Zhou, M. Ding, X. Tong, Y. He, A novel development of green ultra-high performance concrete (UHPC) based on appropriate application of recycled cementitious material, Journal of Cleaner Production 261 (2020) 121231.

[104] R. Yang, R. Yu, Z. Shui, X. Gao, X. Xiao, D. Fan, Z. Chen, J. Cai, X. Li, Y. He, Feasibility analysis of treating recycled rock dust as an environmentally friendly alternative material in Ultra-High Performance Concrete (UHPC), Journal of Cleaner Production 258 (2020) 120673.

[105] J.N. Wang, R. Yu, W.Y. Xu, C.Y. Hu, Z.H. Shui, D. Qian, Y. Leng, K.N. Liu, D.S. Hou, X.P. Wang, A novel design of low carbon footprint Ultra-High Performance Concrete (UHPC) based on full scale recycling of gold tailings, Construction and Building Materials 304 (2021) 124664.

[106] V.-T.-A. Van, C. Rößler, D.-D. Bui, H.-M. Ludwig, Rice husk ash as both pozzolanic admixture and internal curing agent in ultra-high performance concrete, Cement and Concrete Composites 53 (2014) 270–278.

[107] M. Vigneshwari, K. Arunachalam, A. Angayarkanni, Replacement of silica fume with thermally treated rice husk ash in Reactive Powder Concrete, Journal of Cleaner Production 188 (2018) 264–277.

[108] H. Huang, X. Gao, H. Wang, H. Ye, Influence of rice husk ash on strength and permeability of ultra-high performance concrete, Construction and Building Materials 149 (2017) 621–628.

[109] N. van Tuan, G. Ye, K. van Breugel, O. Copuroglu, Hydration and microstructure of ultra high performance concrete incorporating rice husk ash, Cement and Concrete Research 41 (2011) 1104–1111.

[110] H.R. Sobuz, P. Visintin, M.S. Mohamed Ali, M. Singh, M.C. Griffith, A.H. Sheikh, Manufacturing ultra-high performance concrete utilising conventional materials and production methods, Construction and Building Materials 111 (2016) 251–261.

[111] A. Alsalman, C.N. Dang, W. Micah Hale, Development of ultra-high performance concrete with locally available materials, Construction and Building Materials 133 (2017) 135–145.

[112] S.-H. Kang, Y. Jeong, K.H. Tan, J. Moon, The use of limestone to replace physical filler of quartz powder in UHPFRC, Cement and Concrete Composites 94 (2018) 238–247.

[113] R. Yang, R. Yu, Z. Shui, C. Guo, S. Wu, X. Gao, S. Peng, The physical and chemical impact of manufactured sand as a partial replacement material in ultra-high performance concrete (UHPC), Cement and Concrete Composites 99 (2019) 203–213.

[114] Y. Jiao, Y. Zhang, M. Guo, L. Zhang, H. Ning, S. Liu, Mechanical and fracture properties of ultra-high performance concrete (UHPC) containing waste glass sand as partial replacement material, Journal of Cleaner Production 277 (2020) 123501.

[115] N.A. Soliman, A. Tagnit-Hamou, Using glass sand as an alternative for quartz sand in UHPC, Construction and Building Materials 145 (2017) 243–252.

[116] A. Cwirzen, V. Penttala, C. Vornanen, Reactive powder based concretes: Mechanical properties, durability and hybrid use with OPC, Cement and Concrete Research 38 (2008) 1217–1226.

[117] P. Robins, S. Austin, P. Jones, Pull-out behaviour of hooked steel fibres, Materials and Structures 35 (2002) 434–442.

[118] H. Huang, X. Gao, K.H. Khayat, A. Su, Influence of fiber alignment and length on flexural properties of UHPC, Construction and Building Materials 290 (2021) 122863.

[119] Z. Wu, K.H. Khayat, C. Shi, How do fiber shape and matrix composition affect fiber pullout behavior and flexural properties of UHPC?, Cement and Concrete Composites 90 (2018) 193–201.

[120] Z. Wu, C. Shi, W. He, L. Wu, Effects of steel fiber content and shape on mechanical properties of ultra high performance concrete, Construction and Building Materials 103 (2016) 8–14.

[121] B. Boulekbache, M. Hamrat, M. Chemrouk, S. Amziane, Flowability of fibre-reinforced concrete and its effect on the mechanical properties of the material, Construction and Building Materials 24 (2010) 1664–1671.

[122] R. Wang, X. Gao, H. Huang, G. Han, Influence of rheological properties of cement mortar on steel fiber distribution in UHPC, Construction and Building Materials 144 (2017) 65–73.

[123]   H. Huang, X. Gao, Le Teng, Fiber alignment and its effect on mechanical properties of UHPC: An overview, Construction and Building Materials 296 (2021) 123741.

[124]   H. Huang, X. Gao, K.H. Khayat, Contribution of fiber alignment on flexural properties of UHPC and prediction using the Composite Theory, Cement and Concrete Composites 118 (2021) 103971.

[125]   T. Liu, H. Wei, A. Zhou, D. Zou, H. Jian, Multiscale investigation on tensile properties of ultra-high performance concrete with silane coupling agent modified steel fibers, Cement and Concrete Composites 111 (2020) 103638.

[126]   H. Huang, G. Ye, Examining the "time-zero" of autogenous shrinkage in high/ultra-high performance cement pastes, Cement and Concrete Research 97 (2017) 107–114.

[127]   T. Xie, C. Fang, M.S. Mohamad Ali, P. Visintin, Characterizations of autogenous and drying shrinkage of ultra-high performance concrete (UHPC): An experimental study, Cement and Concrete Composites 91 (2018) 156–173.

[128]   M. Collepardi, A. Borsoi, S. Collepardi, J.J. Ogoumah Olagot, R. Troli, Effects of shrinkage reducing admixture in shrinkage compensating concrete under non-wet curing conditions, Cement and Concrete Composites 27 (2005) 704–708.

[129]   M. Wyrzykowski, P. Trtik, B. Münch, J. Weiss, P. Vontobel, P. Lura, Plastic shrinkage of mortars with shrinkage reducing admixture and lightweight aggregates studied by neutron tomography, Cement and Concrete Research 73 (2015) 238–245.

[130]   A. Leemann, P. Nygaard, P. Lura, Impact of admixtures on the plastic shrinkage cracking of self-compacting concrete, Cement and Concrete Composites 46 (2014) 1–7.

[131]   G. Sant, B. Lothenbach, P. Juilland, G. Le Saout, J. Weiss, K. Scrivener, The origin of early age expansions induced in cementitious materials containing shrinkage reducing admixtures, Cement and Concrete Research 41 (2011) 218–229.

[132]   D.P. Bentz, M.R. Geiker, K.K. Hansen, Shrinkage-reducing admixtures and early-age desiccation in cement pastes and mortars, Cement and Concrete Research 31 (2001) 1075–1085.

[133]   J. Justs, M. Wyrzykowski, D. Bajare, P. Lura, Internal curing by superabsorbent polymers in ultra-high performance concrete, Cement and Concrete Research 76 (2015) 82–90.

[134]   C. Schröfl, V. Mechtcherine, M. Gorges, Relation between the molecular structure and the efficiency of superabsorbent polymers (SAP) as concrete admixture to mitigate autogenous shrinkage, Cement and Concrete Research 42 (2012) 865–873.

[135]   V. Mechtcherine, E. Secrieru, C. Schröfl, Effect of superabsorbent polymers (SAPs) on rheological properties of fresh cement-based mortars — Development of yield stress and plastic viscosity over time, Cement and Concrete Research 67 (2015) 52–65.

[136]   J. Liu, N. Farzadnia, C. Shi, Effects of superabsorbent polymer on interfacial transition zone and mechanical properties of ultra-high performance concrete, Construction and Building Materials 231 (2020) 117142.

[137]   Y. Liu, Y. Wei, Effect of calcined bauxite powder or aggregate on the shrinkage properties of UHPC, Cement and Concrete Composites 118 (2021) 103967.

[138]   K. Liu, R. Yu, Z. Shui, X. Li, C. Guo, B. Yu, S. Wu, Optimization of autogenous shrinkage and microstructure for ultra-high performance concrete (UHPC) based on appropriate application of porous pumice, Construction and Building Materials 214 (2019) 369–381.

[139]   S.-H. Kang, Y. Jeong, K.H. Tan, J. Moon, High-volume use of limestone in ultra-high performance fiber-reinforced concrete for reducing cement content and autogenous shrinkage, Construction and Building Materials 213 (2019) 292–305.

[140]   Z. Wu, C. Shi, K.H. Khayat, Investigation of mechanical properties and shrinkage of ultra-high performance concrete: Influence of steel fiber content and shape, Composites Part B: Engineering 174 (2019) 107021.

[141]   S. Ahmad, M. Rasul, S.K. Adekunle, S.U. Al-Dulaijan, M. Maslehuddin, S.I. Ali, Mechanical properties of steel fiber-reinforced UHPC mixtures exposed to elevated temperature: Effects of exposure duration and fiber content, Composites Part B: Engineering 168 (2019) 291–301.

[142]   Y. Zhu, H. Hussein, A. Kumar, G. Chen, A review: Material and structural properties of UHPC at elevated temperatures or fire conditions, Cement and Concrete Composites 123 (2021) 104212.

[143]   D. Zhang, A. Dasari, K.H. Tan, On the mechanism of prevention of explosive spalling in ultra-high performance concrete with polymer fibers, Cement and Concrete Research 113 (2018) 169–177.

[144]   J.-C. Liu, K.H. Tan, Y. Yao, A new perspective on nature of fire-induced spalling in concrete, Construction and Building Materials 184 (2018) 581–590.

[145]   Y. Li, K.H. Tan, E.-H. Yang, Influence of aggregate size and inclusion of polypropylene and steel fibers on the hot permeability of ultra-high performance concrete (UHPC) at elevated temperature, Construction and Building Materials 169 (2018) 629–637.

[146]   Y. Li, P. Pimienta, N. Pinoteau, K.H. Tan, Effect of aggregate size and inclusion of polypropylene and steel fibers on explosive spalling and pore pressure in ultra-high-

performance concrete (UHPC) at elevated temperature, Cement and Concrete Composites 99 (2019) 62–71.

[147]   Y. Li, K.H. Tan, E.-H. Yang, Synergistic effects of hybrid polypropylene and steel fibers on explosive spalling prevention of ultra-high performance concrete at elevated temperature, Cement and Concrete Composites 96 (2019) 174–181.

[148]   J. von Werder, S. Simon, C. Lehmann, C. Selleng, P. Fontana, B. Meng, Autoclaving of ultra-high performance concrete (UHPC), ce/papers 2 (2018) 131–136.

[149]   S.H. Kang, J.H. Lee, S.G. Hong, J. Moon, Microstructural investigation of heat-treated ultra-high performance concrete for optimum production, Materials (Basel) 10 (2017).

[150]   P. Shen, L. Lu, Y. He, F. Wang, S. Hu, The effect of curing regimes on the mechanical properties, nano-mechanical properties and microstructure of ultra-high performance concrete, Cement and Concrete Research 118 (2019) 1–13.

[151]   V.Y. Garas, K.E. Kurtis, L.F. Kahn, Creep of UHPC in tension and compression: Effect of thermal treatment, Cement and Concrete Composites 34 (2012) 493–502.

[152]   H. Zhang, T. Ji, X. Lin, Pullout behavior of steel fibers with different shapes from ultra-high performance concrete (UHPC) prepared with granite powder under different curing conditions, Construction and Building Materials 211 (2019) 688–702.

[153]   S.H. Kang, S.G. Hong, J. Moon, Shrinkage characteristics of heat-treated ultra-high performance concrete and its mitigation using superabsorbent polymer based internal curing method, Cement and Concrete Composites 89 (2018) 130–138.

[154]   W. Li, Z. Huang, G. Hu, W. Hui Duan, S.P. Shah, Early-age shrinkage development of ultra-high-performance concrete under heat curing treatment, Construction and Building Materials 131 (2017) 767–774.

[155]   J. von Werder, S. Simon, A. Gardei, P. Fontana, B. Meng, Thermal and hydrothermal treatment of UHPC: influence of the process parameters on the phase composition of ultra-high performance concrete, Materials and Structures 54 (2021).

2 Publications

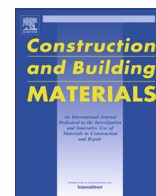## 2.1 Influence of foreign ions on calcium silicate hydrate under hydrothermal conditions: A review

Publisher's version

Published in the journal "Construction and Building Materials"

Volume 301, 27 September 2021, 124071

https://doi.org/10.1016/j.conbuildmat.2021.124071

Authors: Hongwei Tian, Dietmar Stephan, Barbara Lothenbach, Christian Lehmann

Review

Influence of foreign ions on calcium silicate hydrate under hydrothermal conditions: A review

Hongwei Tian [a], Dietmar Stephan [a,*], Barbara Lothenbach [b], Christian Lehmann [a]

[a] Institute of Civil Engineering, Technische Universität Berlin, 13355 Berlin, Germany
[b] Empa, Swiss Federal Laboratories for Materials Science and Technology, Laboratory for Concrete & Construction Chemistry, 8600 Dübendorf, Switzerland

HIGHLIGHTS

- The influence of Ca/Si ratio, Al^{3+}, Na^+, K^+, Mg^{2+}, Fe^{3+}, and SO_4^{2-} is reviewed.
- Foreign ions affect C-S-H gel formation and its transformation to crystalline phases.
- Foreign ions can change the structure, morphology, and thermal stability of C-S-H.
- Mixture components can be optimised to control C-S-H formation and its properties.

ARTICLE INFO

ABSTRACT

Cementitious materials have long been used also in hydrothermal conditions, where hydration is significantly different from ambient temperature conditions. The high temperature accelerates mineral dissolution, especially of supplementary cementitious materials (SCMs). This paper reviews the influence of the foreign ions Al^{3+}, Na^+, K^+, Mg^{2+}, Fe^{3+} and SO_4^{2-} dissolved from SCMs and cement clinkers as well as the Ca/Si ratio on the hydration kinetics, including the formation of amorphous C-S-H and its transformation into crystalline phases, and hydrates characteristics under hydrothermal conditions. When SCMs are present under hydrothermal conditions, in addition to the physical parameters, the chemical and mineralogical compositions of the SCMs considerably influences the types and amounts of hydrates. Therefore, the compositions of mixtures can be optimised in order to control the formation rate and sequence of hydrates and their properties.

© 2021 Elsevier Ltd. All rights reserved.

Contents

* Corresponding author.
  E-mail address: stephan@tu-berlin.de (D. Stephan).

1. Introduction

1.1. Hydrothermal conditions

Cementitious materials are widely used in various environments including hot oil and geothermal wells [1,2], as well as corrosive marine environments [3–5]. Hydrothermal conditions strongly affect hydration kinetics and the hydrates formed [6–8]. Up to now, hydrothermal conditions that cementitious materials are subjected to can be divided into two forms: active curing [9,10] and passive resistance [2,11]:

Curing at ambient temperature is generally carried out under moist conditions; the cement hydration and the strength gain proceed relatively slow. In contrast, hydrothermal curing leads to a very fast hydration and strength development, which is advantageous for precast concrete industry and other applications, where a high early strength is of importance [12–14]. Typical hydrothermal curing used in concrete technology includes ambient pressure curing and high-pressure steam curing. High-pressure steam curing not only increase the early strength and activate components which remain inert under ambient conditions such as quartz powder and sand, but also induce the formation of new crystalline phases [10,15,16]. Possible applications include autoclaved aerated concrete (AAC), ultra-high performance concrete (UHPC) and calcium silicate board (CSB).

AAC has attracted much attention because of its excellent heat insulation properties combined with good mechanical properties. It is produced by treating a mixture of quartz sand, lime, cement, gypsum, and other additives under saturated steam pressure (typically 0.8–1.4 MPa, 180–200 °C) [17–19]. It is reported that the quantities of crystalline 1.1 nm tobermorite and poorly crystalline C-S-H phase formed in AAC are highly related to the matrix properties [20–22]. In respect to autoclaving curing, UHPC presents superior strength and durability and is considered to have a wide application range, especially in large-span components, anti-explosive structures, and high-abrasion, high-corrosion environments [23–29]. CSB is a kind of partition board with excellent properties of moisture resistance, light weight, sound insulation, and flame resistance. It is produced by using ordinary Portland cement (OPC) as a calcium supplier, quartz sand as siliceous material, and fibres for reinforcement. After being moulded by compression, the specimens are subject to autoclaving treatment at a water-saturated steam pressure of 1.0–2.3 MPa (180–220 °C) for a certain time [30–35].

A second form of hydrothermal conditions, referred to passive resistance, is caused by the higher temperature of the environment in which concrete is used, such as oil and geothermal well cementing for displacing drilling fluid and filling annular space between pipes and rock formation [2,36] and the application of constructing water tanks for thermal storage [37]. In these environments, cementitious materials must resist high temperature and high pressure for a longer time compared to active curing. In the petroleum and geothermal industry, where temperature exceeds about 110 °C during well cementing, the predominant hydrates α-dicalcium silicate hydrate α-C$_2$SH [Ca$_2$SiO$_3$(OH)$_2$] and jaffeite C$_6$S$_2$H$_3$ [Ca$_6$(Si$_2$O$_7$)(OH)$_6$] are formed. They cause due to their low water content and thus low solid volume degradation of the microstructure accompanied by a permeability increase and strength retrogression. Therefore, in order to avoid this problem, special cement formulations have been developed which introduce additional silica (approximately 35 wt%) to reduce the Ca/Si ratio to approximately 1.0, preventing the formation of α-C$_2$SH and C$_6$S$_2$H$_3$. Instead, other C-S-H are generated, such as tobermorite and xonotlite, depending on the temperature, bulk Ca/Si ratio and the type of added silica. These hydrates can produce a matrix with greater strength and lower permeability [2].

In the past years, the influence of temperature on cementitious material hydration has attracted considerable attention. When the temperature exceeds 100 °C, usually at water-saturated steam pressure, the hydrates formed under this condition differ substantially from those formed at normal temperature or even below 100 °C. Different crystalline phases of C-S-H are generated instead of amorphous C-S-H gel predominant below 100 °C, depending on the Ca/Si ratio and temperature. Furthermore, in the presence of quartz powder/sand, a pozzolanic reaction occurs consuming portlandite and yielding additional C-S-H. In this paper, the behaviours of C-S-H at a temperature above 100 °C with saturated steam pressure are reviewed.

1.2. Supplementary cementitious materials

Various supplementary cementitious materials (SCMs) are used in concretes, such as blast furnace slag, fly ash, silica fume, trass powder, and metakaolin, with the purpose of compensating the high CO$_2$ emissions of Portland cement production, on the one hand, and improving the concrete properties by increasing the solid volume taking advantage of pozzolanic effect on the other hand. In a conventional environment, the influences of the introduced SCMs are largely determined by their physical properties, although in the long term SCMs can chemically react changing hydrate composition depending on their chemical compositions. Furthermore, the production mode may also have an influence. For example, the steel slag produced by a basic oxygen furnace mostly has a similar chemical composition and mineral phases to Portland cement clinker, while another form produced by an electric arc furnace mainly contains dicalcium silicate (C$_2$S), merwinite (C$_3$MS$_2$) or kirschsteinite (CFS) [38]. Fig. 1 shows the chemical
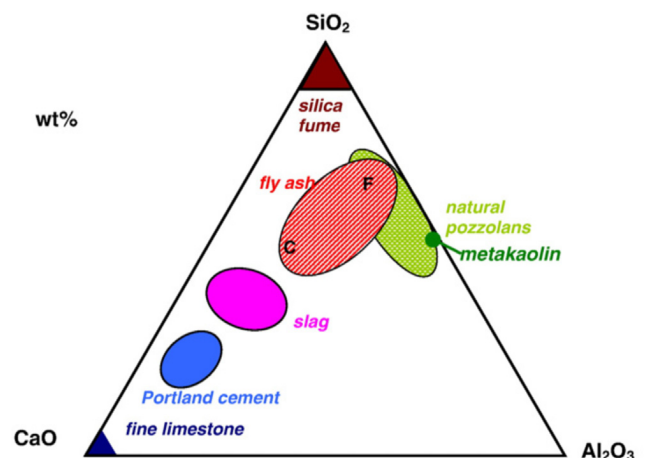

Fig. 1. Al$_2$O$_3$-CaO-SiO$_2$ ternary diagram of cementitious materials [39].

compositions of some common SCMs based on a Al_2O_3-CaO-SiO_2 ternary diagram illustrating the significant differences between varied materials. This diagram is limited to only three elements of Ca, Si, and Al, while the existence of other elements in SCMs such as Mg and Fe also varies significantly and exerts significant influences on hydrate formation under hydrothermal conditions.

Unlike at room temperature, under hydrothermal conditions these SCMs exhibit a relatively high reactivity and affect thus more strongly the hydration kinetics, the content and composition of hydrates, as well as their properties. Furthermore, this influence is considerably amplified above 100 °C with saturated stream pressure. Under such conditions, the pozzolanic reaction occurs rapidly consuming portlandite and transforming amorphous C-S-H gel. Due to the incorporation of SCMs, the transformation becomes highly complicated as the foreign ions, Al^{3+}, Na^+, K^+, Mg^{2+}, Fe^{3+} and SO_4^{2-} reviewed in this paper, are involved in this process by suppressing or promoting the dissolution of silica-bearing compounds and the crystallisation of hydrates and penetrating the hydrate's structure. For an effective application of SCMs under hydrothermal conditions, it is important to understand the influence of the major elements present in cements on the formation and stability of C-S-H.

2. Influence of silicon and foreign elements on C-S-H

2.1. Siliceous materials: Ca/Si ratio

Siliceous materials have long been used as one of the components of the cement matrix used in hydrothermal environments to avoid strength degradation and permeability increase due to the changes in solid phase composition. The amorphous C-S-H gel formed at room temperature ceases to be stable at above 110 °C and converts into various crystalline products depending on the bulk chemical composition [2]. The incorporation of additional silica can consume calcium hydroxide, leading to the formation of hydrates with a lower Ca/Si ratio and densifying the microstructure of a hardened cement matrix [2]. Silica fume and

quartz powder almost exclusively consist of SiO_2, and therefore a system with silica fume or quartz powder is generally selected to study the behaviour of C-S-H and phase assemblage under hydrothermal conditions.

2.1.1. Influence of hydrothermal conditions

Under hydrothermal conditions, the crystallinity of C-S-H is greatly increased, and the time required for this process diminishes qualitatively with increasing temperature [6]. Assarsson et al. [6] pointed out in their research that first poorly crystallised C-S-H without a definitive Ca/Si ratio forms from the rapid reaction of $Ca(OH)_2$ with reactive SiO_2. In a second step recrystallization under high temperature transforms unstable and amorphous phase into more stable crystalline phases [40,41] which can be accompanied by leaching Ca^{2+} [16,42]. The pathway of this transformation depends on the chemical compositions. Kikuma and co-workers [21,43,44] suggested that tobermorite form at higher temperature can incorporate different foreign ions in a liquid–solid reaction, where tobermorite crystallises from the liquid phase: quartz, katoite, hydroxylellestadite, C-S-H → Si^{4+}, Ca^{2+}, Al^{3+}, OH^- (liquid) → tobermorite. Both katoite and hydroxylellestadite have been previously reported as the important intermediates in tobermorite formation [21,45,46].

The structure of C-S-H is rather complex, and more than 30 crystalline hydrates have been identified [47]. The composition of these hydrates varies significantly, with the Ca/Si ratio ranging from approximately 0.6 to 3.0 [48]. Concerning the thermal stability of these phases, experiments have been carried out over a broad temperature range. The first well-known phase diagram was proposed by Taylor in 1964, where a series of products were synthesised with different Ca/Si ratios in the temperature range of 50 to 1000 °C [49]. Later Hong et al. set up a revised diagram, as shown in Fig. 2, by synthesising products with different SiO_2 and $Ca(OH)_2$ contents [48]. The phases with a Ca/Si ratio of 0.4 to 0.6, Z-phase, $Ca(H_3SiO_4)_2$, and truscottite, suggested by Assarsson et al. [6,7] are not included, as they do not appear in nature, indicating that they may be metastable. It should be noted that Taylor found
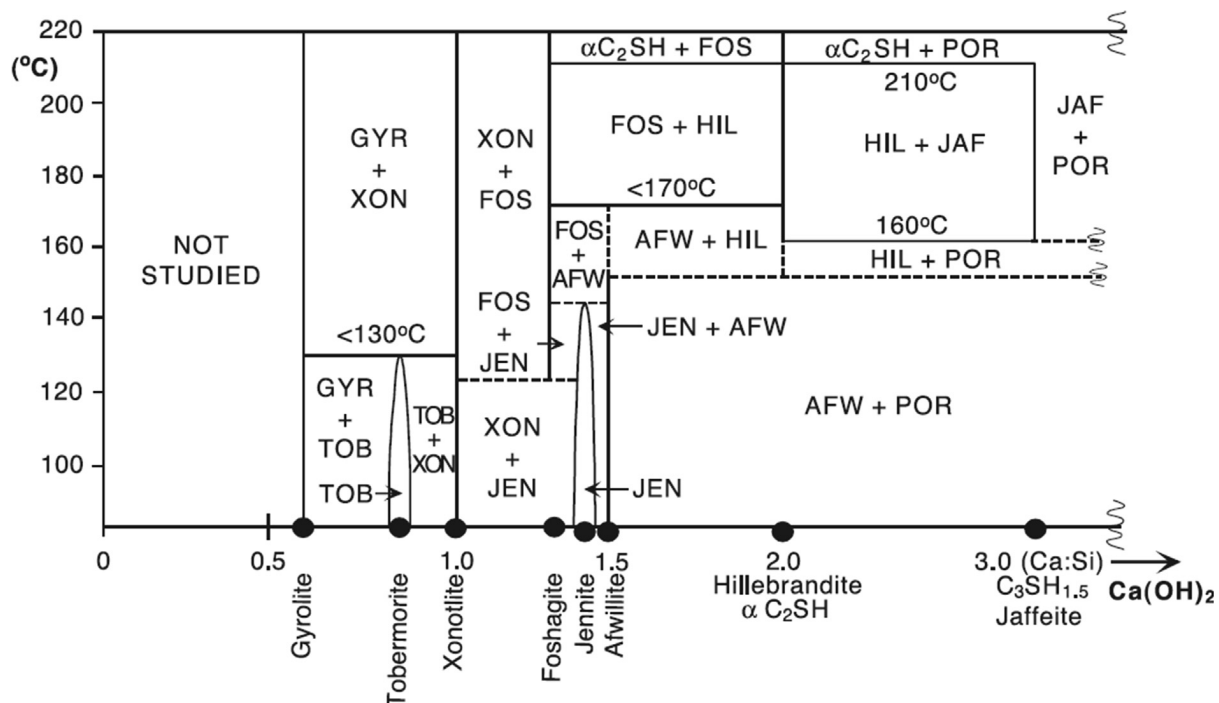

Fig. 2. The phase diagram in the CaO-SiO_2-H_2O system under hydrothermal conditions (dashed lines indicate uncertainties), . reproduced from [48]

11 Å and 14 Å tobermorite formed at 100 °C and 60 °C respectively [49,50], resulting in speculation that higher temperatures favor the 11 Å phase with a lower water content [51]. However, in the study of Hong et al. [48], bulk composition and temperature were observed to determine together which solid forms. In a system of Ca/Si ratios ≤1.1 at 85 °C after 130 days, 14 Å tobermorite was observed, while at higher Ca/Si ratios, 11 Å tobermorite predominated. At 130 °C for 150 days, 11 Å tobermorite formed exclusively at Ca/Si ratios ≥1.1, while 11 Å and 14 Å tobermorite coexisted at Ca/Si = 0.91 and 1.01, indicating that an increased Ca content (Ca/Si > 0.83) helps to stabilise 14 Å tobermorite at higher temperatures [48]. Recently, Blanc et al. [52] proposed a refined CaO-SiO$_2$-H$_2$O phase diagram based on thermodynamic calculations, although the stability field of jaffeite and α-C$_2$SH should be further refined [52].

In contrast to the research carried out on CaO-SiO$_2$-H$_2$O system, Meller et al. added varying proportions of silica and corundum to oil well cement paste and characterised the main mineralogical hydrates after 5 d of hydration at 200–350 °C as shown in Fig. 3 [53,54]. Compared with the CaO-SiO$_2$-H$_2$O system, there are some apparent deviations. The thermal stability of α-C$_2$SH is extended to 200 °C and of 11 Å tobermorite (incorporating Al) to 300 °C [53]. It has been suggested that the impurities in cement change the phases' boundaries relative to those shown in Fig. 2. It is one of the purposes of this paper to review the influence of impurities on the kind of C-S-H formed. Furthermore, it should be noted that phase equilibrium might not be achieved in all cases as metastable intermediates may persist.

2.1.2. Influence of the physicochemical properties of raw materials

Generally, the Ca/Si ratio of the matrix can be easily altered by changing the relative amount of CaO and SiO$_2$ added to the system. However, many studies have found that due to the different physiochemical properties, size and crystallinity, the addition of silica materials does not necessarily produce the presumptive results.

2.1.2.1. Size effect. The dissolution rate of silica is proportional to the available surface area, which changes the available Ca/Si ratio accordingly. Krakowiak et al. [55] conducted at 200 °C a comparative study, using different sizes of crystalline α-quartz which affected tobermorite formation. In the samples containing coarser quartz, gyrolite and 11 Å tobermorite coexist and dominate as shown in Fig. 4(a), while in the presence of fine quartz, poorly crystalline C-S-H (with a structure and composition similar to 11 Å tobermorite) predominates for three months without conversion to the thermodynamically more stable 11 Å tobermorite or gyrolite as shown in Fig. 4(b). The presence of fine quartz reduced the Ca/Si ratio stabilising poorly crystalline C-S-H. Previous research reported that the C-S-H with a low Ca/Si ratio tends to have long and cross-linked chains of silica tetrahedral [56–58], which could be more difficult to transform into tobermorite, as a high number of bonds need to be reorganised compared with those of Ca/Si > 1 [41,56,59]. Similarly, Eilers et al. found that the Portland cement mixture with 35–40 wt% of fine quartz (<45 μm) remains stable in contact with a dense brine at a temperature ≥232 °C, while a mixture with the same amount of coarse quartz (>45 μm) deteriorates [60]. This is because in the presence of reac-
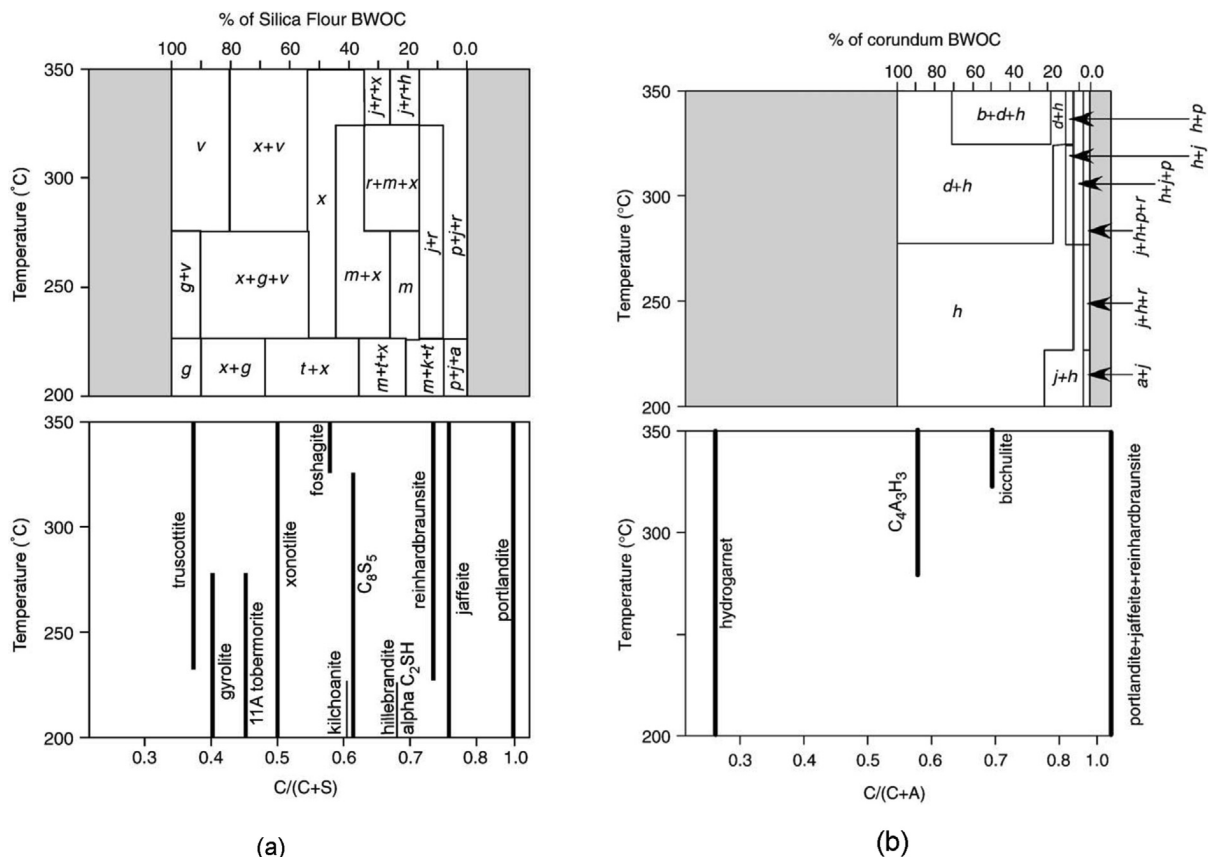

Fig. 3. Phase diagram (lower figure) and phase map (upper figure) for the cement with silica flour (a) or corundum (b). The phase diagram shows the temperatures over which phases >10 wt% are present. The phase map illustrates the major phases formed in different mixtures. Phases are abbreviated by *a*: alpha dicalcium silicate hydrate; *b*: bicchulite; *d*: calcium alumina hydrate; *g*: gyrolite; *h*: hydrogarnet; *j*: jaffeite; *k*: Kilchoanite; *m*: calcium silicate; *p*: portlandite; *r*: reinhardbraunsite; *t*: 1.1 nm tobermorite; *v*: truscottite; *x*: xonotlite. . Adapted from [53]
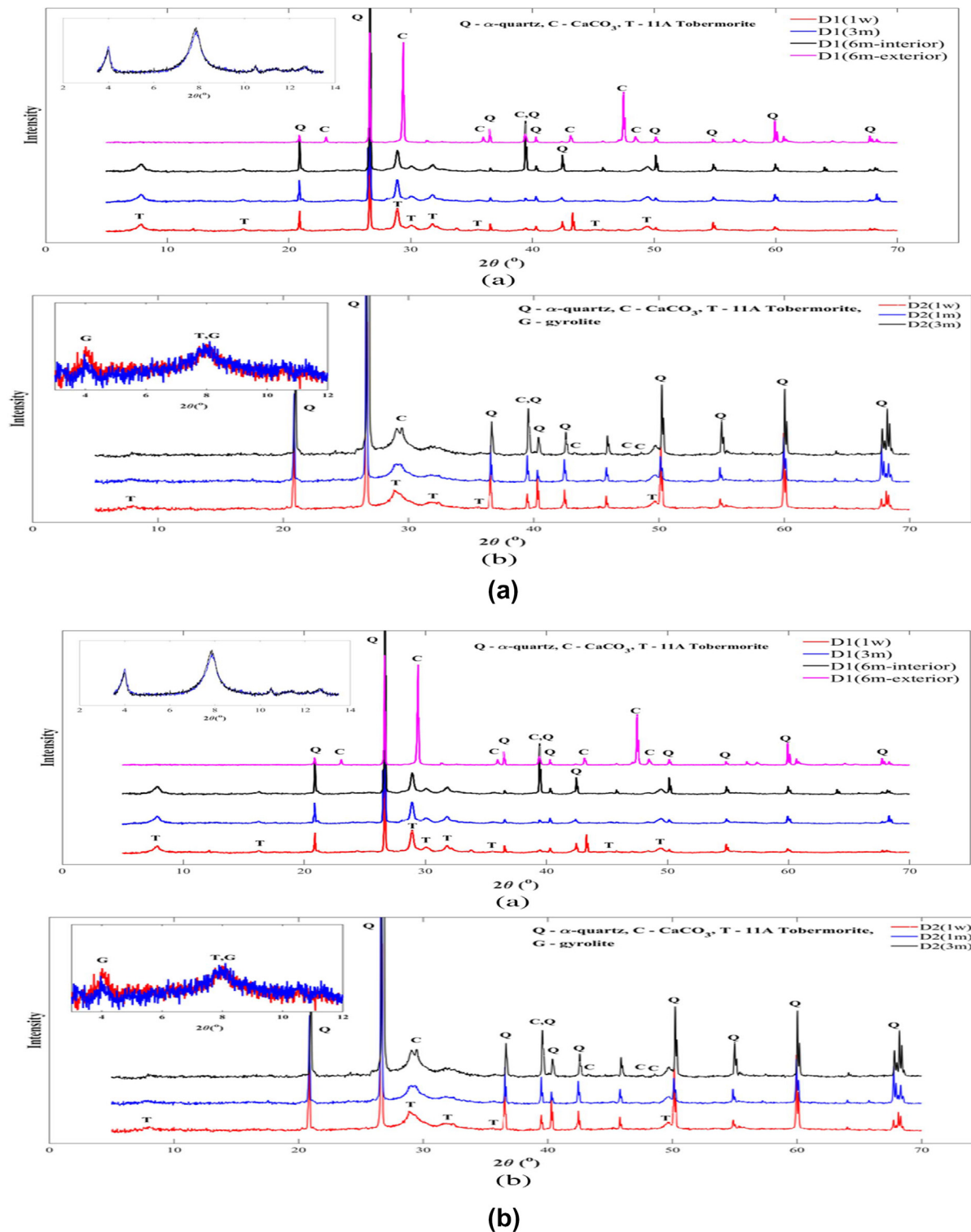
Fig. 4. X-ray powder diffraction spectra of the samples with different combinations of two particle sizes of quartz: fine silica/coarse silica (% by volume of the blend) = 15/50 (a); 25/40 (b) [55].

tive fine quartz, xonotlite is formed, while in the presence of coarse quartz, which reacts less, Ca-rich kilchoanite ($Ca_3Si_2O_7$) is formed resulting in lower strength and higher permeability.

In addition, also the morphology of the hydrates formed can be affected by the SiO_2 accessibility. Grabowski et al. [36] reported that use of fine reactive silica fume instead of quartz powder leads

to a decrease in compressive strength after hydrothermal treatment (230 °C for 6 d), although the major phase in both samples is xonotlite. This has been attributed to the fact that the incorporation of active silica fume results first in the formation of fine granular C-S-H I (Ca/Si ≤ 1.5), which morphology is retained in the subsequently formed xonotlite. Conversely, in the sample with
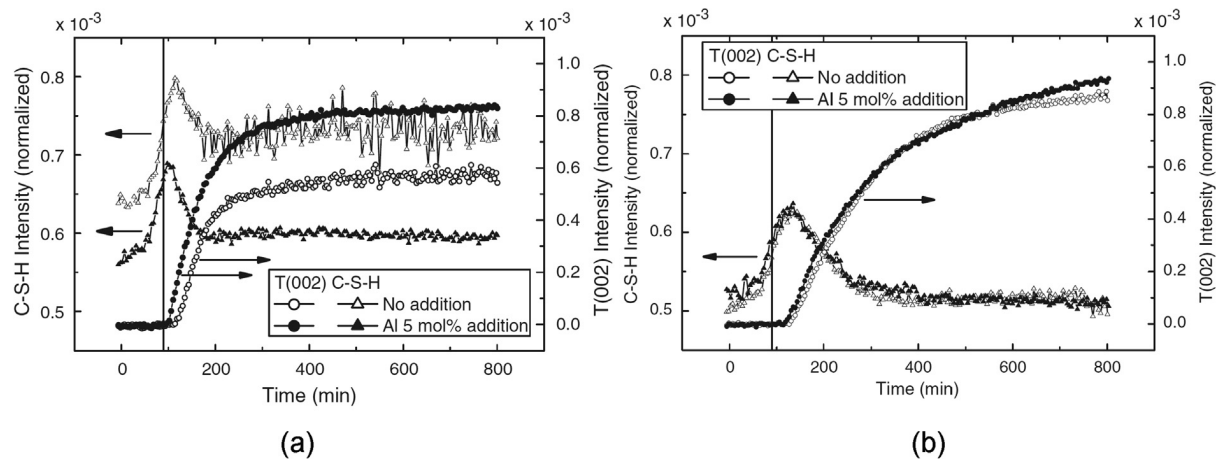
Fig. 5. Time dependence of peak intensities for tobermorite (002, at 2θ of ~7.7°) and C-S-H in the samples with (a) low crystallinity quartz, (b) high crystallinity quartz and in the absence (empty symbols) and presence of Al$_2$O$_3$ (filled symbols), . reproduced from [21]

coarse quartz powder, the needle-like xonotlite is generated epitaxially from the needle-like C-S-H II (Ca/Si > 1.5) resulting in higher-strength [61].

2.1.2.2. Crystallinity effect. In addition to the size effect, Matsui et al. [21] compared two kinds of quartz with similar average particle sizes (30.3 μm of Fig. 5(a) and 28.3 μm of Fig. 5(b)) but different crystallinity, which also affects its reactivity. They found for a sample with a high crystallinity, low reactivity quartz, most of the Ca-rich C-S-H converted into tobermorite with only little C-S-H remaining (Fig. 5(b)). The opposite was observed for the sample with low crystallinity quartz, where significant amount of Si-rich C-S-H remained until the end of curing (Fig. 5(a)). It should be noted that the impact of the reactivity of the raw materials originating from the different size and crystallinity also is in effect in the presence of foreign ions discussed in further sections.

2.1.2.3. Reaction mechanism. The differences in hydrate formation are caused by the fact that the reaction mechanism is affected by the size and crystallinity of silica. It was observed that a product layer or rim on the surface can form (see Fig. 6) under many conditions such as oil well cement systems [62,63], autoclaved UHPC [64,65] and other kinds of cementitious products treated by hydrothermal curing [66,67]. Such a rim of reaction products can

Fig. 6. SEM image with BSE detector of an example of partially reacted coarse and low reactivity quartz particles with a characteristic reaction rim (the sample was subjected to hydrothermal treatment at 200 °C and 20.7 MPa for three months) [55].

slow down transport and thus the reaction rate [68,69]. In systems with little reactive SiO$_2$, the limited availability can control the overall reaction rate, while systems with a large amount of fine and high activity silica [20,70], rather the formation kinetics of products in the matrix will determine formation rate [55].

For a given mixture, the mineralogical composition in equilibrium is determined by the temperature and the raw materials, including the Ca/Si ratio and the reactivity of the material. Generally, different working environments have specific requirements for the chemical and mineralogical composition, as the crystal phases have a different thermal stability, permeability, and mechanical properties. The siliceous materials used should have appropriate reactivity to adequately providing silicon on the one hand and preventing the formation of hydrates with an excessively low Ca/Si ratio originating from the overactive silica on the other hand. Furthermore, the required amount of total silica depends on the fineness and crystallinity, and finer silica reacts more effectively. Eilers et al. [60] reported that under hydrothermal conditions an equal amount or more (based on Portland cement) of quartz sand (75–212 μm, av. 105 μm) is required to the same compressive strength and low permeability as achieved by 35 wt% silica flour (<45 μm, av. 15 μm). Therefore, the appropriate combination of different types of silica is important for the effective utilisation of siliceous materials.

2.2. Aluminium

The wide utilisation of Al-bearing raw materials such as kaolin, metakaolin, fly ash, and zeolite has increased the research interest on the effect of Al on the CaO-SiO$_2$-H$_2$O system. Al is omnipresent in SCMs, but their Al content and availability vary significantly [71]. Al can enter the structure of amorphous C-S-H as well as crystalline phases, especially of 11 Å tobermorite, and is present between layers and/or replaces Si in the bridging position of the silica chains [72–77], forming the so-called calcium aluminium silicate hydrates (C-A-S-H). The presence of Al leads to a stabilisation of tobermorite and destabilisation of C-S-H [21] as illustrated in Fig. 5. At high Al-contents, secondary Al-containing phases are formed, at ambient temperatures Al(OH)$_3$ and/or strätlingite [76], while under hydrothermal conditions, the formation of hydrogarnet instead of strätlingite is observed [78].

2.2.1. Influence of aluminium on the properties of tobermorite

The incorporation of Al plays a significant role in the characteristics of hydrates, including their structure [73,76,79–82], the
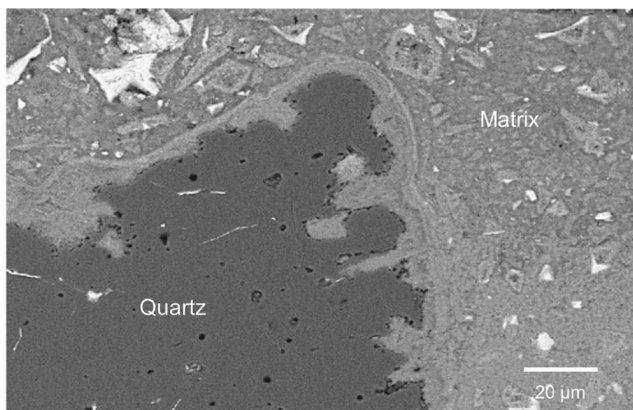
cation and anion exchange [83–85], mechanical properties [86,87] and morphology [87,88]. Most studies on the role of Al in C-S-H formation have been carried out at room temperature, but little at elevated temperatures under saturated steam pressure (>100 °C) where different hydrates are present. Most of the available research has focused on tobermorite, which is discussed in this section.

The presence of Al can accelerate the formation of tobermorite by expediting its crystallisation, and the accelerating effect increases with Al dosage under autoclaving conditions as shown in Fig. 7. [21,41]. This autoclaving treatment was carried out at 190 °C with water-saturated steam pressure for 12 h in the

tailor-made autoclave cell. Combined with synchrotron radiation which allows the X-rays to penetrate the small cell, in-situ time-resolved XRD analysis was achieved [21]. In addition, the chemical composition and structure of hydrates are affected by the presence of Al. XRD [77] and NMR [74] measurements show that there is no significant substitution of Al on Ca-O sheets due to the different charge and ionic radii between Ca (0.99 Å) and Al (0.50 Å) [89], indicating that the fundamental Ca-Si structure of tobermorite is not essentially changed by the incorporation of Al^{3+} and OH^- for Si^{4+} and O^{2-} to maintain the charge balance [75,90]. Tetrahedral Al[4] is present in the bridging tetrahedral sites of the silica chains. Al[5] and Al[6] have also been suggested to be present in the bridging sites and/or in the interlayer [17,75,77,80,91]. The Al[4] can be charge-balanced by alkali cations, Al[5] and Al[6] (Al[4]-O-Al[5,6] linkages), and Ca^{2+} and H^+ [17,75,77,80]. The basal spacing increases with the incorporation of Al at bridging sites [44,92,93]. When the temperature is increasing (80 °C), the Al substitution leads to more cross-linked sites, which decreases the basal spacing and significantly increases the polymerisation of aluminosilicate chains [94,95]. In some early research, d(002) was reported to increase with Al substitution under hydrothermal conditions although diverse results are shown that d(002) increases from 11.4 to 11.6 Å (180 °C, 4 h) [96], 11.31 to 11.44 Å (175 °C, 4d) [97], and 11.1 to 11.7 Å (175 °C, 24 h) [98]. Additionally, the incorporation of Al into tobermorite improves its thermal stability [99].

In addition, Al also influences the morphology of tobermorite. Tobermorite has been found to grow with various morphologies, from tabulate-like to lath-like or highly fibrous elongated in one direction [72,100]. Bell et al. [100] suggested two possible reasons for these morphological differences: 1) different nucleation mechanisms which may cause platelets to originate from heterogeneous nucleation and fibres to result from homogeneous nucleation; 2) different cross-linking Si-O-Si bond numbers where the relationship between morphology and Ca/Si ratio may be established so that a Ca/Si ratio of 0.83 tends to favour the plate habit [99] and Ca/Si ratio between 0.83 and 1.0 shows a mixture of plate and lath or fibrous habit [101]. According to Bell et al., the growth of plate-like tobermorite results from a growth preference, which extends the existing main layer of silicate tetrahedra and CaO [100]. Al incorporation increases the length of the (Al)Si tetrahedral chains, leading to preferential growth along the b-axis, resulting in lath-like and needle-like morphology as shown in Fig. 8 [77]. As Al content increases, the typical plates of tobermorite break into regular patches and then into needle-like deposits that are covered on the surface of the laths until the needle-like shapes dominate [77]. Similar phenomena are also reported by other researchers [99,102]. It should be noted that some studies present conflicting data on morphology which may be due to the interference of other ions such as Na^+ [103] and SO_4^{2-} [99]. Al with high concentrations of sodium at Ca/Si of 1.0 yields tobermorite with plate-like morphology (Fig. 9(a)) [103]. Lamellar tobermorite is formed in the case of Al with sulphate (Fig. 9(b)) [99]. Moreover, the curing period and water/solid ratio also influence the morphology: tobermorite in AAC cured at 183 °C for 2 h presents plates and then converts to crumbled foiled tobermorite after 24 h [101]. Also different water/-solid ratio and thus the space available for crystal growth affect the morphology as different surfaces are generated with possibly different surface properties [100].

2.2.2. Hydrogarnet
The incorporation of Al into tobermorite has an upper limit, above which other secondary phases form [75,76,79]. Klimesch et al. observed a decrease of the crystallinity of tobermorite with increasing Al addition at Al/(Al + Si) >0.03 [71]; a maximum Al substitution for Si of around 15–20 mol% was observed for samples cured at 175 °C for 4 d [97]. Under hydrothermal conditions,
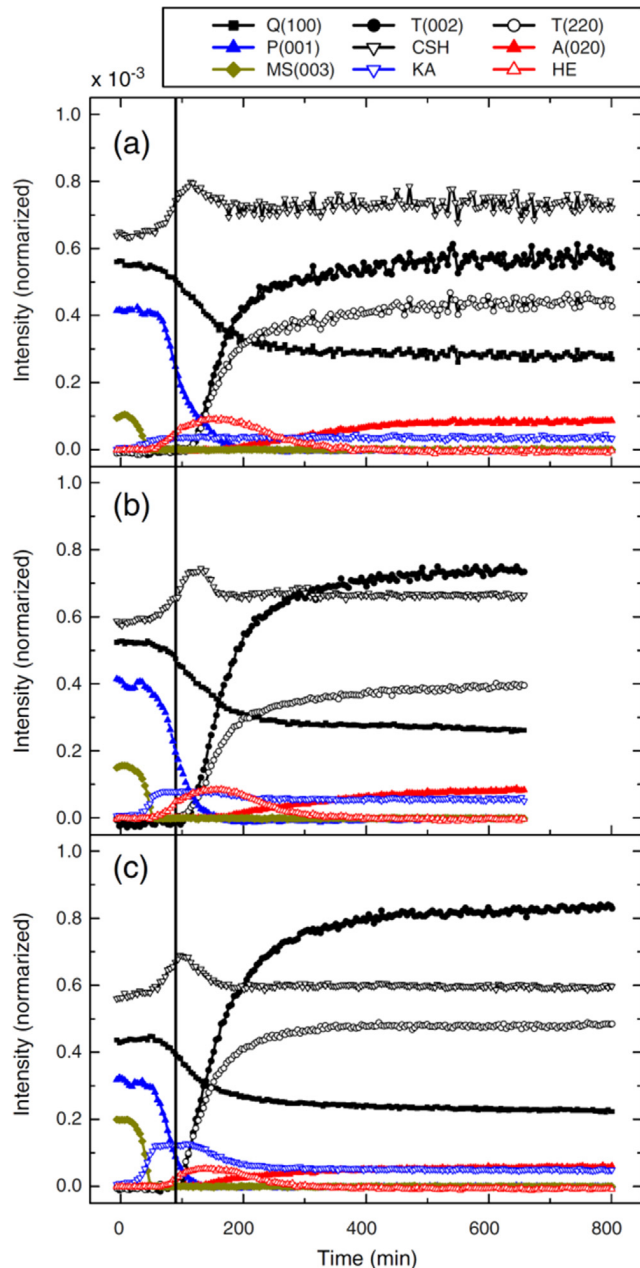
Fig. 7. Time dependence of peak intensities or major constituents during the autoclave process: (a) reference sample, (b) sample with Al/(Al + Si) ratio of 0.063, and (c) sample with Al/(Al + Si) ratio of 0.088. T: tobermorite, P: portlandite, Q: quartz, MS: monosulphate, KA: katoite, HE: hydroxylellestadite, A: anhydrite, C-S-H: non-crystalline calcium silicate hydrate. The vertical line at 90 min indicates the time at which the temperature reached 190 °C [21].

Fig. 8. Morphology of tobermorite prepared at 180 °C for 7 h with different Al dosages, denoted as Al/(Al + Si) = 0 (a), 0.01 (b), 0.03 (c), 0.06 (d), 0.09 (e), and 0.12 (f). Reproduced from [77] with permission from the Royal Society of Chemistry.
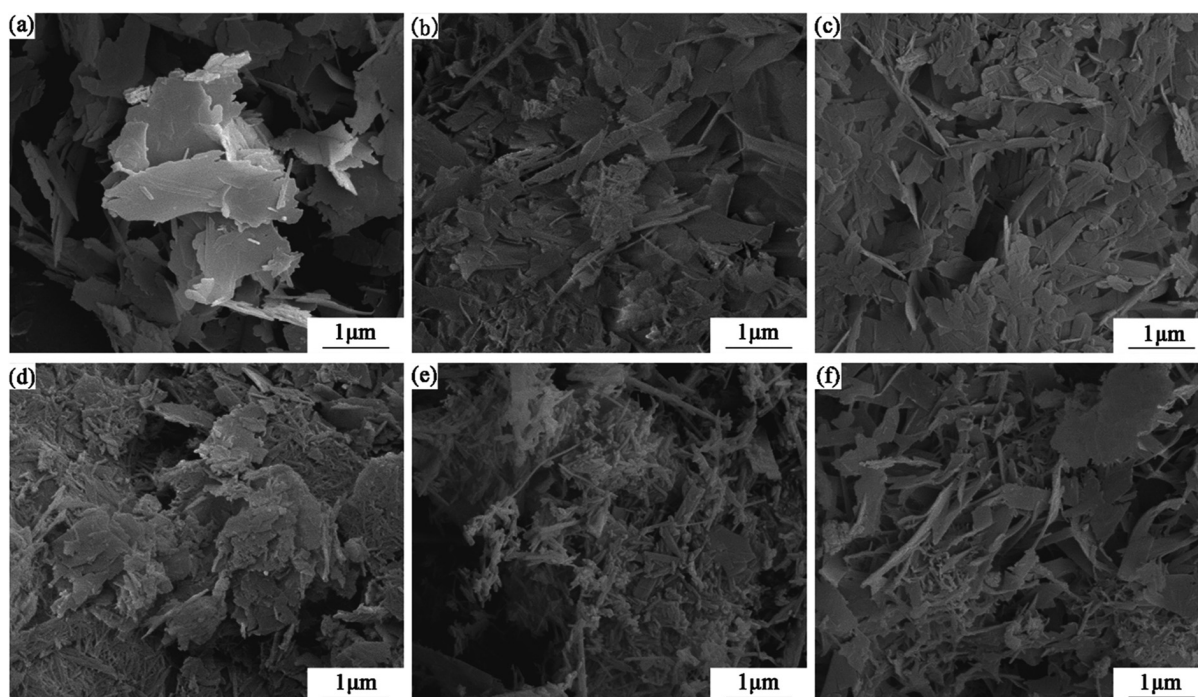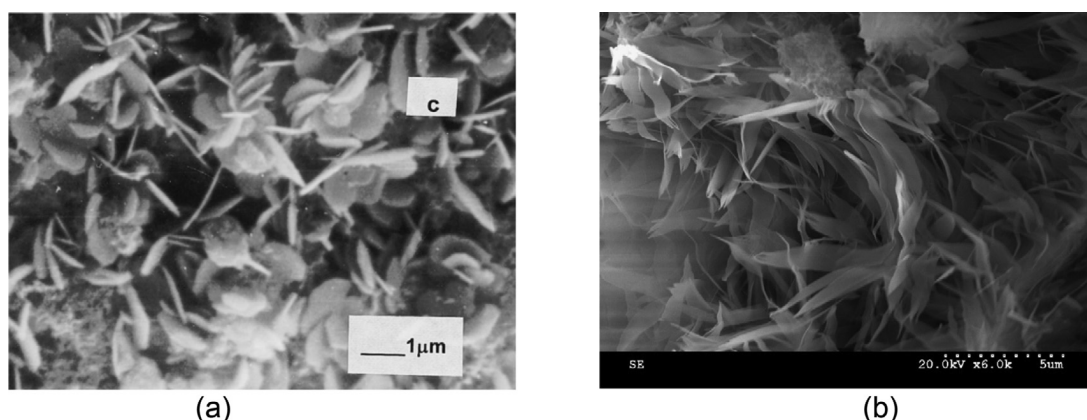

(a) (b)

Fig. 9. Morphology of tobermorite (a) 20 wt% Na_2O + 10 wt% Al_2O_3, cured at 200 °C for 2 h [103] and (b) Ca/(Si + Al + S) = 0.83, Al/Si = S/Si = 0.0208, cured at 175 °C for 24 h [99].

hydrogarnet starts to form at Al/(Al + Si) >0.03 [71,101,104–106]. This retards the reaction between CaO and SiO_2 and the transformation of C-S-H into tobermorite as the formation of hydrogarnet consumes Ca^{2+} and lowers the Ca/Si in C-S-H [101,104].

Hydrogarnets $(Ca_3Al_2(SiO_4)_{3-y}(OH)_{4y})$ designate the solid solution series between grossular $(Ca_3Al_2(SiO_4)_3, y = 0)$ and katoite $(Ca_3Al_2(OH)_{12}, y = 3)$, and a miscibility gap exists between (2.24 < y < 2.58) at 95 °C. The formation of hydrogarnets depends not only on the bulk composition but also on the temperature and is promoted by the presence of Fe [41,53,71,77,78,107–109]. At Al/(Si + Al) $\leq$ 0.13, Al-containing tobermorite is stabilised with respect to hydrogarnet in the system Al_2O_3-CaO-SiO_2-H_2O under hydrothermal conditions, while at Al/(Si + Al) > 0.13, hydrogarnet will coexist with tobermorite at 175/180 °C [71,106]. At a relatively low temperature of 120 °C, there is no hydrogarnet detected, although the Al/(Al + Si) ratio is as high as 0.15 [41]. Furthermore, the y value and unit cell size of hydrogarnets tend to move towards lower val-

ues with increasing temperature [94]. Due to the different availability of SiO_2, Si-free katoite, $Ca_3Al_2(OH)_{12}$ is formed when quartz powder is used as a silica source, while $Ca_3Al_2(SiO_4)_{0.5}(OH)_{10}$ is generated in the presence of amorphous silica [106].

2.3. Alkali ions

2.3.1. Sodium

Portland cement includes roughly 0.2–2.0 wt% alkali oxides, Na_2O and K_2O, which exist in clinker phases and alkali sulphates. Alkali ions are also widely found in SCMs with varying contents. In addition, the utilisation of an alkali activator in geopolymer increases the alkali content of the system. Alkali ions also affect the stability of C-S-H and secondary phases.

2.3.1.1. Sodium suppresses transformation. According to the literature, the influence of sodium is highly related to its accessible con-

tent. Nelson and Kalousek synthesised tobermorite with varying sodium content, (Na + Ca)/Si = 0.83 at 175 °C for 7 d, and found that tobermorite formed at a low sodium content was replaced gradually by C-S-H I at higher addition of sodium. At very high sodium contents, pectolite (NaCa$_2$Si$_3$O$_8$(OH)) was stabilised, which has a large thermal stability range from 180 to 325 °C and can coexist with xonotlite, truscottite, foshagite and tobermorite [110]. This suppression of Na on the transformation of C-S-H I into crystalline phases has been observed in different studies: in alkaline solution the conversion of initially formed poorly crystalline phase into tobermorite is slower than in pure water [111]. Similarly, at Ca/Si = 1 within 24 h at 200 °C, predominately xonotlite is formed in the absence of sodium, while in the presence of sodium rather C-S-H I is detected; C-S-H I is the only phase at a Na$_2$O content of 20 wt% [103]. When the Na$_2$O content is increased further, different sodium- C-S-H, NaAlSi$_2$O$_6$·H$_2$O [112], NaCaHSiO$_4$ [111,113] and NaCa$_2$Si$_3$O$_8$(OH) [103], are generated according to the relative amounts of Al and Si in the system. These phenomena together underline that Na$^+$ suppresses the transformation of poorly-ordered C-S-H into crystalline phases [103,114]. The higher pH values in the presence of Na$_2$O and NaOH accelerate the dissolution of

silica-bearing components [115] and the reaction rate of quartz [111]. The faster dissolution of quartz results in the formation of C-S-H with low Ca/Si , which is more difficult to rearrange into the stable crystalline phases [59,116]. Interestingly, the addition of Al$_2$O$_3$ with a high amount of sodium accelerates the transformation hindering the precipitation of pectolite [103].

2.3.1.2. Incorporation into structures. Na$^+$ is known to enter the structure of poorly crystalline C-S-H and tobermorite, in particular at low Ca/Si [117,118]. The incorporation of Al in the bridging sites of SiO$_4$ chain can increase the content of bound Na$^+$ as the charge deficit due to the replacement of Si^{4+} by Al^{3+} can be balanced by binding monovalent Na$^+$ or K$^+$ [118–121]. The schematic representation is shown in Fig. 10 [121]. Although this combined uptake has been observed at room temperature only, it can be expected to be present under hydrothermal conditions as well. Levinskas et al. synthesised gyrolite at 200 °C for 48 h from a CaO and SiO$_2$·nH$_2$O mixture (Ca/Si = 0.66). However, in the presence of 5 wt% Na$_2$O, the morphology of gyrolite was transferred from plate to fibre/-plate as shown in Fig. 11 [122].
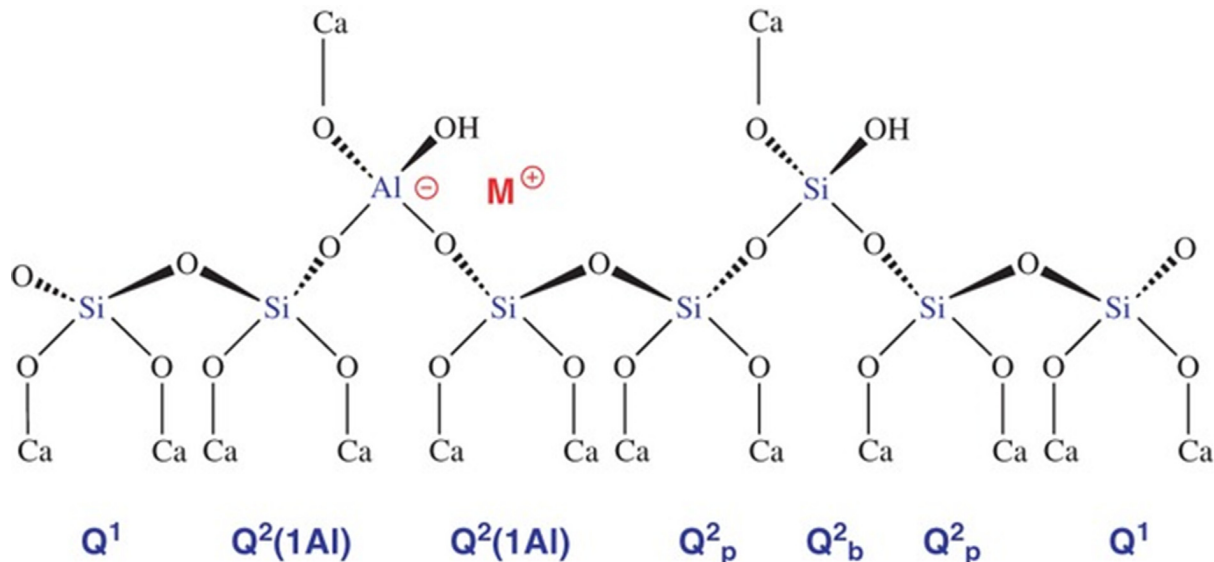

Fig. 10. Schematic representation of the interaction between alkali ions and Al upon incorporation into C-S-H at the bridging site (M$^+$ represents the monovalent Na$^+$ or K$^+$) [121].
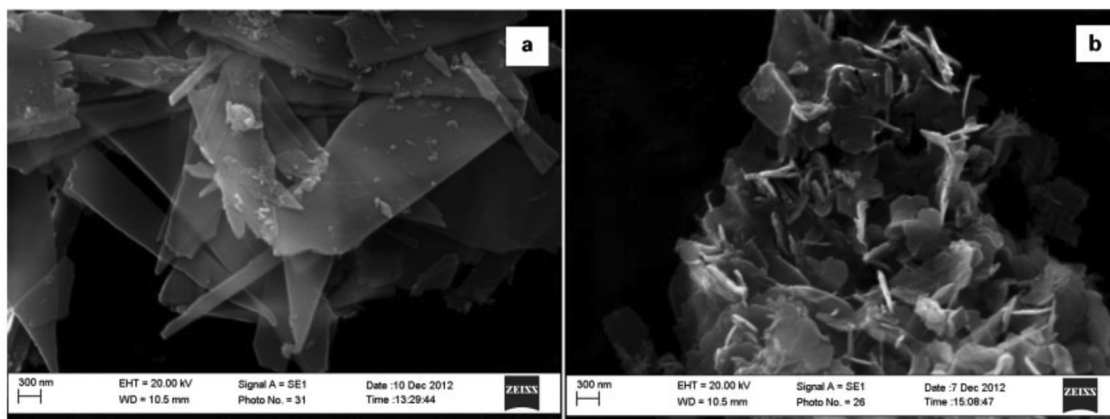

Fig. 11. SEM Images of pure gyrolite (a) and gyrolite with intercalated Na$^+$ (b) [122].

The uptake of Na+ has been reported for tobermorite and gyrolite, but not for crystalline phases with high Ca/Si ratio such as xonotlite, foshagite [110], and α-C$_2$SH [115]. However, the presence of Na+ and the resulting higher pH values may also influence stability of different crystalline phases. For example, at 200 °C in the presence of Na$_2$O (5 wt%), α-C$_2$SH does not transform into hillebrandite (Ca$_2$SiO$_3$(OH)$_2$) but rather to killalaite (2Ca$_3$Si$_2$O$_7$·H$_2$O) [48,115].

2.3.2. Potassium

Interestingly, there are some differences in the effect of potassium and sodium on C-S-H stabilisation. Liu et al. [123] used K$_2$SiO$_3$ and Na$_2$SiO$_3$ as siliceous materials (keeping the ratios of K/Si and Na/Si constant at 2) to synthesise xonotlite at Ca/Si = 1 and 225 °C and found that only pectolite is observed in the samples with Na$_2$SiO$_3$, while xonotlite is formed as the main crystalline phase in samples with K$_2$SiO$_3$. Furthermore, when Na$_2$O is added to the system with K$_2$SiO$_3$, xonotlite persists up to 5 wt% of Na$_2$O, while at high Na$_2$O contents, xonotlite is gradually replaced by pectolite as shown in Fig. 12. These phenomena indicate a significant influence of Na+ on the hydrates formed, while K+ has little effect. Similarly, Wang et al. [124] found a stabilisation of tobermorite in the presence of K$_2$SO$_4$ but not for Na$_2$SO$_4$; the effect of

Fig. 12. XRD diffractograms of the products synthesised under hydrothermal conditions (15 h at 225 °C, Ca/Si = 1) in the presence of K$_2$SiO$_3$ and different contents of Na$_2$O: (a) 5 wt%, (b) 10 wt%, and (c) 15 wt%, reproduced from [123].

the sulphate introduced will be discussed in section 2.6. It can be concluded that under hydrothermal conditions, Na+ stabilises pectolite over xonotlite or tobermorite [123], while the presence of potassium enhances the formation of crystalline C-S-H such as xonotlite or tobermorite.

2.4. Magnesium

Several studies have investigated the effect of Mg on C-S-H at room temperature, and very little uptake of Mg in C-S-H has been observed (Mg/Ca < 0.01), but the formation of a separate magnesium silicate hydrate phase (M-S-H) [125,126]. M-S-H is also observed at cement/clay interfaces where a decalcification of the cement occurs [127,128] and at the surfaces of cementitious materials in contact with groundwater or seawater rich in Mg^{2+} as a secondary product [129–131].

The information on Mg uptake at higher temperature are somewhat contradictory, which could at least partially relate to the difficulties to identify poorly crystalline M-S-H phases. Fernandez et al. [132,133] synthesised a series of C-S-H by hydrating C$_3$S in the presence of MgO at 100 °C for 23 d and interpreted the data as Mg incorporation with a four-fold coordination in the silica chains of C-S-H. At 175 °C, Mostafa et al. reported for Ca/Si = 0.83 and Mg/Ca = 0.04, that the existence of MgO increases the polymerisation of silicate chains and the crystallinity of tobermorite which exhibits larger lath-like morphology after 24 h of autoclaving (see Fig. 13) [134] indicating that a low amount of Mg could be incorporated in C-S-H. At a temperature of 180–300 °C, Qian et al. [135] studied the influence of Mg on crystallisation based on the system MgO-CaO-SiO$_2$-H$_2$O, and the results are summarised in Table 1. The authors attribute the phenomenon that Mg(OH)$_2$ and Mg$_3$Si$_2$O$_5$(OH)$_4$ are not detected in the samples with Mg/Ca = 0.2 to the incorporation of Mg into tobermorite and xonotlite. Based on the EDX results, xonotlite seems to have a stronger capability to bind Mg than tobermorite, while the lattice parameters of xonotlite are negligibly changed by the assumed Mg incorporation. The effect of hydrothermal duration on incorporation is quite small, and the idealised formulas for incorporated tobermorite and xonotlite would correspond to Ca$_{4.36}$Mg$_{0.60}$Si$_{6.02}$(OH)$_2$·4H$_2$O and Ca$_{3.58}$Mg$_{2.41}$Si$_{6.04}$O$_{17}$(OH)$_2$, respectively [135]. In contrast, Mitsuda et al. concluded that Mg could not enter the tobermorite structure or only to a very low amount as the natural tobermorite specimens are very low in Mg [136]. Together these literature data indicate the uptake of some Mg in crystalline C-S-H phases, and possibly a higher tendency at higher temperatures.
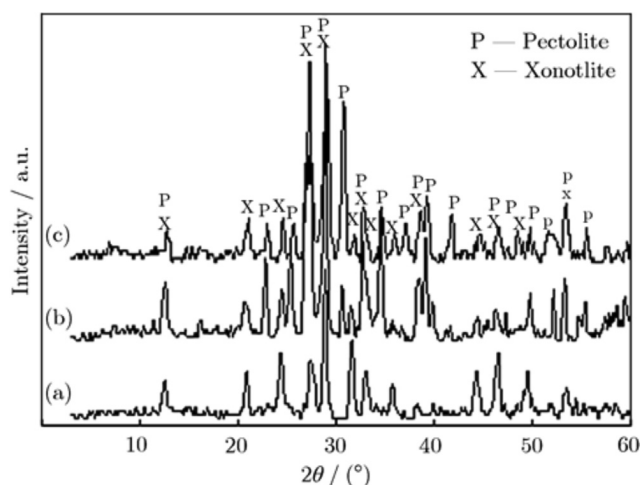
(a)   (b)   (c)
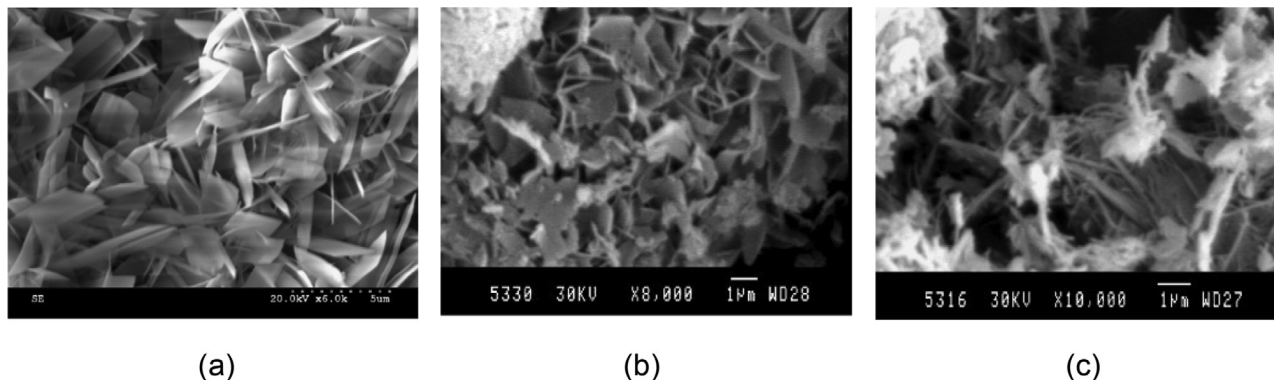
Fig. 13. Morphology of tobermorite synthesised under hydrothermal conditions: (a) pure tobermorite after 24 h with typical platy morphology [99], (b) tobermorite in the presence of MgO after 4 h with typical platy morphology, (c) tobermorite in the presence of MgO after 24 h with lath-like morphology [134].

Table 1
The effect of magnesium on the formation of tobermorite and xonotlite at a Mg/Ca range of 0–1.0 [135].

| Mg/Ca	Ca/Si = 0.8					Ca/Si = 1.5				
	0	0.2	0.4	0.6	1.0	0	0.2	0.4	0.6	1.0
180 °C, 10 h	Tob+	Tob+	Tob++MH	Tob++MH	Tob++MH	Tob++Xon	Tob++Xon	Tob++Xon + MH	Tob++Xon + MH	Tob++Xon + MH
180 °C, 3 d	Tob++Xon	Tob++Xon	Tob++Xon + MH	Tob++Xon + MH	Tob++Xon + MH					
240 °C, 10 h	Xon++Tob	Xon++Tob	Xon++Tob + MH	Xon++Tob + MH	Xon++Tob + MH					
240 °C, 24 h	Xon+	Xon+	Xon+	Xon++ M-S-H	Xon++ M-S-H	Xon+	Xon+	Xon++	Xon++ M-S-H	Xon++ M-S-H
300 °C, 10 h	Xon+	Xon+	Xon+	Xon++ M-S-H	Xon++ M-S-H					
300 °C, 24 h	Xon+	Xon+	Xon+	Xon++ M-S-H	Xon++ M-S-H					
300 °C, 3 d	Xon+	Xon+	Xon+	Xon++ M-S-H	Xon++ M-S-H	Xon+	Xon+	Xon++ M-S-H	Xon++ M-S-H	Xon++ M-S-H

Abbreviation: Tob=tobermorite, Xon=xonotlite, MH=magnesium hydroxide Mg(OH)$_2$, M-S-H=magnesium silicate Mg$_3$Si$_2$O$_5$(OH)$_4$. The superscript + marks the phase as the main phase.

2.5. Iron

Portland cements generally contain 2–5 wt% of iron, mainly present in the alumino-ferrite (Ca$_4$(Al$_x$Fe$_{x-1}$)$_4$O$_{10}$) phase [137]. The hydration rate of alumino-ferrite is relatively slow and the dissolved Fe precipitates at room temperature mainly as siliceous hydrogarnet [78,137]. Iron also widely exists in SCMs, such as fly ash (Fe$_2$O$_3$ of 6–16 wt%) [138], kaolinite (Fe$_2$O$_3$ of <2 wt%) [139,140], and granulated ground blast furnace slag (Fe$_2$O$_3$ of <2 wt%) [138]. A low amount of Fe can be incorporated in C-S-H (Fe/Si < 0.01) at room temperature [141], somewhat more under hydrothermal conditions.

In the study of Qian et al., Fe-hydrogarnet was formed as the main product from a steel slag, autoclaved at 345 °C. When quartz was added to the system (Ca/Si = 0.8), Fe-substituted tobermorite was observed as the main hydrate with an incorporated amount around 10–15 wt% based on EDX spectroscopy [38]. Labhasetwar et al. [142] observed that Fe^{3+} enters the tobermorite structure and takes the position of interlayer Ca^{2+} without much loss of crystallinity, which was later confirmed by Haastrup et al. [143].

As for the influence of Fe incorporation, it is reported that the imperfection of tobermorite is intensified at 175 °C after 4 h of autoclaving, but the crystallinity after 16 h is increased, characterised by improved silicate chain polymerisation and chain cross-linkage, leading to the morphology of tobermorite conversion from a typical platy shape to a fibre shape growing parallel to the *b*-axis (along the silicate chains) [134]. Conversely, in other literature, for the system CaO-SiO$_2$-H$_2$O (Ca/Si = 1) under 200 °C, the number of Q^3 sites and the Q^3/Q^2 ratio are observed to decrease with a higher Fe concentration, and the authors suggested that the existence of Fe^{3+} leads to defect formation on the Q^3 sites of xonotlite and tobermorite, which contributes the space for the incorporation of foreign ions and the decrease in the crosslinking degree [143,144]. Furthermore, xonotlite is at 200 °C gradually replaced by a mixture of tobermorite, amorphous phase, and calcite with increasing Fe^{3+} from Fe/Si = 0 to 0.013. This phenomenon is attributed to that the Fe incorporation leads to charge defects, which increases the formation of the amorphous phase. The destabilisation of xonotlite to tobermorite leads to an excess of CaO, which reacts with CO$_2$ producing calcite [143]. Although the study seems to indicate that the presence of Fe stabilises tobermorite over xonotlite even at 200 °C, it also could be a kinetic effect as the autoclaving duration was not stated in [143]. Similarly another paper has reported [38], that Fe-substituted tobermorite remain stable above 345 °C without conversion to xonotlite.

2.6. Sulphate

Sulphate is widely present in cementitious materials. At room temperature, the dissolved SO$_4^{2-}$ from raw materials generally precipitates in AFt and AFm phases, while under hydrothermal conditions, rather hydroxyl ellestadite and anhydrite are stable [145].

At ambient conditions, SO$_4^{2-}$ can be co-sorbed on the surface and interlayer of C-S-H together with Ca^{2+}, and sulphate uptake increases with Ca/Si and sulphate concentration [146]. However under hydrothermal conditions, sulphate stabilises tobermorite with respect to C-S-H and sulphate has been reported to replace SiO$_4^{4-}$ in tobermorite [99].

At 200 °C and for the system CaO-SiO$_2$-H$_2$O with a Ca/(Si + S) ratio of 0.66 (corresponding to gyrolite), the presence of SO$_4^{2-}$ favours initially the formation of poorly crystalline Assarsson's Z-phase, which after longer autoclaving recrystallizes into well-ordered gyrolite and anhydrite. Some SO$_4^{2-}$ enters the gyrolite structure, which does not significantly affect the thermal stability of gyrolite as the recrystallization temperature of gyrolite into wollastonite is not changed [147]. At a higher Ca/Si ratio of 0.83, it is
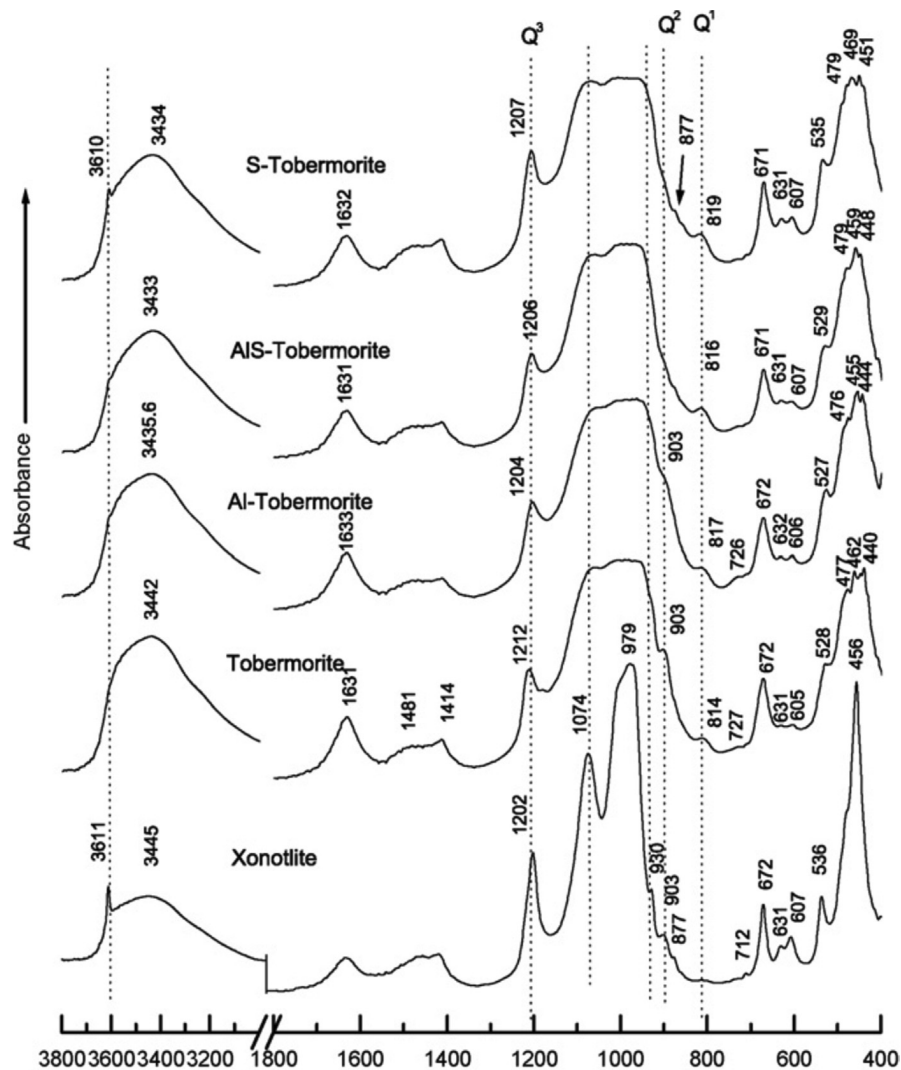
Fig. 14. FTIR spectra of tobermorite and xonotlite (S-Tobermorite, AlS-Tobermorite, and Al-Tobermorite represent sulphate substituted tobermorite, aluminium and sulphate substituted tobermorite, and aluminium substituted tobermorite) [99].

found that the transformation of amorphous C-S-H gel into tobermorite is accelerated by SO_4^{2-} (S/(Si + S) ratio of 0.02 and 175 °C [99], S/(Si + S) of 0.0125 and 200 °C[148]). The diffraction peak
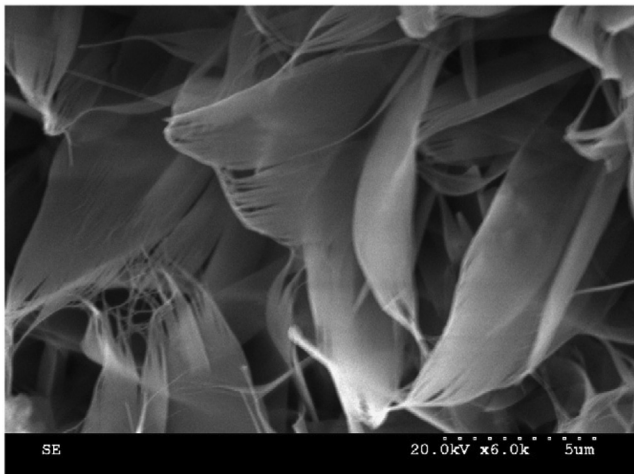
Fig. 15. Morphology of sulphate substituted tobermorite with larger leafy shape, cured at 175 °C under saturated steam pressure for 24 h [99].

with respect to the basal spacing of 1.1 nm tobermorite diffuses, indicating that the incorporation of SO_4^{2-} leads to crystal defects affecting the basal spacing [99]. The incorporation of SO_4^{2-} led to the presence of CaO-H groups in tobermorite (see stretching and bending modes at 3610 and 631 cm^{-1}, respectively in Fig. 14) [99]. It has also been observed that sulphate can stabilise tobermorite at 100 °C [104], which is much lower than the temperature that is generally used to synthesise tobermorite. However, at higher sulphate contents S/(Si + S) = 0.025, in addition to tobermorite, $CaSO_4$ and xonotlite are also formed [148] and the content of tobermorite decreases [149]. In the presence of sulphate, tobermorite crystals form large leafy shapes (see Fig. 15), larger compared with the typical tobermorite morphology shown in Fig. 13 [99,149].

3. Conclusions

Hydrothermal curing leads to fast hydration and strength development, which is advantageous for precast concrete industry, where high early strength is important. For the applications of AAC and CSB, hydrothermal curing is indispensable. In addition, in hydrothermal environments, such as hot oil and geothermal well cementing, cementitious materials have to resist high temper-

41

Table 2
Influence of foreign ions on the formation of amorphous intermediate under hydrothermal conditions.

	Dissolution of silica-bearing raw materials	Formation of intermediate	Transformation into crystalline phases	Reference
Al^{3+}	–	–	+[a]	[41,45,150,151]
Na^+	+	+	–	[103,111,115]
K^+	×	×	×	[123,124]
SO_4^{2-}	×	+	+[a]	[99,147,148]

+ and – represent an accelerating and suppressing effect respectively, × means ignorable effect; Superscript a means that the effect is highly related to the concentration. Excessive Al leads to hydrogarnet formation, which consumes plenty of Ca^{2+}, resulting in a shortage of Ca-rich C-S-H formation.

Table 3
Influence of foreign ions on crystalline C-S-H phases under hydrothermal conditions.

	Incorporation manner	Stabilisation of C-S-H	Secondary phase[b]	Incorporation site	Morphology	Reference
Al^{3+}	$Al^{3+} \leftrightarrow Si^{4+}$	Tobermorite	Hydrogarnet (high Ca)	Bridging and crosslinked sites	platy shape → lath or needle shape	[17,75,80,94,95]
Na^+	Charge compensation [a]	–	pectolite	Interlayer	–	[110,118,120,121]
K^+	Charge compensation	–	–	Interlayer	–	[118,121]
Mg^{2+}	$Mg^{2+} \leftrightarrow Ca^{2+}$	–	Magnesium silicate hydrate	interlayer	platy shape → lath shape	[133,134]
Fe^{3+}	$Fe^{3+} \leftrightarrow Ca^{2+}$	Tobermorite	Hydrogarnet (high Ca)	Interlayer	platy shape → lath or needle shape	[134,152]
SO_4^{2-}	$SO_4^{2-} \leftrightarrow SiO_4^{4-}$	Tobermorite	Ellestadite	–	platy shape → larger leafy shape	[99,149]

[a] The substitution of Na^+ in tobermorite is small, and no substitution is observed in xonotlite, foshagite, and α-C_2SH. The incorporation ability of Na^+ is enhanced by the incorporation of Al in the bridging sites of SiO_4 tetrahedra.
[b] The presence of foreign elements can stabilise respective C-S-H, while induce the formation of secondary phases at high contents.

ature and high pressure for a long period of time. In order to improve the durability and performance of concrete, SCMs are often utilised. In the cement and SCMs, different foreign elements (mainly Al, Na, K, Fe, Mg, and sulphate) are also present and affect the formation and stability of hydrates, especially C-S-H. Under hydrothermal conditions, the influence of the foreign elements is magnified. Foreign elements can influence the formation of amorphous or poorly crystalline intermediates by accelerating or suppressing the dissolution of raw materials, lead to the uptake of ions in C-S-H, stabilise or destabilise crystalline phases, and result in the presence of additional phases.

The effects are summarised in Tables 2 and 3. Alkalis and sulphate can accelerate the dissolution of silica-bearing raw materials, which is favourable to the formation of amorphous intermediate C-S-H, while Al retards dissolution. The formation and stabilisation of amorphous C-S-H can retard or even prevent transformation into crystalline phases, such as tobermorite, xonotlite or gyrolite. This has been attributed to the accelerated silica dissolution in the presence of some elements, which leads to the formation of C-S-H with low Ca/Si ratio that does not easily convert into crystalline phases. In addition, the uptake of Al, Mg, and Fe results in the preferential growth of tobermorite along the *b*-axis (silicate chains) forming a lath-like and needle-like morphology, while sulphate-substituted tobermorite crystals present larger leafy shapes.

The incorporation of foreign elements in C-S-H has been observed by various methods such as NMR, FTIR, Raman spectroscopy, and SEM-EDX elemental analysis. The manner of foreign ions incorporation into the structure of C-S-H occurs at different sites: aluminium and sulphate replace silicon, magnesium and possibly iron replaces calcium in the interlayer, while alkali ions compensate negative charges. The incorporation sites of the foreign elements are influenced by their charge, ionic radius, coordination number, speciation, and solubility. The uptake of Al^{3+} and alkali ions is relatively well investigated under hydrothermal conditions, while very limited information only is available for iron,

magnesium, and sulphate incorporation into the structure of C-S-H. Aluminium, iron, and sulphate can stabilise tobermorite, while sodium does the reverse. Excessive foreign elements induce the formation of secondary phases, which aluminium and iron precipitate in hydrogarnet, sodium precipitates in sodium-C-S-H such as pectolite, and magnesium precipitates in magnesium silicate hydrates.

This review has highlighted that Ca/Si ratio and the amount of Al^{3+}, Fe^{3+}, Na^+, K^+, Mg^{2+}, and SO_4^{2-} have a significant effect on the composition and stability of C-S-H under hydrothermal conditions but also that there is a lack of knowledge in many cases. It can be expected that more SCMs as well as more divers types of SCMs will be used in the future, which makes the understanding of the effect of foreign ions even more important. In this context, in particular understanding the role of Mg, originating from the use of low-grade limestone containing dolomite $(CaMg(CO_3)_2)$, could be of interest [153,154], both on the reaction kinetics as well as on the phases formed. Similarly, carbonate can be also introduced by SCMs, carbonate activator (alkali-activated system), carbonation curing, and carbonic acid environment (well cementing), which may lead to the formation of calcium silicate carbonate depending on the bulk chemical composition. Scawtite $(Ca_7(Si_6O_{18})(CO_3)\cdot 2H_2O)$ is a typically encountered crystalline phase which is suggested as xonotlite $(Ca_6Si_6O_{17}(OH)_2)$ with 5.28% CO_2 (molecular weight) replacing part of silica [61], while other research about the influence of carbonate on C-S-H under autoclaving conditions is still limited.

It should be noted that most of the literature reviewed in this paper is based on a $CaO-SiO_2-H_2O$ system rather than on actual cements, where many different elements are present at the same time. This is expected to result in divers effects on the formation and stability of C-S-H under hydrothermal conditions, a topic on which but very little systematic knowledge is available.

Based on the knowledge of the simple C-S-H system under hydrothermal conditions, some important conclusion can be drawn for the efficient use of SCMs: the appropriate use of Al-

rich materials such as metakaolin in autoclaved cements is expected to accelerate and to stabilise tobermorite formation. This accelerating effect can be utilised to reduce the autoclaving temperature and duration, saving energy and improving production efficiency. Also, the thermal stability of tobermorite can be significantly improved by Al and Al can increase its capability to bind alkali ions. This additional alkali binding may be exploited to improve the alkalinity tolerance of the mixture, making it possible to use highly alkaline raw materials. Similarly, Na and K can accelerate the reaction and at the same time hinder the formation of crystalline hydrates, which can affect compressive strength positively, although it remains unclear whether this a permanent or just a temporary effect.

An improved knowledge will also make it possible to develop appropriate thermodynamic models to predict the composition of hydrothermal cements and construct stability diagrams in the presence of different amounts of Al^{3+}, Fe^{3+}, Na^+, K^+, Mg^{2+}, and SO_4^{2-} under hydrothermal conditions.

Declaration of Competing Interest

The authors declare that they have no known competing financial interests or personal relationships that could have appeared to influence the work reported in this paper.

Acknowledgment

References

[1] SPE Oilfield and Geothermal Chemistry Symposium, Society of Petroleum Engineers, 1979.

[2] E.B. Nelson, D. Guillot, Well cementing, second ed., Sugar Land Tex, Schlumberger, 2006.

[3] F. Qu, W. Li, W. Dong, V.W.Y. Tam, T. Yu, Durability deterioration of concrete under marine environment from material to structure: a critical review, J. Build. Eng. 35 (2021) 102074.

[4] H.-W. Song, C.-H. Lee, K.Y. Ann, Factors influencing chloride transport in concrete structures exposed to marine environments, Cem. Concr. Compos. 30 (2008) 113–121.

[5] B. Martín-Pérez, H. Zibara, R.D. Hooton, M.D.A. Thomas, A study of the effect of chloride binding on service life predictions, Cem. Concr. Res. 30 (2000) 1215–1223.

[6] G.O. Assarsson, Hydrothermal reactions between calcium hydroxide and amorphous silica: the reactions between 180 and 220°, J. Phys. Chem. 61 (1957) 473–479.

[7] G.O. Assarsson, Hydrothermal reactions between calcium hydroxide and amorphous silica: the reactions between 120 and 160°, J. Phys. Chem. 62 (1958) 223–228.

[8] S. Goñi, A. Guerrero, M.P. Luxán, A. Macías, Activation of the fly ash pozzolanic reaction by hydrothermal conditions, Cem. Concr. Res. 33 (2003) 1399–1405.

[9] T. Zdeb, An analysis of the steam curing and autoclaving process parameters for reactive powder concretes, Constr. Build. Mater. 131 (2017) 758–766.

[10] N. Arabi, R. Jauberthie, N. Chelghoum, L. Molez, Formation of C-S-H in calcium hydroxide–blast furnace slag–quartz–water system in autoclaving conditions, Adv. Cem. Res. 27 (2015) 153–162.

[11] S.L. Colston, P. Barnes, A.C. Jupe, S.D.M. Jacques, C. Hall, P. Livesey, J. Dransfield, N. Meller, G.C. Maitland, An in situ synchrotron energy-dispersive diffraction study of the hydration of oilwell cement systems under high temperature/autoclave conditions up to 130 °C, Cem. Concr. Res. 35 (2005) 2223–2232.

[12] O.M. Abdulkareem, A. Ben Fraj, M. Bouasker, A. Khelidj, Effect of chemical and thermal activation on the microstructural and mechanical properties of more sustainable UHPC, Constr. Build. Mater. 169 (2018) 567–577.

[13] P.R. Prem, A. Ramachandra Murthy, B.H. Bharatkumar, Influence of curing regime and steel fibres on the mechanical properties of UHPC, Mag. Concr. Res. 67 (2015) 988–1002.

[14] I. Schachinger, H. Hilbig, T. Stengel, E. Fehling, Effect of curing temperature at an early age on the long-term strength development of UHPC, in: 2nd International Symposium on Ultra High Performance Concrete, Kassel University Kassel, Gemany, pp. 205–213.

[15] H. Connan, A. Ray, P. Thomas, J.-P. Guerbois, Effect of autoclaving temperature on calcium silicate-based building products containing clay-brick waste, J. Therm. Anal. Calorim. 88 (2007) 115–119.

[16] T. Mitsuda, K. Sasaki, H. Ishida, Phase evolution during autoclaving process of aerated concrete, J. Am. Ceram. Soc. 75 (1992) 1858–1863.

[17] X. Qu, X. Zhao, Previous and present investigations on the components, microstructure and main properties of autoclaved aerated concrete – a review, Constr. Build. Mater. 135 (2017) 505–516.

[18] L. Nguyen Trong, S. Asamoto, K. Matsui, Sorption isotherm and length change behavior of autoclaved aerated concrete, Cem. Concr. Compos. 94 (2018) 136–144.

[19] Y.-L. Chen, M.-S. Ko, J.-E. Chang, C.-T. Lin, Recycling of desulfurization slag for the production of autoclaved aerated concrete, Constr. Build. Mater. 158 (2018) 132–140.

[20] N. Isu, H. Ishida, T. Mitsuda, Influence of quartz particle size on the chemical and mechanical properties of autoclaved aerated concrete (I) tobermorite formation, Cem. Concr. Res. 25 (1995) 243–248.

[21] K. Matsui, J. Kikuma, M. Tsunashima, T. Ishikawa, S.-Y. Matsuno, A. Ogawa, M. Sato, In situ time-resolved X-ray diffraction of tobermorite formation in autoclaved aerated concrete: influence of silica source reactivity and Al addition, Cem. Concr. Res. 41 (2011) 510–519.

[22] J. Schreiner, D. Jansen, D. Ectors, F. Goetz-Neunhoeffer, J. Neubauer, S. Volkmann, New analytical possibilities for monitoring the phase development during the production of autoclaved aerated concrete, Cem. Concr. Res. 107 (2018) 247–252.

[23] C. Shi, Z. Wu, J. Xiao, D. Wang, Z. Huang, Z. Fang, A review on ultra high performance concrete: Part I. Raw materials and mixture design, Constr. Build. Mater. 101 (2015) 741–751.

[24] C. Wang, C. Yang, F. Liu, C. Wan, X. Pu, Preparation of ultra-high performance concrete with common technology and materials, Cem. Concr. Compos. 34 (2012) 538–544.

[25] A. Tafraoui, G. Escadeillas, T. Vidal, Durability of the ultra high performances concrete containing metakaolin, Constr. Build. Mater. 112 (2016) 980–987.

[26] M.A.A. Aldahdooh, N. Muhamad Bunnori, M.A. Megat Johari, Development of green ultra-high performance fiber reinforced concrete containing ultrafine palm oil fuel ash, Constr. Build. Mater. 48 (2013) 379–389.

[27] W. Wang, J. Liu, F. Agostini, C.A. Davy, F. Skoczylas, D. Corvez, Durability of an Ultra High Performance Fiber Reinforced Concrete (UHPFRC) under progressive aging, Cem. Concr. Res. 55 (2014) 1–13.

[28] E. Fehling, M. Schmidt, J.C. Walraven, T. Leutbecher, S. Fröhlich, Ultra-High Performance Concrete UHPC: Fundamentals – Design – Examples, Ernst & Sohn, Berlin, 2014.

[29] C. Wu, J. Li, Y. Su (Eds.), Development of Ultra-High Performance Concrete Against Blasts Woodhead Publishing Series in Civil and Structural Engineering, Woodhead Publishing, 2018.

[30] M. Chen, L. Lu, S. Wang, P. Zhao, W. Zhang, S. Zhang, Investigation on the formation of tobermorite in calcium silicate board and its influence factors under autoclaved curing, Constr. Build. Mater. 143 (2017) 280–288.

[31] Z. Wang, S. Ma, S. Zheng, J. Ding, X. Wang, Flexural strength and thermal conductivity of fiber-reinforced calcium silicate boards prepared from fly ash, J. Mater. Civ. Eng. 31 (2019) 4019140.

[32] M. Chen, Y. Zheng, X. Zhou, L. Li, S. Wang, P. Zhao, L. Lu, X. Cheng, Recycling of paper sludge powder for achieving sustainable and energy-saving building materials, Constr. Build. Mater. 229 (2019) 116874.

[33] L. Zhang, Y. Bai, W. Chen, F.-X. Ding, H. Fang, Thermal performance of modular GFRP multicellular structures assembled with fire resistant panels, Compos. Struct. 172 (2017) 22–33.

[34] T. Morgado, J.R. Correia, A. Moreira, F.A. Branco, C. Tiago, Experimental study on the fire resistance of GFRPpultruded tubular columns, Compos. B Eng. 69 (2015) 201–211.

[35] L. Zhang, Y. Bai, Y. Qi, H. Fang, B. Wu, Post-fire mechanical performance of modular GFRP multicellular slabs with prefabricated fire resistant panels, Compos. B Eng. 143 (2018) 55–67.

[36] E. Grabowski, J.E. Gillott, Effect of replacement of silica flour with silica fume on engineering properties of oilwell cements at normal and elevated temperatures and pressures, Cem. Concr. Res. 19 (1989) 333–344.

[37] D. Mangold, Seasonal storage–a German success story, Sun & Wind Energy 1 (2007) 48–58.

[38] G. Qian, D.D. Sun, J.H. Tay, Z. Lai, G. Xu, Autoclave properties of kirschsteinite-based steel slag, Cem. Concr. Res. 32 (2002) 1377–1382.

[39] B. Lothenbach, K. Scrivener, R.D. Hooton, Supplementary cementitious materials, Cem. Concr. Res. 41 (2011) 1244–1256.

[40] G.O. Assarsson, E. Rydberg, Hydrothermal reactions between calcium hydroxide and amorphous silica, J. Phys. Chem. 60 (1956) 397–404.

[41] T. Mitsuda, H.F.W. Taylor, Influence of aluminium on the conversion of calcium silicate hydrate gels into 11 Å tobermorite at 90°C and 120°C, Cem. Concr. Res. 5 (1975) 203–209.

[42] F.P. Glasser, S.Y. Hong, Thermal treatment of C–S–H gel at 1 bar H_2O pressure up to 200 C, Cem. Concr. Res. 33 (2003) 271–279.

[43] J. Kikuma, M. Tsunashima, T. Ishikawa, S.Y. Matsuno, A. Ogawa, K. Matsui, M. Sato, Hydrothermal formation of tobermorite studied by in situ X-ray diffraction under autoclave condition, J. Synchrotron Radiat. 16 (2009) 683–686.

[44] J. Kikuma, M. Tsunashima, T. Ishikawa, S.-Y. Matsuno, A. Ogawa, K. Matsui, M. Sato, In Situ Time-resolved X-ray diffraction of tobermorite formation process under autoclave condition, J. Am. Ceram. Soc. 93 (2010) 2667–2674.

[45] M. Sakiyama, T. Mitsuda, Hydrothermal reaction between C-S-H and kaolinite for the formation of tobermorite at 180 °C, Cem. Concr. Res. 7 (1977) 681–685.

[46] D.S. Klimesch, A. Ray, Effects of quartz particle size on hydrogarnet formation during autoclaving at 180°c in the cao-al2o3-sio2-h2o system, Cem. Concr. Res. 28 (1998) 1309–1316.

[47] H.F.W. Taylor, Cement Chemistry, secnd ed., Thomas Telford, London, 1997.

[48] S.Y. Hong, F.P. Glasser, Phase relations in the CaO-SiO2-H2O system to 200 °C at saturated steam pressure, Cem. Concr. Res. 34 (2004) 1529–1534.

[49] H.F.W. Taylor, The Chemistry of Cement, Academic Press, London, 1964.

[50] H.F.W. Taylor, Hydrated calcium silicates. Part V. The water content of calcium silicate hydrate (I), J. Chem. Soc. (1953) 163–171.

[51] G.L. Kalousek, R. Roy, Crystal chemistry of hydrous calcium silicates: II, Characterization of interlayer water, J. Am. Ceram. Soc. 40 (1957) 236–239.

[52] P. Blanc, X. Bourbon, A. Lassin, E.C. Gaucher, Chemical model for cement-based materials: Temperature dependence of thermodynamic functions for nanocrystalline and crystalline C–S–H phases, Cem. Concr. Res. 40 (2010) 851–866.

[53] N. Meller, K. Kyritsis, C. Hall, The mineralogy of the CaO–Al2O3–SiO2–H2O (CASH) hydroceramic system from 200 to 350 °C, Cem. Concr. Res. 39 (2009) 45–53.

[54] N. Meller, C. Hall, J.S. Phipps, A new phase diagram for the CaO–Al2O3–SiO2-H2O hydroceramic system at 200 °C, Mater. Res. Bull. 40 (2005) 715–723.

[55] K.J. Krakowiak, J.J. Thomas, S. James, M. Abuhaikal, F.-J. Ulm, Development of silica-enriched cement-based materials with improved aging resistance for application in high-temperature environments, Cem. Concr. Res. 105 (2018) 91–110.

[56] J.J. Chen, J.J. Thomas, H.F.W. Taylor, H.M. Jennings, Solubility and structure of calcium silicate hydrate, Cem. Concr. Res. 34 (2004) 1499–1519.

[57] I.G. Richardson, Tobermorite/jennite- and tobermorite/calcium hydroxide-based models for the structure of C-S-H: applicability to hardened pastes of tricalcium silicate, β-dicalcium silicate, Portland cement, and blends of Portland cement with blast-furnace slag, metakaolin, or silica fume, Cem. Concr.te Res. 34 (2004) 1733–1777.

[58] A. Nonat, The structure and stoichiometry of C-S-H, Cem. Concr. Res. 34 (2004) 1521–1528.

[59] H. Sato, M. Grutzeck, Effect of starting materials on the synthesis of tobermorite, MRS Proceedings 245 (1991) 172.

[60] L.H. Eilers, E.B. Nelson, Effect of silica particle size on degradation of silica stabilized portland cement, SPE Oilfield and Geothermal Chemistry Symposium, Society of Petroleum Engineers, 1979.

[61] L.H. Eilers, E.B. Nelson, L.K. Moran, High-temperature cement compositions-pectolite, scawtite, truscottite, or xonotlite: which do you want?, J Petrol. Technol. 35 (1983) 1373–1377.

[62] K.J. Krakowiak, J.J. Thomas, S. Musso, S. James, A.-T. Akono, F.-J. Ulm, Nano-chemo-mechanical signature of conventional oil-well cement systems: effects of elevated temperature and curing time, Cem. Concr. Res. 67 (2015) 103–121.

[63] M. Palou, V. Živica, T. Ifka, M. Boháč, M. Zmrzlý, Effect of hydrothermal curing on early hydration of G-Oil well cement, J. Therm. Anal. Calorim. 116 (2013) 597–603.

[64] P. Shen, L. Lu, Y. He, F. Wang, S. Hu, The effect of curing regimes on the mechanical properties, nano-mechanical properties and microstructure of ultra-high performance concrete, Cem. Concr. Res. 118 (2019) 1–13.

[65] M. Courtial, M.N. de Noirfontaine, F. Dunstetter, M. Signes-Frehel, P. Mounanga, K. Cherkaoui, A. Khelidj, Effect of polycarboxylate and crushed quartz in UHPC: microstructural investigation, Constr. Build. Mater. 44 (2013) 699–705.

[66] A.M. Rashad, S.R. Zeedan, H.A. Hassan, A preliminary study of autoclaved alkali-activated slag blended with quartz powder, Constr. Build. Mater. 33 (2012) 70–77.

[67] T. Peters, R. Iberg, T. Mumenthaler, Comparative study of the use of a quartz poor sand and a pure quartz sand for lime silica bricks and the kinetics of the hydrothermal hardening mechanism, Cem. Concr. Res. 8 (1978) 415–424.

[68] S. Bernstein, K.T. Fehr, The formation of 1.13 nm tobermorite under hydrothermal conditions: 1. The influence of quartz grain size within the system CaO–SiO2–D2O, Prog. Cryst. Growth Charact. Mater. 58 (2012) 84–91.

[69] S.O. Oyefesobi, D.M. Roy, Hydrothermal studies of type V cement-quartz mixes, Cem. Concr. Res. 6 (1976) 803–810.

[70] J. Kikuma, M. Tsunashima, T. Ishikawa, S. Matsuno, A. Ogawa, K. Matsui, M. Sato, Effects of quartz particle size and water-to-solid ratio on hydrothermal synthesis of tobermorite studied by in-situ time-resolved X-ray diffraction, J. Solid State Chem. 184 (2011) 2066–2074.

[71] D.S. Klimesch, A. Ray, Hydrogarnet formation during autoclaving at 180°C in unstirred metakaolin-lime-quartz slurries, Cem. Concr. Res. 28 (1998) 1109–1117.

[72] G.L. Kalousek, A.F. Prebus, Crystal chemistry of hydrous calcium silicates: III, Morphology and other properties of tobermorite and related phases, J. Am. Ceram. Soc. 41 (1958) 124–132.

[73] P. Faucon, A. Delagrave, C. Richet, J.M. Marchand, H. Zanni, Aluminum incorporation in calcium silicate hydrates (C–S–H) depending on their Ca/Si ratio, J. Phys. Chem. B 103 (1999) 7796–7802.

[74] P. Faucon, J.C. Petit, T. Charpentier, J.F. Jacquinot, F. Adenot, Silicon substitution for aluminum in calcium silicate hydrates, J. Am. Ceram. Soc. 82 (1999) 1307–1312.

[75] G.K. Sun, J.F. Young, R.J. Kirkpatrick, The role of Al in C-S-H: NMR, XRD, and compositional results for precipitated samples: NMR, XRD, and compositional results for precipitated samples, Cem. Concr. Res. 36 (2006) 18–29.

[76] E. L'Hôpital, B. Lothenbach, G. Le Saout, D. Kulik, K. Scrivener, Incorporation of aluminium in calcium-silicate-hydrates, Cem. Concr. Res. 75 (2015) 91–103.

[77] X. Qu, Z. Zhao, X. Zhao, Microstructure and characterization of aluminum-incorporated calcium silicate hydrates (C–S–H) under hydrothermal conditions, RSC Adv. 8 (2018) 28198–28208.

[78] B.Z. Dilnesa, B. Lothenbach, G. Renaudin, A. Wichser, D. Kulik, Synthesis and characterization of hydrogarnet Ca3(AlxFe1−x)2(SiO4)y(OH)4(3−y), Cem. Concr. Res. 59 (2014) 96–111.

[79] X. Pardal, I. Pochard, A. Nonat, Experimental study of Si–Al substitution in calcium-silicate-hydrate (C-S-H) prepared under equilibrium conditions, Cem. Concr. Res. 39 (2009) 637–643.

[80] M.D. Andersen, H.J. Jakobsen, J. Skibsted, Incorporation of aluminum in the calcium silicate hydrate (C-S-H) of hydrated portland cements: a high-field 27Al and 29Si MAS NMR investigation, Inorg. Chem. 42 (2003) 2280–2287.

[81] Z. Dai, T.T. Tran, J. Skibsted, H. Jennings, Aluminum incorporation in the C-S-H phase of white portland cement-metakaolin blends studied by27Al and29Si MAS NMR spectroscopy, J. Am. Ceram. Soc. 97 (2014) 2662–2671.

[82] I.G. Richardson, G.W. Groves, The incorporation of minor and trace elements into calcium silicate hydrate (C-S-H) gel in hardened cement pastes, Cem. Concr. Res. 23 (1993) 131–138.

[83] O.P. Shrivastava, R. Shrivastava, Sr2+ uptake and leachability study on cured aluminum-substituted tobermorite-OPC admixtures, Cem. Concr. Res. 31 (2001) 1251–1255.

[84] N.J. Coleman, Interactions of Cd(II) with waste-derived 11 Å tobermorites, Sep. Purif. Technol. 48 (2006) 62–70.

[85] N.J. Coleman, D.S. Brassington, A. Raza, A.P. Mendham, Sorption of Co2+ and Sr2+ by waste-derived 11 Å tobermorite, Waste Manage. 26 (2006) 260–267.

[86] J.E. Oh, S.M. Clark, P.J.M. Monteiro, Does the Al substitution in C-S–H(I) change its mechanical property?, Cem. Concr. Res. 41 (2011) 102–106.

[87] G. Geng, R.J. Myers, J. Li, R. Maboudian, C. Carraro, D.A. Shapiro, P.J. Monteiro, Aluminum-induced dreierketten chain cross-links increase the mechanical properties of nanocrystalline calcium aluminosilicate hydrate, Sci. Rep. 7 (2017) 44032.

[88] E. Kapeluszna, Ł. Kotwica, A. Różycka, Ł. Gołek, Incorporation of Al in C-A-S-H gels with various Ca/Si and Al/Si ratio: microstructural and structural characteristics with DTA/TG, XRD, FTIR and TEM analysis, Constr. Build. Mater. 155 (2017) 643–653.

[89] M.D. Andersen, H.J. Jakobsen, J. Skibsted, A new aluminium-hydrate species in hydrated Portland cements characterized by 27Al and 29Si MAS NMR spectroscopy, Cem. Concr. Res. 36 (2006) 3–17.

[90] A.C. Jupe, A.P. Wilkinson, K. Luke, G.P. Funkhouser, Class H cement hydration at 180 °C and high pressure in the presence of added silica, Cem. Concr. Res. 38 (2008) 660–666.

[91] A. Kunhi Mohamed, P. Moutzouri, P. Berruyer, B.J. Walder, J. Siramanont, M. Harris, M. Negroni, S.C. Galmarini, S.C. Parker, K.L. Scrivener, L. Emsley, P. Bowen, The atomic-level structure of cementitious calcium aluminate silicate hydrate, J. Am. Chem. Soc. 142 (2020) 11060–11071.

[92] S. Diamond, J.L. White, W.L. Dolch, Effects of isomorphous substitution in hydrothermally-synthesized tobermorite, Am. Mineral. 51 (1966) 388–401.

[93] S. Komarneri, D.M. Roy, R. Roy, Al-substituted tobermorite: shows cation exchange, Cem. Concr. Res. 12 (1982) 773–780.

[94] A.R. Brough, A. Atkinson, Sodium silicate-based, alkali-activated slag mortars: Part I. Strength, hydration and microstructure, Cem. Concr. Res. 32 (2002) 865–879.

[95] J. Li, G. Geng, R. Myers, Y.-S. Yu, D. Shapiro, C. Carraro, R. Maboudian, P.J.M. Monteiro, The chemistry and structure of calcium (alumino) silicate hydrate: a study by XANES, ptychographic imaging, and wide- and small-angle scattering, Cem. Concr. Res. 115 (2019) 367–378.

[96] S.A.S. El-Hemaly, T. Mitsuda, H.F.W. Taylor, Synthesis of normal and anomalous tobermorites, Cem. Concr. Res. 7 (1977) 429–438.

[97] M. Tsuji, S. Komarneni, P. Malla, Substituted tobermorites: 27Al and 29Si MASNMR, cation exchange, and water sorption studies, J. Am. Ceram. Soc. 74 (1991) 274–279.

[98] G.L. Kalousek, Crystal chemistry of hydrous calcium silicates: I, Substitution of aluminum in lattice of tobermorite, J. Am. Ceram. Soc. 40 (1957) 74–80.

[99] N.Y. Mostafa, A.A. Shaltout, H. Omar, S.A. Abo-El-Enein, Hydrothermal synthesis and characterization of aluminium and sulfate substituted 1.1nm tobermorites, J. Alloy. Compd. 467 (2009) 332–337.

[100] N.S. Bell, S. Venigalla, P.M. Gill, J.H. Adair, Morphological forms of tobermorite in hydrothermally treated calcium silicate hydrate gels, J. Am. Ceram. Soc. 79 (1996) 2175–2178.

[101] N.Y. Mostafa, Influence of air-cooled slag on physicochemical properties of autoclaved aerated concrete, Cem. Concr. Res. 7 (2005) 1349–1357.

[102] W. Tan, G. Zhu, Y. Liu, Z. Zhang, L. Liu, Effects and mechanism research of the crystalline state for the semi-crystalline calcium silicate, Cem. Concr. Res. 72 (2015) 69–75.

[103] W. NocuÒ-Wczelik, Effect of Na and Al on the phase composition and morphology of autoclaved calcium silicate hydrates, Cem. Concr. Res. 29 (1999) 1759–1767.

15

44

[104] N.Y. Mostafa, S.A.S. El-Hemaly, E.I. Al-Wakeel, S.A. El-Korashy, P.W. Brown, Activity of silica fume and dealuminated kaolin at different temperatures, Cem. Concr. Res. 31 (2001) 905–911.

[105] K. Kyritsis, N. Meller, C. Hall, Chemistry and morphology of hydrogarnets formed in cement-based CASH hydroceramics cured at 200° to 350°C, J. Am. Ceram. Soc. 92 (2009) 1105–1111.

[106] R. Siauciunas, A. Baltusnikas, Influence of SiO2 modification on hydrogarnets formation during hydrothermal synthesis, Cem. Concr. Res. 33 (2003) 1789–1793.

[107] M.U. Okoronkwo, F.P. Glasser, Stability of strätlingite in the CASH system, Mater. Struct. 49 (2016) 4305–4318.

[108] T.R. Jensen, A.N. Christensen, J.C. Hanson, Hydrothermal transformation of the calcium aluminum oxide hydrates CaAl2O4·10H2O and Ca2Al2O5·8H2O to Ca3Al2(OH)12 investigated by in situ synchrotron X-ray powder diffraction, Cem. Concr. Res. 35 (2005) 2300–2309.

[109] D.S. Klimesch, A. Ray, DTA–TGA of unstirred autoclaved metakaolin–lime–quartz slurries. The formation of hydrogarnet, Thermochim. Acta 316 (1998) 149–154.

[110] E.B. Nelson, G.L. Kalousek, Effects of Na2O on calcium silicate hydrates at elevated temperatures, Cem. Concr. Res. 7 (1977) 687–694.

[111] E.A. Blakeman, J.A. Gard, C.G. Ramsay, H.F.W. Taylor, Studies on the system sodium oxide-calcium oxide-silica-water, J. Appl. Chem. Biotech. 24 (1974) 239–245.

[112] C.A. Langton, E.L. White, M.W. Grutzeck, D.M. Roy, High temperature cements with geothermal applications, in: Ed. Septima, 1980, V-145–151.

[113] J. Alan Gard, C.G. Ramsay, Taylor, F.W. Harry, The unit cell of NaCaHSiO4: An electron-microscope and X-ray study, J. Appl. Chem. Biotechnol. 23 (1973) 87–91.

[114] W. Nocuń-Wczelik, Effect of some inorganic admixtures on the formation and properties of calcium silicate hydrates produced in hydrothermal conditions, Cem. Concr. Res. 27 (1997) 83–92.

[115] R. Siauciunas, A. Bankauskaite, K. Baltakys, M. Stankeviciute, The impact of Na2O on the synthesis of α-C2SH with different mineral composition and the stability of intermediate and final products, Ceram. Int. 45 (2019) 2846–2851.

[116] Y. Okada, H. Ishida, T. Mitsuda, 29Si NMR spectroscopy of silicate anions in hydrothermally formed C-S-H, J. Am. Ceram. Soc. 77 (1994) 765–768.

[117] E. L'Hôpital, B. Lothenbach, K. Scrivener, D.A. Kulik, Alkali uptake in calcium alumina silicate hydrate (C-A-S-H), Cem. Concr. Res. 85 (2016) 122–136.

[118] S.-Y. Hong, F.P. Glasser, Alkali binding in cement pastes: Part I. The C-S-H phase, Cem. Concr. Res. 29 (1999) 1893–1903.

[119] B. Lothenbach, A. Nonat, Calcium silicate hydrates: solid and liquid phase composition, Cem. Concr. Res. 78 (2015) 57–70.

[120] H. Viallis, P. Faucon, J.-C. Petit, A. Nonat, Interaction between salts (NaCl, CsCl) and calcium silicate hydrates (C−S−H), J. Phys. Chem. B 103 (1999) 5212–5219.

[121] J. Skibsted, M.D. Andersen, The effect of alkali ions on the incorporation of aluminum in the calcium silicate hydrate (C-S-H) phase resulting from portland cement hydration studied by 29 Si MAS NMR, J. Am. Ceram. Soc. 41 (2012) n/a-n/a.

[122] R. Levinskas, A. Baltušnikas, I. Lukošiūtė, K. Baltakys, R. Kalpokaitė-Dičkuvienė, A. Grybėnas, Modification of structure of synthetic gyrolite, Mater. Res. Innovations 17 (2013) 495–500.

[123] F. Liu, X.-D. Wang, J.-X. Cao, Effect of Na+ on xonotlite crystals in hydrothermal synthesis, Int. J. Miner. Metall. Mater. 20 (2013) 88–93.

[124] Shuping Wang, Xiaoqin Peng, Lu. Luping Tang, Cong Lan Zeng, Influence of inorganic admixtures on the 11 Å-tobermorite formation prepared from steel slags: XRD and FTIR analysis, Constr. Build. Mater. 60 (2014) 42–47.

[125] E. Bernard, B. Lothenbach, C. Cau-dit-Coumes, C. Chlique, A. Dauzères, I. Pochard, Magnesium and calcium silicate hydrates, Part I: Investigation of the possible magnesium incorporation in calcium silicate hydratVe (C-S-H) and of the calcium in magnesium silicate hydrate (M-S-H), Appl. Geochem. 89 (2018) 229–242.

[126] B. Lothenbach, D. Nied, E. L'Hôpital, G. Achiedo, A. Dauzères, Magnesium and calcium silicate hydrates, Cem. Concr. Res. 77 (2015) 60–68.

[127] A. Dauzeres, P. Le Bescop, P. Sardini, C. Cau Dit Coumes, Physico-chemical investigation of clayey/cement-based materials interaction in the context of geological waste disposal: experimental approach and results, Cem. Concr. Res. 40 (2010) 1327–1340.

[128] A. Dauzeres, G. Achiedo, D. Nied, E. Bernard, S. Alahrache, B. Lothenbach, Magnesium perturbation in low-pH concretes placed in clayey environment—solid characterizations and modeling, Cem. Concr. Res. 79 (2016) 137–150.

[129] J.L. García Calvo, A. Hidalgo, C. Alonso, L. Fernández Luco, Development of low-pH cementitious materials for HLRW repositories: resistance against ground waters aggression, Cem. Concr. Res. 40 (2010) 1290–1297.

[130] U.H. Jakobsen, K. de Weerdt, M.R. Geiker, Elemental zonation in marine concrete, Cem. Concr. Res. 85 (2016) 12–27.

[131] M. Vespa, B. Lothenbach, R. Dähn, T. Huthwelker, E. Wieland, Characterisation of magnesium silicate hydrate phases (M-S-H): a combined approach using synchrotron-based absorption-spectroscopy and ab initio calculations, Cem. Concr. Res. 109 (2018) 175–183.

[132] L. Fernandez, C. Alonso, A. Hidalgo, C. Andrade, The role of magnesium during the hydration of C 3 S and C-S-H formation. Scanning electron microscopy and mid-infrared studies, Adv. Cem. Res. 17 (2005) 9–21.

[133] L. Fernandez, C. Alonso, C. Andrade, A. Hidalgo, The interaction of magnesium in hydration of C3S and CSH formation using 29Si MAS-NMR, J. Mater. Sci. 43 (2008) 5772–5783.

[134] N.Y. Mostafa, E.A. Kishar, S.A. Abo-El-Enein, FTIR study and cation exchange capacity of Fe3+- and Mg2+-substituted calcium silicate hydrates, J. Alloy. Compd. 473 (2009) 538–542.

[135] G. Qian, G. Xu, H. Li, A. Li, Mg-Xonotlite and its coexisting phases, Cem. Concr. Res. 27 (1997) 315–320.

[136] T. Mitsuda, Paragenesis of 11 Å tobermorite and poorly crystalline hydrated magnesium silicate, Cem. Concr. Res. 3 (1973) 71–80.

[137] B.Z. Dilnesa, E. Wieland, B. Lothenbach, R. Dähn, K.L. Scrivener, Fe-containing phases in hydrated cements, Cem. Concr. Res. 58 (2014) 45–55.

[138] Y.M. Amran, R. Alyousef, H. Alabduljabbar, M. El-Zeadani, Clean production and properties of geopolymer concrete, A review, J. Clean. Prod. 251 (2020) 119679.

[139] V. Arslan, O. Bayat, Removal of Fe from kaolin by chemical leaching and bioleaching, Clays Clay Miner. 57 (2009) 787–794.

[140] A. Zegeye, S. Yahaya, C.I. Fialips, M.L. White, N.D. Gray, D.A.C. Manning, Refinement of industrial kaolin by microbial removal of iron-bearing impurities, Appl. Clay Sci. 86 (2013) 47–53.

[141] A. Mancini, E. Wieland, G. Geng, R. Dähn, J. Skibsted, B. Wehrli, B. Lothenbach, Fe(III) uptake by calcium silicate hydrates, Appl. Geochem. 113 (2020) 104460.

[142] N.K. Labhasetwar, O.P. Shrivastava, Y.Y. Medikov, Mössbauer study on iron-exchanged calcium silicate hydrate: Ca5−xFexSi6O18H2 · nH2O, J. Solid State Chem. 93 (1991) 82–87.

[143] Sonja Haastrup, Yu. Donghong, Yuanzheng Yue, Impact of minor iron content on crystal structure and properties of porous calcium silicates during synthesis, Mater. Chem. Phys. 205 (2018) 180–185.

[144] S.V. Churakov, P. Mandaliev, Structure of the hydrogen bonds and silica defects in the tetrahedral double chain of xonotlite, Cem. Concr. Res. 38 (2008) 300–311.

[145] M. Sakiyama, Y. Oshio, T. Mitsuda, Influence of gypsum on the hydrothermal reaction of lime-quartz system and on the strength of autoclaved calcium silicate product, J. Soc. Inorg. Mater., Jpn. 7 (2000) 685–691.

[146] R. Barbarulo, H. Peycelon, S. Leclercq, Chemical equilibria between C-S–H and ettringite, at 20 and 85 °C, Cem. Concr. Res. 37 (2007) 1176–1181.

[147] K. Baltakys, R. Siauciunas, Influence of gypsum additive on the gyrolite formation process, Cem. Concr. Res. 40 (2010) 376–383.

[148] K. Baltakys, Influence of gypsum additive on the formation of calcium silicate hydrates in mixtures with C/S = 0.83 or 1.0, Materials Science Poland Vol. 27, No. 4/1 (2009).

[149] E. Helanova, R. Drochytka, V. Cerný, Influence of gypsum additive on the formation of tobermorite in autoclaved aerated concrete, Key Eng. Mater. 714 (2016) 116–121.

[150] T. Chappex, K.L. Scrivener, H. Jennings, The effect of aluminum in solution on the dissolution of amorphous silica and its relation to cementitious systems, J. Am. Ceram. Soc. (2012) 592–597.

[151] S. Shaw, S.M. Clark, C.M.B. Henderson, Hydrothermal formation of the calcium silicate hydrates, tobermorite (Ca5Si6O16(OH)2·4H2O) and xonotlite (Ca6Si6O17(OH)2): an in situ synchrotron study, Chem. Geol. 167 (2000) 129–140.

[152] D.L. Rayment, A.J. Majumdar, The composition of the C-S-H phases in portland cement pastes, Cem. Concr. Res. 12 (1982) 753–764.

[153] A. Zingoni, Insights and innovations in structural engineering, mechanics and computation, Proceedings of the sixth international conference on structural Engineering, Mechanics and Computation, Cape Town, South Africa, 5–7 September 2016, CRC Press, 2016.

[154] W. Dai, Effect of MgO on calcination and properties of belite-barium calcium sulphoaluminate cement clinker with Na2O and K2O, Ceram. Silik. (2018) 121–130.

2.2 Mechanical strength and microstructure of ultra-high performance concrete under long-term autoclaving

1 **Mechanical strength and microstructure of ultra-high performance concrete**

2 **under long-term autoclaving**

3

4 Hongwei Tian [1], Dietmar Stephan [2], Christian Lehmann [3]

5 [1] Ph.D. Candidate, Institute of Civil Engineering, Technische Universität Berlin, 13355,

6 Berlin, Germany

7 [2] Professor, Institute of Civil Engineering, Technische Universität Berlin, 13355, Berlin,

8 Germany (corresponding author, E-mail: stephan@tu-berlin.de)

9 [3] Ph.D., Institute of Civil Engineering, Technische Universität Berlin, 13355, Berlin,

10 Germany

11

12 **Abstract:**

13 Solar thermal energy is a technology by collecting radiant energy from the sun to generate

14 heat or electricity. Thermal energy storage is required to compensate for the solar thermal

15 energy variations across time scales, and a popular strategy is storing thermal energy in hot

16 water tanks. Due to the superior strength and durability, ultra-high performance concrete

17 (UHPC) is exploited to construct such water tanks for the applications at 200 °C. Therefore,

18 the mechanical strength and microstructure of UHPC after long-term temperature-pressure

19 load (autoclaving) is studied. The compressive strength of UHPC can stay robust due to the

20 accelerated formation of hydrates, while the flexural strength is vulnerable to long-term

21 autoclaving due to the transformation of amorphous C-S-H to more ordered phases. The main

22 hydrates in autoclaved samples are poorly crystallized C-S-H, hydroxylellestadite, and

23 hydrogarnet. The porosity of autoclaved samples is not strictly related to the mechanical

24 strength, and the influence of hydrate assemblage outweighs that of porosity on mechanical

25 strength after long-term autoclaving. The partial replacement of cement by limestone powder

26 can decrease crystalline hydrates and increase poorly crystallized C-S-H, which densifies the

microstructure and enhances the mechanical strength. However, excessive poorly crystallized C-S-H aggravates the thermal mismatch between the matrix and quartz aggregates after autoclaved samples cooling to room temperature, leading to interstice in matrix-quartz interfaces and thus reduced mechanical strength. Therefore, an appropriate addition of limestone powder is required to induce the hydrate assemblage with appropriate poorly crystallized C-S-H, ensuring durable UHPC structures under autoclaving.

Keywords:

Ultra-high performance concrete; Limestone; Autoclaving; C-S-H; Compressive and flexural strength

Introduction

Energy is indispensable to our modern society, and the demand continues to rise due to economic growth and urbanization. The dominant shares of the world's primary energy supply remain the conventional energy resources, such as coal and oil, which cause damage to the ecological environment (IEA 2020). Renewable energy collected from renewable resources like wind, tides, geothermal heat, and sunlight can be naturally replenished on a human timescale. Solar energy possesses a huge potential because within two hours, enough sunlight strikes the earth to cover the energy demand of the entire planet for a whole year (IEA 2019). To compensate for the sunlight variations across time scales, solar thermal energy storage, which stocks thermal energy by heating or cooling a storage medium for later conversion to electricity and heating or cooling applications, is a popular strategy to harness the radiative energy of sunshine. A hot water tank schematically shown in Fig. 1 is a reliable and affordable strategy for thermal energy storage. However, due to corrosion, leakage, and high cost, the water tanks made of copper, stainless steel, and vitreous enamel-lined carbon steel suffer from a short life cycle and are hard to be used on a large scale. Concrete has also been exploited to construct such water tanks and possesses a relatively longer working life and commercially

54   available cost for large-scale application (Bauer et al. 2010; Heller 2000; Mangold 2007;

55   Papanicolaou and Belessiotis 2009). Storing 200 °C water is one method to increase the

56   energy storage density (the amount of energy per unit of volume or mass) of the system,

57   meaning that a concrete structure has to withstand long-term high temperature-pressure

58   loading (autoclaving). Ultra-high performance concrete (UHPC) has superior strength and

59   durability and holds the potential as the construction material of such hot water tanks.
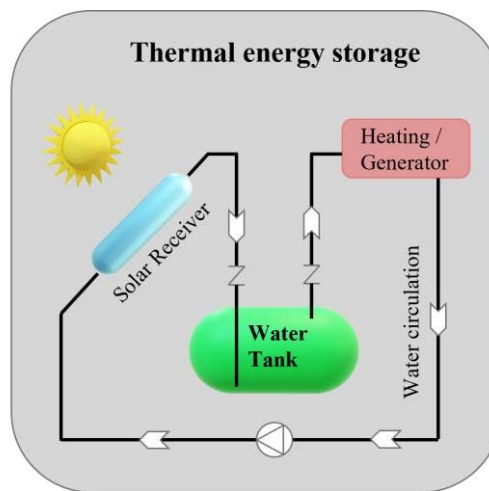

60

61   Fig. 1 Schematic illustration of an example of the solar thermal storage system (water as a

62   storage medium).

63   Supplementary cementitious materials (SCMs) are increasingly introduced in UHPC to

64   improve sustainability and decrease the production cost of UHPC (Arora et al. 2018; Camiletti

65   et al. 2012; Ghafari et al. 2016; Yazıcı et al. 2008; Yazıcı et al. 2010; Yu et al. 2015). Unlike

66   fly ash and slag, limestone is a natural material and possesses a wide geographical distribution.

67   Recently, the effective utilization of limestone powder as a replacement of cement in UHPC

68   has been well documented. For fresh concrete, Yu et al. designed UHPC based on the

69   modified Andreasen & Andersen particle packing model and found that the workability can be

70   improved by partially replacing cement with limestone (D_{50} = 10 μm) (Yu et al. 2014). In the

71   study of Arora et al., limestone powders with two median particle sizes, 1.5 and 3.0 μm, were

72   used to improve packing density. Meanwhile, the increased flowability was also observed,

73   attributed to the reduced inter-particle forces, yield stress, and plastic viscosity (Arora et al.

49

74   2018; Vikan and Justnes 2007). For hydrated concrete, limestone can influence hydration

75   kinetics and mechanism in two ways: filler effect and reaction with aluminates. Fine limestone

76   powders (e.g. below 4 μm) can accelerate clinker hydration by providing nucleation sites for

77   C-S-H, also known as seeding effect (Antoni et al. 2012; Lothenbach et al. 2008). Besides,

78   limestone reacts with aluminates, leading to the formation of carboaluminates at the expense

79   of monosulfoaluminate and promoting the reconversion of monosulfoaluminate to ettringite

80   (Antoni et al. 2012; Bonavetti et al. 2001; Lothenbach et al. 2008; Puerta-Falla et al. 2015).

81   Furthermore, these effects caused by limestone are highly related to its content and fineness

82   (Bentz 2006; Kumar et al. 2013). Appropriate incorporation of limestone in cement-based

83   materials can reduce the CO_2 footprint and improve the mechanical properties, as reported in

84   (Arora et al. 2019b; Arora et al. 2019a; Huang et al. 2017; Li et al. 2019; Proske et al. 2013;

85   Wu et al. 2018).

86   However, most of the published studies are based on normal environments, while the

87   performance of UHPC, especially the mixtures with limestone, under long-term autoclaving is

88   still unknown. Although short-term hydrothermal curing with hot water/steam (60/90 $^{\circ}$C) for 24-

89   48 h or autoclaving for several hours can improve the performance of UHPC (Chen et al. 2018;

90   Fehling et al. 2014; Werder et al. 2018; Zdeb 2017), the influence of long-term autoclaving on

91   the mechanical strength and microstructure is rarely reported. In this study, a typical UHPC

92   mixture and blended UHPC mixtures with limestone powder partially replacing cement are

93   subjected to long-term autoclaving at 200 $^{\circ}$C corresponding to the working environment for

94   thermal energy storage. The mechanical properties of UHPC after autoclaving are tested, and

95   the microstructure variation is characterized to uncover the influence of autoclaving and the

96   role of limestone in UHPC.

97   **Materials and methods**

98   **Materials**

99   Portland cement CEM I 52.5 R complying with European standard EN 197-1 is used in this

100   study. Silica fume and quartz powder are used as fillers. Quartz sand with a particle size of 0-

101   2 mm was used as fine aggregate. The sizes of limestone powder and cement are comparable

102   to eliminate the effect caused by variation of particle size distribution. The chemical

103   compositions of these materials determined by X-ray fluorescence are shown in Table 1, and

104   the particle size distributions measured by Mastersizer 2000 (Malvern Panalytical Ltd) are
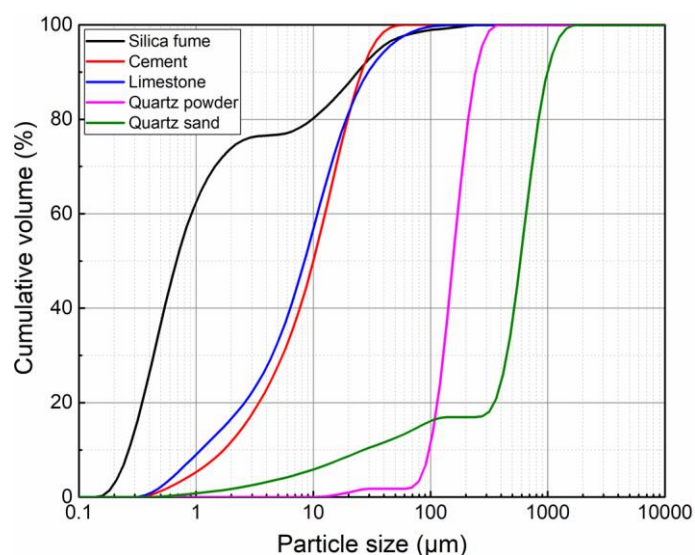
105   given in Fig. 2.

106

107   Fig. 2 Particle size distributions of the raw materials measured by laser diffraction.

108   **Mixtures and autoclaving treatment**

109   The mixtures are designed based on the modified Andreasen & Andersen particle packing

110   model (Funk and Dinger 1993), and the distribution modulus as an indicator of proportion

111   between fine and coarse particles in the mixture is assigned as 0.23 according to the

112   experience in (Hüsken and Brouwers 2008; Yu et al. 2014). The UHPC mixtures are shown in

113   Table 2, and the water/binder (w/b) ratio is set as 0.20. The starting materials are first dry-

114   mixed by a high-performance mixer (Type EL5 Eco, Maschinenfabrik Gustav Eirich GmbH &

115   Co KG) at the counter-current mode for 2 min. The water previously mixed with half amount of

116   the precalculated superplasticizer is then added, and the mixture is homogenized for 3 min in

117   counter-current mode at a speed of 300 rpm. After a pause of 1 min, the remaining

118   superplasticizer is added, and the mixing is restarted for another 3 min. The mixture

119   temperature is monitored throughout the mixing process, avoiding premature solidification

120   caused by over-high temperature. The thoroughly mixed mixtures are cast into prismatic

121 moulds with a dimension of 40·40·160 mm^3. The samples are sealed at 20 ± 2 °C for 24 h.

122 Afterwards, the hardened samples are demoulded followed by 24 h of pre-curing in water at

123 20 ± 2 °C and then subjected to the autoclaving treatment. The autoclave is heated from room

124 temperature to 200 °C, 1.55 MPa in ~1 h and kept for 10 d. After cooling to room temperature,

125 the inner parts of the samples are extracted and immersed in isopropanol for one day, followed

126 by freeze-drying. Quartz sand is eliminated in the samples prepared for microstructure

127 characterization. In contrast, another batch of samples is normally cured in water at 20 °C ± 2

128 °C for 28 d.

129 **Mechanical properties**

130 After autoclaving, the prismatic samples were used for flexural and compressive strength

131 measurements according to DIN EN 196-1 (*DIN EN 196-1:2016-11, Prüfverfahren für*

132 *Zement_- Teil_1: Bestimmung der Festigkeit; Deutsche Fassung EN_196-1:2016*). Three

133 samples of each mixture were loaded in a 3-point bending test (unnotched), and the flexural

134 strength was calculated from the breaking force. Six samples of each mixture were loaded on

135 a 40·40 mm² surface until breakage, and the average value was calculated as compressive

136 strength.

137 **X-ray diffraction**

138 The evolution of the mineralogical composition induced by autoclaving was studied by X-ray

139 diffraction (XRD) using an Empyrean PANalytical diffractometer with CuKα radiation (k =

140 1.540598 Å). HighScore Plus software equipped with ICSD database was used to identify

141 mineralogical phases. The measurements were conducted in continuous mode at 40 kV and

142 40 mA for a 2θ range from 3° to 65°. The scanning speed was 0.0172°/s with a resolution of

143 0.0131°.

144 **Thermogravimetric analysis**

145 The thermogravimetric analysis (TG) was conducted by TG 209 F3 Tarsus® (NETZSCH) under

146 a nitrogen atmosphere with a 30 mL/min flow rate. About 20 ± 1 mg of powder sample was

147   used for each mixture, and the temperature was heated from 20 °C to 1000 °C at a rate of 10

148   °C/min.

149   **Scanning electron microscopy**

150   A Zeiss Gemini SEM500 Nano VP equipped with an EDX detector was used to observe

151   hydrates and interfaces between matrix and filler. Twenty images for each mixture were taken.

152   The sample pieces were impregnated by a low-viscosity epoxy resin and polished down to 1

153   μm using successive diamond abrasives. The chemical compositions of hydrates in autoclaved

154   samples were further measured by point element analysis (Bruker EDX-System: Quantax

155   XFlash 6-60) on a fifty data point set. Besides, element mapping was also conducted to study

156   the element distribution.

157   **Mercury intrusion porosimetry**

158   Due to the chemical reactions activated by autoclaving, the matrix pore structure is inevitably

159   varied. Mercury intrusion porosimetry (MIP) was carried out on small cubic samples using

160   Porotec porosimeter (Pascal 240/440). Approx. 2 g of each sample was used in the

161   experiments under 22 °C to characterize the porosity and pore size distribution. The mercury

162   surface tension and contact angle were assigned to 0.48 N/m and 140°, respectively. The

163   intrusion pressure was up to 400 MPa with an increase/decrease speed of 5-17 MPa/min.

164   **Experimental results**

165   **Mechanical properties**

166   The influence of different curing on the compressive and flexural strength of UHPC is shown

167   in Fig. 3. The bars represent one standard deviation for the triplicate measurements. After

168   normal curing, the compressive strength of L0 is 151.7 MPa, while the replacement of cement

169   by limestone leads to a gradual decrease. Such phenomenon is also reported in other literature

170   (Li et al. 2020; Yang et al. 2020; Yu et al. 2015) and is generally attributed to the dilution effect

171   and the reduction of cementitious hydration products. Because the limestone powder used in

172   this study has a comparable size with cement, the seeding and filler effect provided by nano-

173   and micro-limestone, which benefits mechanical strength (Arora et al. 2018; Camiletti et al.

174   2012; Li et al. 2015), are not apparent. The compressive strength of L0 after the long-term

175   autoclaving is 152.7 MPa without strength degradation. It is well reported that amorphous C-

176   S-H transforms to more ordered or higher polymerized phases under long-term heat treatment,

177   leading to the so-called pore coarsening (Bahafid et al. 2017; Gallucci et al. 2013; Nelson et

178   al. 1981). Besides, the hydration products of aluminate from the clinker, e.g., ettringite and

179   AFm (Al_2O_3-Fe_2O_3-monophase), are also unstable and convert to hydrogarnet under

180   autoclaving. However, the strength degradation caused by the aforementioned detrimental

181   effect is not observed in autoclaved L0. In the petroleum and geothermal industry, a large

182   amount of silica (approx. 35-40 wt. %) is usually introduced to prevent matrix permeability

183   increase and strength retrogression during well cementing under hydrothermal conditions

184   (Nelson and Guillot 2006). As for UHPC, silica fume and quartz powder seem to play a positive

185   role in maintaining compressive strength, although their addition initially aims to compact the

186   mixture packing density. Interestingly, the compressive strength of autoclaved L2 is higher

187   than that of autoclaved L0, while autoclaved L1 and L3 present a slightly lower compressive

188   strength. Nonetheless, the compressive strength of all autoclaved samples exceeds that of

189   normal cured samples, indicating that UHPC can stay robust under long-term autoclaving.

190   Appropriate addition of limestone may induce some beneficial effect to compressive strength,

191   which is further discussed in the following microstructure analysis.

192   The flexural strength of L0 after normal curing is around 21.7 MPa, and the influence of

193   limestone on flexural strength is similar to that on compressive strength. Once subjected to

194   autoclaving, the flexural strength of L0 is significantly decreased. This phenomenon is also

195   observed in other autoclaved products, attributed to the deterioration of matrix bond property

196   (Chen et al. 2018; Yazıcı et al. 2009; Yazıcı et al. 2013). However, for blended samples, the

197   flexural strength firstly increases with the addition of limestone and then decreases, implying

198   that the appropriate addition of limestone can mitigate the detrimental effect caused by long-
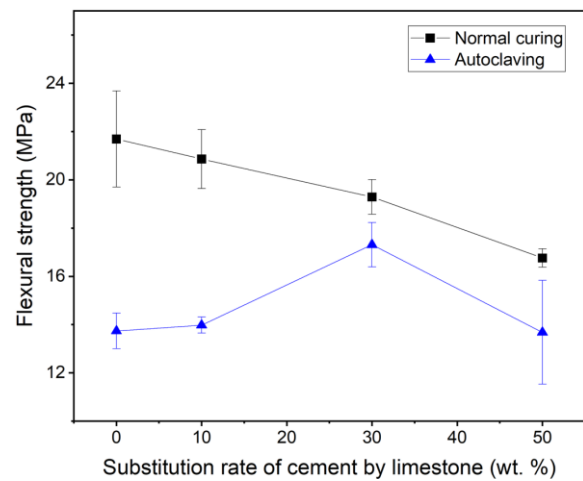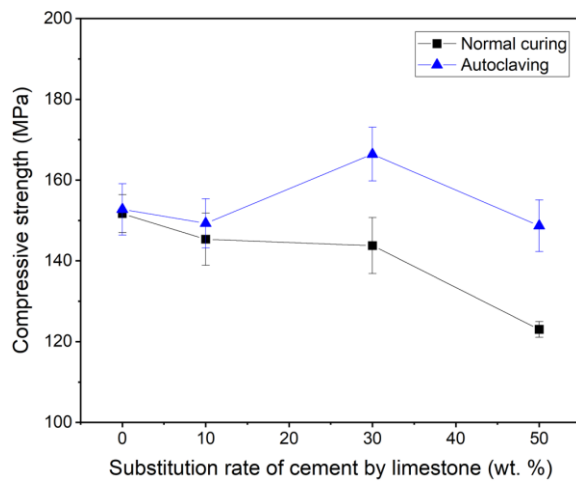
199   term autoclaving.

(a)

(b)

Fig. 3. Mechanical properties of UHPC after different curing treatments: (a) compressive strength and (b) flexural strength.

XRD analysis

The mineralogical compositions of the samples after different curing are characterized by XRD, as shown in Fig. 4. For normal cured L0, the typical hydration products of ettringite, portlandite, and amorphous C-S-H are identified. The peak intensity of portlandite is quite small due to the pozzolanic reaction with silica fume. A significant amount of clinker phases C_2S and C_3S remain due to the low w/b ratio of UHPC. With limestone replacing cement, the peak intensity of limestone gradually increases, while the peak intensity of C_2S and C_3S decreases accordingly. However, there is no apparent signal of C_2S and C_3S identified in autoclaved samples, indicating a higher degree of cement hydration under autoclaving. Portlandite also disappears owing to the accelerated pozzolanic reaction by autoclaving. Hydrogarnet is identified in autoclaved L0, which converts from ettringite and AFm phases (Meller et al. 2009a; Šatava Vladimír and Vepek 1975). Hydroxylellestadite $Ca_5(SiO_4,SO_4)_3(OH)$ is formed in autoclaved L0. In addition to hydrogarnet, the decomposition of ettringite and AFm generates sulfate ions SO_4^{2-} (Meller et al. 2009a; Šatava Vladimír and Vepek 1975). It is reported that SO_4^{2-} can be co-sorbed on the surface and interlayer of poorly crystallized C-S-H together with

55

220   Ca^{2+} (Barbarulo et al. 2007). Therefore, the other part of released SO$_4^{2-}$ probably precipitates

221   in hydroxylellestadite under autoclaving as no other sulfate-containing phase is identified. The

222   type of newly formed hydrates depends on the temperature and composition of raw materials

223   (Hong and Glasser 2004; Meller et al. 2009b; Nelson and Guillot 2006). Assuming that the

224   clinkers and active silica fume entirely participate in hydrothermal reactions, the matrix Ca/Si

225   ratio is thus calculated as ~1.5, which is far less than the Ca/Si ratio of hydroxylellestadite.

226   Lehmann pointed out that under autoclaving, hydroxylellestadite can form in the area occupied

227   by portlandite, i.e., calcium-rich area (Lehmann 2013), which probably explains the formation

228   of hydroxylellestadite in the matrix with a low Ca/Si ratio. With limestone addition, hydrogarnet

229   and hydroxylellestadite gradually decrease due to the decrease of cement that exclusively

230   supplies Al and S.

231

232   (a)   (b)
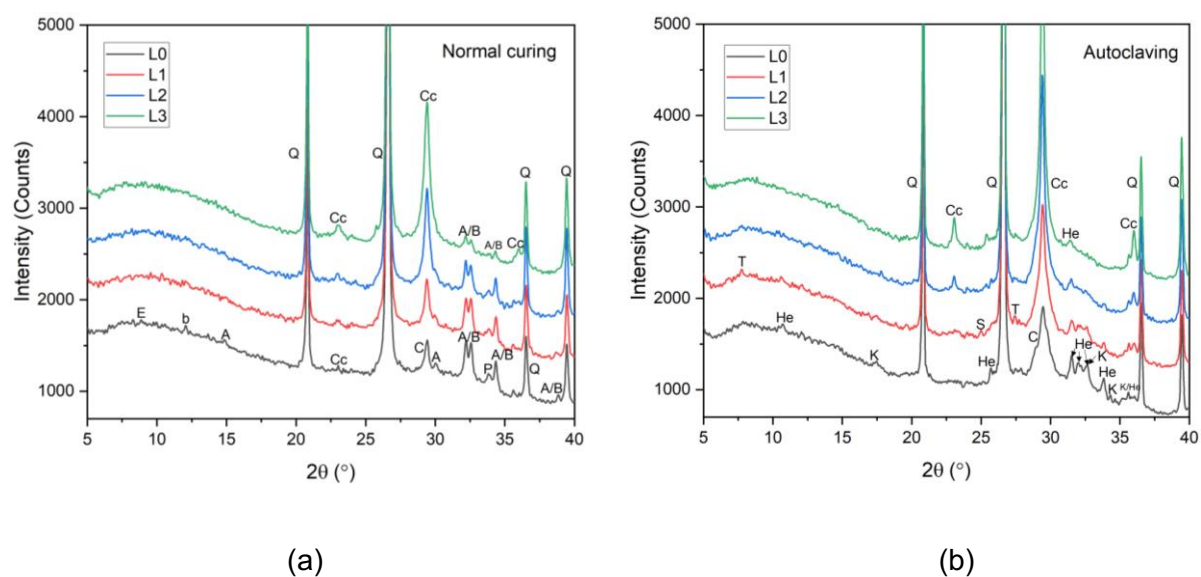
233   Fig. 4 XRD diagrams of the samples after different curing: (a) normal curing and (b)

234   autoclaving (Cc: calcite, Q: quartz, A: alite, B: belite, b: calcium aluminoferrite, E: ettringite,

235   P: portlandite, T: tobermorite, S: scawtite, He: hydroxylellestadite, K: hydrogarnet).

236   In addition to the crystalline hydrates hydrogarnet and hydroxylellestadite, a diffused peak at

237   2θ ~29.4° is observed in autoclaved L0, indicating the existence of poorly crystallized C-S-H.

238   However, many studies have reported that amorphous C-S-H gel formed at normal

239   environment converts to crystalline phases at hydrothermal conditions (Hong and Glasser

240   2004; Meller et al. 2009b; Taylor 1964). The persistence of such poorly crystallized C-S-H

241   under autoclaving is also observed in (Krakowiak et al. 2018; Matsui et al. 2011). It is reported

242   that the high solid volume fraction in the matrix can restrict the C-S-H transformation to the

243   crystalline phase as the limited space hinders the crystallization. This suppressing effect

244   results in the hydrate with small crystallite and poorly ordered structure expressed by the XRD

245   peak broadening (Young 2002). Therefore, the poorly crystallized C-S-H is maintained in the

246   autoclaved UHPC owing to the low w/b ratio and densified microstructure, providing limited

247   space for crystallization. Besides, the structure of the C-S-H precursor should also affect the

248   C-S-H transformation as the crystalline phase is converted from C-S-H precursor (initially

249   formed amorphous C-S-H) by recrystallization (Assarsson and Rydberg 1956; Mitsuda and

250   Taylor 1975). This effect is further studied by SEM-EDS in section 3.4.

251   As for the blended samples, the peak of calcite becomes stronger with limestone addition.

252   However, due to the peak overlap with limestone at 2θ ~29.4°, it is unreliable to analyze the

253   evolution of crystal size and crystallinity of the poorly crystallized C-S-H with limestone addition

254   based on the peak shape.

255   **TG analysis**

256   TG and DTG results of the samples after different curing treatments are shown in Fig. 5. For

257   normal cured L0, four main peaks of mass loss are confirmed by the differential curve. The

258   first peak up to ~230 °C is assigned to the water loss in ettringite and amorphous C-S-H gel

259   (Guo et al. 2017; Myers et al. 2015). The peak of portlandite dehydroxylation is identified at

260   ~400 °C, and the following peak at ~635 °C is related to the carbonate decomposition. The

261   last peak at ~835 °C should correspond to the dehydroxylation and recrystallization of C-S-H

262   into wollastonite ($Ca_3Si_3O_9$). Besides, the broad and shallow peak from around 250 to 370 °C

263   originates from the dehydroxylation of aluminium hydroxide from ettringite columns and the

264   loss of layer water from AFm (Scrivener et al. 2016).

265   For blended samples, the addition of limestone gradually decreases the water loss in the first

266   peak, indicating the decrease of the hydration products C-S-H and ettringite, which is

267   consistent with the decrease of mechanical strength. Correspondingly, the dehydroxylation

268   peak of portlandite also gradually decreases and disappears in L3. The decomposition peak

269   of carbonate centred at ~690 °C becomes stronger with increased limestone content. A

270   shoulder peak at around 570 °C is observed in the blended sample may be due to the presence

271   of amorphous calcium carbonate, which decarbonates at lower temperatures than crystallized

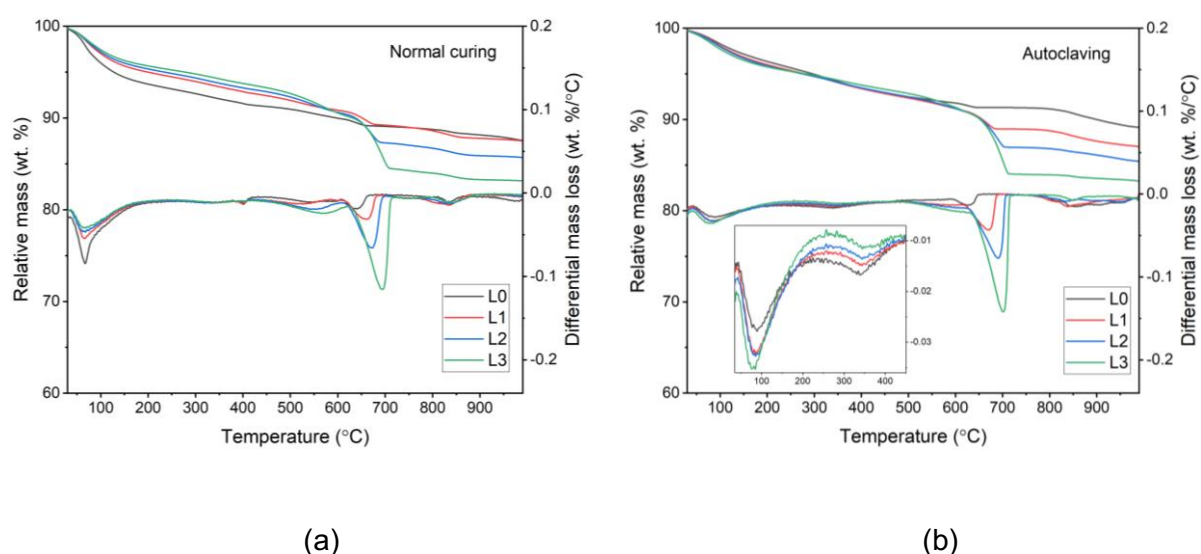272   calcite (Goto et al. 1995; Lothenbach et al. 2008; Sevelsted and Skibsted 2015).

273

274   (a)   (b)

275   Fig. 5 TG and DTG diagrams of the samples after different curing treatments: (a) normal

276   curing and (b) autoclaving.

277   For autoclaved L0, the first peak up to around 220 °C is significantly decreased. This is

278   because ettringite decomposes to hydrogarnet and amorphous C-S-H transforms to more

279   ordered phases, losing the excessive gel water under autoclaving. Interestingly, the mass loss

280   of the first peak is gradually increased by limestone addition, which is opposite to the influence

281   of limestone on the normal cured samples. The variation of mass loss in this temperature range

282   probably relates to the change of poorly crystallized C-S-H caused by limestone addition, which

283   is detailly discussed in section 3.4. The dehydroxylation peak of portlandite disappears, and a

284   wide and shallow peak from around 220 to 450 °C appears instead, which originates from the

285   decomposition of hydrogarnet (Rivas-Mercury et al. 2008), scawtite, and hydroxylellestadite

286   (Marincea et al. 2001). It can be seen that this peak gradually decreases with limestone

287   addition, indicating the decrease of hydrogarnet, scawtite, and hydroxylellestadite, which is

288   consistent with the XRD result. The decomposition peak of carbonate at ~690 °C increases

289   with the limestone addition, and the calcium carbonate contents in L0, L1, L2, and L3 are

290   roughly calculated as 0.014, 0.081, 0.140, and 0.221 (g/g solid), respectively. However,

291   limestone contents in raw materials of L0, L1, L2, and L3 are roughly 0.015, 0.059, 0.147,

292   0.235 (g/g solid), respectively, indicating that only a small amount of limestone involves in the

293   hydrates formation. Due to the low solubility product, the presence of CO_3^{2-} in liquid, which can

294   only be reduced by insertion into C-S-H, restricts the further dissolution of limestone. The high

295   amount of carbonate in autoclaved L1 is probably because of the formation of scawtite

296    $Ca_7Si_6O_{18}(CO_3) \cdot 2H_2O$, which decomposes to xonotlite $Ca_6Si_6O_{17}(OH)_2$ and calcite at around

297   400 °C (Marincea et al. 2001).

298   **SEM analysis**

299   SEM analysis is carried out to study the microstructure of autoclaved samples. As shown in

300   Fig. 6, autoclaved L0 shows the quartz particles with a blurred surface, indicating the

301   participation in hydrothermal reactions. It is reported that silica reactivity is positively related to

302   its available surface area and crystallinity (Eilers and Nelson 1979; Krakowiak et al. 2018;

303   Matsui et al. 2011). The presence of active silica suppresses the reaction of inactive silica

304   (Krakowiak et al. 2018). In this study, the reacted surface of large quartz particles implies that

305   silica fume may be entirely consumed by pozzolanic reaction under autoclaving. In this point,

306   assumed the entire reaction of cement and silica fume, the matrix Si/Ca ratio is calculated as

307   ~0.67. This value is lower than the tested Si/Ca ratio (Fig. 9), confirming the total consumption

308   of silica fume and partial reaction of quartz powder. The interface between quartz particles and

309   the matrix is densified, while several cracks are observed which do not extend along the

310   contour of quartz particles (Fig. 6). This phenomenon suggests that the interface between

311   quartz particles and matrix is not the weak point, but the solid volume shrinkage caused by

312   amorphous C-S-H converting into more ordered phases may lead to cracks, which contributes

313   to the low flexural strength after autoclaving. With a closer look, the areas marked as weak

314   areas seem porous and loose. These areas are probably caused by the decomposition of

315 aluminous product and the transformation of amorphous C-S-H into more ordered phases,

316 resulting in a decrease of solid volume. Furthermore, an interstice can be observed in the

317 enlarged picture of the weak area.

318 An absence of silicate within the clinker is observed in Fig. 6, which is consistent with the XRD

319 result. Due to the transformation of amorphous C-S-H into more ordered phases under

320 autoclaving, more free water is released, and the hydration of the clinker can thus achieve a

321 higher degree. In contrast, partially hydrated aluminoferrite particles (marked as C_4AF in Fig.

322 6) are observed. Aluminoferrite generally hydrates fast under early hydration, and calcium

323 sulphates are usually added to suppress its hydration, preventing premature stiffening by the

324 adsorption of sulfate ion on active dissolution sites and forming sulfate-AFm around anhydrous

325 particles (Ectors et al. 2013; Morin et al. 2017). However, sulfate-AFm is not observed in this

326 study due to its instability under autoclaving, but a reaction rim (or called hydrate layer)

327 encases the aluminoferrite particle, as shown in Fig. 6.

328

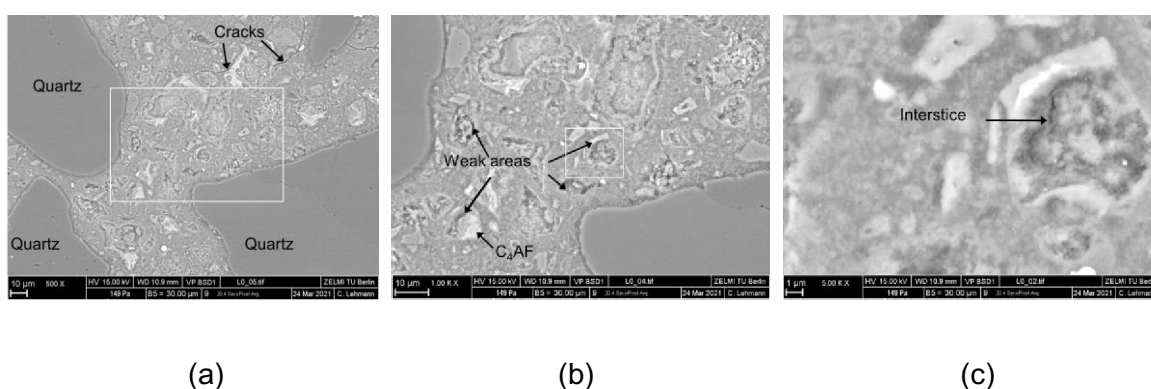329   (a)   (b)   (c)

330 Fig. 6 SEM images of autoclaved L0. (b) is the enlargement of the rectangle-marked area in

331   (a), and (c) is the enlargement of the rectangle-marked area in (b).

332 A typical example of the aluminoferrite is further observed, as shown in Fig. 7, and the element

333 point analysis by EDX is shown in Table 3. Considering the possible product containing Ca, Si,

334 Al, Fe, and S in Portland cement under autoclaving, Al intermixed siliceous hydrogarnet

335 $(Ca_3(Al_xFe_{1-x})_2(SiO_4)_y(OH)_{4(3-y)}; 0<x<1, 0<y<3)$ is reported (Dilnesa et al. 2014). However, it

336 can be seen that the element ratio of Ca/(Al + Fe) in the hydrate layer is much higher than that

337 in the hydrogarnet. It is reported that in addition to Al, which is well known to incorporate into

60

338   C-S-H, Fe (Labhasetwar et al. 1991; Qian et al. 2002; Sonja Haastrup et al. 2018) and S

339   (Baltakys 2009; Baltakys and Siauciunas 2010; Mostafa et al. 2009) can also insert into C-S-

340   H under autoclaving (175 and 200 °C). Because the Si/Ca ratio of the hydrate layer is slightly

341   lower than that of the matrix (point 5 and 6), it is speculated that the dense hydrate layer is

342   built by C-S-H inserted with Al, Fe, and S. The retardation of the ferrite phase after heat curing

343   is also reported in (Yang and Sharp 2001), and a higher temperature exerts a stronger

344   retardation effect (20-100 °C). The hydrate formed in the cavity (point 4) is rich in S and

345   deficient in Al and thus speculated as hydroxylellestadite whose stoichiometric ratio of Ca/(Si

346   + S) is roughly consistent with the data shown in Table 3. The S in hydroxylellestadite

347   originates from the decomposition of ettringite and AFm, which preferentially form around

348   aluminous clinkers. It seems that in the cavity, hydroxylellestadite obtains enough space for

349   crystallization as it is identified in XRD by high crystallinity. However, due to the high density

350   (~3.1 g/cm^3), the hydroxylellestadite formation around the aluminoferrite phase leads to the

351   unfilled cavity, which is detrimental to mechanical strength.
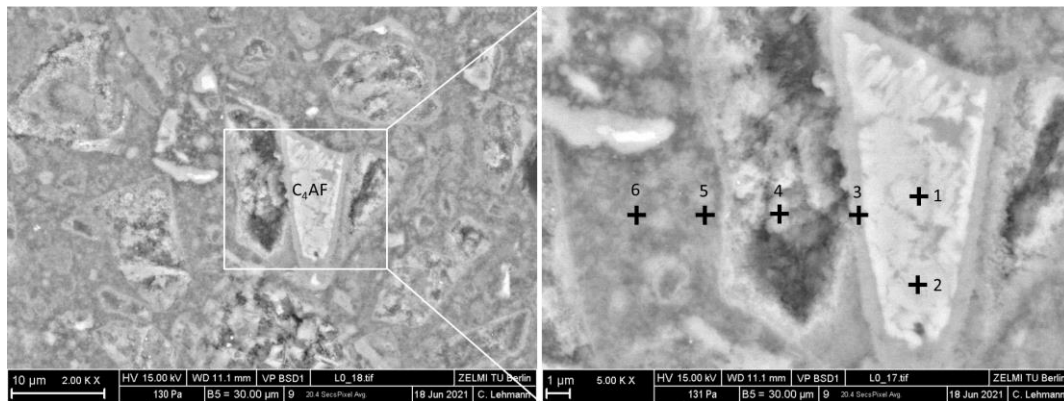
352

353   Fig. 7 A typical sample of partially hydrated aluminoferrite phase encased by hydrate layer

354   (element point analysis on the cross mark is shown in Table 3).

355   For the blended and autoclaved sample L2 (Fig. 8), limestone particles are evenly distributed

356   in the matrix. The etched surface of limestone indicates that it partially participates in the

357   hydrothermal reaction, while the densified limestone-matrix interface is observed. The weak

358   areas accompanied by aluminous clinker phases discussed in autoclaved L0 are decreased

359   due to the lower cement content in L2. The chemical composition of hydrates is analyzed by

360   EDX point analysis, as shown in Fig. 9. Because the interaction volume of the electron spot is

361   around 1 µm^3, the collected signal often reflects a mix of hydrates. Thus, a reliable way to

362   define the composition of the hydrate is by plotting Al/Ca vs Si/Ca ratio (Durdziński et al. 2017;

363   Famy et al. 2003). There is no apparent difference in Si/Ca ratio in autoclaved L0 and L1. The

364   replacement of cement by limestone increases the ratio of silica fume to cement, while partially

365   dissolved limestone can provide some Ca, leading to the comparable Si/Ca ratio in autoclaved

366   L0 and L1. However, due to the low solubility, a large amount of limestone in autoclaved L2

367   cannot provide Ca as effectively as cement does. Therefore, autoclaved L2 presents a slightly

368   higher Si/Ca ratio, leading to more C-S-H with a high Si/Ca ratio. The C-S-H precursor with a

369   high Si/Ca ratio tends to possess long and cross-linked chains of silica tetrahedra and is

370   relatively hard to transform to crystalline phase as more bonds need to be reorganized

371   compared with the C-S-H precursor with a low Si/Ca ratio (Chen et al. 2004; Nonat 2004;

372   Richardson 2004). Therefore, such C-S-H with high Si/Ca ratio can persist under autoclaving,

373   which is consistent with the result in Fig. 5(b) that autoclaved L2 shows a more significant

374   water loss between 30-220 °C than autoclaved L0.

375   For autoclaved L3 (Fig. 10), the unreacted limestone particles massively distribute in the matrix.

376   Element analysis shown in Fig. 9 indicates that the Si/Ca ratio of autoclaved L3 is further

377   increased compared with autoclaved L2 due to the significant increase of the ratio of silica

378   fume to cement. The C-S-H with a higher Si/Ca ratio and lower convertibility to crystalline

379   phase forms in autoclaved L3, contributing a more significant water loss in 30-220 °C in TG-

380   DTG analysis (Fig. 5(b)). According to Si and Ca mapping, there is no apparent color difference

381   between the matrix and interface around limestone. EDS point analysis was conducted on the

382   areas around limestone as marked by the cross (Fig. 10). The average Si/Ca, and C/Ca ratios

383   are ~1.2 and ~0.9, respectively. The high C/Ca ratio indicates that the CO_3^{2-} dissolved by

384   limestone adsorbs onto the poorly crystallized C-S-H (Kumar et al. 2017; Oey et al. 2013)

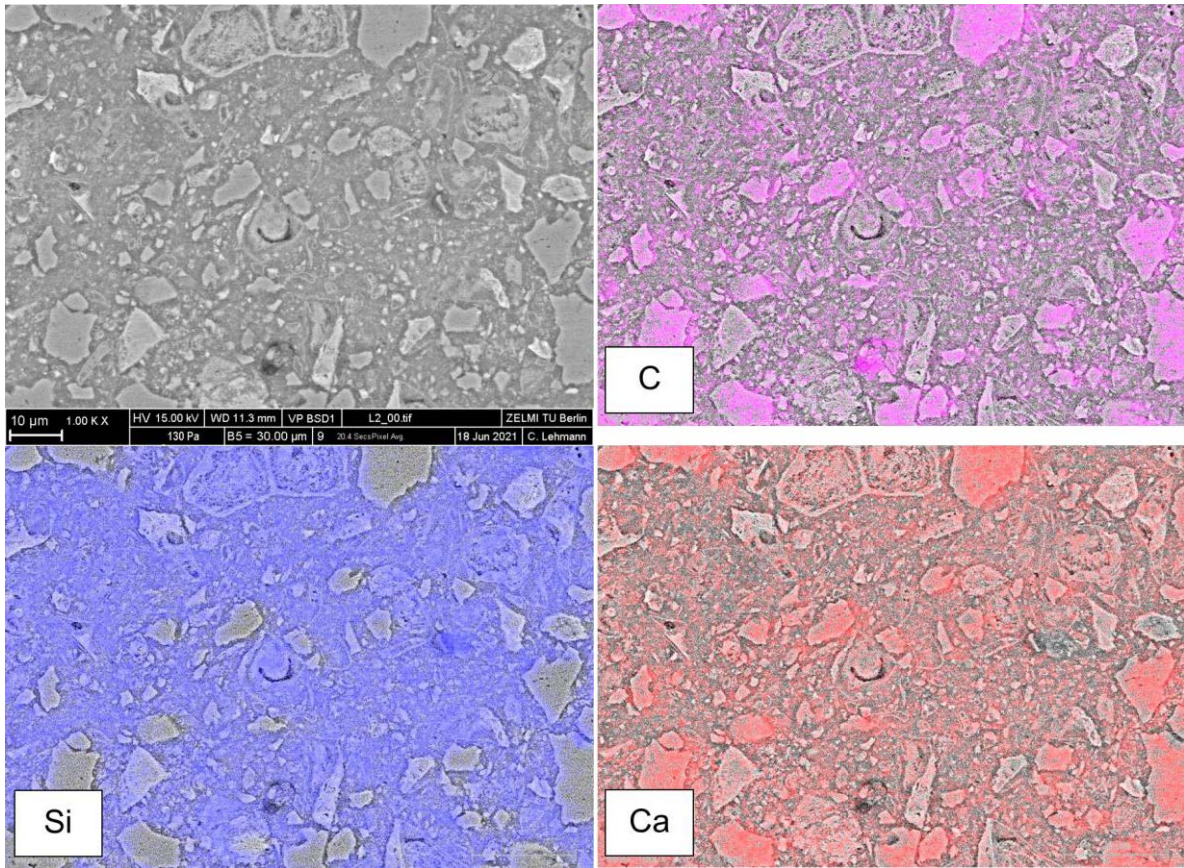385   and/or the amorphous calcium carbonate intermixes with C-S-H.

386

387   Fig. 8 SEM-EDS element mapping of autoclaved L2.
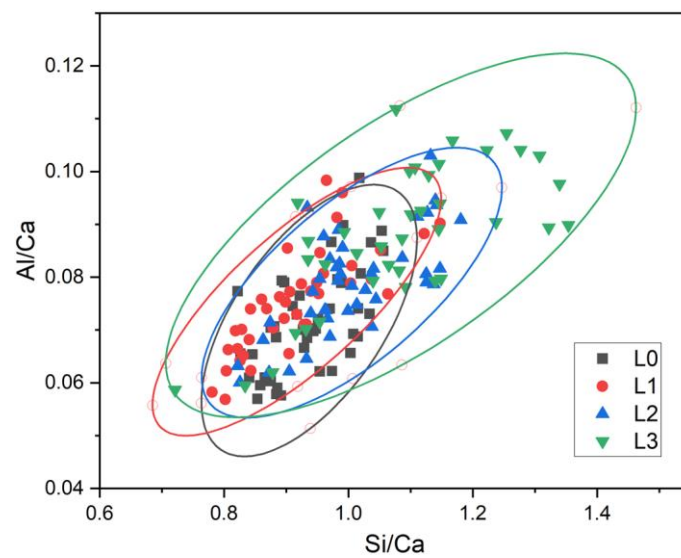
388

389

390   Fig. 9 SEM-EDS element point analysis on the hydrates in autoclaved samples (confidence

391   ellipse drawn by 95% confidence level).

392 Interestingly, hydroxylellestadite is again observed (Fig. 10), but it presents a leafy shape and

393 is not around the aluminous clinker as discussed in autoclaved L0. The hydroxylellestadite with

394 a leafy shape is also reported in (Lehmann 2013), which hydroxylellestadite pseudomorphically

395 forms in the track of portlandite under autoclaving. Therefore, hydroxylellestadite can form in

396 two ways under autoclaving: formation in the track of portlandite and around the aluminous

397 clinker. The platelike portlandite provides a Ca-rich environment for hydroxylellestadite, and

398 hydroxylellestadite fills the area initially occupied by portlandite. Similarly, the area around the

399 aluminous clinker is rich in Ca and S, favoring the formation of hydroxylellestadite, but such

400 hydroxylellestadite leads to the unfilled cavity and loose structure, which may be detrimental

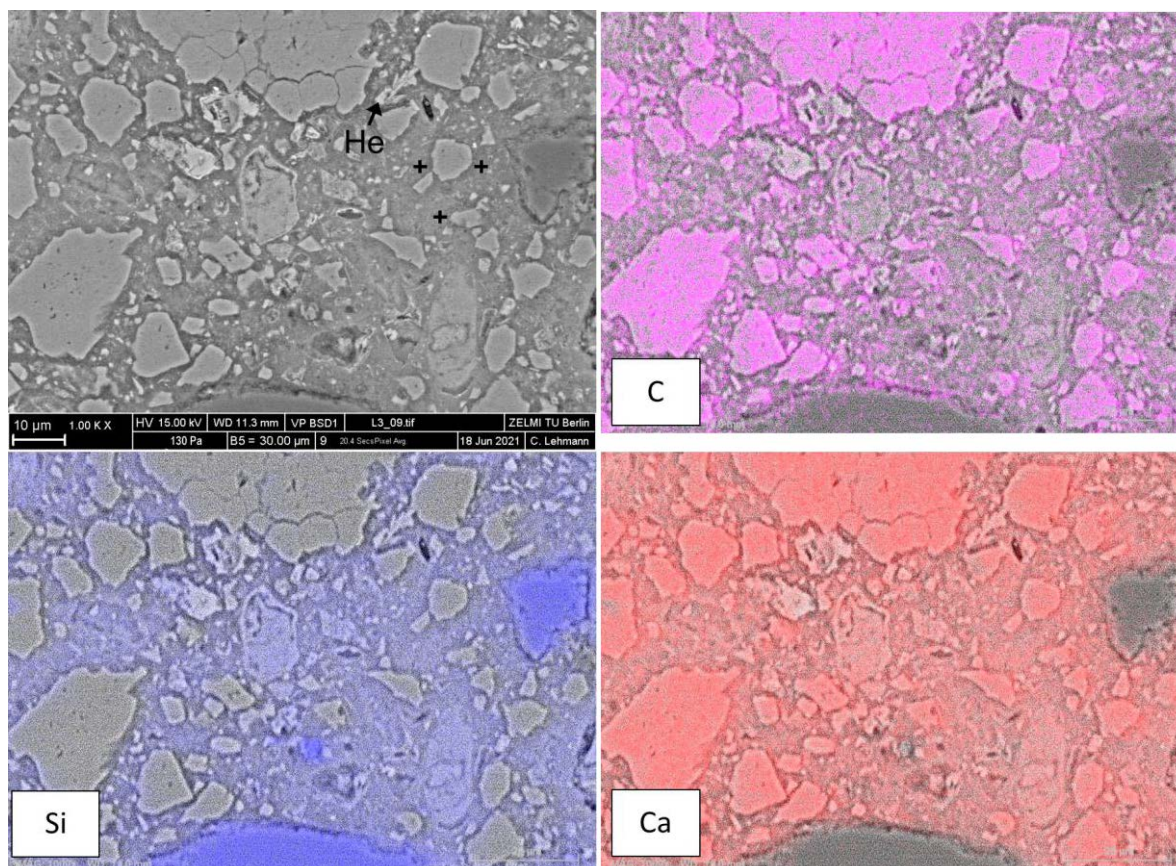401 to mechanical strength.

403 Fig. 10 SEM-EDS element mapping of autoclaved L3 (He: Hydroxylellestadite; Point analysis

404 was conducted on the cross marked area).

Pore structure analysis

The influence of autoclaving on the pore structure of pure and blended UHPC is shown in Fig. 11. Compared with normal cured L0, autoclaved L0 presents a higher porosity and finer texture with a high proportion of gel pore. As confirmed by XRD and SEM, cement hydration achieves a higher degree under autoclaving, but the high degree of hydration does not result in low porosity. Long-term autoclaving substantially changes the type of hydrates. Rather than ettringite, AFm, and amorphous C-S-H, high-density products of hydrogarnet, hydroxylellestadite, and poorly crystallized C-S-H form under autoclaving, resulting in a decrease of solid volume fraction and thus an increase of porosity. Nonetheless, the accelerated formation of hydrates by autoclaving fills up the capillary pore and generates gel pore (10 nm as the dividing point between gel and capillary pores) in autoclaved L0.

For blended samples, autoclaved L1 and L2 present comparable porosity that is lower than autoclaved L0. Compared with autoclaved L0, the addition of limestone decreases hydrogarnet, hydroxylellestadite, and partially hydrated ferrite, which is beneficial to densify microstructure. Autoclaved L2 has less capillary and more gel porosity than autoclaved L1 (Fig. 11(b)). As discussed in section 3.4, the replacement of a large amount of cement by limestone greatly increases the ratio of silica fume to cement in autoclaved L2, leading to the C-S-H with a high Si/Ca ratio. The persistence of such C-S-H with low density ensures a high solid volume, generating more gel porosity and less capillary porosity. Autoclaved L3 shows the lowest porosity, benefiting from the further decrease of cement and more poorly crystallized C-S-H with high Si/Ca.
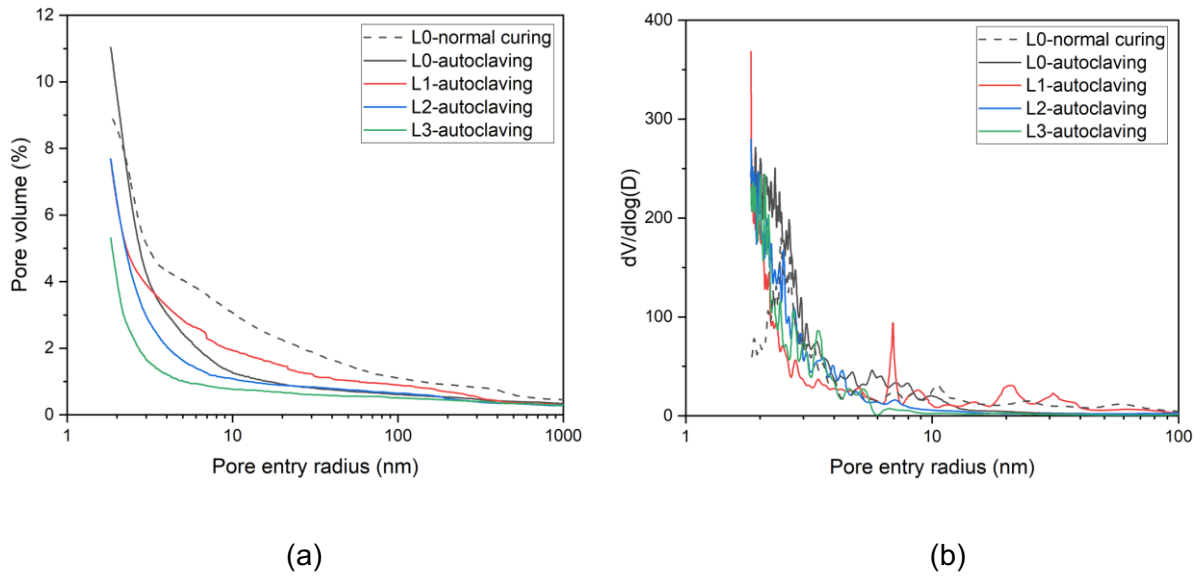
426

427   (a)   (b)

428   Fig. 11 The influence of autoclaving on the pore structure of pure and blended samples: (a)

429   cumulative intrusion curves and (b) pore size distributions.

430   **Discussion**

431   The influence of limestone on the mechanical strength and microstructure of UHPC under

432   autoclaving mainly originates from the variation in the ratio of silica to cement. The

433   compressive strength of autoclaved samples can stay robust due to the accelerated formation

434   of hydrates, while the flexural strength is more vulnerable to autoclaving. It is reported that the

435   bond property of amorphous C-S-H gel is mainly contributed by hydrogen bonds and

436   electrostatic interactions of calcium with counterions (Bonnaud et al. 2013). The transformation

437   of amorphous C-S-H to poorly crystallized C-S-H with higher crystallinity and lower water

438   content under autoclaving deteriorates the bond strength of the matrix (Bonnaud et al. 2013;
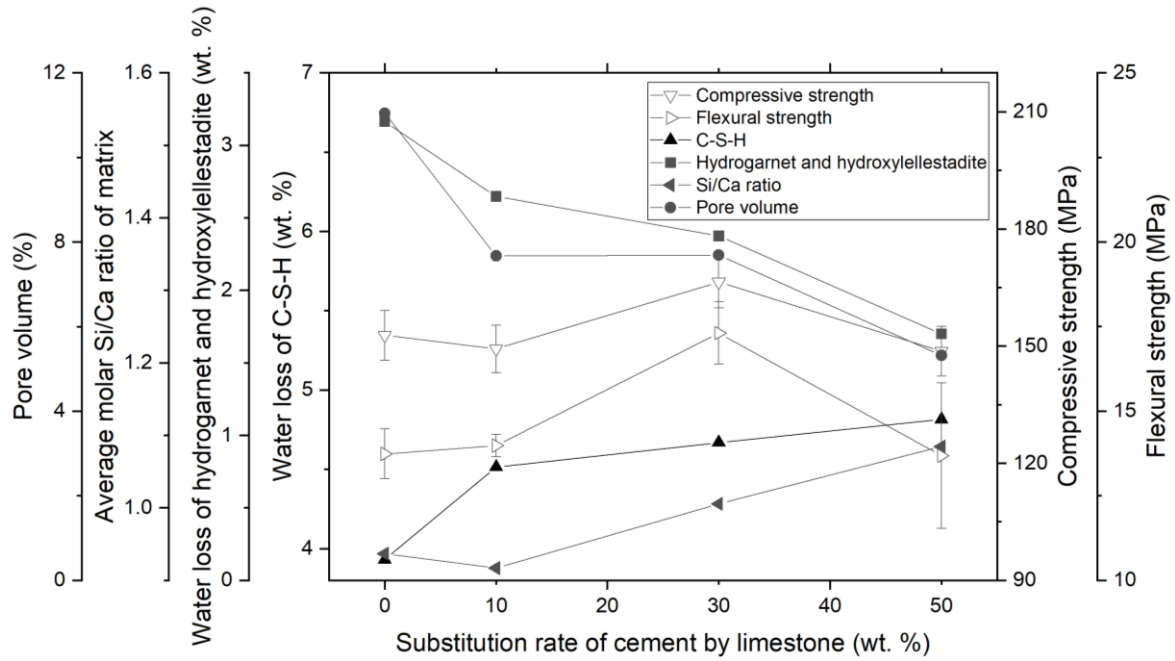
439   Ouyang et al. 2017) and thus the flexural strength.

440

441   Fig. 12 The influence of partial substitution of cement by limestone on hydrates assemblage

442   and mechanical strength.

443   The strength of autoclaved samples is not strictly related to their porosity: autoclaved L2 has

444   the highest compressive and flexural strength, but autoclaved L3 has the lowest porosity, and

445   autoclaved L1 has a comparable porosity with autoclaved L2. It seems that the effect of hydrate

446   assemblage outweighs that of porosity concerning mechanical strength under autoclaving. The

447   variation of hydrate assemblage (precisely the proportion of crystalline and poorly crystallized

448   hydrate) is caused by the different compositions of the matrix. The influence of partial

449   substitution of cement by limestone is comprehensively plotted in Fig. 12. As ettringite and

450   AFm phases are not present in autoclaved samples, the first peak of water loss in Fig. 5(b) is

451   predominantly contributed by the dehydration of poorly crystallized C-S-H, which can be

452   regarded as an indicator of the content of C-S-H. Similarly, the water loss at around 240-450

453   °C is considered as an indicator of the total content of hydrogarnet and hydroxylellestadite.

454   The average molar Si/Ca ratio is calculated from the SEM-EDX results. As shown in Fig. 12,

455   the crystalline products of hydrogarnet and hydroxylellestadite gradually decrease with

456   limestone, accompanied by the decrease of porous and loose areas, as discussed in the

457   section on SEM analysis. Meanwhile, the Si/Ca ratio of C-S-H increases with limestone due to

458 the increased ratio of silica to cement. The convertibility of C-S-H to more ordered phases

459 under autoclaving is related to its Si/Ca ratio, which the C-S-H precursor with Si/Ca > 1 is

460 relatively hard to transform to crystalline phase compared with the C-S-H precursor with Si/Ca

461 < 1 (Chen et al. 2004; Nonat 2004; Richardson 2004). Therefore, autoclaved L3 has more

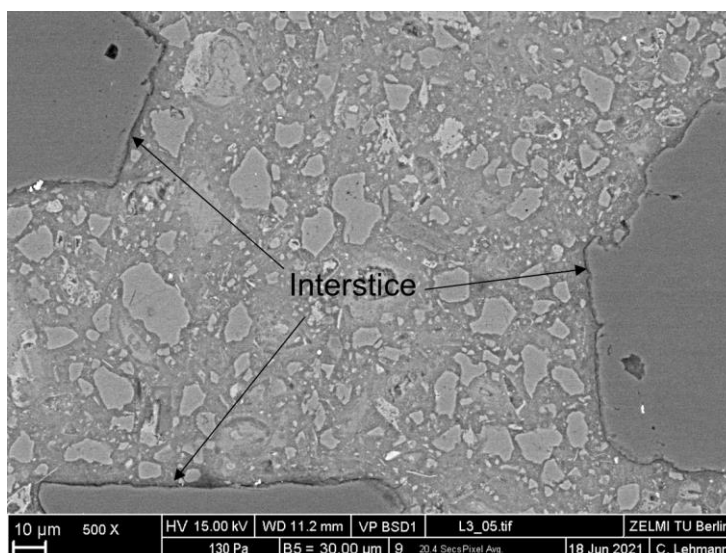462 poorly crystallized C-S-H with low density and thus low porosity of the matrix.

463

464   Fig. 13 SEM images on the interstice along the contour of quartz powders in autoclaved L3.

465 However, these beneficial effects do not lead to a better mechanical strength in autoclaved L3,

466 while autoclaved L2 presents the highest mechanical strength. Therefore, the interface

467 between matrix and quartz powder in autoclaved L3 is further observed, as shown in Fig. 13.

468 The interstice can be observed along the contour of quartz powder, which is a typical

469 phenomenon of thermal mismatch caused by the shrinkage of the matrix during sample cooling

470 after autoclaving. The thermal mismatch is a ticklish problem for the concrete encountering

471 high temperature, which may lead to preferential cracking at matrix-aggregate interfaces and

472 thus thermal damage (El Bitouri et al. 2017; Hettema 1996). It is reported that the coefficient

473 of thermal expansion of C-S-H increases with water content (Cagnon et al. 2016). Autoclaved

474 L3 has more poorly crystallized C-S-H with high Si/Ca ratio and water content (Fig. 5), resulting

475 in large deformation, internal strain, and thus interstice around quartz powder after the sample

476 cooling to room temperature. Therefore, autoclaved L3 presents low mechanical strength,

477   although it has the lowest porosity. It is concluded that in a system with low Si/Ca ratio, the

478   increase of the ratio of silica to cement leads to robust mechanical strength, benefiting from

479   the increase of poorly crystallized hydrate and decrease of crystalline hydrate. However, when

480   the content of poorly crystallized hydrate exceeds a critical value, the detrimental thermal

481   mismatch predominately controls the mechanical strength (i.e., leading to low mechanical

482   strength).

483   **Conclusion**

484   The influence of limestone on mechanical strength and microstructure of UHPC under

485   autoclaving was studied. Rather than amorphous C-S-H, portlandite, and ettringite, poorly

486   crystallized C-S-H (semi-crystalline C-S-H), hydroxylellestadite, and hydrogarnet form in the

487   autoclaved samples. The crystalline hydrates of hydroxylellestadite and hydrogarnet decrease

488   with the addition of limestone due to the decreased cement that exclusively supplies Al and S.

489   A small addition of limestone leads to a roughly unchanged Si/Ca ratio in C-S-H due to the

490   dissolution of limestone. Further addition of limestone greatly increases the ratio of silica to

491   cement, leading to the formation of poorly crystallized C-S-H with a high Si/Ca ratio, which can

492   persist under autoclaving. The influence of limestone mainly originates from the variation in

493   the ratio of silica to cement. Limestone powder is a practicable SCM to adjust the compositions

494   of the matrix without introducing interfering ions concerning C-S-H.

495   The compressive strength stays robust due to the accelerated formation of hydrates by

496   autoclaving, while the flexural strength is vulnerable to autoclaving as the transformation of

497   amorphous C-S-H into more ordered phases deteriorates the bond property. The mechanical

498   strength of autoclaved samples is not strictly related to their porosity, and the effect of hydrate

499   assemblage outweighs that of porosity concerning mechanical strength under autoclaving. The

500   decrease of crystalline hydrates and increase of poorly crystallized C-S-H densifies

501   microstructure and decreases porosities. However, poorly crystallized C-S-H aggravates the

502   thermal mismatch when the autoclaved samples are cooled to room temperature, leading to

503   interstice in matrix-quartz powder interfaces and thus low mechanical strength. Appropriate

504 addition of limestone can achieve the applicable hydrate assemblage, ensuring superior

505 mechanical strength and durable properties of UHPC under autoclaving, and the sustainability

506 is also improved.

507 **Data Availability Statement**

508 Some or all data, models, or code that support the findings of this study are available from the

509 corresponding author upon reasonable request, including the data of mechanical test and

510 microstructure characterisation.

514 **References**

515 Antoni, M., J. Rossen, F. Martirena, and K. Scrivener. 2012. "Cement substitution by a

516   combination of metakaolin and limestone." *Cement and Concrete Research*, 42(12): 1579–

517   1589. https://doi.org/10.1016/j.cemconres.2012.09.006.

518 Arora, A., M. Aguayo, H. Hansen, C. Castro, E. Federspiel, B. Mobasher, and N. Neithalath.

519   2018. "Microstructural packing- and rheology-based binder selection and characterization

520   for Ultra-high Performance Concrete (UHPC)." *Cement and Concrete Research*, 103: 179–

521   190. https://doi.org/10.1016/j.cemconres.2017.10.013.

522 Arora, A., A. Almujaddidi, F. Kianmofrad, B. Mobasher, and N. Neithalath. 2019a. "Material

523   design of economical ultra-high performance concrete (UHPC) and evaluation of their

524   properties." *Cement   and   Concrete   Composites*,   104:   103346.

525   https://doi.org/10.1016/j.cemconcomp.2019.103346.

526 Arora, A., Y. Yao, B. Mobasher, and N. Neithalath. 2019b. "Fundamental insights into the

527   compressive and flexural response of binder- and aggregate-optimized ultra-high

528   performance concrete (UHPC)." *Cement and Concrete Composites*, 98: 1–13.

529   https://doi.org/10.1016/j.cemconcomp.2019.01.015.

530 Assarsson, G. O., and E. Rydberg. 1956. "Hydrothermal reactions between calcium hydroxide

531   and amorphous silica." *The Journal of Physical Chemistry*, 60(4): 397–404.

532 Bahafid, S., S. Ghabezloo, M. Duc, P. Faure, and J. Sulem. 2017. "Effect of the hydration

533   temperature on the microstructure of Class G cement: C-S-H composition and density."

534   *Cement   and   Concrete   Research*,   95:   270–281.

535   https://doi.org/10.1016/j.cemconres.2017.02.008.

536   Baltakys, K. 2009. "Influence of gypsum additive on the formation of calcium silicate hydrates
537   in mixtures with C/S = 0.83 or 1.0." *Materials Science Poland*, Vol. 27, No. 4/1.

538   Baltakys, K., and R. Siauciunas. 2010. "Influence of gypsum additive on the gyrolite formation
539   process." *Cement and Concrete Research*, 40(3): 376–383.
540   https://doi.org/10.1016/j.cemconres.2009.11.004.

541   Barbarulo, R., H. Peycelon, and S. Leclercq. 2007. "Chemical equilibria between C–S–H and
542   ettringite, at 20 and 85 °C." *Cement and Concrete Research*, 37(8): 1176–1181.
543   https://doi.org/10.1016/j.cemconres.2007.04.013.

544   Bauer, D., R. Marx, J. Nußbicker-Lux, F. Ochs, W. Heidemann, and H. Müller-Steinhagen.
545   2010. "German central solar heating plants with seasonal heat storage." *Solar Energy*,
546   84(4): 612–623. https://doi.org/10.1016/j.solener.2009.05.013.

547   Bentz, D. P. 2006. "Modeling the influence of limestone filler on cement hydration using
548   CEMHYD3D." *Cement and Concrete Composites*, 28(2): 124–129.
549   https://doi.org/10.1016/j.cemconcomp.2005.10.006.

550   Bonavetti, V., V. Rahhal, and E. Irassar. 2001. "Studies on the carboaluminate formation in
551   limestone filler-blended cements." *Cement and Concrete Research*, 31(6): 853–859.
552   https://doi.org/10.1016/S0008-8846(01)00491-4.

553   Bonnaud, P. A., Q. Ji, and K. J. van Vliet. 2013. "Effects of elevated temperature on the
554   structure and properties of calcium–silicate–hydrate gels: the role of confined water." *Soft
555   Matter*, 9(28). https://doi.org/10.1039/c3sm50975c.

556   Cagnon, H., T. Vidal, A. Sellier, C. Soula, X. Bourbon, and G. Camps. 2016. "Effects of water
557   and temperature variations on deformation of limestone aggregates, cement paste, mortar
558   and High Performance Concrete (HPC)." *Cement and Concrete Composites*, 71: 131–143.
559   https://doi.org/10.1016/j.cemconcomp.2016.05.013.

560   Camiletti, J., A. M. Soliman, and M. L. Nehdi. 2012. "Effects of nano- and micro-limestone
561   addition on early-age properties of ultra-high-performance concrete." *Materials and
562   Structures*, 46(6): 881–898. https://doi.org/10.1617/s11527-012-9940-0.

563   Chen, J. J., J. J. Thomas, H. F. W. Taylor, and H. M. Jennings. 2004. "Solubility and structure
564   of calcium silicate hydrate." *Cement and Concrete Research*, 34(9): 1499–1519.
565   https://doi.org/10.1016/j.cemconres.2004.04.034.

566   Chen, T., X. Gao, and M. Ren. 2018. "Effects of autoclave curing and fly ash on mechanical
567   properties of ultra-high performance concrete." *Construction and Building Materials*, 158:
568   864–872. https://doi.org/10.1016/j.conbuildmat.2017.10.074.

569   Dilnesa, B. Z., B. Lothenbach, G. Renaudin, A. Wichser, and D. Kulik. 2014. "Synthesis and
570   characterization of hydrogarnet $Ca_3(Al_xFe_{1-x})_2(SiO_4)_y(OH)_{4(3-y)}$." *Cement and Concrete
571   Research*, 59: 96–111. https://doi.org/10.1016/j.cemconres.2014.02.001.

572 *DIN EN 196-1:2016-11, Prüfverfahren für Zement_- Teil_1: Bestimmung der Festigkeit;*
573   *Deutsche Fassung EN_196-1:2016*, Berlin.

574 Durdziński, P. T., M. Ben Haha, M. Zajac, and K. L. Scrivener. 2017. "Phase assemblage of
575   composite cements." *Cement and Concrete Research*, 99: 172–182.
576   https://doi.org/10.1016/j.cemconres.2017.05.009.

577 Ectors, D., J. Neubauer, and F. Goetz-Neunhoeffer. 2013. "The hydration of synthetic
578   brownmillerite in presence of low Ca-sulfate content and calcite monitored by quantitative
579   in-situ-XRD and heat flow calorimetry." *Cement and Concrete Research*, 54: 61–68.
580   https://doi.org/10.1016/j.cemconres.2013.08.011.

581 Eilers, L. H., and E. B. Nelson. 1979. "Effect of silica particle size on degradation of silica
582   stabilized portland cement." In *Proc., SPE Oilfield and Geothermal Chemistry Symposium*.

583 El Bitouri, Y., F. Jamin, C. Pélissou, and M. S. El Youssoufi. 2017. "Tensile and shear bond
584   strength between cement paste and aggregate subjected to high temperature." *Materials*
585   *and Structures*, 50(6). https://doi.org/10.1617/s11527-017-1105-8.

586 Famy, C., A. R. Brough, and H. Taylor. 2003. "The C-S-H gel of Portland cement mortars: Part
587   I. The interpretation of energy-dispersive X-ray microanalyses from scanning electron
588   microscopy, with some observations on C-S-H, AFm and AFt phase compositions."
589   *Cement and Concrete Research*, 33(9): 1389–1398. https://doi.org/10.1016/S0008-
590   8846(03)00064-4.

591 Fehling, E., M. Schmidt, J. C. Walraven, T. Leutbecher, and S. Fröhlich. 2014. *Ultra-high*
592   *performance concrete UHPC: Fundamentals - design - examples*, Berlin: Ernst & Sohn.

593 Funk, J. E., and D. Dinger. 1993. *Predictive process control of crowded particulate*
594   *suspensions: Applied to ceramic manufacturing*: Springer Science & Business Media.

595 Gallucci, E., X. Zhang, and K. L. Scrivener. 2013. "Effect of temperature on the microstructure
596   of calcium silicate hydrate (C-S-H)." *Cement and Concrete Research*, 53: 185–195.
597   https://doi.org/10.1016/j.cemconres.2013.06.008.

598 Ghafari, E., S. A. Ghahari, H. Costa, E. Júlio, A. Portugal, and L. Durães. 2016. "Effect of
599   supplementary cementitious materials on autogenous shrinkage of ultra-high performance
600   concrete." *Construction and Building Materials*, 127: 43–48.
601   https://doi.org/10.1016/j.conbuildmat.2016.09.123.

602 Goto, S., K. Suenaga, T. Kado, and M. Fukuhara. 1995. "Calcium Silicate Carbonation
603   Products." *Journal of the American Ceramic Society*, 78(11): 2867–2872.
604   https://doi.org/10.1111/j.1151-2916.1995.tb09057.x.

605 Guo, X., F. Meng, and H. Shi. 2017. "Microstructure and characterization of hydrothermal
606   synthesis of Al-substituted tobermorite." *Construction and Building Materials*, 133: 253–
607   260. https://doi.org/10.1016/j.conbuildmat.2016.12.059.

608 Heller, A. 2000. "15 Years of R&D in central solar heating in Denmark." *Solar Energy*, 69(6):
609   437–447. https://doi.org/10.1016/S0038-092X(00)00118-3.

610 Hettema, M. H. H. 1996. *The thermo-mechanical behaviour of sedimentary rock: An*
611   *experimental study*.

612 Hong, S. Y., and F. P. Glasser. 2004. "Phase relations in the $CaO\text{-}SiO_2\text{-}H_2O$ system to 200 °C
613   at saturated steam pressure." *Cement and Concrete Research*, 34(9): 1529–1534.
614   https://doi.org/10.1016/j.cemconres.2003.08.009.

615 Huang, W., H. Kazemi-Kamyab, W. Sun, and K. Scrivener. 2017. "Effect of cement substitution
616   by limestone on the hydration and microstructural development of ultra-high performance
617   concrete (UHPC)." *Cement and Concrete Composites*, 77: 86–101.
618   https://doi.org/10.1016/j.cemconcomp.2016.12.009.

619 Hüsken, G., and H. Brouwers. 2008. "A new mix design concept for earth-moist concrete: A
620   theoretical and experimental study." *Cement and Concrete Research*, 38(10): 1246–1259.
621   https://doi.org/10.1016/j.cemconres.2008.04.002.

622 IEA. 2019. "Solar Energy: Mapping the Road Ahead." <https://www.iea.org/reports/solar-
623   energy-mapping-the-road-ahead>.

624 IEA. 2020. "World Energy Outlook 2020." <https://www.iea.org/reports/world-energy-outlook-
625   2020>.

626 Krakowiak, K. J., J. J. Thomas, S. James, M. Abuhaikal, and F.-J. Ulm. 2018. "Development
627   of silica-enriched cement-based materials with improved aging resistance for application in
628   high-temperature environments." *Cement and Concrete Research*, 105: 91–110.
629   https://doi.org/10.1016/j.cemconres.2018.01.004.

630 Kumar, A., T. Oey, G. Falzone, J. Huang, M. Bauchy, M. Balonis, N. Neithalath, J. Bullard, and
631   G. Sant. 2017. "The filler effect: The influence of filler content and type on the hydration
632   rate of tricalcium silicate." *Journal of the American Ceramic Society*, 100(7): 3316–3328.
633   https://doi.org/10.1111/jace.14859.

634 Kumar, A., T. Oey, S. Kim, D. Thomas, S. Badran, J. Li, F. Fernandes, N. Neithalath, and G.
635   Sant. 2013. "Simple methods to estimate the influence of limestone fillers on reaction and
636   property evolution in cementitious materials." *Cement and Concrete Composites*, 42: 20–
637   29. https://doi.org/10.1016/j.cemconcomp.2013.05.002.

638 Labhasetwar, N. K., O. P. Shrivastava, and Y. Y. Medikov. 1991. "Mo¨ssbauer study on iron-
639   exchanged calcium silicate hydrate: $Ca_{5-x}Fe_xSi_6O_{18}H_2 \cdot nH_2O$." *Journal of Solid State*
640   *Chemistry*, 93(1): 82–87. https://doi.org/10.1016/0022-4596(91)90277-O.

641 Lehmann, C. 2013. *Neue Perspektiven für Ultra-Hochleistungsbeton durch gezielte*
642   *Beeinflussung des Nanogefüges*.

643 Li, P. P., H. Brouwers, W. Chen, and Q. Yu. 2020. "Optimization and characterization of high-
644   volume limestone powder in sustainable ultra-high performance concrete." *Construction*
645   *and Building Materials*, 242: 118112. https://doi.org/10.1016/j.conbuildmat.2020.118112.

646 Li, P. P., Y. Cao, H. Brouwers, W. Chen, and Q. L. Yu. 2019. "Development and properties
647   evaluation of sustainable ultra-high performance pastes with quaternary blends." *Journal*
648   *of Cleaner Production*, 240: 118124. https://doi.org/10.1016/j.jclepro.2019.118124.

649 Li, W., Z. Huang, F. Cao, Z. Sun, and S. P. Shah. 2015. "Effects of nano-silica and nano-
650   limestone on flowability and mechanical properties of ultra-high-performance concrete
651   matrix." *Construction and Building Materials*, 95: 366–374.
652   https://doi.org/10.1016/j.conbuildmat.2015.05.137.

653 Lothenbach, B., G. Le Saout, E. Gallucci, and K. Scrivener. 2008. "Influence of limestone on
654   the hydration of Portland cements." *Cement and Concrete Research*, 38(6): 848–860.
655   https://doi.org/10.1016/j.cemconres.2008.01.002.

656 Mangold, D. 2007. "Seasonal storage–a German success story." *Sun & Wind Energy*, 1(2007):
657   48–58.

658 Marincea, S., E. Bilal, J. Verkaeren, M.-L. Pascal, and M. Fonteilles. 2001. "Superposed
659   parageneses in the spurrite-, tilleyite-and gehlenite-bearing skarns from Cornet Hill,
660   Apuseni Mountains, Romania." *The Canadian Mineralogist*, 39(5): 1435–1453.

661 Matsui, K., J. Kikuma, M. Tsunashima, T. Ishikawa, S.-Y. Matsuno, A. Ogawa, and M. Sato.
662   2011. "In situ time-resolved X-ray diffraction of tobermorite formation in autoclaved aerated
663   concrete: Influence of silica source reactivity and Al addition." *Cement and Concrete*
664   *Research*, 41(5): 510–519. https://doi.org/10.1016/j.cemconres.2011.01.022.

665 Meller, N., K. Kyritsis, and C. Hall. 2009a. "The hydrothermal decomposition of calcium
666   monosulfoaluminate 14-hydrate to katoite hydrogarnet and β-anhydrite: An in-situ
667   synchrotron X-ray diffraction study." *Journal of Solid State Chemistry*, 182(10): 2743–2747.
668   https://doi.org/10.1016/j.jssc.2009.07.029.

669 Meller, N., K. Kyritsis, and C. Hall. 2009b. "The mineralogy of the $CaO–Al_2O_3–SiO_2–H_2O$
670   (CASH) hydroceramic system from 200 to 350 °C." *Cement and Concrete Research*, 39(1):
671   45–53. https://doi.org/10.1016/j.cemconres.2008.10.002.

672 Mitsuda, T., and H. F. W. Taylor. 1975. "Influence of aluminium on the conversion of calcium
673   silicate hydrate gels into 11 Å tobermorite at 90°C and 120°C." *Cement and Concrete*
674   *Research*, 5(3): 203–209. https://doi.org/10.1016/0008-8846(75)90001-0.

675 Morin, V., P. Termkhajornkit, B. Huet, and G. Pham. 2017. "Impact of quantity of anhydrite,
676   water to binder ratio, fineness on kinetics and phase assemblage of belite-ye'elimite-ferrite
677   cement." *Cement and Concrete Research*, 99: 8–17.
678   https://doi.org/10.1016/j.cemconres.2017.04.014.

679 Mostafa, N. Y., A. A. Shaltout, H. Omar, and S. A. Abo-El-Enein. 2009. "Hydrothermal
680   synthesis and characterization of aluminium and sulfate substituted 1.1nm tobermorites."
681   *Journal of Alloys and Compounds*, 467(1): 332–337.
682   https://doi.org/10.1016/j.jallcom.2007.11.130.

683 Myers, R. J., E. L'Hôpital, J. L. Provis, and B. Lothenbach. 2015. "Effect of temperature and
684   aluminium on calcium (alumino)silicate hydrate chemistry under equilibrium conditions."
685   *Cement and Concrete Research*, 68: 83–93.
686   https://doi.org/10.1016/j.cemconres.2014.10.015.

687 Nelson, E. B., L. H. Eilers, and G. L. Kalousek. 1981. "Formation and behavior of calcium
688   silicate hydrates in a geothermal environment." *Cement and Concrete Research*, 11(3):
689   371–381. https://doi.org/10.1016/0008-8846(81)90109-5.

690 Nelson, E. B., and D. Guillot. 2006. *Well cementing*, Sugar Land, Tex.: Schlumberger.

691 Nonat, A. 2004. "The structure and stoichiometry of C-S-H." *Cement and Concrete Research*,
692   34(9): 1521–1528. https://doi.org/10.1016/j.cemconres.2004.04.035.

693 Oey, T., A. Kumar, J. W. Bullard, N. Neithalath, and G. Sant. 2013. "The filler effect: the
694   influence of filler content and surface area on cementitious reaction Rates." *Journal of the
695   American Ceramic Society*, 96(6): 1978–1990. https://doi.org/10.1111/jace.12264.

696 Ouyang, X., D. A. Koleva, G. Ye, and K. van Breugel. 2017. "Understanding the adhesion
697   mechanisms between C S H and fillers." *Cement and Concrete Research*, 100: 275–283.
698   https://doi.org/10.1016/j.cemconres.2017.07.006.

699 Papanicolaou, E., and V. Belessiotis. 2009. "Transient development of flow and temperature
700   fields in an underground thermal storage tank under various charging modes." *Solar
701   Energy*, 83(8): 1161–1176. https://doi.org/10.1016/j.solener.2009.01.017.

702 Proske, T., S. Hainer, M. Rezvani, and C.-A. Graubner. 2013. "Eco-friendly concretes with
703   reduced water and cement contents — Mix design principles and laboratory tests." *Cement
704   and Concrete Research*, 51: 38–46. https://doi.org/10.1016/j.cemconres.2013.04.011.

705 Puerta-Falla, G., M. Balonis, G. Le Saout, G. Falzone, C. Zhang, N. Neithalath, and G. Sant.
706   2015. "Elucidating the role of the aluminous source on limestone reactivity in cementitious
707   materials." *Journal of the American Ceramic Society*, 98(12): 4076–4089.
708   https://doi.org/10.1111/jace.13806.

709 Qian, G., D. D. Sun, J. H. Tay, Z. Lai, and G. Xu. 2002. "Autoclave properties of kirschsteinite-
710   based steel slag." *Cement and Concrete Research*, 32(9): 1377–1382.
711   https://doi.org/10.1016/S0008-8846(02)00790-1.

712 Richardson, I. G. 2004. "Tobermorite/jennite- and tobermorite/calcium hydroxide-based
713   models for the structure of C-S-H: applicability to hardened pastes of tricalcium silicate, β-
714   dicalcium silicate, Portland cement, and blends of Portland cement with blast-furnace slag,

metakaolin, or silica fume." *Cement and Concrete Research*, 34(9): 1733–1777. https://doi.org/10.1016/j.cemconres.2004.05.034.

Rivas-Mercury, J. M., P. Pena, A. H. de Aza, and X. Turrillas. 2008. "Dehydration of $Ca_3Al_2(SiO_4)_y(OH)_{4(3-y)}$ (0<y<0.176) studied by neutron thermodiffractometry." *Journal of the European Ceramic Society*, 28(9): 1737–1748. https://doi.org/10.1016/j.jeurceramsoc.2007.12.038.

Šatava Vladimír, and O. Vepek. 1975. "Thermal decomposition of ettringite under hydrothermal conditions." *Journal of the American Ceramic Society*, 58(7-8): 357–359. https://doi.org/10.1111/j.1151-2916.1975.tb11513.x.

Scrivener, K. L., R. Snellings, and B. Lothenbach. 2016. *A Practical Guide to Microstructural Analysis of Cementitious Materials*: CRC Press.

Sevelsted, T. F., and J. Skibsted. 2015. "Carbonation of C–S–H and C–A–S–H samples studied by 13 C, 27 Al and 29 Si MAS NMR spectroscopy." *Cement and Concrete Research*, 71: 56–65. https://doi.org/10.1016/j.cemconres.2015.01.019.

Sonja Haastrup, Donghong Yu, and Yuanzheng Yue. 2018. "Impact of minor iron content on crystal structure and properties of porous calcium silicates during synthesis." *Materials Chemistry and Physics*, 205: 180–185. https://doi.org/10.1016/j.matchemphys.2017.11.024.

Taylor, H. F. W. 1964. *The Chemistry of Cements*, London: Academic Press Inc.

Vikan, H., and H. Justnes. 2007. "Rheology of cementitious paste with silica fume or limestone." *Cement and Concrete Research*, 37(11): 1512–1517. https://doi.org/10.1016/j.cemconres.2007.08.012.

Werder, J. von, S. Simon, C. Lehmann, C. Selleng, P. Fontana, and B. Meng. 2018. "Autoclaving of ultra-high performance concrete (UHPC)." *ce/papers*, 2(4): 131–136. https://doi.org/10.1002/cepa.866.

Wu, Z., C. Shi, and K. H. Khayat. 2018. "Multi-scale investigation of microstructure, fiber pullout behavior, and mechanical properties of ultra-high performance concrete with nano-CaCO3 particles." *Cement and Concrete Composites*, 86: 255–265. https://doi.org/10.1016/j.cemconcomp.2017.11.014.

Yang, R., and J. H. Sharp. 2001. "Hydration characteristics of Portland cement after heat curing: I, Degree of hydration of the anhydrous cement phases." *Journal of the American Ceramic Society*, 84(3): 608–614. https://doi.org/10.1111/j.1151-2916.2001.tb00707.x.

Yang, R., R. Yu, Z. Shui, X. Gao, J. Han, G. Lin, D. Qian, Z. Liu, and Y. He. 2020. "Environmental and economical friendly ultra-high performance-concrete incorporating appropriate quarry-stone powders." *Journal of Cleaner Production*, 260: 121112. https://doi.org/10.1016/j.jclepro.2020.121112.

751 Yazıcı, H., E. Deniz, and B. Baradan. 2013. "The effect of autoclave pressure, temperature
752   and duration time on mechanical properties of reactive powder concrete." *Construction and*
753   *Building Materials*, 42: 53–63. https://doi.org/10.1016/j.conbuildmat.2013.01.003.

754 Yazıcı, H., M. Y. Yardımcı, S. Aydın, and A. Ş. Karabulut. 2009. "Mechanical properties of
755   reactive powder concrete containing mineral admixtures under different curing regimes."
756   *Construction and Building Materials*, 23(3): 1223–1231.
757   https://doi.org/10.1016/j.conbuildmat.2008.08.003.

758 Yazıcı, H., M. Y. Yardımcı, H. Yiğiter, S. Aydın, and S. Türkel. 2010. "Mechanical properties of
759   reactive powder concrete containing high volumes of ground granulated blast furnace slag."
760   *Cement and Concrete Composites*, 32(8): 639–648.
761   https://doi.org/10.1016/j.cemconcomp.2010.07.005.

762 Yazıcı, H., H. Yiğiter, A. Ş. Karabulut, and B. Baradan. 2008. "Utilization of fly ash and ground
763   granulated blast furnace slag as an alternative silica source in reactive powder concrete."
764   *Fuel*, 87(12): 2401–2407. https://doi.org/10.1016/j.fuel.2008.03.005.

765 Young, R. A., ed. 2002. *The Rietveld method*, Oxford: Oxford Univ. Press.

766 Yu, R., P. Spiesz, and H. J. H. Brouwers. 2014. "Mix design and properties assessment of
767   Ultra-High Performance Fibre Reinforced Concrete (UHPFRC)." *Cement and Concrete*
768   *Research*, 56: 29–39. https://doi.org/10.1016/j.cemconres.2013.11.002.

769 Yu, R., P. Spiesz, and H. J. H. Brouwers. 2015. "Development of an eco-friendly Ultra-High
770   Performance Concrete (UHPC) with efficient cement and mineral admixtures uses."
771   *Cement and Concrete Composites*, 55: 383–394.
772   https://doi.org/10.1016/j.cemconcomp.2014.09.024.

773 Zdeb, T. 2017. "An analysis of the steam curing and autoclaving process parameters for
774   reactive powder concretes." *Construction and Building Materials*, 131: 758–766.
775   https://doi.org/10.1016/j.conbuildmat.2016.11.026.

776

777

778

779

780

781

782

783   **Table 1**. Chemical compositions of the raw materials (wt. %).

	SiO_2	CaO	Al_2O_3	K_2O	MgO	Mn_2O_3	Na_2O	P_2O_5	Fe_2O_3	SO_3	TiO_2	LOI	Sum
Cement	18.85	61.16	4.85	1.07	1.74	0.06	0.22	0.07	2.83	3.62	0.22	4.92	99.61
Silica fume	98.40	0.20	0.20	0.20	0.10	-	0.15	-	0.01	0.10	-	-	99.27
Limestone powder	6.29	49.63	1.84	0.11	0.88	0.01	-	0.03	0.83	0.16	0.09	40.37	100.24
Quartz powder	98.93	-	0.17	-	-	-	-	-	0.02	0.02	0.05	0.15	99.34

784

785   **Table 2.** Formulas of the mixtures (mass ratio).

	Limestone	Cement	Silica fume	Quartz powder	Quartz sand
L0	0	1	0.26	0.76	1.1
L1	0.1	0.9	0.26	0.76	1.1
L2	0.3	0.7	0.26	0.76	1.1
L3	0.5	0.5	0.26	0.76	1.1

786

787   **Table 3.** The contents of main elements around the aluminoferrite phase (atom %).

	Ca	Al	Fe	Si	S	O
Point 1	18.2	9.6	4.2	6.2	0.3	57.0
Point 2	18.8	10.3	3.4	6.6	0.3	56.6
Point 3	19.3	2.9	0.8	12.1	0.9	62.0
Point 4	22.0	1.1	0.3	11.0	1.9	62.4
Point 5	16.7	1.2	0.3	15.2	0.3	65.4
Point 6	17.6	1.5	0.4	13.7	0.4	65.0

788   Note: The point number corresponds to the cross mark in Fig. 7.

789

2.3 The influence of long-term autoclaving on the properties of ultra-high performance concrete

The Influence of Long-Term Autoclaving on the Properties of Ultra-High Performance Concrete

Hongwei Tian, Tamino Hirsch, Dietmar Stephan* and Christian Lehmann

Institute of Civil Engineering, Technische Universität Berlin, Berlin, Germany

Thermal energy storage is a key component in harnessing renewable resources, compensating for the energy variations across time scales. A popular strategy for thermal energy storage is storing thermal energy in hot water tanks, which are generally made of copper, stainless steel, and vitreous enamel-lined carbon steel. However, these materials usually suffer a high production cost and short life cycle. UHPC with superior strength and durability holds the potential as a construction material for hot water tanks, which are commercially available and affordable for large-scale applications. During the charging process of hot water tanks, the UHPC structures are thus loaded by a long-term temperature-pressure load (autoclaving condition). However, the influence of long-term autoclaving on UHPC is still unclear. Therefore, the influence of long-term autoclaving at 200°C on the mechanical properties and microstructure of UHPC is studied here. The effect of the long-term autoclaving depends on the UHPC compositions. The compressive strength can stay robust owing to the accelerated formation of hydrates, while the flexural strength is vulnerable to the long-term autoclaving. Katoite, hydroxylellestadite, and scawtite are identified as the new hydrates in the autoclaved UHPC with typical components. The transformation of amorphous C-S-H into more ordered phases results in the low flexural strength and the undensified interface between the matrix and steel fibres. The partial replacement of cement by fly ash mitigates the detrimental effect of the long-term autoclaving. The incorporation of fly ash provides additional silica and increases the ratio of silica to cement, leading to more poorly crystallized C-S-H with a low Ca/Si ratio, which benefits microstructure densification and mechanical strength. The decrease of Ca/Si ratio and the increase of Al by fly ash accelerate the decomposition of katoite and hydroxylellestadite and formation of tobermorite. This study clarifies the influence of the long-term autoclaving on UHPC and provides guidance for developing an applicable and sustainable UHPC as the construction material for hot water tanks.

Keywords: ultra-high performance concrete (UHPC), autoclaving, fly ash, C-S-H, compressive and flexural strength

1 INTRODUCTION

Ultra-high performance concrete (UHPC) is an innovative and promising cementitious composite (Fehling et al., 2014). The ultra-high performance typically comprises two aspects: ultra-high durability and ultra-high mechanical properties (Richard and Cheyrezy 1995; Matte and Moranville 1999; Fehling et al., 2014). The ways to obtain this superior performance include eliminating coarse aggregate, optimizing granulometric distribution, incorporating ultra-fine components, and decreasing the water/binder ratio (Richard and Cheyrezy 1995; Arora et al., 2018; Lee et al., 2018; Arora et al., 2019). However, UHPC usually possesses a brittle fracture and poor ductility. One popular strategy to compensate for such a defect without sacrificing compressive strength is to introduce discrete fibres as reinforcement. Up to now, many types of fibres have been used in UHPC, e.g., organic fibres (Liu and Tan 2018; Pourfalah 2018; Missemer et al., 2019; Park et al., 2019), mineral fibres (Hassan and Wille 2018; Dong et al., 2019; Yonggui et al., 2020), and metallic fibres. Steel fibre is a popular type for UHPC reinforcement, and its influence on mechanical performance, which depends on many factors, such as geometry, distribution, and content, has been extensively studied (Park et al., 2012; Yoo et al., 2017; Zhang et al., 2018). In addition, the variation in matrix microstructure can also affect the bond properties between steel fibre and matrix. Compared with normal curing, short-term hydrothermal curing at 60 and 90°C can lead to the more densified microstructure and fibre-matrix interface in UHPC, exhibiting higher mechanical strength (Garas et al., 2012). However, for the UHPC exposed to elevated temperatures (fire resistance experiment), the hydration products may decompose and porosity increases, causing cracks and the degradation of bond strength between the matrix and fibres (Ahmad et al., 2019; Huang et al., 2019).

Thermal energy storage is known to play a vital role in harnessing renewable resources, especially solar energy, compensating for the sunlight variations across time scales (Alva et al., 2017). A hot water tank, which stocks thermal energy by heating or cooling the storage medium (water) for later conversion to electricity and heating or cooling applications, is a popular strategy for thermal energy storage. The water tanks are generally made of copper, stainless steel, and vitreous enamel-lined carbon steel. However, these materials have a short life cycle due to the commonly encountered corrosion and leakage. Concrete has also been used to construct such water tanks and possesses a relatively longer working life, which is commercially available and affordable for large-scale applications. Furthermore, a concrete water tank can be designed for larger capabilities and buried underground, minimizing the visual impact. However, the temperature of stored water is generally lower than 100°C, i.e., below the water boiling point, which restricts the energy storage density (the amount of energy per unit of volume or mass) and the applications of stored thermal energy (Heller 2000; Mangold 2007; Papanicolaou and Belessiotis 2009; Bauer et al., 2010). At a constant tank volume, increasing the temperature of stored water is a viable solution, which means that the concrete structure has to withstand a temperature-pressure load. UHPC
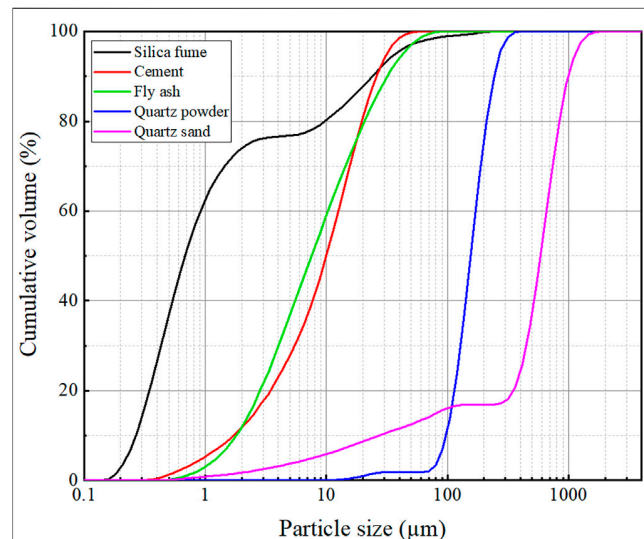

FIGURE 1 | Particle size distributions of raw materials measured by laser diffraction.

with superior strength and durability has been widely used in large-span components, anti-explosive structures, and high-abrasion, high-corrosion environments, and it may fulfil the requirements for the water tank, holding potential as an alternative material for the construction of hot water pressure accumulators (Wang et al., 2012; Aldahdooh et al., 2013; Fehling et al., 2014; Wang et al., 2014; Shi et al., 2015; Tafraoui et al., 2016; Wu et al., 2018).

In this project, the hot water with 200°C was to be stored, and the UHPC mixtures were thus loaded by long-term autoclaving. In general, short-term hydrothermal curing is applied in prefabricated UHPC components to obtain high early strength. Such hydrothermal curing is normally with hot water/steam (60/90°C) for 24–48 h or autoclaving for several hours (Fehling et al., 2014; Zdeb 2017; Chen et al., 2018; Werder et al., 2018). However, the influence of a long period of autoclaving on the properties of UHPC is still unclear. Furthermore, supplementary cementitious materials (SCMs) are increasingly used in UHPC to compensate for the high production cost and high CO_2 emissions during Portland cement production on the one hand and to improve the concrete properties by filler effect and/or pozzolanic reaction on the other hand. In a conventional environment, the influence of SCMs is mainly determined by their physical properties, although in the long term, SCMs can chemically react and change the hydrate assemblage depending on their chemical compositions. Under autoclaving, SCMs are highly activated, and the chemical elements introduced by SCMs can exert significant influence on the hydrates' transformation and their thermal stability (Eilers et al., 1983; Colston et al., 2005; Biagioni et al., 2016).

Therefore, two mixtures, including one typical UHPC mixture and one mixture with fly ash, were investigated in the current study. After the long-term autoclaving treatment at 200°C, the samples were characterized by compressive and flexural tests, X-ray diffraction, thermogravimetric analysis, Mercury intrusion

81

TABLE 1 | Chemical compositions of raw materials (wt%).

	SiO$_2$	CaO	Al$_2$O$_3$	K$_2$O	MgO	Mn$_2$O$_3$	Na$_2$O	P$_2$O$_5$	Fe$_2$O$_3$	SO$_3$	TiO$_2$	LOI	Sum
Cement	18.85	61.16	4.85	1.07	1.74	0.06	0.22	0.07	2.83	3.62	0.22	4.92	99.61
Silica fume	98.40	0.20	0.20	0.20	0.10	-	0.15	-	0.01	0.10	-	-	99.27
Fly ash	54.25	5.56	21.03	2.08	2.36	0.09	1.05	0.98	7.98	0.30	0.92	3.29	99.89
Quartz powder	98.93	-	0.17	-	-	-	-	-	0.02	0.02	0.05	0.15	99.34

TABLE 2 | Recipes of the mixtures (mass ratio).

Mixtures	Cement	Fly ash	Silica fume	Quartz powder	Quartz sand	W/b ratio
C1	1	0	0.26	0.76	1.10	0.21
C2	0.8	0.2	0.26	0.76	1.10	0.21

porosimeter, and scanning electron microscopy to clarify the influence of long-term autoclaving.

2 MATERIALS AND METHODS

2.1 Materials

Portland cement CEM I 52.5 R complying with European standard EN 197-1 was used in this study. Quartz sand with a particle size of 0–2 mm was used as a fine aggregate. To optimize the particle size distribution and increase the packing density, silica fume and quartz powder were also introduced. The fly ash (Class F) used in this study was rich in silicon and aluminium. The particle size distributions of these materials measured with a Mastersizer 2000 (Malvern Panalytical Ltd.) are given in **Figure 1**, and the chemical compositions determined by X-ray fluorescence are shown in **Table 1**. The high performance superplasticizer of MasterGlenium ACE 430 based on a polycarboxylic ether was used to disperse the UHPC mixtures. The steel fiber used in this study had a length of 12.5 mm and a diameter of 0.2 mm.

2.2 Mixtures and Curing Regimes

The mixture recipes are shown in **Table 2** and were optimized by the modified Andreasen & Andersen packing model (Funk and Dinger 1993; Chen et al., 2019; Li et al., 2022). The water/binder (w/b) ratio was fixed at 0.21, and steel fibre content is set as 2 vol %. C1 is a typical UHPC mixture, and C2 is the blended mixture with 20 wt% fly ash replacing cement. The starting materials were first dry-mixed by a high-performance mixer (Type EL5 Eco, Maschinenfabrik Gustav Eirich GmbH and Co. KG) in the counter-current mode for 2 min. The water previously mixed with half the amount of the precalculated superplasticizer was then added, and the mixture was homogenized for 3 min in counter-current mode at a speed of 300 rpm. After a pause of 1 min, the remaining superplasticizer was added, and the mixing was restarted for another 3 min. Afterwards, the steel fiber was gradually introduced in 2 min. The mixture temperature was monitored throughout the mixing process, avoiding premature solidification caused by excessive temperature. Prismatic specimens 160·40.40 mm³ were cast for compressive and flexural strength tests without any mechanical consolidation.

For the samples prepared for microstructure characterization, quartz sand and steel fibre were eliminated. The freshly cast samples were sealed at 20 ± 2°C for 24 h, and then the hardened samples were demoulded followed by 24 h of pre-curing in water at 20 ± 2°C. One batch of samples were placed in water at 20 ± 2°C for 28 days as the reference samples. Another batch of samples were loaded by the temperature-pressure load at 200°C with saturated steam pressure 1.55 MPa for 10 days, simulating the working environment of hot water pressure accumulators. For the samples subjected to the long-term temperature-pressure load, the temperature was heated from room temperature to 200°C in ~1 h and kept for 10 days. For the microstructure analyses, after cooling to room temperature, the inner parts of samples were extracted and immersed in isopropanol for 1 day, followed by freeze-drying.

2.3 Mechanical Properties

A three-point bending test (centre-point loading) was performed on prismatic samples 40·40 160 mm³ at a span length of 100 mm to evaluate the flexural properties. An MTS load frame was used to apply a load at a controlled displacement rate of 0.2 mm/min. The mid-span deflection of the specimen was recorded by linear variable differential transformers (LVDTs), and the average values from three samples were reported. The flexural strength can be calculated by the peak load in the load-deflection curve. The flexural toughness was evaluated by energy absorption capacity, which was calculated as the area of load versus the deflection curve up to the deflection point of 3 mm, according to ASTM C348. Compressive strength was loaded on a surface of 40·40 mm^2 of the broken samples after a flexural test at a loading rate of 2.4 kN/s, according to ASTM C349. The average value of six samples for each batch was reported as compressive strength. A statistical analysis by t-test was used to analyse the mechanical results, and a significance level of $p \leq 0.05$ was chosen.

2.4 X-Ray Diffraction

The mineralogical composition analysis was performed by X-ray diffraction (XRD) using an Empyrean PANalytical diffractometer with CuKα radiation (k = 1.540,598 Å). The measurements were performed at 40 kV and 40 mA in continuous mode with a resolution of 0.0131° and speed of 0.0172°/s for a 2θ range

Mechanical strength	Normal curing		Autoclaving	
	C1	C2	C1	C2
Compressive strength (MPa)	178.0 ± 10.1	169.9 ± 7.7	195.5 ± 11.0	218.0 ± 21.4
Flexural strength (MPa)	26.4 ± 2.5	24.0 ± 3.5	18.8 ± 2.2	26.5 ± 1.8
Energy absorption capacity (kN·mm)	15.4 ± 1.9	15.7 ± 0.4	13.2 ± 1.3	16.3 ± 0.3

from 3° to 65°. HighScore Plus software equipped with an ICSD database was used to identify the mineralogical phases.

2.5 Thermogravimetric Analysis

Thermogravimetric (TG) analysis was carried out using a TG 209 F3 Tarsus® (NETZSCH) in a nitrogen atmosphere with a 30 ml/min flow rate. 10 ± 1 mg of powder sample was used for each measurement. The temperature was increased from 20 to 1,000°C at a rate of 10°C/min.

2.6 Scanning Electron Microscope

A Zeiss Gemini SEM500 Nano VP equipped with an EDX detector was used to observe hydrates and the interface between the matrix and steel fibres. The small pieces used for SEM analysis were cut from the inner part of the UHPC samples with steel fibres. A low-viscosity epoxy resin was used to saturate the sample pieces and the surface of the hardened samples was then polished down to 1 μm using successive diamond abrasives. The chemical compositions of hydrates in autoclaved samples were measured by point element analysis. In addition, the element mapping was also conducted to study the distributions of the elements.

2.7 Mercury Intrusion Porosimetry

Due to the chemical reactions activated by the high temperature, the matrix pore structure is inevitably varied. Mercury intrusion porosimetry (MIP) using a Porotec porosimeter (Pascal 240/440) was carried out on small cubic samples. Approx. 2 g of each sample was used in the experiments under 22°C to characterize the porosity and pore size distribution. The Mercury surface tension and contact angle were assigned to 0.48 N/m and 140°, respectively. The intrusion pressure was up to 400 MPa with an increase/decrease speed of 3–7 MPa/min.

3 RESULTS AND DISCUSSION

3.1 Mechanical Properties

The compressive strength of the samples cured under different conditions is shown in **Table 3**. After normal curing for 28 days, the compressive strengths of C1 and C2 are 178.0 and 169.9 MPa, respectively. The partial replacement of cement by fly ash leads to a slight decrease in compressive strength, which is different from the influence of fly ash in normal concrete. In normal blended concrete, fly ash usually causes a low early age strength due to its low activity, while the late strength may be improved, benefiting from the pozzolanic reaction providing additional gel product (Kovács 1975; Feldman et al., 1990). However, in UHPC with a

relatively low w/b ratio, cement hydration and pozzolanic reaction compete with water, and the active cement clinker phases take precedence over fly ash. Furthermore, silica fume, generally used in UHPC to optimize the particle size distribution and densify the microstructure, possesses a higher pozzolanic activity than fly ash. The pH in the liquid environment can be effectively decreased by silica fume, which also restricts the reaction of fly ash. This phenomenon is also reported in other blended UHPC mixtures (Yu et al., 2015; Zhang et al., 2017; Chang and Zheng 2020).

After the 10 days of autoclaving, the compressive strength of autoclaved C1 is 195.5 MPa, which is higher than that of normally cured C1 (*t*-test, *p* = 0.0228). Similarly, the autoclaved C2 also presents a higher compressive strength of 218.0 MPa than normal cured C2 (*t*-test, *p* = 0.0057). It is well reported that several hours of autoclaving can significantly activate the pozzolanic reaction between silica and portlandite, leading to more C-S-H being formed, which is beneficial to the mechanical properties. However, long-term autoclaving can induce the transformation of amorphous C-S-H into crystalline phases, resulting in the volume reduction of hydrates and pore coarsening (Glasser and Hong 2003; Hong and Glasser 2004; Meller et al., 2007; Kyritsis et al., 2009b). Abd Elrahman et al. reported that the compressive strength of the high performance concrete (HPC) consisting of cement (CEM I 32.5 R), quartz powder, quartz sand, and coarse aggregate is significantly decreased by long-term autoclaving (200°C) (Abd Elrahman and Hillemeier 2015). According to the experience in oil and geothermal well cementing under hydrothermal conditions, α-dicalcium silicate hydrate $Ca_2(SiO_3OH)OH$ (α-C_2SH) is usually encountered, causing microstructure degradation. To avoid this problem, additional silica (approx. 35-40 wt%) is introduced to reduce the Ca/Si ratio to approx. 1.0, leading to other C-S-H phases, such as tobermorite $Ca_5Si_6O_{16}(OH)_2 \cdot 4(H_2O)$ and xonotlite $Ca_6(Si_6O_{17})$ $(OH)_2$, depending on the temperature and effective Ca/Si ratio (Colston et al., 2005; Nelson and Guillot 2006; Kyritsis et al., 2009a). In this way, the UHPC components quartz powder and silica fume make it robust in long-term autoclaving to prevent strength degradation, although the addition of these materials initially aims to enhance the packing density and microstructure. Note that the physicochemical properties (size and crystallinity) of silica-containing materials should be considered, as the silica-containing materials with different activity can change the hydrates assemblage. For example, Krakowiak et al. (Krakowiak et al., 2018) conducted a comparative study on the crystalline α-quartz with different sizes at 200°C. It was found that gyrolite $Ca_8(Si_4O_{10})_3(OH)_4 \cdot 7H_2O$ and 11 Å tobermorite dominate in the samples containing coarser quartz, while

FIGURE 2 | Flexural load-deflection curves of the samples after different treatments.

FIGURE 3 | Diffraction patterns of the samples after different treatments (Q: quartz, A: alite, B: belite, b: calcium aluminoferrite, E: ettringite, P: portlandite, T: tobermorite, S: scawtite, H: hydroxylellestadite, K: katoite, R: rutile).
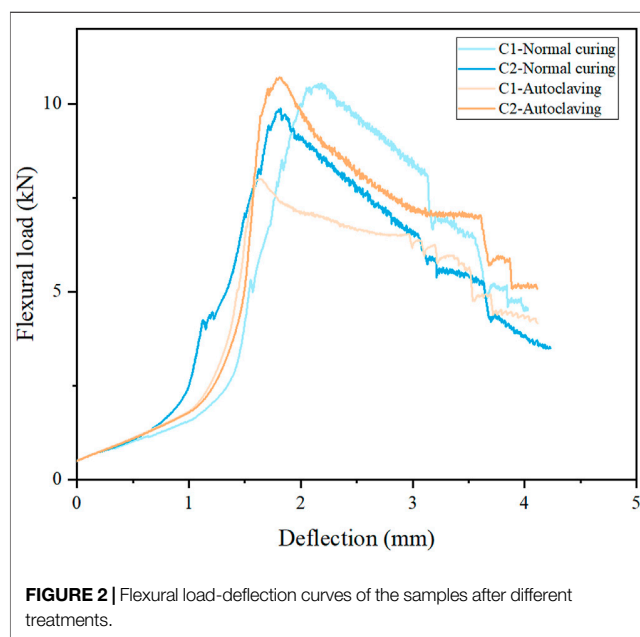
poorly crystalline C-S-H predominates in the samples with fine quartz. Besides, the morphology of the hydrates can be also affected by the silica accessibility. The sample with active silica fume presents the granular xonotlite (major phase), while the sample with quartz powder generates needle-like xonotlite (major phase) accompanied by higher mechanical strength (Eilers et al., 1983).

The influence of autoclaving on sample behaviour under flexural testing is shown in **Figure 2**. After normal curing, the flexural strengths of C1 and C2 are 26.4 and 24.0 MPa, respectively, indicating that the addition of fly ash also decreases the flexural strength. However, once subjected to autoclaving, the flexural strength of autoclaved C1 significantly decreases to 18.8 MPa (t-test, $p = 0.0022$, compared with normally cured C1), although its compressive strength is increased by autoclaving. A similar phenomenon was also reported in (Yazıcı et al., 2009; Chen et al., 2018; Yazıcı et al., 2013), probably because the bond strength of hydrates is decreased by long-term autoclaving due to the transformation of amorphous C-S-H into more ordered phases. The energy absorption capacity was calculated to evaluate the flexural toughness as shown in **Table 3**. It can be seen that normally cured C1 and C2 present comparable energy absorption capabilities (15.4 kN·mm and 15.7 kN·mm for normally cured C1 and C2, respectively). However, the energy absorption capacity of autoclaved C1 is significantly decreased to 13.2 kN·mm, consistent with the decrease of flexural strength after autoclaving. It seems that the mixture of C1 can ensure the robust compressive strength, but cannot prevent the detrimental effect on flexural properties caused by long-term autoclaving. Krakowiak et al. reported that the strength retrogression is associated with a change of the proportions of C-S-H gel and crystalline C-S-H in the matrix (Krakowiak et al., 2015).
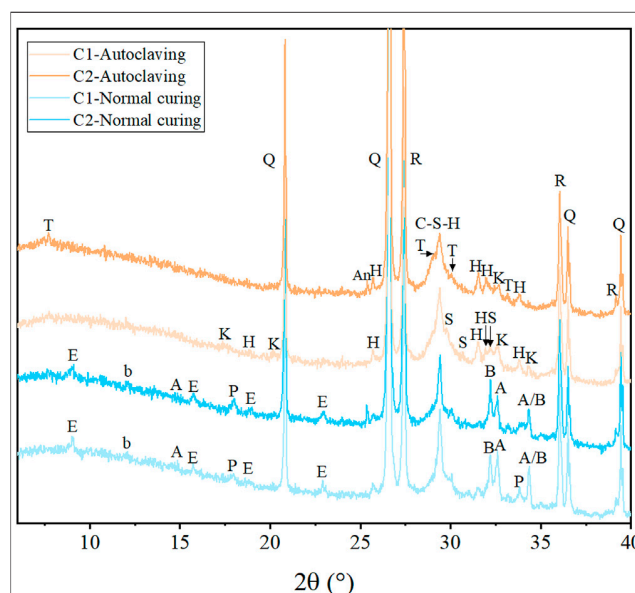
Interestingly, the addition of fly ash in autoclaved C2 increases the flexural strength to 24.8 MPa (t-test, $p = 0.0279$, compared with autoclaved C1; t-test, $p = 0.3243$, compared with normally cured C2), while the energy absorption capacity is also improved to 16.3 kN·mm. The results imply that the influence of long-term autoclaving on UHPC is highly related to the mixture composition. The partial replacement of cement by fly ash can mitigate the degradation of mechanical properties caused by long-term autoclaving. The similar effect was also reported in the literature (Abd Elrahman and Hillemeier 2015) that the addition of fly ash mitigates the strength degradation caused by long-term autoclaving. As the fly ash used in this study is rich in Si and Al, the partial replacement of cement by fly ash decreases the effective Ca/Si ratio in the matrix, leading to the C-S-H phases with a low Ca/Si ratio, associated with high mechanical strength. In addition to fly ash, metakaolin as a material rich in Si and Al is also studied in combination with cement and/or silica powder under hydrothermal conditions (Kuzielová 2018; Kuzielová et al., 2019). The increase of Al in the matrix can accelerate the formation of hydrogarnet. Such phase may degrade the microstructure and mechanical strength due to its high density. However, in the matrix with a low Ca/Si ratio, the addition of Al-rich materials can stabilize tobermorite at temperature above 150°C, which benefits mechanical strength (Eℓ-Hemaly et al., 1977; Biagioni et al., 2016; Chen et al., 2017). For example, the compressive strength of the Portland cement pastes is increased by the appropriate addition of metakaolin under hydrothermal conditions (Bu et al., 2016). However, the content of Al should be controlled because excessive Al, which exceeds the upper limit of the incorporation of Al into
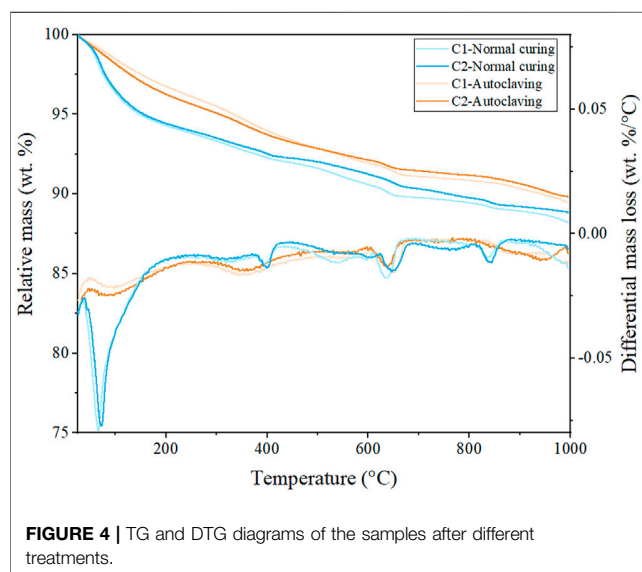
FIGURE 4 | TG and DTG diagrams of the samples after different treatments.

tobermorite, leads to the formation of hydrogarnet (Kyritsis et al., 2009a; Kyritsis et al., 2009b; Meller et al., 2009b). Therefore, the phases assemblage and microstructure are further discussed in the following sections.

3.2 XRD Analysis

The mineralogical compositions of the mixtures after different treatments are characterized by XRD, as shown in **Figure 3**. 10 wt % rutile was added as an internal standard to quantify the mineral content. However, due to the severe peak overlaps, the quantification result is unreliable and not presented here, but the rutile peaks can also work as an indicator to roughly estimate the phase evolution. For normal cured samples, the typical hydration products ettringite, portlandite, and amorphous C-S-H can be clearly identified. However, the hydrates in autoclaved samples are substantially changed. Both portlandite and ettringite disappear in autoclaved C1 and C2. Ettringite is known to be unstable at high temperatures and decompose with formation of phases like sulphate-AFm $Ca_4Al_2O_6(SO_4) \cdot 14H_2O$ and potentially bassanite $CaSO_4.0.5H_2O$, depending on the chemical composition of the matrix and the temperature-pressure conditions. At even higher temperatures, bassanite decomposes to anhydrite $CaSO_4$, and sulphate-AFm disappears, forming katoite $(Ca_3Al_2(SiO_4)_x (OH)_{4(3-x)}; 0 \leq x \leq 3)$ and sulphate-containing phases (Vladimír and Vepek 1975; Meller et al., 2009a). In this study, the peaks of katoite are identified in both autoclaved C1 and C2, while its intensity in autoclaved C1 is stronger than that in autoclaved C2. Besides, hydroxylellestadite $Ca_{10}(SiO_4)_3(SO_4)_3(OH)_2$ as a sulphate-containing phase forms in autoclaved samples, which the sulphate originates from the decomposition of ettringite (Sauman and Vavrin 1980; Vladimír 1992).

According to the C-S-H diagrams by Taylor (Taylor 1964), Hong and Glasser (Hong and Glasser 2004), and Meller et al. (Meller et al., 2005; Meller et al. 2009b; Meller et al. 2007), the initially formed amorphous C-S-H gel converts to crystalline

phases at hydrothermal conditions. The type and formation rate of newly formed crystalline phases vary with the temperature and the composition of raw materials. Scawtite $Ca_7(Si_6O_{18})$ $(CO_3) \cdot 2H_2O$, which is stable at 140–300 °C (Harker 1965), is observed in autoclaved C1. According to the SEM point element analysis (**Section 3.4**), the Ca/Si ratio of the hydrates in autoclaved C1 ranges between around 1.0–2.0, consistent with the formation of scawtite. In such chemical environment, crystalline C-S-H xonotlite is usually encountered at 200°C (Hong and Glasser 2004). However, there is no apparent signal of xonotlite identified in autoclaved C1, probably because the carbonation transforms xonotlite to scawtite (Nelson 1979; Eilers et al., 1983; Grabowski and Gillott 1989) and the densified UHPC matrix restricts the crystallization of xonotlite which is discussed later. It is reported that scawtite can strongly affect the matrix performance and cause brittleness (Berger 1979; Eilers et al., 1983). This may contribute to the low flexural strength of autoclaved C1.

Tobermorite as the only crystalline C-S-H phase is identified in autoclaved C2. The partial replacement of cement by Si-rich fly ash increases the ratio of silica to cement, leading to a reduced Ca/Si ratio, which favours tobermorite formation in autoclaved C2. This effect is further confirmed by SEM analysis in **Section 3.4**. Due to the reduced Ca/Si ratio in autoclaved C2, katoite decomposes as an important intermediate of tobermorite, which coincides with the result that the peaks of katoite in autoclaved C2 are weaker than that in autoclaved C1. Another intermediate of tobermorite under hydrothermal conditions is hydroxylellestadite (Matsui et al., 2011). Accordingly, anhydrite as a decomposition product of hydroxylellestadite is identified in autoclaved C2, indicating the transformation of hydroxylellestadite to tobermorite. Furthermore, the addition of fly ash increases the Al content in the matrix (see **Section 3.4**), and the incorporation of Al into tobermorite can improve its thermal stability, preventing the conversion of tobermorite to xonotlite and scawtite under long-term autoclaving (Shaw et al., 2000a; Hong and Glasser 2004). Compared with scawtite, katoite, and hydroxylellestadite, tobermorite has a low density and thus a high solid volume. The transformation of katoite and hydroxylellestadite to tobermorite and the prevention of tobermorite to scawtite densify the UHPC microstructure, benefiting the high mechanical strength of autoclaved C2. The benefiting effect of tobermorite on microstructure and mechanical strength is also confirmed in the fabrication of calcium silicate boards (Chen et al., 2017; Wang et al., 2019), autoclaved aerated concrete (Mitsuda et al., 1992; Shams et al., 2021), and well cementing (Nelson and Guillot 2006).

Except for the crystalline phases in autoclaved C1 and C2, a diffuse peak at ~29.4° 2θ is observed, indicating that the poorly crystallized C-S-H remains until the end of autoclaving without conversion to crystalline phases. The XRD peak broadening mainly originates from the small crystallite size and a low-ordered crystal structure (Young 2002). This phenomenon of poorly crystallized C-S-H remaining after autoclaving is also observed in the literature (Matsui et al., 2011; Krakowiak et al., 2018), which has two explanations. The high solid volume fraction of the matrix provides limited space for crystallization and restricts the transformation of poorly

FIGURE 5 | Element mapping of the autoclaved C1 **(A)** and C2 **(B)**.
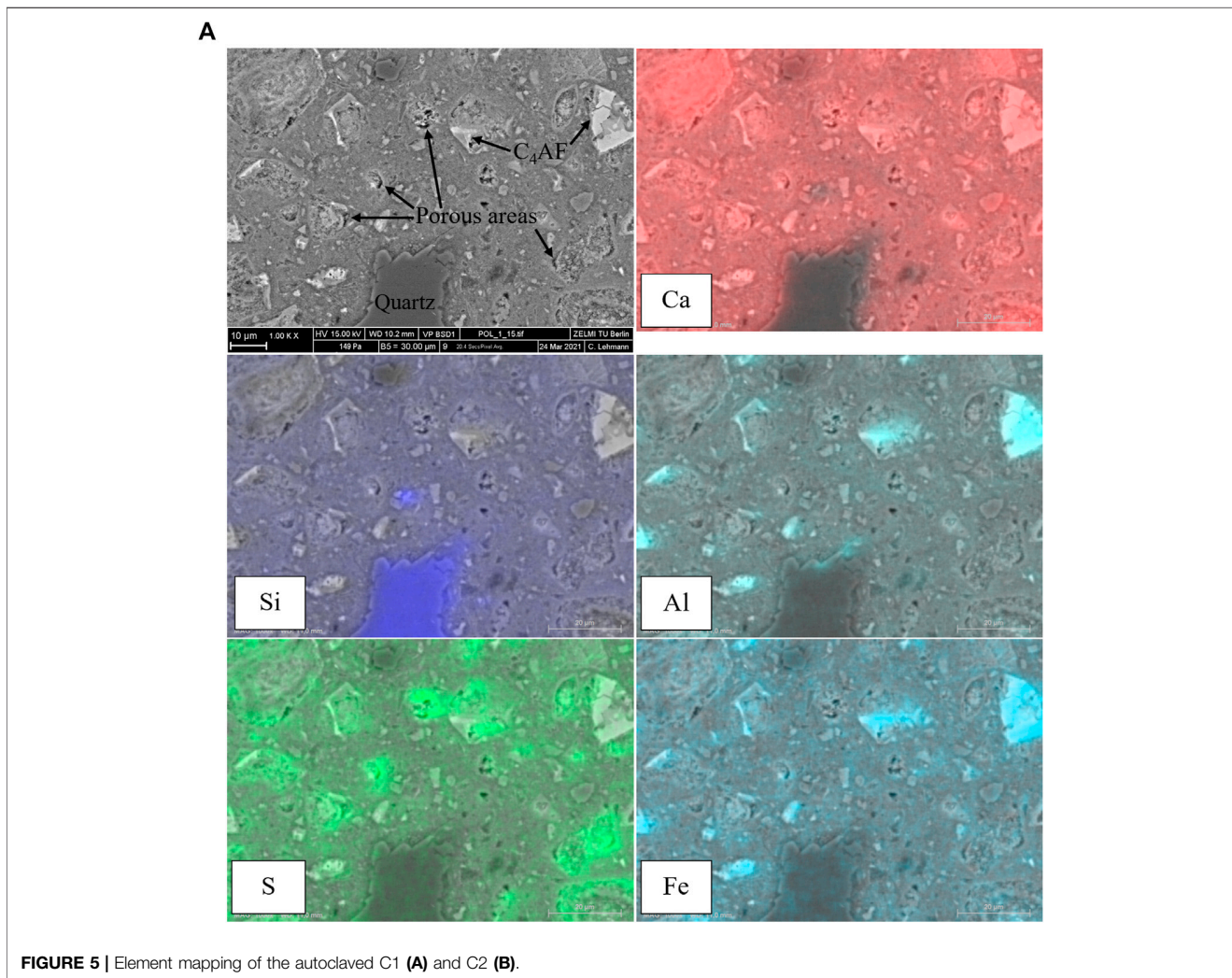
crystallized C-S-H into crystalline phases. Besides, the C-S-H precursor with Ca/Si < 1 contains long and cross-linked chains of silicate tetrahedra, which is relatively hard to transform into crystalline phases, as a larger number of bonds need to be reorganized compared to the C-S-H precursor with Ca/Si > 1 (Chen et al., 2004; Nonat 2004; Richardson 2004). In this study, the UHPC mixtures have a low w/b ratio and the densified microstructure of matrix provides insufficient space for crystallization, suppressing the transformation of poorly crystallized C-S-H to crystalline phases in autoclaved C1 and C2. This effect is infrequent in other hydrothermal conditions which the mixtures possess relatively higher w/b ratios (Abd Elrahman and Hillemeier 2015; Cheng et al., 2021). Furthermore, in autoclaved C2, the partial replacement of cement by fly ash decreases the Ca/Si ratio of the matrix and thus leads to the formation of C-S-H precursor with a low Ca/Si ratio which has less convertibility to crystalline phases. Therefore, compared with autoclaved C1, more poorly crystallized C-S-H is maintained in autoclaved C2, without conversion to crystalline phases, which strengthens the bond property and provides higher flexural strength. This effect is further discussed in **Section 3.3** and **Section 3.4** , considering the results of TG and SEM analysis.

3.3 TG Analysis
TG and DTG diagrams of the samples after different curing treatments are shown in **Figure 4**. For normally cured samples, the first peak up to ~230°C of the differential curve corresponds to the water loss in ettringite and C-S-H gel (Myers et al., 2015; Guo et al., 2017). The following small peak from around 260–370°C belongs to the dehydroxylation of aluminium hydroxide from ettringite columns. AFm (Al_2O_3-Fe_2O_3-monophase) also loses the layer water in this temperature range (Scrivener et al., 2016). The peak centred at ~400°C is assigned to the portlandite dehydroxylation, and the carbonate decomposition occurs at ~640°C. The last peak at ~840°C is related to the dehydroxylation and recrystallization of C-S-H to wollastonite ($Ca_3Si_3O_9$). It can be seen that the partial replacement of cement by fly ash slightly decreases the hydration products of ettringite and amorphous C-S-H in normally cured C2, which leads to the
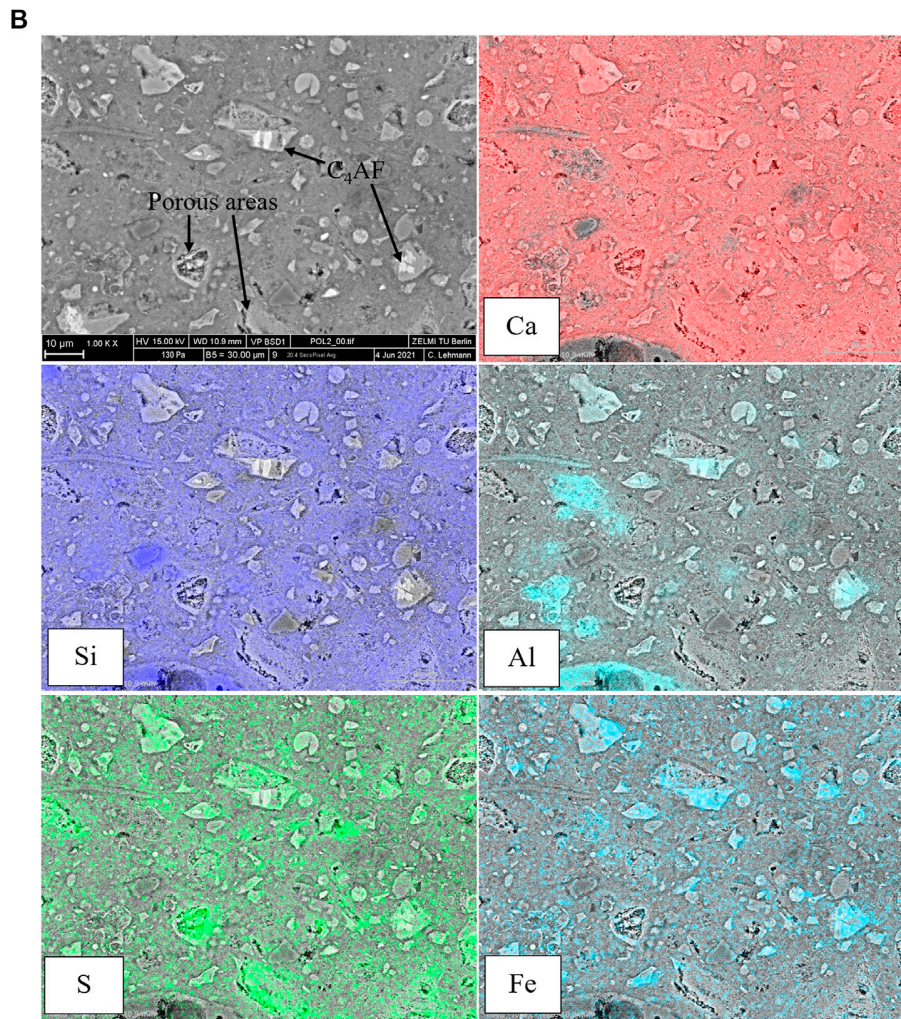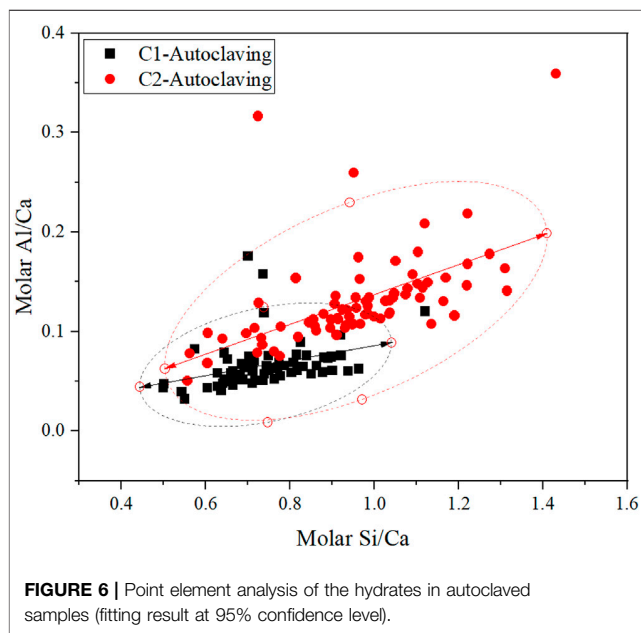
FIGURE 5 | (Continue)

relatively low mechanical strength of normally cured C2, compared with normally cured C1.

The signals of the autoclaved samples are quite different. The first water loss peak up to around 250°C significantly decreases. This is because ettringite decomposes under autoclaving condition and a part of the C-S-H gel transforms into more ordered phases, losing the excessive gel water after autoclaving. Furthermore, the water loss of autoclaved C2 in this temperature range is more significant than that of autoclaved C1. This is consistent with the discussion in **Section 3.2** that due to the partial replacement of cement by fly ash, more poorly crystallized C-S-H with a low Ca/Si ratio remains in autoclaved C2, providing more loosely bound water. It is reported that the fracture toughness is positively related to the specific surface area of the solid building blocks of the matrix (Krakowiak et al., 2015). The maintenance of a higher amount of poorly crystallized C-S-H in autoclaved C2 provides a higher specific surface area, leading to the enhanced flexural properties. Besides,

tobermorite formed in autoclaved C2 loses its four interlayer water molecules per formula unit between 50 and 250°C (Shaw et al., 2000b; Biagioni et al., 2016). The addition of fly ash increases the Al content in matrix, and the uptake of Al in C-S-H is thus accelerated, which may also increase the water content in C-(A-)S-H (Gartner et al., 2017). The sharp peak of portlandite dehydroxylation is not observed in autoclaved samples. Instead, a broad and flat peak from 250 to 600°C appears in both autoclaved C1 and C2. It is reported that the remaining molecular water of tobermorite (except the preceding four loosely bound water molecules) is lost in this temperature range (dehydroxylation process) (Shaw et al., 2000b; Biagioni et al., 2016). However, katoite decomposes at above 260°C (Rivas-Mercury et al., 2008), and scawtite decomposes at around 400°C (Marincea et al., 2001). Therefore, for autoclaved C1, the water loss from 250 to 600°C is mainly contributed by the decomposition of katoite and scawtite, while for autoclaved C2, the water loss in this temperature range mainly originates

FIGURE 6 | Point element analysis of the hydrates in autoclaved samples (fitting result at 95% confidence level).

FIGURE 7 | SEM images on the interface between steel fibres and the matrix of autoclaved C1 **(A)** and C2 **(B)**.

from the dehydroxylation of tobermorite. Interestingly, compared with autoclaved C2, autoclaved C1 presents a higher mass loss at ~640°C, which is probably due to the more calcite being decomposed from scawtite. The last broad peak from ~800°C to the end of heating is assigned to the C-S-H dehydroxylation in autoclaved C1 and C2, for which the temperature is higher than that in normally cured C1 and C2. Due to the pozzolanic reaction, the C-S-H formed in autoclaved samples possesses a lower Ca/Si ratio characterized by higher polymerization degree and longer silicate chains, requiring more energy to dehydroxylate and reorganize into wollastonite (Chen et al., 2004; Nonat 2004; Richardson 2004).

3.4 SEM Analysis

To further clarify the influence of the long-term autoclaving on UHPC, SEM element mapping is carried out. For autoclaved C1 (**Figure 5A**), a quartz particle with a blurred surface is observed, which is also reported in oil well cement systems (Palou et al., 2013; Krakowiak et al., 2015) and other kinds of cementitious products treated by hydrothermal curing (Peters et al., 1978; Rashad et al., 2012). Silica reactivity is proportional to its available surface area and crystallinity (Eilers and Nelson 1979; Matsui et al., 2011; Krakowiak et al., 2018). The presence of silica with high reactivity, e.g., silica fume, restricts the reaction of silica with low reactivity, e.g., quartz powder. In this study, the highly reacted surface of quartz particles indicates that the silica fume in UHPC probably has been exhausted by the active pozzolanic reaction under the long-term autoclaving.

On the other hand, some calcium aluminoferrite particles (marked as C_4AF) remain unhydrated after the long-term autoclaving, while no silicate clinker is observed, as confirmed by the XRD results. Due to the low w/b ratio in UHPC, cement hardly hydrates entirely at room temperature. However, during the long-term autoclaving, excessive gel water is released through the
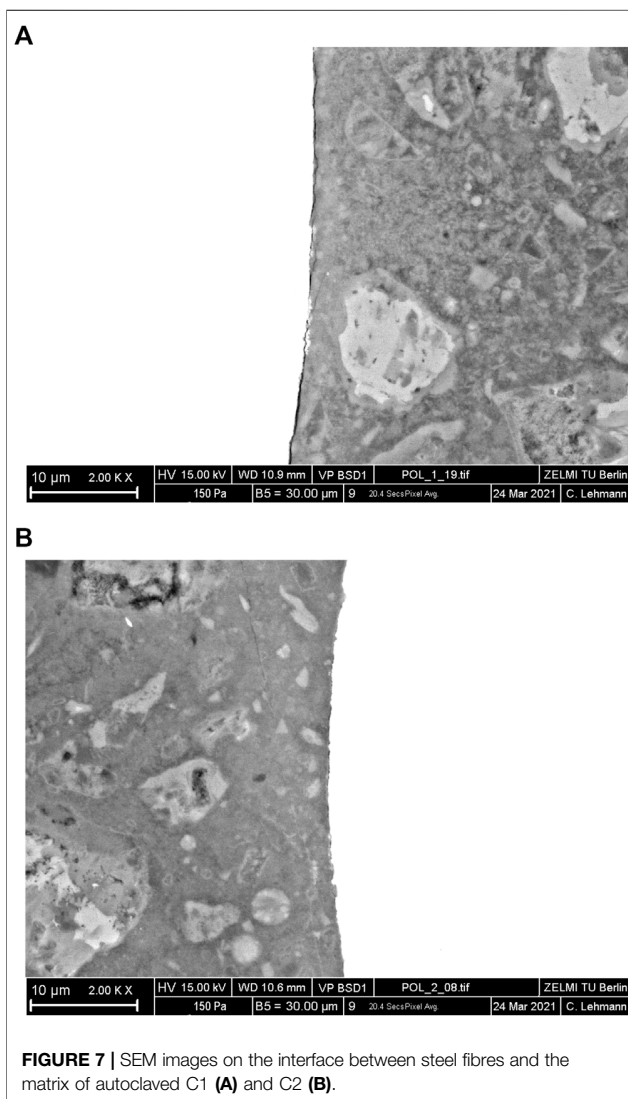
transformation of amorphous C-S-H into more ordered phases, and the clinker hydration can thus achieve a higher degree, compared with the normally cured samples. Aluminoferrite phase generally has fast kinetics under early hydration once in contact with water. Calcium sulphates, e.g., anhydrite and gypsum, can suppress its hydration, which are used to prevent premature stiffening. Possible suppression mechanisms are the adsorption of sulphate ions at active dissolution sites and the formation of sulphate-AFm around anhydrous particles (Ectors et al., 2013; Morin et al., 2017). In this study, sulphate-AFm is unstable under the long-term autoclaving condition, while a large amount of S still concentrates around the ferrite particles, as shown in S mapping (**Figure 5A**), which indicates that rather than sulphate-AFm, the newly formed sulphate-containing phase under the long-term autoclaving hinders the hydration of aluminoferrite phase. Furthermore, the retardation of aluminoferrite phase after heat curing is also reported in the literature (Yang and Sharp 2001), and a higher temperature exerts stronger retardation effect (20–100°C).
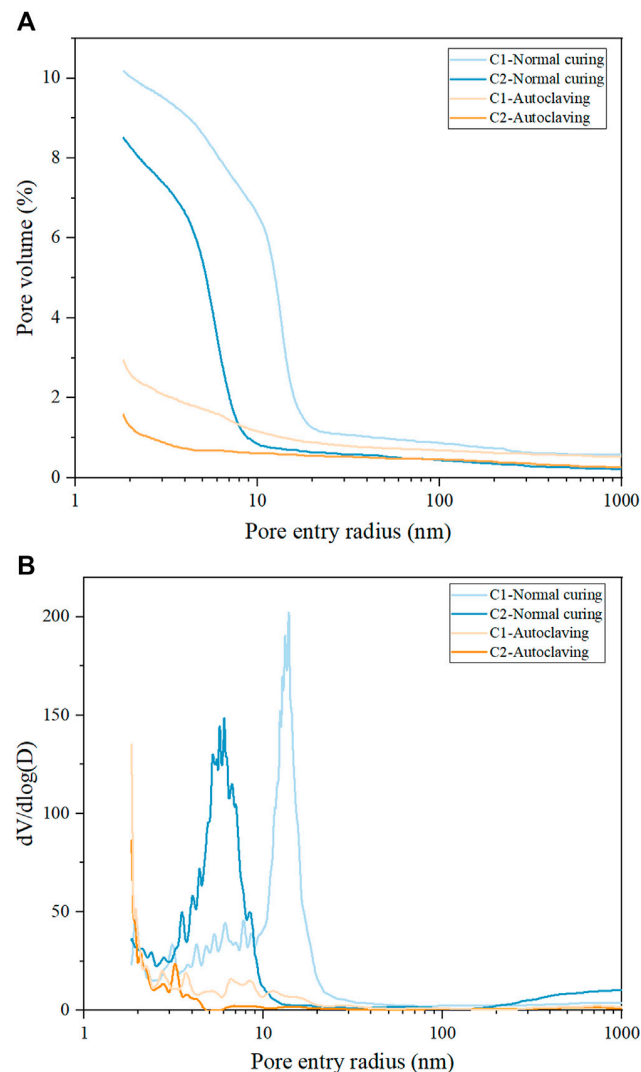
FIGURE 8 | Cumulative intrusion curves **(A)** and pore size distributions **(B)** obtained on the samples after different treatments.

Except for the aforementioned S concentrated around aluminoferrite particles, some S also accumulates in the areas that are initially occupied by other clinker phases and/or hydrates and then filled by the sulphate-containing phase, as shown in **Figure 5A**. According to the XRD results, the crystalline sulphate-containing phase is identified as hydroxylellestadite. However, it is reported that sulphate can be co-sorbed on the surface and interlayer of poorly crystallized C-S-H together with Ca^{2+} (Barbarulo et al., 2007) and inserted into the structure of crystalline C-S-H under hydrothermal conditions (Mostafa et al., 2009). Therefore, the sulphate-containing phase observed in S mapping could be a mixture of hydroxylellestadite and C-S-H incorporated with sulphate. Note that the areas filled by the sulphate-containing phase seem porous and leaky, which is probably due to the high density (low solid volume) of crystalline hydroxylellestadite. Thus, the persistence of hydroxylellestadite in autoclaved C1 may contribute to the low mechanical strength,

compared with autoclaved C2. As for Al mapping (**Figure 5A**), Al widely distributes in the matrix in addition to the part concentrated around aluminoferrite particles. This is because Al can also incorporate into C-S-H, and hydrothermal curing accelerates the incorporation (Andersen et al., 2006; Jupe et al., 2008; Matsui et al., 2011). Therefore, the widely distributed Al in the matrix mainly originates from the C-(A-)S-H and katoite (decomposition product of ettringite).

Unreacted aluminoferrite particles are also observed in autoclaved C2 (**Figure 5B**). According to S mapping, the sulphate-containing phase is again observed in autoclaved C2. Similarly, due to the high density (low solid volume) of hydroxylellestadite, the areas occupied by the sulphate-containing phase present porous and leaky. However, the partial replacement of cement by fly ash decreases the content of sulphate, suppressing the formation of hydroxylellestadite. This effect benefits the microstructure densification and thus the high

mechanical strength. Besides, the transformation of hydroxylellestadite together with silica to tobermorite increases the solid volume as tobermorite has a relatively low density, which also contributes to the high mechanical strength of autoclaved C2.

Element point analysis on the autoclaved samples is further conducted, as shown in **Figure 6**. The Si/Ca ratio of hydrates in autoclaved C1 ranges between around 0.5–1.0, consistent with the formation of scawtite as discussed in **Section 3.2**. The partial replacement of cement by fly ash increases the Si/Ca ratio in autoclaved C2, originating from the increased ratio of silica to cement and the introduced Si by fly ash. Compared with autoclaved C1, autoclaved C2 can thus generate the C-S-H precursor with a higher Si/Ca ratio, which has lower convertibility to crystalline phases. Therefore, more poorly crystallized C-S-H with a high Si/Ca ratio can persist in autoclaved C2 after the long-term autoclaving, improving the microstructure and mechanical strength. Note that the Si/Ca ratio of the tobermorite solid solution is between 1.2 and 1.5 (Biagioni et al., 2015), consistent with the increased Si/Ca ratio of autoclaved C2 as shown in **Figure 6**. Besides, compared with autoclaved C1, the Al/Ca ratio of autoclaved C2 is also increased, indicating that the Al-rich fly ash can actively participate in the hydrates formation.

The interface between steel fibres and matrix was further observed, as shown in **Figure 7**. A clear interstice appears between the steel fibres and matrix in autoclaved C1 (**Figure 7A**). XRD and TG results confirmed that the C-S-H gel converts to more ordered phases, losing the excessive gel water and resulting in solid volume shrinkage. Furthermore, more katoite and scawtite formation in autoclaved C1 also contributes to the decrease of solid volume, which leads to the undensified interface between steel fibres and matrix. However, autoclaved C2 presents a denser interface between steel fibres and matrix (**Figure 7B**). This is because more poorly crystallized C-S-H with a low Ca/Si ratio remains in autoclaved C2, mitigating the degradation of matrix bonding and the solid volume shrinkage. Besides, the formation of Al-stabilized tobermorite through the decomposition of hydroxylellestadite and katoite in autoclaved C2 can increase the solid volume, which benefits the microstructure densification.

3.5 Pore Structure Analysis

The cumulative porosity curves and pore size distributions of the samples after different treatments are shown in **Figure 8**. Compared with normally cured samples, the porosities of autoclaved C1 and C2 are significantly decreased by the long-term autoclaving (**Figure 8A**). According to the literature (Matsui et al., 2011; Krakowiak et al., 2018), large crystals with a high density and crystallinity are usually observed in the mixtures with a high w/b ratio and low solid volume fraction after hydrothermal treatment, accompanied by the reported pore coarsening phenomenon. In this study, the transformation of amorphous C-S-H to crystalline phases is also confirmed. However, in the UHPC with a quite low w/b ratio and dense microstructure, the limited space suppresses the crystallization, leading to poorly crystallized C-S-H without conversion to crystalline phases. Furthermore, the typical UHPC components silica fume and quartz powder are further activated by the long-term autoclaving, generating additional C-S-H, filling the porosity, and densifying the microstructure. Therefore, compared

with the normally cured samples, the critical pore entry radii of autoclaved C1 and C2 are also shifted to lower values, as shown in the curves of pore size distribution (**Figure 8B**). However, this phenomenon is not observed in other hydrothermally cured mixtures with relatively higher w/b ratios, such as that the porosities and gel pores of the blended cement pastes with metakaolin, fly ash, or silica fume increase after hydrothermal curing (150/165/200°C) (Kuzielová et al., 2017; Kuzielová 2018). The quite low w/b ratio and the high amount of silica component favors the microstructure densification of UHPC after long-term autoclaving.

Interestingly, the porosity of autoclaved C2 is lower than that of autoclaved C1. According to the pore size distribution curve, the pore volume of autoclaved C2 is dominated by gel porosity, assuming 10 nm as the dividing value between gel and capillary pores (Berodier and Scrivener 2015; Durdziński et al., 2017). As confirmed by SEM, the partial replacement of cement by fly ash provides additional Si and increases the ratio of silica to cement, resulting in more poorly crystallized C-S-H with Ca/Si < 1. This kind of C-S-H is hard to transform into crystalline phases under autoclaving, which provides more solid volume and prevents the increase of porosity. Therefore, gel pores dominate in the microstructure of autoclaved C2, which mainly originates from the fine internal porosity of hydrates. However, compared with autoclaved C2, a larger fraction of the pores from 3 to 40 nm is shown in the differential curve of autoclaved C1. This part of pores contains gel and capillary porosity, probably because more crystalline hydrates of scawtite, hydroxylellestadite, and katoite form in autoclaved C1, leading to the shrinkage of solid volume.

It is interesting to point out that there is no strict correlation between porosity and mechanical strength for the UHPC under the long-term autoclaving. Compared with normally cured C1, the porosity of autoclaved C1 is significantly decreased, but the flexural strength of autoclaved C1 is far lower than that of normal cured C1. It seems that the type of hydrates can strongly affect the flexural strength. Under the long-term autoclaving, amorphous C-S-H with high bond strength converts to more ordered phases accompanied by bond degradation. This is further confirmed by the result that more poorly crystallized C-S-H is maintained in autoclaved C2 and autoclaved C2 thus presents high flexural strength. However, the compressive strength of autoclaved C1 and C2 can stay robust under the long-term autoclaving. Compared with normally cured C1 and C2, more hydrate formation in autoclaved C1 and C2 builds the solid skeleton, benefiting the compressive strength. Compared with autoclaved C1, the persistence of more poorly crystallized C-S-H with low Ca/Si and tobermorite in autoclaved C2 ensures the higher compressive strength.

4 CONCLUSION

The influence of long-term autoclaving at 200°C with saturated pressure on the mechanical properties and microstructure of UHPC was studied. For the UHPC with typical components (silica fume, cement, quartz powder and quartz sand), the compressive strength of autoclaved C1 is increased by long-

term autoclaving, compared with that of normally cured C1. However, the flexural strength of autoclaved C1 is significantly decreased. The transformation of amorphous C-S-H to more ordered phases and the formation of katoite and hydroxylellestadite degrades the microstructure, leading to the reduced flexural strength and undensified interface between steel fibres and matrix. However, compared with normally cured C1, autoclaved C1 presents a finer texture and lower porosity, benefiting from the quite low w/b ratio and high amount of silica. Therefore, it is concluded that there is no strict correlation between the porosity and flexural strength of UHPC under long-term autoclaving, and the effect of hydrates assemblage outweighs that of porosity concerning flexural strength.

The partial replacement of cement by fly ash ensures autoclaved C2 superior compressive and flexural strength. The incorporation of fly ash increases the ratio of silica to cement, leading to more poorly crystallized C-S-H with a low Ca/Si ratio. The addition of fly ash also provides additional Al, which accelerates and stabilizes tobermorite at the expense of katoite and hydroxylellestadite under long-term autoclaving. The maintenance of poorly crystallized C-S-H (without conversion to crystalline phases) and the formation of tobermorite contribute to the densified microstructure and the enhanced mechanical strength of autoclaved C2. Autoclaved C2 thus presents a lower porosity and finer texture than autoclaved C1.

The influence of long-term autoclaving is highly related to the UHPC compositions. Due to the quite low w/b ratio and the typical components of silica fume and quartz powder, the compressive strength of UHPC can stay robust under long-term autoclaving, but exceptional attention should be paid to flexural properties. For designing UHPC working under autoclaving, the accelerated hydrothermal reactions by autoclaving should also be considered, as the traditional design rules are mainly based on the physical properties of the raw materials, aiming at a compact packing. Given the appropriate flowability, a low w/b ratio or high solid volume fraction is preferred to restrict the C-S-H transformation to crystalline phases. Additional silica, probably silica-rich SCMs of silica fume or fly ash, may be needed to maintain the poorly crystallized C-S-H with a low Ca/Si ratio under autoclaving. As for future research, permeability as an important indicator of durability is of particular concern and could be a complicated topic as the transportation of water and gas under autoclaving is quite different from that under normal conditions.

DATA AVAILABILITY STATEMENT

The original contributions presented in the study are included in the article/Supplementary Material, further inquiries can be directed to the corresponding author.

AUTHOR CONTRIBUTIONS

HT conceived and performed the experiments and wrote the manuscript. All authors participated in discussion of the research and contributed to the manuscript revision.

FUNDING

ACKNOWLEDGMENTS

REFERENCES

Abd Elrahman, M., and Hillemeier, B. (2015). Influence of Hydrothermal Conditions with 200°C and 15.5bars on the Properties of Hardened HPC. *Construction Building Mater.* 85, 38–48. doi:10.1016/j.conbuildmat.2015.03.027

Ahmad, S., Rasul, M., Adekunle, S. K., Al-Dulaijan, S. U., Maslehuddin, M., and Ali, S. I. (2019). Mechanical Properties of Steel Fiber-Reinforced UHPC Mixtures Exposed to Elevated Temperature: Effects of Exposure Duration and Fiber Content. *Composites B: Eng.* 168, 291–301. doi:10.1016/j.compositesb.2018.12.083

Aldahdooh, M. A. A., Muhamad Bunnori, N., and Megat Johari, M. A. (2013). Development of green Ultra-high Performance Fiber Reinforced concrete Containing Ultrafine palm Oil Fuel Ash. *Construction Building Mater.* 48, 379–389. doi:10.1016/j.conbuildmat.2013.07.007

Alva, G., Liu, L., Huang, X., and Fang, G. (2017). Thermal Energy Storage Materials and Systems for Solar Energy Applications. *Renew. Sustain. Energ. Rev.* 68, 693–706. doi:10.1016/j.rser.2016.10.021

Andersen, M. D., Jakobsen, H. J., and Skibsted, J. (2006). A New Aluminium-Hydrate Species in Hydrated Portland Cements Characterized by 27Al and 29Si MAS NMR Spectroscopy. *Cement Concrete Res.* 36, 3–17. doi:10.1016/j.cemconres.2005.04.010

Arora, A., Aguayo, M., Hansen, H., Castro, C., Federspiel, E., Mobasher, B., et al. (2018). Microstructural Packing- and Rheology-Based Binder Selection and Characterization for Ultra-high Performance Concrete (UHPC). *Cement Concrete Res.* 103, 179–190. doi:10.1016/j.cemconres.2017.10.013

Arora, A., Almujaddidi, A., Kianmofrad, F., Mobasher, B., and Neithalath, N. (2019). Material Design of Economical Ultra-high Performance concrete (UHPC) and Evaluation of Their Properties. *Cement and Concrete Composites* 104, 103346. doi:10.1016/j.cemconcomp.2019.103346

Barbarulo, R., Peycelon, H., and Leclercq, S. (2007). Chemical Equilibria between C-S-H and Ettringite, at 20 and 85 °C. *Cement Concrete Res.* 37, 1176–1181. doi:10.1016/j.cemconres.2007.04.013

Bauer, D., Marx, R., Nußbicker-Lux, J., Ochs, F., Heidemann, W., and Müller-Steinhagen, H. (2010). German central Solar Heating Plants with Seasonal Heat Storage. *Solar Energy* 84, 612–623. doi:10.1016/j.solener.2009.05.013

Berger, R. L. (1979). Stabilization of Silicate Structures by Carbonation. *Cement Concrete Res.* 9, 649–651. doi:10.1016/0008-8846(79)90150-9

Berodier, E., and Scrivener, K. (2015). Evolution of Pore Structure in Blended Systems. *Cement Concrete Res.* 73, 25–35. doi:10.1016/j.cemconres.2015.02.025

Biagioni, C., Bonaccorsi, E., Lezzerini, M., and Merlino, S. (2016). Thermal Behaviour of Al-Rich Tobermorite. *ejm* 28, 23–32. doi:10.1127/ejm/2015/0027-2499

Biagioni, C., Merlino, S., and Bonaccorsi, E. (2015). The Tobermorite Supergroup: a New Nomenclature. *Mineralogical Mag.* 79, 485–495. doi:10.1180/minmag.2015.079.2.22

Bu, Y., Du, J., Guo, S., Liu, H., and Huang, C. (2016). Properties of Oil Well Cement with High Dosage of Metakaolin. *Construction Building Mater.* 112, 39–48. doi:10.1016/j.conbuildmat.2016.02.173

91

Chang, W., and Zheng, W. (2020). Effects of Key Parameters on Fluidity and Compressive Strength of Ultra-high Performance concrete. *Struct. Concrete* 21, 747–760. doi:10.1002/suco.201900167

Chen, J. J., Thomas, J. J., Taylor, H. F. W., and Jennings, H. M. (2004). Solubility and Structure of Calcium Silicate Hydrate. *Cement Concrete Res.* 34, 1499–1519. doi:10.1016/j.cemconres.2004.04.034

Chen, M., Lu, L., Wang, S., Zhao, P., Zhang, W., and Zhang, S. (2017). Investigation on the Formation of Tobermorite in Calcium Silicate Board and its Influence Factors under Autoclaved Curing. *Construction Building Mater.* 143, 280–288. doi:10.1016/j.conbuildmat.2017.03.143

Chen, T., Gao, X., and Ren, M. (2018). Effects of Autoclave Curing and Fly Ash on Mechanical Properties of Ultra-high Performance concrete. *Construction Building Mater.* 158, 864–872. doi:10.1016/j.conbuildmat.2017.10.074

Chen, Y., Matalkah, F., Soroushian, P., Weerasiri, R., and Balachandra, A. (2019). Optimization of Ultra-high Performance concrete, Quantification of Characteristic Features. *Cogent Eng.* 6, 1558696. doi:10.1080/23311916.2018.1558696

Cheng, X., Yang, X., Zhang, C., Gao, X., Yu, Y., Mei, K., et al. (2021). Effect of Red Mud Addition on Oil Well Cement at High Temperatures. *Adv. Cement Res.* 33, 28–38. doi:10.1680/jadcr.18.00224

Colston, S. L., Barnes, P., Jupe, A. C., Jacques, S. D. M., Hall, C., Livesey, P., et al. (2005). An *In Situ* Synchrotron Energy-Dispersive Diffraction Study of the Hydration of Oilwell Cement Systems under High Temperature/autoclave Conditions up to 130 °C. *Cement Concrete Res.* 35, 2223–2232. doi:10.1016/j.cemconres.2004.09.005

Dong, Z., Wu, G., Zhao, X.-L., Zhu, H., and Shao, X. (2019). Behaviors of Hybrid Beams Composed of Seawater Sea-Sand concrete (SWSSC) and a Prefabricated UHPC Shell Reinforced with FRP Bars. *Construction Building Mater.* 213, 32–42. doi:10.1016/j.conbuildmat.2019.04.059

Durdziński, P. T., Ben Haha, M., Zajac, M., and Scrivener, K. L. (2017). Phase Assemblage of Composite Cements. *Cement Concrete Res.* 99, 172–182. doi:10.1016/j.cemconres.2017.05.009

Ectors, D., Neubauer, J., and Goetz-Neunhoeffer, F. (2013). The Hydration of Synthetic Brownmillerite in Presence of Low Ca-Sulfate Content and Calcite Monitored by Quantitative In-Situ-XRD and Heat Flow Calorimetry. *Cement Concrete Res.* 54, 61–68. doi:10.1016/j.cemconres.2013.08.011

Eilers, L. H., and Nelson, E. B. (1979). "Effect of Silica Particle Size on Degradation of Silica Stabilized portland Cement," in SPE Oilfield and Geothermal Chemistry Symposium, Houston, Texas, 1979-01-22 (Houston, TX: Society of Petroleum Engineers). doi:10.2118/7875-MS

Eilers, L. H., Nelson, E. B., and Moran, L. K. (1983). High-temperature Cement Compositions-Pectolite, Scawtite, Truscottite, or Xonotlite: Which Do You Want? *J. Pet. Technol.* 35 (07), 1,373–1,377. doi:10.2118/9286-pa

Eł-Hemaly, S., Mitsuda, T., and Taylor, H. (1977). Synthesis of normal and Anomalous Tobermorites. *Cement Concrete Res.* 7, 429–438. doi:10.1016/0008-8846(77)90071-0

Fehling, E., Schmidt, M., Walraven, J. C., Leutbecher, T., and Fröhlich, S. (2014). *Ultra-high Performance concrete UHPC: Fundamentals - Design - Examples (BetonKalender)*. Berlin: Ernst & Sohn.

Feldman, R. F., Carette, G. G., and Malhotra, V. M. (1990). Studies on Mechanics of Development of Physical and Mechanical Properties of High-Volume Fly Ash-Cement Pastes. *Cement and Concrete Composites* 12, 245–251. doi:10.1016/0958-9465(90)90003-G

Funk, J. E., and Dinger, D. (1993). *Predictive Process Control of Crowded Particulate Suspensions: Applied to Ceramic Manufacturing*. Berlin, Germany: Springer Science & Business Media.

Garas, V. Y., Kurtis, K. E., and Kahn, L. F. (2012). Creep of UHPC in Tension and Compression: Effect of thermal Treatment. *Cement and Concrete Composites* 34, 493–502. doi:10.1016/j.cemconcomp.2011.12.002

Gartner, E., Maruyama, I., and Chen, J. (2017). A New Model for the C-S-H Phase Formed during the Hydration of Portland Cements. *Cement Concrete Res.* 97, 95–106. doi:10.1016/j.cemconres.2017.03.001

Glasser, F. P., and Hong, S.-Y. (2003). Thermal Treatment of C-S-H Gel at 1 Bar H2O Pressure up to 200 °C. *Cement Concrete Res.* 33 (2), 271–279. doi:10.1016/s0008-8846(02)00959-6

Grabowski, E., and Gillott, J. E. (1989). Effect of Replacement of Silica Flour with Silica Fume on Engineering Properties of Oilwell Cements at normal and Elevated Temperatures and Pressures. *Cement Concrete Res.* 19, 333–344. doi:10.1016/0008-8846(89)90023-9

Guo, X., Meng, F., and Shi, H. (2017). Microstructure and Characterization of Hydrothermal Synthesis of Al-Substituted Tobermorite. *Construction Building Mater.* 133, 253–260. doi:10.1016/j.conbuildmat.2016.12.059

Harker, R. I. (1965). Scawtite and its Synthesis. *Mineral. Mag. J. Mineral. Soc.* 34, 232–236. doi:10.1180/minmag.1965.034.268.18

Hassan, M., and Wille, K. (2018). Comparative Experimental Investigations on the Compressive Impact Behavior of Fiber-Reinforced Ultra High-Performance Concretes Using Split Hopkinson Pressure Bar. *Construction Building Mater.* 191, 398–410. doi:10.1016/j.conbuildmat.2018.10.020

Heller, A. (2000). 15 Years of R&D in central Solar Heating in Denmark. *Solar Energy* 69, 437–447. doi:10.1016/S0038-092X(00)00118-3

Hong, S.-Y., and Glasser, F. P. (2004). Phase Relations in the CaO-SiO2-H2o System to 200 °C at Saturated Steam Pressure. *Cement Concrete Res.* 34, 1529–1534. doi:10.1016/j.cemconres.2003.08.009

Huang, H., Wang, R., and Gao, X. (2019). Improvement Effect of Fiber Alignment on Resistance to Elevated Temperature of Ultra-high Performance concrete. *Composites Part B: Eng.* 177, 107454. doi:10.1016/j.compositesb.2019.107454

Jupe, A. C., Wilkinson, A. P., Luke, K., and Funkhouser, G. P. (2008). Class H Cement Hydration at 180 °C and High Pressure in the Presence of Added Silica. *Cement Concrete Res.* 38, 660–666. doi:10.1016/j.cemconres.2007.12.004

Kovács, R. (1975). Effect of the Hydration Products on the Properties of Fly-Ash Cements. *Cement Concrete Res.* 5, 73–82. doi:10.1016/0008-8846(75)90109-X

Krakowiak, K. J., Thomas, J. J., James, S., Abuhaikal, M., and Ulm, F.-J. (2018). Development of Silica-Enriched Cement-Based Materials with Improved Aging Resistance for Application in High-Temperature Environments. *Cement Concrete Res.* 105, 91–110. doi:10.1016/j.cemconres.2018.01.004

Krakowiak, K. J., Thomas, J. J., Musso, S., James, S., Akono, A.-T., and Ulm, F.-J. (2015). Nano-chemo-mechanical Signature of Conventional Oil-Well Cement Systems: Effects of Elevated Temperature and Curing Time. *Cement Concrete Res.* 67, 103–121. doi:10.1016/j.cemconres.2014.08.008

Kuzielová, E., Žemlička, M., Másilko, J., and Palou, M. T. (2019). Development of G-Oil Well Cement Phase Composition during Long Term Hydrothermal Curing. *Geothermics* 80, 129–137. doi:10.1016/j.geothermics.2019.03.002

Kuzielová, E., Žemlička, M., Másilko, J., and Palou, M. T. (2017). Pore Structure Development of Blended G-Oil Well Cement Submitted to Hydrothermal Curing Conditions. *Geothermics* 68, 86–93. doi:10.1016/j.geothermics.2017.03.001

Kuzielová, E., Žemlička, M., Másilko, J , et al.Žemlička, M., Másilko, J., Palou, M. T. (2018). Effect of Additives on the Performance of Dyckerhoff Cement, Class G, Submitted to Simulated Hydrothermal Curing. *J. Therm. Anal. Calorim.* 133, 63–76. doi:10.1007/s10973-017-6806-2

Kyritsis, K., Hall, C., Bentz, D. P., Meller, N., and Wilson, M. A. (2009a). Relationship between Engineering Properties, Mineralogy, and Microstructure in Cement-Based Hydroceramic Materials Cured at 200°-350°C. *J. Am. Ceram. Soc.* 92, 694–701. doi:10.1111/j.1551-2916.2008.02914.x

Kyritsis, K., Meller, N., and Hall, C. (2009b). Chemistry and Morphology of Hydrogarnets Formed in Cement-Based CASH Hydroceramics Cured at 200° to 350°C. *J. Am. Ceram. Soc.* 92, 1105–1111. doi:10.1111/j.1551-2916.2009.02958.x

Lee, N. K., Koh, K. T., Kim, M. O., and Ryu, G. S. (2018). Uncovering the Role of Micro Silica in Hydration of Ultra-high Performance concrete (UHPC). *Cement Concrete Res.* 104, 68–79. doi:10.1016/j.cemconres.2017.11.002

Li, L. G., Feng, J. J., Lu, Z. C., Xie, H. Z., Xiao, B. F., Kwan, A. K. H., et al. (2022). Effects of Aggregate Bulking and Film Thicknesses on Water Permeability and Strength of Pervious concrete. *Powder Technol.* 396, 743–753. doi:10.1016/j.powtec.2021.11.019

Liu, J.-C., and Tan, K. H. (2018). Mechanism of PVA Fibers in Mitigating Explosive Spalling of Engineered Cementitious Composite at Elevated Temperature. *Cement and Concrete Composites* 93, 235–245. doi:10.1016/j.cemconcomp.2018.07.015

Mangold, D. (2007). Seasonal Storage–A German success story. *Sun & Wind Energy* 1, 48–58.

Marincea, S., Bilal, E., Verkaeren, J., Pascal, M.-L., and Fonteilles, M. (2001). Superposed Parageneses in the Spurrite-, Tilleyite-And Gehlenite-Bearing Skarns from Cornet Hill, Apuseni Mountains, Romania. *Can. Mineral.* 39 (5), 1435–1453. doi:10.2113/gscanmin.39.5.1435

92

Matsui, K., Kikuma, J., Tsunashima, M., Ishikawa, T., Matsuno, S.-Y., Ogawa, A., et al. (2011). *In Situ* time-resolved X-ray Diffraction of Tobermorite Formation in Autoclaved Aerated concrete: Influence of Silica Source Reactivity and Al Addition. *Cement Concrete Res.* 41, 510–519. doi:10.1016/j.cemconres.2011.01.022

Matte, V., and Moranville, M. (1999). Durability of Reactive Powder Composites: Influence of Silica Fume on the Leaching Properties of Very Low Water/binder Pastes. *Cement and Concrete Composites* 21 (1), 1–9. doi:10.1016/s0958-9465(98)00025-0

Meller, N., Hall, C., Kyritsis, K., and Giriat, G. (2007). Synthesis of Cement Based CaO-Al2O3-SiO2-H2o (CASH) Hydroceramics at 200 and 250 °C: *Ex-Situ* and *In-Situ* Diffraction. *Cement Concrete Res.* 37 (6), 823–833. doi:10.1016/j.cemconres.2007.03.006

Meller, N., Hall, C., and Phipps, J. S. (2005). A New Phase Diagram for the CaOAl2O3SiO2H2O Hydroceramic System at 200°C. *Mater. Res. Bull.* 40, 715–723. doi:10.1016/j.materresbull.2005.03.001

Meller, N., Kyritsis, K., and Hall, C. (2009a). The Hydrothermal Decomposition of Calcium Monosulfoaluminate 14-hydrate to Katoite Hydrogarnet and β-anhydrite: An *In-Situ* Synchrotron X-ray Diffraction Study. *J. Solid State. Chem.* 182, 2743–2747. doi:10.1016/j.jssc.2009.07.029

Meller, N., Kyritsis, K., and Hall, C. (2009b). The Mineralogy of the CaO-Al2O3-SiO2-H2o (CASH) Hydroceramic System from 200 to 350 °C. *Cement Concrete Res.* 39, 45–53. doi:10.1016/j.cemconres.2008.10.002

Missemer, L., Ouedraogo, E., Malecot, Y., Clergue, C., and Rogat, D. (2019). Fire Spalling of Ultra-high Performance concrete: From a Global Analysis to Microstructure Investigations. *Cement Concrete Res.* 115, 207–219. doi:10.1016/j.cemconres.2018.10.005

Mitsuda, T., Sasaki, K., and Ishida, H. (1992). Phase Evolution during Autoclaving Process of Aerated concrete. *J. Am. Ceram. Soc.* 75, 1858–1863. doi:10.1111/j.1151-2916.1992.tb07208.x

Morin, V., Termkhajornkit, P., Huet, B., and Pham, G. (2017). Impact of Quantity of Anhydrite, Water to Binder Ratio, Fineness on Kinetics and Phase Assemblage of Belite-Ye'elimite-Ferrite Cement. *Cement Concrete Res.* 99, 8–17. doi:10.1016/j.cemconres.2017.04.014

Mostafa, N. Y., Shaltout, A. A., Omar, H., and Abo-El-Enein, S. A. (2009). Hydrothermal Synthesis and Characterization of Aluminium and Sulfate Substituted 1.1nm Tobermorites. *J. Alloys Compd.* 467, 332–337. doi:10.1016/j.jallcom.2007.11.130

Myers, R. J., L'Hôpital, E., Provis, J. L., and Lothenbach, B. (2015). Effect of Temperature and Aluminium on Calcium (Alumino)silicate Hydrate Chemistry under Equilibrium Conditions. *Cement Concrete Res.* 68, 83–93. doi:10.1016/j.cemconres.2014.10.015

Nelson, E. B. (1979). Development of Geothermal-Well-Completion Systems. *Final Rep. (Doe/et/28324-9)*. Available at: https://digital.library.unt.edu/ark:/67531/metadc1103485/.

Nelson, E. B., and Guillot, D. (2006). "Well Cementing," in *Developments in Petroleum Science*. 2nd ed. (Sugar Land, Tex: Schlumberger), Vol. 28.

Nonat, A. (2004). The Structure and Stoichiometry of C-S-H. *Cement Concrete Res.* 34, 1521–1528. doi:10.1016/j.cemconres.2004.04.035

Palou, M., Živica, V., Ifka, T., Boháč, M., and Zmrzlý, M. (2013). Effect of Hydrothermal Curing on Early Hydration of G-Oil Well Cement. *J. Therm. Anal. Calorim.* 116, 597–603. doi:10.1007/s10973-013-3511-7

Papanicolaou, E., and Belessiotis, V. (2009). Transient Development of Flow and Temperature fields in an Underground thermal Storage Tank under Various Charging Modes. *Solar Energy* 83, 1161–1176. doi:10.1016/j.solener.2009.01.017

Park, J.-J., Yoo, D.-Y., Kim, S., and Kim, S.-W. (2019). Benefits of Synthetic Fibers on the Residual Mechanical Performance of UHPFRC after Exposure to ISO Standard Fire. *Cement and Concrete Composites* 104, 103401. doi:10.1016/j.cemconcomp.2019.103401

Park, S. H., Kim, D. J., Ryu, G. S., and Koh, K. T. (2012). Tensile Behavior of Ultra High Performance Hybrid Fiber Reinforced Concrete. *Cement and Concrete Composites* 34, 172–184. doi:10.1016/j.cemconcomp.2011.09.009

Peters, T., Iberg, R., and Mumenthaler, T. (1978). Comparative Study of the Use of a Quartz Poor Sand and a Pure Quartz Sand for Lime Silica Bricks and the Kinetics of the Hydrothermal Hardening Mechanism. *Cement Concrete Res.* 8, 415–424. doi:10.1016/0008-8846(78)90021-2

Pourfalah, S. (2018). Behaviour of Engineered Cementitious Composites and Hybrid Engineered Cementitious Composites at High Temperatures.

Construction Building Mater. 158, 921–937. doi:10.1016/j.conbuildmat.2017.10.077

Rashad, A. M., Zeedan, S. R., and Hassan, H. A. (2012). A Preliminary Study of Autoclaved Alkali-Activated Slag Blended with Quartz Powder. *Construction Building Mater.* 33, 70–77. doi:10.1016/j.conbuildmat.2011.12.104

Richard, P., and Cheyrezy, M. (1995). Composition of Reactive Powder Concretes. *Cement Concrete Res.* 25 (7), 1501–1511. doi:10.1016/0008-8846(95)00144-2

Richardson, I. G. (2004). Tobermorite/jennite- and Tobermorite/calcium Hydroxide-Based Models for the Structure of C-S-H: Applicability to Hardened Pastes of Tricalcium Silicate, β-dicalcium Silicate, Portland Cement, and Blends of Portland Cement with Blast-Furnace Slag, Metakaolin, or Silica Fume. *Cement Concrete Res.* 34, 1733–1777. doi:10.1016/j.cemconres.2004.05.034

Rivas-Mercury, J. M., Pena, P., de Aza, A. H., and Turrillas, X. (2008). Dehydration of Ca3Al2(SiO4)Y(OH)4(3−y) (0. *J. Eur. Ceram. Soc.* 28, 1737–1748. doi:10.1016/j.jeurceramsoc.2007.12.038

Satava, V., and Veprek, O. (1975). Thermal Decomposition of Ettringite under Hydrothermal Conditions. *J. Am. Ceram. Soc.* 58, 357–359. doi:10.1111/j.1151-2916.1975.tb11513.x

Sauman, Z., and Vavrin, F. (1980). "Conditions of the Hydroxyl Ellestadite Formation in Mixtures Containing Calcium Sulphate," in 7th International Congress on the Chemistry of Cement ICCC, Paris, 106–110.

Scrivener, K. L., Snellings, R., and Lothenbach, B. (2016). *A Practical Guide to Microstructural Analysis of Cementitious Materials*. Boca Raton, Florida, USA: CRC Press.

Shams, T., Schober, G., Heinz, D., and Seifert, S. (2021). Production of Autoclaved Aerated concrete with Silica Raw Materials of a Higher Solubility Than Quartz Part II: Influence of Autoclaving Temperature. *Construction Building Mater.* 287, 123072. doi:10.1016/j.conbuildmat.2021.123072

Shaw, S., Clark, S. M., and Henderson, C. M. B. (2000a). Hydrothermal Formation of the Calcium Silicate Hydrates, Tobermorite (Ca5Si6O16(OH)2·4H2O) and Xonotlite (Ca6Si6O17(OH)2): an *In Situ* Synchrotron Study. *Chem. Geology.* 167, 129–140. doi:10.1016/S0009-2541(99)00205-3

Shaw, S., Henderson, C. M. B., and Komanschek, B. U. (2000b). Dehydration/recrystallization Mechanisms, Energetics, and Kinetics of Hydrated Calcium Silicate Minerals: an *In Situ* TGA/DSC and Synchrotron Radiation SAXS/WAXS Study. *Chem. Geology.* 167, 141–159. doi:10.1016/S0009-2541(99)00206-5

Shi, C., Wu, Z., Xiao, J., Wang, D., Huang, Z., and Fang, Z. (2015). A Review on Ultra High Performance concrete: Part I. Raw Materials and Mixture Design. *Construction Building Mater.* 101, 741–751. doi:10.1016/j.conbuildmat.2015.10.088

Tafraoui, A., Escadeillas, G., and Vidal, T. (2016). Durability of the Ultra High Performances Concrete Containing Metakaolin. *Construction Building Mater.* 112, 980–987. doi:10.1016/j.conbuildmat.2016.02.169

Taylor, H. F. W. (1964). *The Chemistry of Cements*. London: Academic Press.

Vladimír, Š. (1992). Hydrothermal Reactions in the System 3CaO·SiO2-CaSO4·2H2O-H2o. *Ceramics - Silikaty* 36 (2), 105–108.

von Werder, J., Simon, S., Simon, C., Selleng, C., Fontana, P., and Meng, B. (2018). Autoclaving of Ultra-high Performance concrete (UHPC). *ce/papers* 2, 131–136. doi:10.1002/cepa.866

Wu C., Li J., and Su Y. (Editors) (2018). *Development of Ultra-high Performance Concrete against Blasts: Woodhead Publishing Series in Civil and Structural Engineering* (Sawston, UK: Woodhead Publishing).

Wang, C., Yang, C., Liu, F., Wan, C., and Pu, X. (2012). Preparation of Ultra-high Performance Concrete with Common Technology and Materials. *Cement and Concrete Composites* 34, 538–544. doi:10.1016/j.cemconcomp.2011.11.005

Wang, W., Liu, J., Agostini, F., Davy, C. A., Skoczylas, F., and Corvez, D. (2014). Durability of an Ultra High Performance Fiber Reinforced Concrete (UHPFRC) under Progressive Aging. *Cement Concrete Res.* 55, 1–13. doi:10.1016/j.cemconres.2013.09.008

Wang, Z., Ma, S., Zheng, S., Ding, J., and Wang, X. (2019). Flexural Strength and thermal Conductivity of Fiber-Reinforced Calcium Silicate Boards Prepared from Fly Ash. *J. Mater. Civil Eng.* 31, 4019140. doi:10.1061/(ASCE)MT.1943-5533.0002726

Yang, R., and Sharp, J. H. (2001). Hydration Characteristics of Portland Cement after Heat Curing: I, Degree of Hydration of the Anhydrous Cement Phases. *J. Am. Ceram. Soc.* 84, 608–614. doi:10.1111/j.1151-2916.2001.tb00707.x

Yazıcı, H., Deniz, E., and Baradan, B. (2013). The Effect of Autoclave Pressure, Temperature and Duration Time on Mechanical Properties of Reactive Powder

93

concrete. *Construction Building Mater.* 42, 53–63. doi:10.1016/j.conbuildmat. 2013.01.003

Yazıcı, H., Yardımcı, M. Y., Aydın, S., and Karabulut, A. Ş. (2009). Mechanical Properties of Reactive Powder concrete Containing mineral Admixtures under Different Curing Regimes. *Construction Building Mater.* 23, 1223–1231. doi:10. 1016/j.conbuildmat.2008.08.003

Yonggui, W., Shuaipeng, L., Hughes, P., and Yuhui, F. (2020). Mechanical Properties and Microstructure of basalt Fibre and Nano-Silica Reinforced Recycled concrete after Exposure to Elevated Temperatures. *Construction Building Mater.* 247, 118561. doi:10.1016/j.conbuildmat.2020.118561

Yoo, D.-Y., Kim, M. J., Kim, S.-W., and Park, J.-J. (2017). Development of Cost Effective Ultra-high-performance Fiber-Reinforced concrete Using Single and Hybrid Steel Fibers. *Construction Building Mater.* 150, 383–394. doi:10.1016/j.conbuildmat.2017.06.018

Young R. A. (Editor) (2002). *The Rietveld Method* (Oxford: Oxford Univ. Press), Vol. 5.

Yu, R., Spiesz, P., and Brouwers, H. J. H. (2015). Development of an Eco-Friendly Ultra-high Performance Concrete (UHPC) with Efficient Cement and mineral Admixtures Uses. *Cement and Concrete Composites* 55, 383–394. doi:10.1016/j. cemconcomp.2014.09.024

Zdeb, T. (2017). An Analysis of the Steam Curing and Autoclaving Process Parameters for Reactive Powder Concretes. *Construction Building Mater.* 131, 758–766. doi:10.1016/j.conbuildmat.2016.11.026

Zhang, J., Zhao, Y., and Li, H. (2017). Experimental Investigation and Prediction of Compressive Strength of Ultra-high Performance Concrete Containing Supplementary Cementitious Materials. *Adv. Mater. Sci. Eng.* 2017, 1–8. doi:10.1155/2017/4563164

Zhang, L., Liu, J., Liu, J., Zhang, Q., and Han, F. (2018). Effect of Steel Fiber on Flexural Toughness and Fracture Mechanics Behavior of Ultrahigh-Performance Concrete with Coarse Aggregate. *J. Mater. Civil Eng.* 30, 4018323. doi:10.1061/(ASCE)MT.1943-5533.0002519

2.4 The evolution of hydrates assemblage and microstructure with autoclaving

Autoclaving can change the hydration kinetics and hydrates assemblage of cement-based materials. The typical hydrates of amorphous C-S-H, portlandite and ettringite at room temperature transform to other new hydrates under autoclaving, depending on the temperature and the composition of raw materials. In Portland cement-based system, the relative contents of the main elements Ca, Si, and Al can significantly influence the hydrates transformation and thus microstructure. In this section, quartz powder and fly ash (rich in Si and Al) are introduced in cement pastes to adjust the chemical composition of the matrix. Moreover, two water/solid (w/s) ratios are used to study the influence of water content on the evolution of hydrates assemblage and microstructure with autoclaving.

2.4.1 Materials and methods

2.4.1.1 Materials

Portland cement CEM I 52.5 R complying with European standard EN 197-1 is used. The chemical compositions of quartz powder and fly ash used in this study are determined by X-ray fluorescence, as shown in Table 2.1. Their particle size distributions are measured by laser diffraction, as shown in Fig. 2.1.
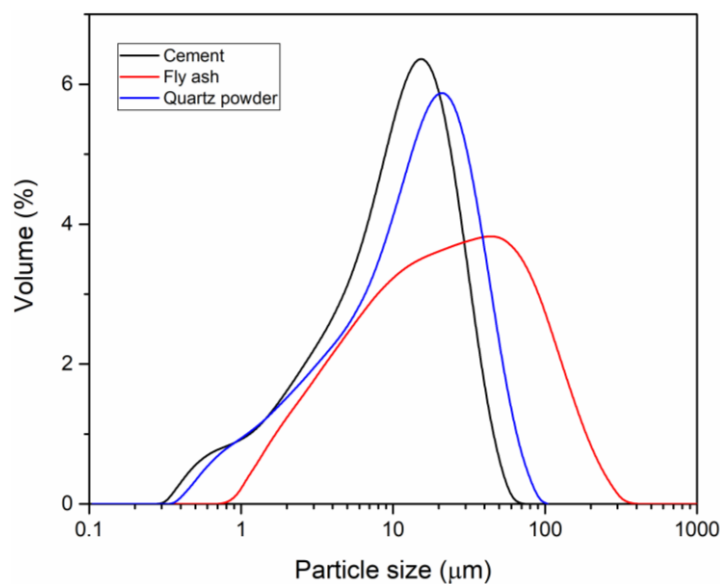
Fig. 2.1 Particle size distributions of the raw materials, measured by laser diffraction.

Table 2.1 Chemical compositions of the raw materials (wt. %).

	Cement	Fly ash	Quartz powder
SiO_2	18.85	53.26	98.93
CaO	61.16	5.40	< DL
Al_2O_3	4.85	20.61	0.17
K_2O	1.07	2.11	< DL
MgO	1.74	2.32	< DL
Mn_2O_3	0.06	0.07	< DL
Na_2O	0.22	0.88	< DL
P_2O_5	0.07	0.99	< DL
Fe_2O_3	2.83	7.68	0.02
SO_3	3.62	0.77	0.02
TiO_2	0.22	0.85	0.05
LOI	4.92	2.99	0.15
Sum	99.61	97.93	99.34

< DL: smaller than the detection limit.

2.4.1.2 Mixtures and autoclaving treatment

Two w/s ratios of 0.20 and 0.29 are used in this section. The quartz powder and fly ash are introduced with dosages of 20 and 40 wt. %, and the mixture formulations are shown in Table 2.2. The cement pastes are thoroughly mixed and cast into cubic molds with a length of 2 cm. The samples are cured sealed at 20 ± 2 °C for 24 h. Afterwards, the hardened samples are demolded followed by 24 h of pre-curing in water at 20 ± 2 °C and then subjected to the cyclic autoclaving treatment. Such cyclic autoclaving is also an indication of the charging and discharging process of the hot water tanks that will be constructed of UHPC. The autoclaving process is schematically shown in Fig. 2.2. The autoclave is heated from room temperature to 200 °C in ~1 h. After maintaining for 6 h, the temperature (200 °C) slowly cools to room temperature overnight (17 h). Thus, a cycle of autoclaving takes 24 h, and the autoclaving runs up to 50 cycles. The inner parts of the samples are extracted after autoclaving and immersed in isopropanol for one day, followed by freeze-drying. In contrast, another batch of samples is normally cured in water at 20 ± 2 °C for 28 d. For the samples nomenclature, in the case of LB-50, the number 50 represents the autoclaving cycles.
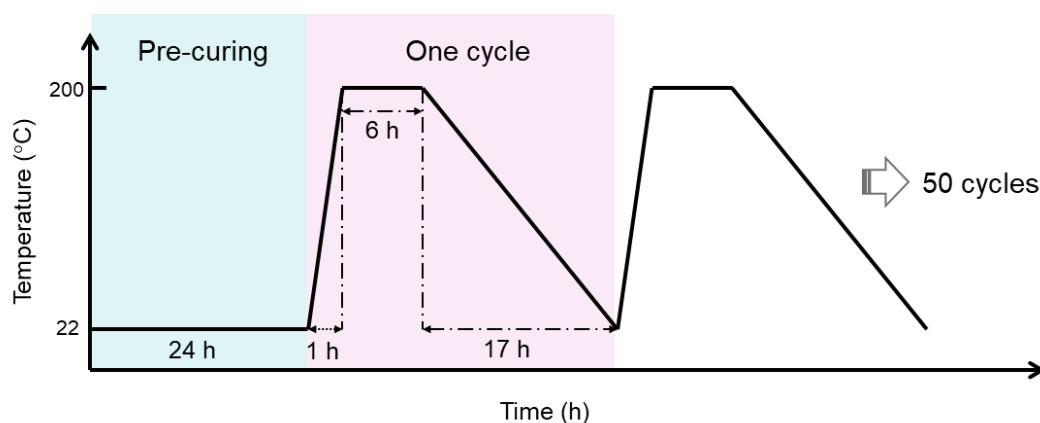
Fig. 2.2 The process of the cyclic autoclaving treatment.

Table 2.2 Recipes of the mixtures (wt. %).

	Cement	Fly ash	Quartz Powder	w/s ratio
LB	100	-	-	0.20
LF20	80	20	-	0.20
LF40	60	40	-	0.20
LQ20	80	-	20	0.20
LQ40	60	-	40	0.20
LQF20	60	20	20	0.20
HB	100	-	-	0.29
HF20	80	20	-	0.29
HF40	60	40	-	0.29
HQ20	80	-	20	0.29
HQ40	60	-	40	0.29
HQF20	60	20	20	0.29

2.4.1.3 X-ray diffraction analysis

The mineralogical compositions are analyzed by XRD using an Empyrean PANalytical diffractometer with CuKα radiation (k = 1.540598 Å). The measurements were operated at 40 kV and 40 mA in continuous mode with a resolution of 0.0131° and speed of 0.0172°/s for 2θ range from 3° to 65°. HighScore Plus software equipped with ICSD database was used to identify mineralogical phases. The profile fitting was also conducted by HighScore Plus software with the function of pseudo-Voigt. Due to overlapping peaks and poorly crystallized

phases, the background was confirmed manually. The parameters of peak position, peak height, peak FWHM, and peak shape were considered. Rietveld refinement was conducted on the samples with fly ash to confirm the compositions of hydrogarnet. The background used in the refinement was the same as that in profile fitting. The parameters of scale factor, zero shift, lattice parameters, halfwidth (W, U, and V), peak shape parameters, site occupancy factor, and B isotropic were refined.

2.4.1.4 Pore structure analysis

MIP was carried out on small cubic samples using a Porotec porosimeter (Pascal 240/440). Approx. 2 g of each sample was used in the experiments under 25 °C to characterize the porosity and pore size distribution. The mercury surface tension and contact angle were assigned to 0.48 N/m and 140 °, respectively. The intrusion pressure was up to 200 MPa with an pressure increase of 6-14 MPa/min.

2.4.2 Results and discussion

2.4.2.1 Hydrates assemblage

2.4.2.1.1 Pure cement pastes

The evolution of hydrates of pure cement pastes under autoclaving is characterized by XRD. For the samples with a low w/s ratio of 0.20 (Fig. 2.3(a)), the main hydration products of reference sample LB-R are ettringite, portlandite, and amorphous C-S-H under room temperature. The autoclaving substantially changes the hydrates assemblage. Ettringite already disappears in LB-1 after one autoclaving cycle due to its instability at high temperatures [1,2]. Instead, hydrogarnet ($Ca_3Al_2(SiO_4)_x(OH)_{4(3-x)}$; $0 \leq x \leq 3$) is identified and keeps constant in the subsequent autoclaving, indicating its high thermal stability [3]. The peak intensity of portlandite in LB-1 is stronger than that in LB-R due to the accelerated hydration by autoclaving, which coincides with the weaker peaks of silicate clinkers (C_2S and C_3S) in autoclaved samples. However, it is difficult to determine whether C_2S and C_3S exist in LB-50 due to the peak overlaps. The diffraction hump of amorphous C-S-H formed at room temperature becomes flatter in autoclaved samples, while the main crystalline silicate hydrates of jaffeite $Ca_6[Si_2O_7](OH)_6$, reinhardbraunsite $Ca_5(SiO_4)_2(OH)_2$, and hydroxylellestadite $Ca_{10}(SiO_4)_3(SO_4)_3(OH)_2$ are identified. Jaffeite possesses a hexagonal crystal system [4] and usually forms in net cement systems with high Ca/Si ratios under hydrothermal conditions [5–7]. The intensity of jaffeite increases from LB-20 to LB-50, and portlandite meanwhile shows a decrease from LB-20 to LB-50. This is probably because the hillebrandite $Ca_2(SiO_3)(OH)_2$

identified in LB-20 converts to jaffeite together with portlandite through the reaction (1) [8]. The decomposition of ettringite releases sulfate, which partially precipitates in hydroxylellestadite.

$$Hillebrandite + Portlandite \rightarrow Jaffeite + H_2O \tag{1}$$
$$2Ca_2(SiO_3)(OH)_2 + 2Ca(OH)_2 \rightarrow Ca_6[Si_2O_7](OH)_6 + H_2O$$
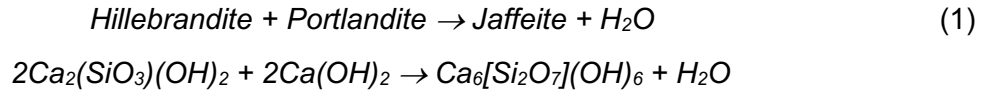
The types of hydrates in HB-50 (Fig. 2.3(b)) are the same as those in LB-50. The peak intensity of jaffeite keeps roughly constant to the end of autoclaving without the increase from LB-20 to LB-50, while the decrease of portlandite is also not observed. However, because hillebrandite has a trace amount and its main peak overlaps with jaffeite at 2θ 30.6°, it is difficult to confirm whether hillebrandite exists in HB-50. Therefore, HB-50 presents more portlandite and less jaffeite compared with LB-50. In a cement paste with limited water, the hydration of C_2S and C_3S competes with water. Compared with LB, HB has higher water content, and thus more C_2S, which has lower activity than C_3S, can react, decreasing the Ca/Si ratio. The lower Ca/Si ratio in HB is adverse to jaffeite and may lead to the hydrates with lower Ca/Si ratios.
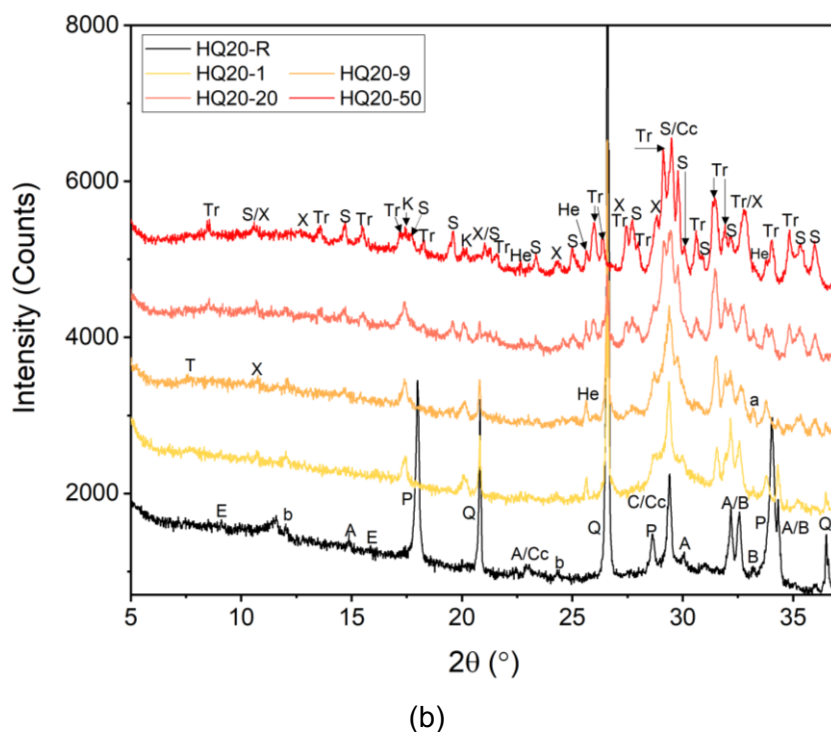

(a)

99

(b)
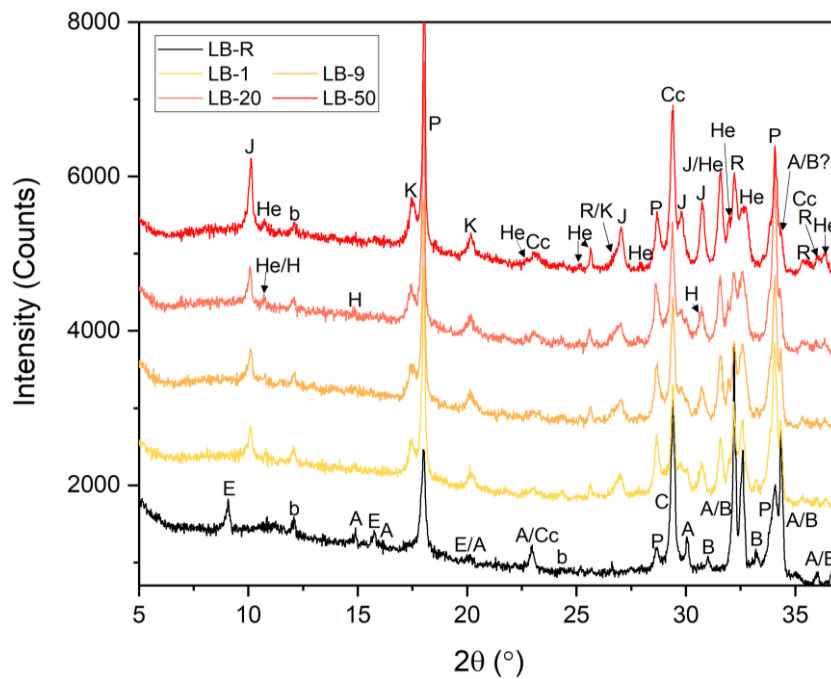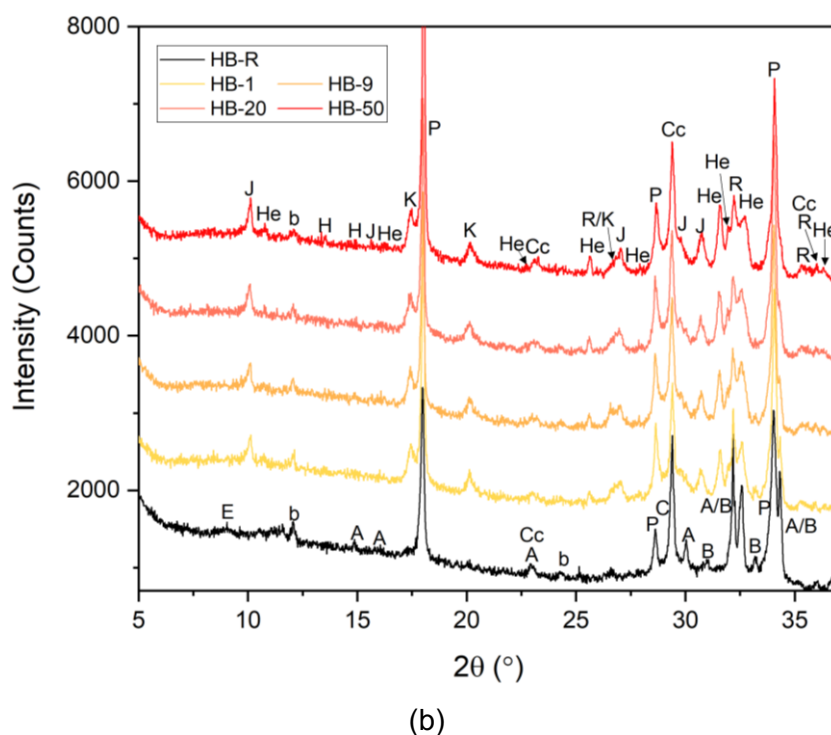
Fig. 2.3 The evolution of hydrates of pure cement pastes with autoclaving: (a) w/s = 0.20 and (b) w/s = 0.29 (J: jaffeite, R: reinhardbraunsite, H: hillebrandite, K: hydrogarnet, He: hydroxylellestadite, C: C-S-H, P: portlandite, E: ettringite, Cc: calcite, Q: quartz, A: alite, B: belite, b: calcium aluminoferrite).

2.4.2.1.2 Pastes from cement and quartz powder

The XRD results of cement paste with 20 wt. % quartz powder are shown in Fig. 2.4. The incorporation of quartz powder leads to a complicated mineralogical composition. The sharp peaks of quartz can be seen in LQ20-R (Fig. 2.4(a)), and it decreases with autoclaving, indicating the active pozzolanic reaction. Accordingly, only weak peaks of portlandite appear in LQ20-1 and then disappear in the subsequent autoclaving. Hydrogarnet is again observed and keeps roughly constant to the end of autoclaving. The main crystalline silicate hydrates of xonotlite $Ca_6[Si_6O_{17}](OH)_2$, scawtite $Ca_7(Si_3O_9)_2CO_3 \cdot 2H_2O$, and hydroxylellestadite are identified in LQ20-50 due to the decreased Ca/Si ratio by quartz powder. Thus, only a trace amount of jaffeite is observed. It is reported that the xonotlite formation in the mixtures with Ca/Si not greatly above 1 is faster than that in the mixtures with Ca/Si exactly equal to 1 [9]. In the presence of carbonate, xonotlite usually transforms to scawtite as a carbonation product [10–12]. Tobermorite $Ca_5[Si_3O_8(OH)]_2 \cdot 4(H_2O)$ and α-dicalcium silicate hydrate α-$Ca_2(HSiO_4) \cdot (OH)$ are identified in the early stage of autoclaving but disappear in LQ20-50. α-dicalcium silicate hydrate is usually encountered in hydrothermal experiments ranging from

120 to 160 °C and transforms to hillebrandite at higher temperatures [9,13]. However, there is no apparent signal of hillebrandite in LQ20-50, probably due to the low content and peak overlaps.

Interestingly, the hydrates assemblage of autoclaved HQ20 (Fig. 2.4(b)) is different from that of autoclaved LQ20. The sharp peaks of quartz are not observed in HQ20-50, indicating that the pozzolanic reaction is promoted by high water content. Portlandite peaks are not even present in HQ20-1. Trabzonite $Ca_4[Si_3O_9(OH)]OH$ as a new crystalline phase is identified. This phase is rarely reported in autoclaved cements and well-cementing systems, probably because Armbruster et al. revised its originally reported chemical formula $Ca_4(Si_3O_{10})\cdot 2H_2O$ (crystal structure contains trisilicate Si_3O_{10} and H_2O) to the current OH-bearing composition in 2012 [14]. Similar to scawtite, trabzonite only essentially forms after HQ20-9. In contrast, xonotlite forms fast in HQ20-1.
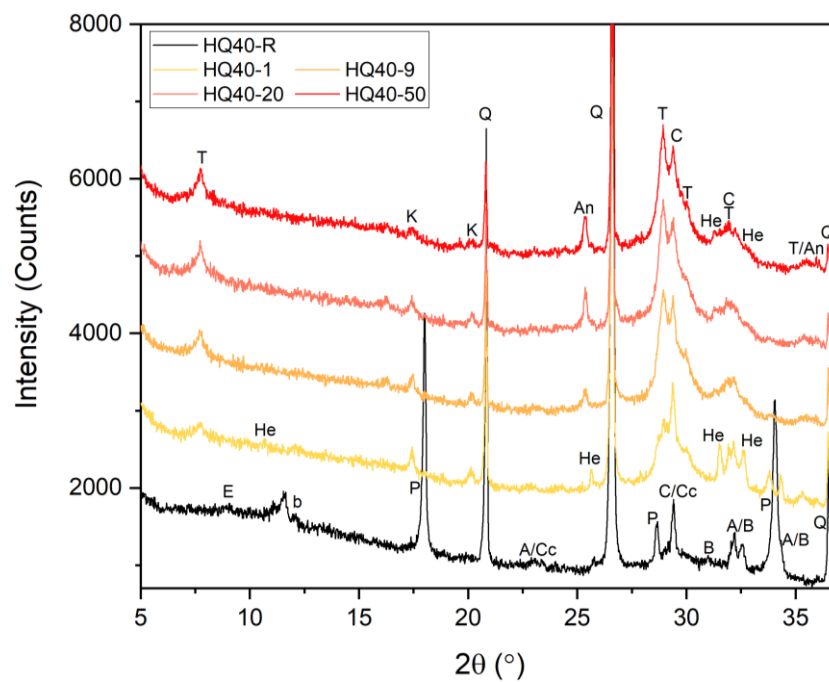

(a)

(b)
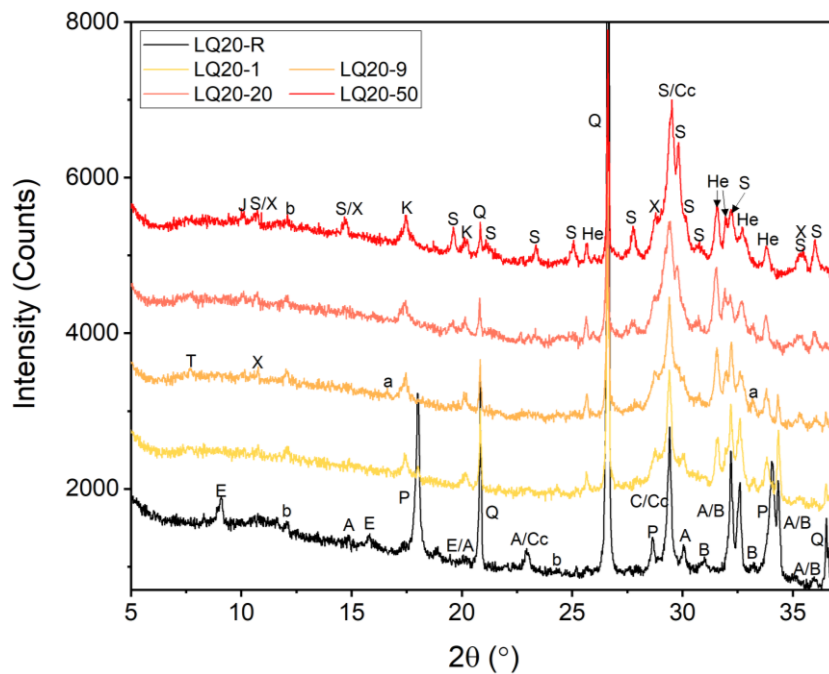
Fig. 2.4 The evolution of hydrates of cement pastes with 20 wt. % quartz powder with autoclaving: (a) w/s = 0.20 and (b) w/s = 0.29 (J: jaffeite, S: scawtite, X: xonotlite, Tr: trabzonite, K: hydrogarnet, He: hydroxylellestadite, T: tobermorite, a: α-dicalcium silicate hydrate, C: C-S-H, P: portlandite, E: ettringite, Cc: calcite, Q: quartz, A: alite, B: belite, b: calcium aluminoferrite).

The XRD results of the blended mixture with 40 wt. % quartz powder are shown in Fig. 2.5. Tobermorite becomes the main crystalline hydrate in LQ40-50 as the Ca/Si ratio of the matrix is further decreased by quartz powder. Tobermorite is unstable under long-term autoclaving at above ~150 °C without Al stabilization [15,16]. However, it can be seen that hydrogarnet fast forms in LQ40-1 and gradually decreases with autoclaving, releasing Al which stabilizes tobermorite [17]. Anhydrite is also identified in the late stage of autoclaving due to the decomposition of hydroxylellestadite [17]. The diffuse peak at ~ 29.4° indicates the presence of poorly crystallized C-S-H [18]. Such poorly crystallized C-S-H is also observed in the samples with 42% and 65% silica (by volume of the blend) autoclaved at 200 °C [19].
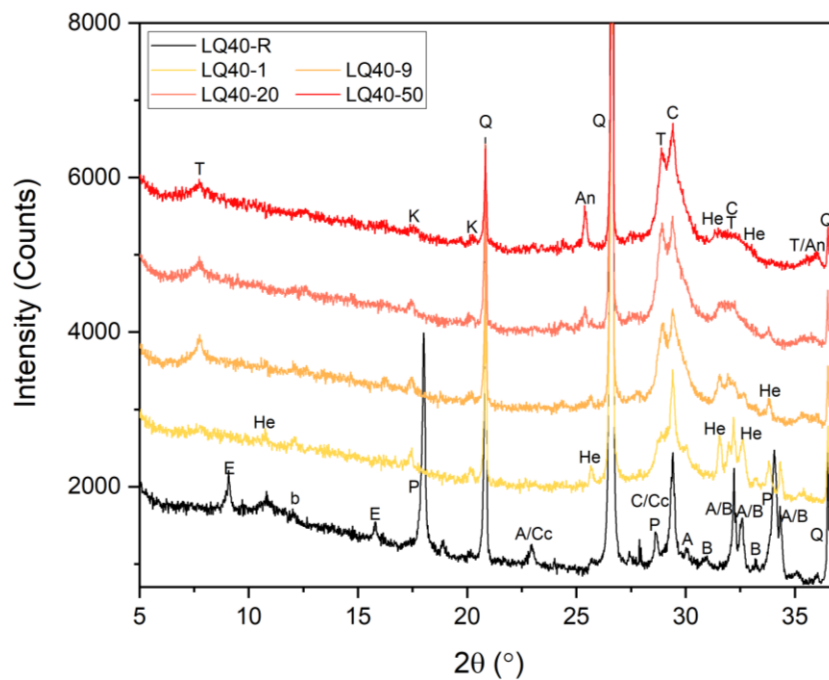
(a)

(b)

Fig. 2.5 The evolution of hydrates of cement pastes with 40 wt. % quartz powder with autoclaving: (a) w/s = 0.20 and (b) w/s = 0.29 (T: tobermorite, K: hydrogarnet, He: hydroxylellestadite, C: C-S-H, An: anhydrite, P: portlandite, E: ettringite, Cc: calcite, Q: quartz, A: alite, B: belite, b: calcium aluminoferrite).

For HQ40-50, tobermorite is also the main crystalline hydrate, and the poorly crystallized C-S-H is again observed. Assarsson et al. [20] pointed out that poorly crystallized C-S-H without a definitive Ca/Si ratio first forms from the rapid reaction of $Ca(OH)_2$ with SiO_2. Recrystallization as the second step under high temperature transforms unstable and amorphous phases into more stable and crystalline phases [21,22]. The transformation depends on the property of the C-S-H precursor and the solid volume fraction of the matrix [17,19]. The C-S-H precursor with a low Ca/Si ratio tends to possess long and cross-linked chains of silicate tetrahedra, which is relatively hard to transform to crystalline phases as more bonds need to be reorganized compared with the C-S-H precursor with a high Ca/Si ratio [23–26]. In this study, the addition of a large amount of quartz powder greatly decreases the Ca/Si ratio of the matrix, leading to the formation of a C-S-H precursor with a low Ca/Si ratio. Besides, Krakowiak et al. pointed out that the high solid volume fraction of a matrix suppresses the transformation of C-S-H to crystalline phases as the limited space restricts crystallization [19]. In order to confirm this effect, XRD profile fitting is further carried out. Because the weight fraction of a phase in the matrix is positively related to the XRD peak area (I), the peak area ratio of tobermorite to poorly crystallized C-S-H can be used as a rough indicator of their relative amounts. The peaks at 2θ 28.9° and 29.4° are selected as the representatives of tobermorite and poorly crystallized C-S-H, respectively. Based on the XRD profile fitting, the peak area ratios $I_{tobermorite}/I_{C-S-H}$ of LQ40-50 and HQ40-50 are calculated as 1.1 and 2.0, respectively. The higher ratio $I_{tobermorite}/I_{C-S-H}$ in HQ40-50 indicates the more conversion of C-S-H to tobermorite due to the higher w/s ratio (lower solid volume fraction), consistent with the result in [19].

### 2.4.2.1.3 Pastes from cement and fly ash

The XRD results of the blended mixture with 20 wt. % fly ash are shown in Fig. 2.6. The peaks of portlandite are identified in LF20-1 and disappear in the following autoclaving due to the pozzolanic reaction with fly ash. Jaffeite, hydroxylellestadite, xonotlite, scawtite, and tobermorite form in LF20-50 as the main crystalline silicate hydrates. The addition of fly ash changes the compositions of hydrogarnet. It is reported that hydrogarnet is a series of solid solutions with a miscibility gap, which the boundary of the miscibility gap relates to the temperature [27,28]. The peak splitting at 2θ ~17.6° indicates the two groups of hydrogarnet: Si-poor hydrogarnet and Si-rich hydrogarnet [28], and the two groups of hydrogarnet can coexist.

To better show the influence of matrix composition and w/s ratio on hydrogarnet, the main peak of hydrogarnet from the autoclaved samples with different contents of fly ash are plotted

together (Fig. 2.7). It is reported that the unit cell size of hydrogarnet decreases linearly with increasing Si content, from 12.57 Å for C_3AH_6 to 11.85 Å for C_3AS_3 [27,28]. Therefore, the composition of hydrogarnet can be estimated by plotting the Si content against the unit cell size derived from the XRD profile refinement. The composition of Si-rich hydrogarnet in this study is marked in Fig. 2.8. Compared with LB and HB, the addition of fly ash induces the formation of Si-rich hydrogarnet due to the increase of Al and Si in the matrix. However, the exclusive addition of quartz powder (LQ20 and HQ20) cannot lead to Si-rich hydrogarnet, which is consistent with the experience that silica-containing hydrogarnet usually forms in Al-rich cement and the OPC added with fly ash or slag [28]. Note that the Si-poor hydrogarnet identified in LQ40 and HQ40 decompose as an intermediate for tobermorite formation. However, both Si-poor and Si-rich hydrogarnet stay constant to the end of autoclaving in LF20-50, probably because the Ca/Si ratio in LF20 is adverse to tobermorite. Therefore, only a trace amount of tobermorite is observed in LF20-50. The types of hydrates in autoclaved HF20-50 are similar to those in autoclaved LF20-50.
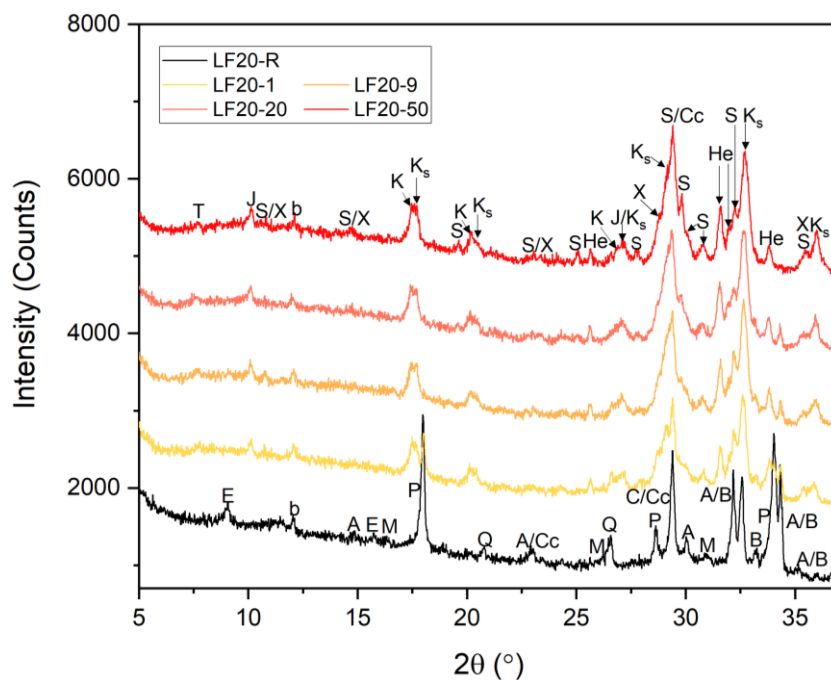
(a)
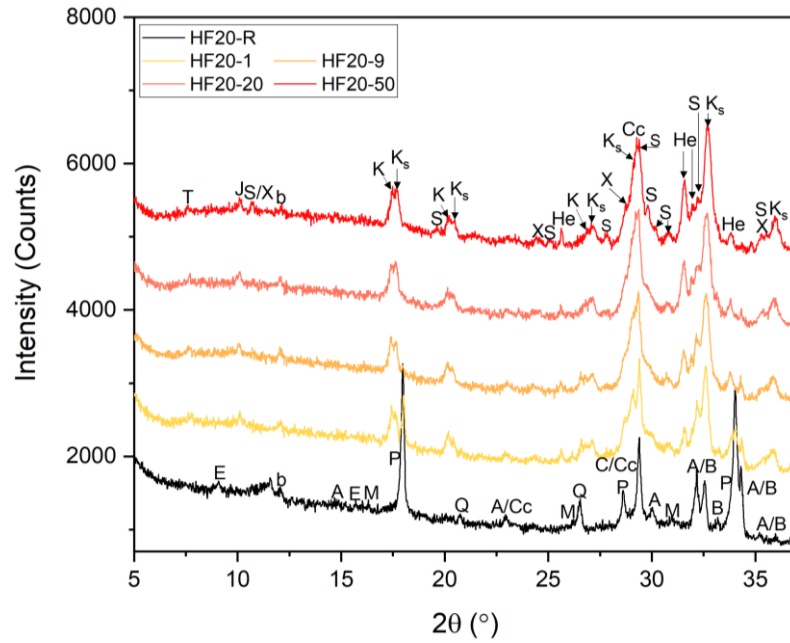
(b)

Fig. 2.6 The evolution of hydrates of cement pastes with 20 wt. % fly ash with autoclaving: (a) w/s = 0.20 and (b) w/s = 0.29 (T: tobermorite, J: jaffeite, S: scawtite, X: xonotlite, He: hydroxylellestadite, K: Si-poor hydrogarnet, K_s: Si-rich hydrogarnet, C: C-S-H, P: portlandite, E: ettringite, Cc: calcite, Q: quartz, M: mullite, A: alite, B: belite, b: calcium aluminoferrite).
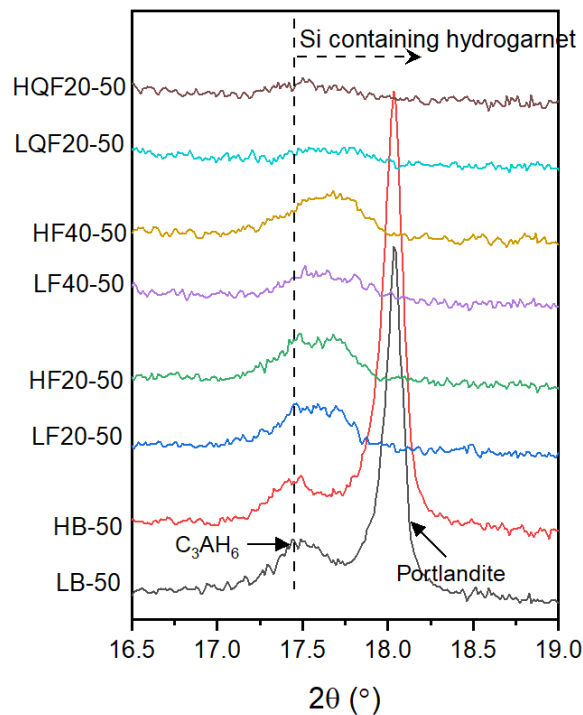

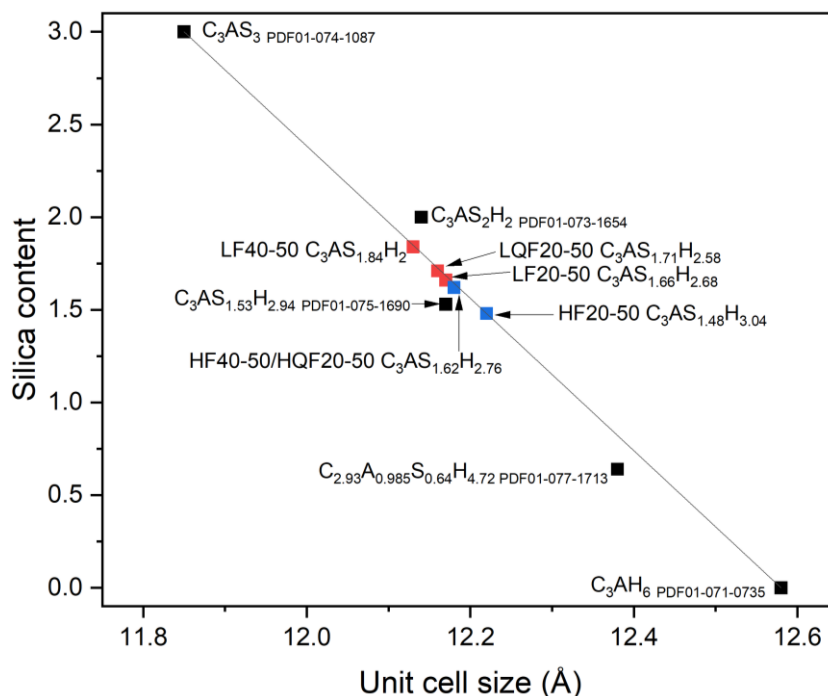Fig. 2.7 The comparison of hydrogarnet in autoclaved samples with different contents of fly ash.

Fig. 2.8 Estimation of the composition of Si-rich hydrogarnet in autoclaved samples with different contents of fly ash (the silica content is represented by the x value in $Ca_3Al_2(SiO_4)_x(OH)_{4(3-x)}$; $0 \leq x \leq 3$. PDF: Powder Diffraction File).

As more fly ash is added in LF40 (Fig. 2.9(a)), the Ca/Si ratio in the matrix is further decreased, and tobermorite thus generates massively. Accordingly, hydroxylellestadite fast formed in LF40-1 gradually decreases with autoclaving as an intermediate of tobermorite [17]. Anhydrite as a decomposition product of hydroxylellestadite is also observed. Interestingly, a large amount of Si-rich hydrogarnet is observed in LF40-50. Furthermore, compared with LF40-50, HF40-50 (Fig. 2.9(b)) presents the Si-rich hydrogarnet with stronger peaks and tobermorite with weaker peaks. It is reported that hydrogarnet can decompose as an intermediate of tobermorite [3,17], and this phenomenon is also observed by the decomposition of Si-poor hydrogarnet with autoclaving in LQ40 and HQ40. However, both Si-poor and Si-rich hydrogarnet are maintained in LF40 and HF40. In addition, compared with LF20-50, LF40-50 presents the Si-rich hydrogarnet with a higher Si content (Fig. 2.8) due to the increased Al and Si in the matrix by more addition of fly ash.

Tobermorite can incorporate Al, but the incorporation has an upper limit, above which hydrogarnet forms under autoclaving conditions [29–32]. It seems that the addition of a large amount of fly ash provides enough Al to stabilize Si-poor and Si-rich hydrogarnet. Furthermore, the stabilizing effect of silica on hydrogarnet is also reported, which the solubility products of

hydrogarnet calculated from the solution composition determined at 20 °C and 25 °C decrease with the increase of silica content (silica-containing hydrogarnet is synthesized at 110 °C) [27]. Another literature also suggested the stabilizing effect of silica on hydrogarnet that Si-free hydrogarnet is unstable with carbonate and sulfate bearing cement phases, e.g., AFt, AFm, gypsum, and calcite, while silica-containing hydrogarnet can persist with these phases [33].

Due to the higher water content in HF40, more Al can be dissolved from fly ash. Hydrogarnet tends to form faster than tobermorite [3]. The massive formation of Si-stabilized hydrogarnet in HF40 decreases the raw materials of Si, Al, and Ca for tobermorite formation, which may explain the low content of tobermorite and the high content of Si-rich hydrogarnet in HF40-50. The carbonation of tobermorite may also contribute to the decrease of tobermorite from HF40-20 to HF40-50 [34]. Hydroxylellestadite keeps roughly constant to the end of autoclaving in HF40 without the decease as shown in LF40, probably because the environment in HF40 is adverse to tobermorite.
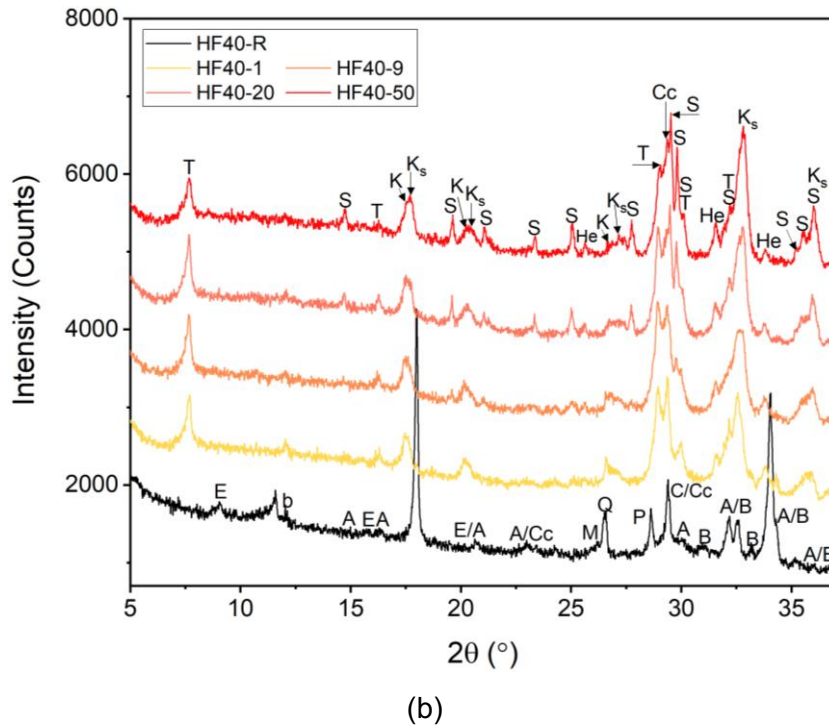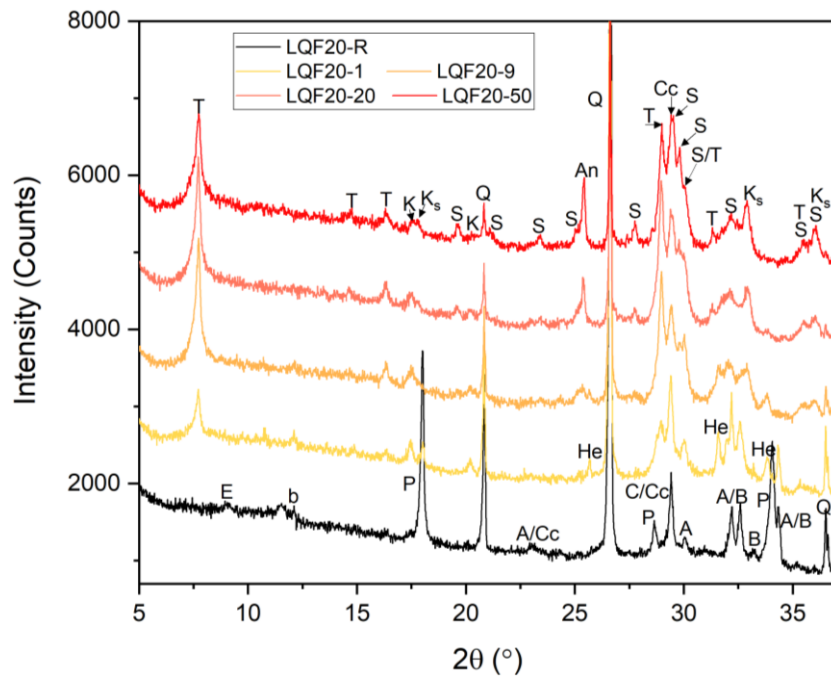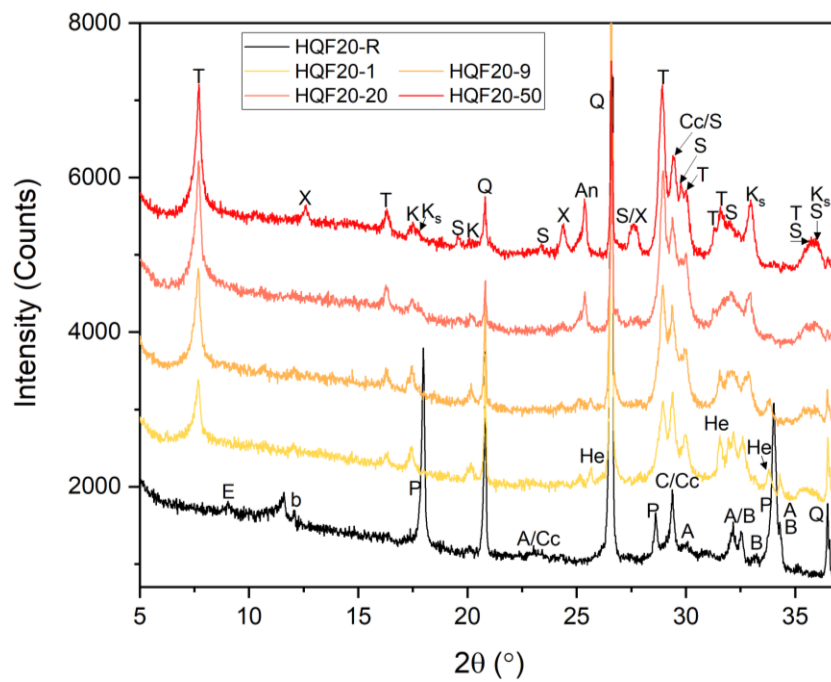

(a)

(b)
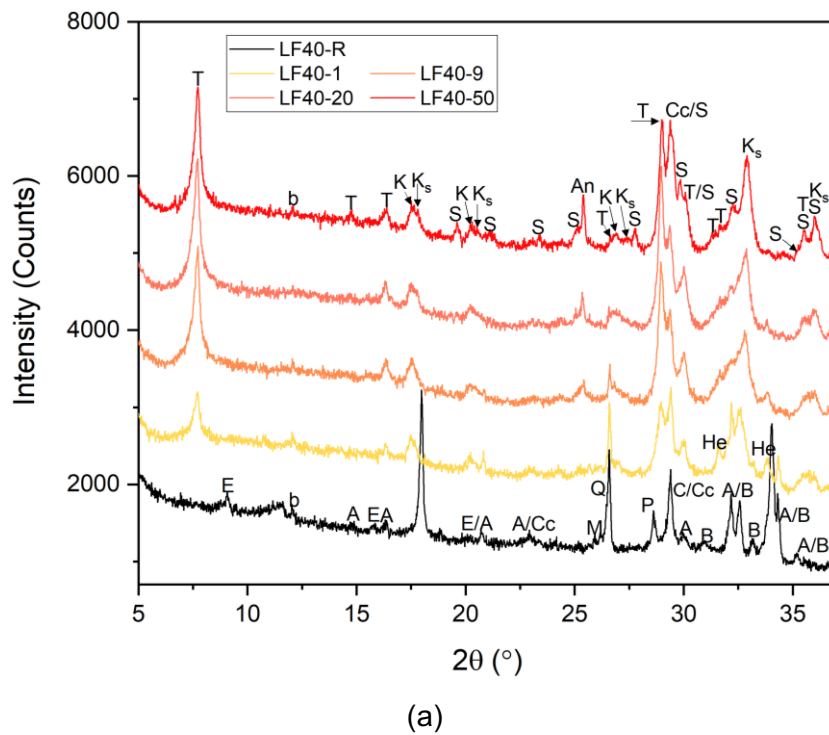
Fig. 2.9 The evolution of hydrates of cement pastes with 40 wt. % fly ash with autoclaving: (a) w/s = 0.20 and (b) w/s = 0.29 (T: tobermorite, S: scawtite, He: hydroxylellestadite, An: anhydrite, K: Si-poor hydrogarnet, K_s: Si-rich hydrogarnet, C: C-S-H, P: portlandite, E: ettringite, Cc: calcite, Q: quartz, M: mullite, A: alite, B: belite, b: calcium aluminoferrite).

The XRD results of the blended pastes with quartz powder and fly ash are shown in Fig. 2.10. Tobermorite and scawtite are the main crystalline silicate hydrates in LQF20-50 (Fig. 2.10(a)). Hydroxylellestadite decreases with autoclaving, accompanied by the formation of anhydrite. Both Si-poor and Si-rich hydrogarnet are identified, but it seems that only Si-poor hydrogarnet decreases with autoclaving, consistent with the foregoing discussion. A similar phenomenon is also observed in HQF20 (Fig. 2.10(b)). In addition to tobermorite and scawtite, xonotlite is also identified in HQF20-50. Note that the Si-rich hydrogarnet in LQF20-50 has a higher Si content than that in LF20-50, indicating that decreasing the Ca/Si ratio of the matrix can also increase the Si content of hydrogarnet in the presence of enough Al. Compared with HF20-50, HQF20-50 also shows the Si-rich hydrogarnet with a higher Si content. Moreover, for the samples with the same content of fly ash and/or quartz powder, a low w/s ratio gives the Si-rich hydrogarnet with a high Si content (more anhydrous, Fig. 2.8).

(a)

(b)

Fig. 2.10 The evolution of hydrates of cement pastes with 40 wt. % fly ash with autoclaving: (a) w/s = 0.20 and (b) w/s = 0.29 (T: tobermorite, S: scawtite, He: hydroxylellestadite, X: xonotlite, An: anhydrite, K: Si-poor hydrogarnet, K_s: Si-rich hydrogarnet, C: C-S-H, P: portlandite, E: ettringite, Cc: calcite, Q: quartz, M: mullite, A: alite, B: belite, b: calcium aluminoferrite).

2.4.2.2 Pore structure analysis

The pore structures of autoclaved cement pastes are shown in Figs. 2.11 and 2.12. For the sample with a low w/s ratio, LB-50 shows a high porosity, and capillary pores dominate in the pore volume, assumed 10 nm as the dividing point between gel and capillary pore. LF20-50 and LF40-50 present similar porosities with LB-50 due to the massive formation of Si-rich hydrogarnet with high density and thus low solid volume. A slightly lower porosity is observed in LQ20-50, probably because the densities of xonotlite and scawtite in LQ20-50 are lower than that of Si-rich hydrogarnet. Similarly, the low content of Si-rich hydrogarnet in LQF20-50 leads to a lower porosity than LF20-50 and LF40-50. Moreover, the critical pore entry diameters of LQ20-50 and LQF20-50 are shifted to lower values than those of LF20-50 and LF40-50. LQ40-50 presents the lowest porosity due to the persistence of poorly crystallized C-S-H and the formation of tobermorite, densifying the matrix microstructure. Tobermorite with low density is a desirable hydrate during oil and geothermal well cementing under hydrothermal conditions (above ~110 °C). Additional silica is usually introduced to decrease the matrix Ca/Si ratio to approx. 1, benefiting tobermorite formation and preventing strength retrogression and permeability increase [35,36].
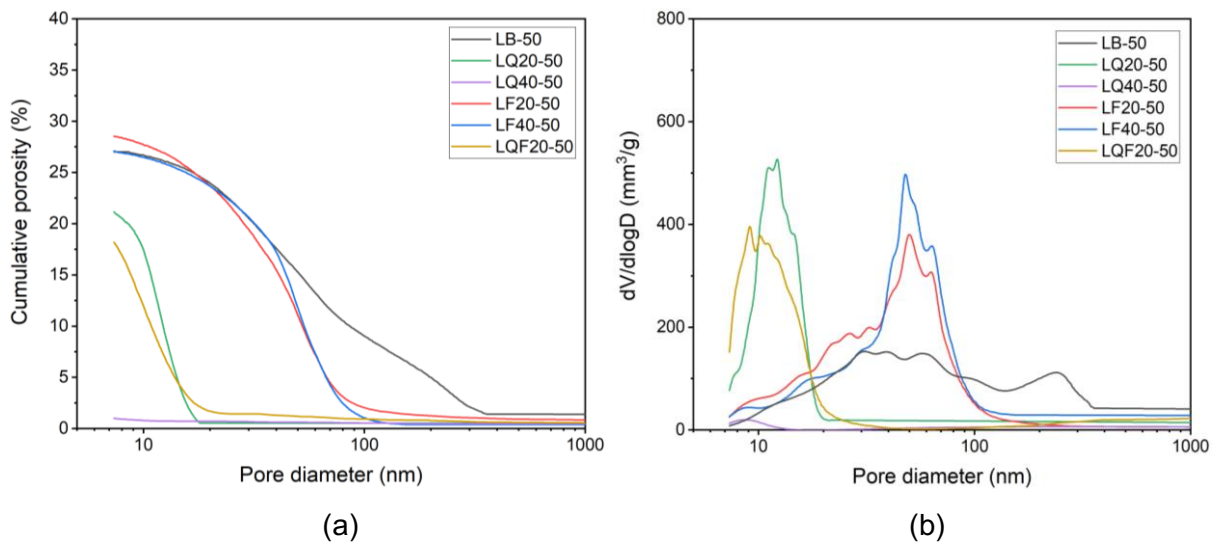

(a)   (b)

Fig. 2.11. Pore structures of the autoclaved samples with w/s ratio of 0.20: (a) cumulative porosity; (b) pore size distribution.
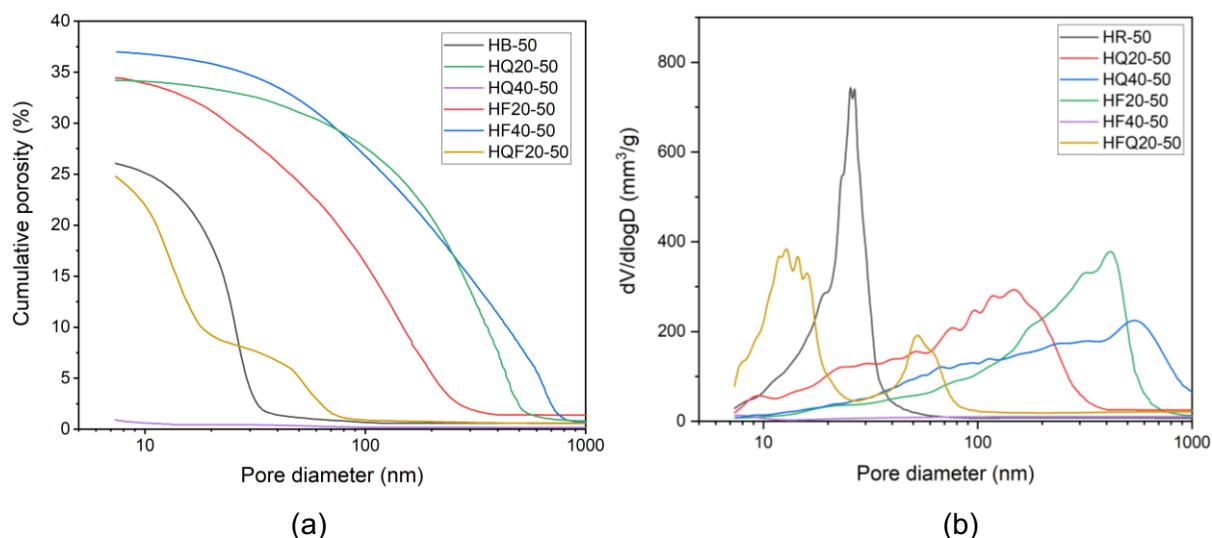
Fig. 2.12 Pore structures of the autoclaved samples with w/s ratio of 0.29: (a) cumulative porosity; (b) pore size distribution.

The samples with a high w/s ratio show a similar rule: the formation of hydrates with low densities benefits microstructure densification, while the hydrates with high densities, e.g., trabzonite and Si-rich hydrogarnet, tend to give large porosities. Note that HB-50 shows a slightly lower porosity than LB-50, indicating that the sample with a low w/s ratio does not necessarily have a low porosity under autoclaving. The variation of hydrates assemblage induced by long-term autoclaving also affects the pore structures.

2.4.3 Conclusion

The evolution of hydrates assemblage and pore structures of cement pastes with autoclaving at 200 °C are studied. The cement hydration is significantly accelerated by autoclaving, and the hydrates are substantially changed. Portlandite, jaffeite, reinhardbraunsite, hydroxylellestadite, and hydrogarnet are the main crystalline hydrates of the pure cement pastes. With the addition of quartz powder, portlandite disappears due to the pozzolanic reaction. The Ca/Si ratio of the matrix is decreased by 20 wt. % quartz powder, leading to the crystalline C-S-H with lower Ca/Si ratios. The addition of 40 wt. % quartz powder results in the formation of tobermorite and poorly crystallized C-S-H, which persist under autoclaving. The addition of fly ash can effectively increase the Al content, leading to the formation of hydrogarnet. The composition of hydrogarnet depends on the contents of Si and Al in the matrix. High contents of Si and Al favor Si-rich hydrogarnet, and the increase of Si and Al can increase the Si content of hydrogarnet.

A high w/s ratio can increase the availability of raw materials, leading to a different hydrates assemblage. Moreover, a high w/s ratio favors the transformation of the C-S-H precursor to tobermorite. For the samples with the same content of fly ash and/or quartz powder, a low w/s ratio gives the hydrogarnet with a higher Si content (more anhydrous). The formation of hydrates with low densities, e.g., tobermorite and poorly crystallized C-S-H, ensure the matrix with low porosity. HB-50 shows a slightly lower porosity than LB-50, although HB-50 has a high w/s ratio.

2.4.4 References

[1] N. Meller, K. Kyritsis, C. Hall, The hydrothermal decomposition of calcium monosulfoaluminate 14-hydrate to katoite hydrogarnet and β-anhydrite: An in-situ synchrotron X-ray diffraction study, Journal of Solid State Chemistry 182 (2009) 2743–2747.

[2] V. Satava, O. Veprek, Thermal decomposition of ettringite under hydrothermal conditions, Journal of the American Ceramic Society 58 (1975) 357–359.

[3] R. Siauciunas, A. Baltusnikas, Influence of SiO_2 modification on hydrogarnets formation during hydrothermal synthesis, Cement and Concrete Research 33 (2003) 1789–1793.

[4] H. Sarp, Donald R. Peacor, Jaffeite, a new hydrated calcium silicate from the kombat mine, Namibia, American Mineralogist 74 (1989) 1203–1206.

[5] M.T. Palou, E. Kuzielová, M. Žemlička, J. Tkácz, J. Másilko, Insights into the hydration of Portland cement under hydrothermal curing, Journal of Thermal Analysis and Calorimetry 138 (2019) 4155–4165.

[6] F. Méducin, B. Bresson, N. Lequeux, M.-N.d. Noirfontaine, H. Zanni, Calcium silicate hydrates investigated by solid-state high resolution ^{1}H and [29]Si nuclear magnetic resonance, Cement and Concrete Research 37 (2007) 631–638.

[7] M.T. Palou, F. Šoukal, M. Boháč, P. Šiler, T. Ifka, V. Živica, Performance of G-Oil Well cement exposed to elevated hydrothermal curing conditions, Journal of Thermal Analysis and Calorimetry 118 (2014) 865–874.

[8] C. Lehmann, Neue Perspektiven für Ultra-Hochleistungsbeton durch gezielte Beeinflussung des Nanogefüges, Technische Universität Berlin, 2013.

[9] A. Aitken, H.F.W. Taylor, Hydrothermal reactions in lime-quartz pastes, Journal of Applied Chemistry 10 (1960) 7–15.

[10] E.B. Nelson, Development of geothermal-well-completion systems. Final report, 1979.

[11] E. Grabowski, J.E. Gillott, Effect of replacement of silica flour with silica fume on engineering properties of oilwell cements at normal and elevated temperatures and pressures, Cement and Concrete Research 19 (1989) 333–344.

[12] L.H. Eilers, E.B. Nelson, L.K. Moran, High-temperature cement compositions-pectolite, scawtite, truscottite, or xonotlite: which do you want?, Journal of Petroleum Technology 35 (1983) 1,373-1,377.

[13] P. Blanc, X. Bourbon, A. Lassin, E.C. Gaucher, Chemical model for cement-based materials: Temperature dependence of thermodynamic functions for nanocrystalline and crystalline C–S–H phases, Cement and Concrete Research 40 (2010) 851–866.

[14] T. Armbruster, B. Lazic, I.O. Galuskina, E.V. Galuskin, E. Gnos, K.M. Marzec, V.M. Gazeev, Trabzonite, $Ca_4(Si_3O_9(OH))OH$: crystal structure, revised formula, new occurrence and relation to killalaite, Mineralogical Magazine 76 (2012) 455–472.

[15] S.Y. Hong, F.P. Glasser, Phase relations in the $CaO-SiO_2-H_2O$ system to 200 °C at saturated steam pressure, Cement and Concrete Research 34 (2004) 1529–1534.

[16] S. Shaw, S. Clark, C. Henderson, Hydrothermal formation of the calcium silicate hydrates, tobermorite ($Ca_5Si_6O_{16}(OH)_2·4H_2O$) and xonotlite ($Ca_6Si_6O_{17}(OH)_2$): an in situ synchrotron study, Chemical Geology 167 (2000) 129–140.

[17] K. Matsui, J. Kikuma, M. Tsunashima, T. Ishikawa, S.-Y. Matsuno, A. Ogawa, M. Sato, In situ time-resolved X-ray diffraction of tobermorite formation in autoclaved aerated concrete: Influence of silica source reactivity and Al addition, Cement and Concrete Research 41 (2011) 510–519.

[18] S. Grangeon, F. Claret, Y. Linard, C. Chiaberge, X-ray diffraction: a powerful tool to probe and understand the structure of nanocrystalline calcium silicate hydrates, Acta Crystallographica Section B Structural Science, Crystal Engineering and Materials 69 (2013) 465–473.

[19] K.J. Krakowiak, J.J. Thomas, S. James, M. Abuhaikal, F.-J. Ulm, Development of silica-enriched cement-based materials with improved aging resistance for application in high-temperature environments, Cement and Concrete Research 105 (2018) 91–110.

[20] G.O. Assarsson, Hydrothermal reactions between calcium hydroxide and amorphous silica: the reactions between 180 and 220°C, The Journal of Physical Chemistry 61 (1957) 473–479.

[21] G.O. Assarsson, E. Rydberg, Hydrothermal reactions between calcium hydroxide and amorphous silica, The Journal of Physical Chemistry 60 (1956) 397–404.

[22] T. Mitsuda, H.F.W. Taylor, Influence of aluminium on the conversion of calcium silicate hydrate gels into 11 Å tobermorite at 90°C and 120°C, Cement and Concrete Research 5 (1975) 203–209.

[23] 5 Hydration of the calcium silicate phases, in: H.F.W. Taylor (Ed.), Cement chemistry, Thomas Telford Ltd, London, 2009, pp. 113–156.

[24] J.J. Chen, J.J. Thomas, H.F.W. Taylor, H.M. Jennings, Solubility and structure of calcium silicate hydrate, Cement and Concrete Research 34 (2004) 1499–1519.

[25] I.G. Richardson, Tobermorite/jennite- and tobermorite/calcium hydroxide-based models for the structure of C-S-H: applicability to hardened pastes of tricalcium silicate, β-dicalcium silicate, Portland cement, and blends of Portland cement with blast-furnace slag, metakaolin, or silica fume, Cement and Concrete Research 34 (2004) 1733–1777.

[26] A. Nonat, The structure and stoichiometry of C-S-H, Cement and Concrete Research 34 (2004) 1521–1528.

[27] B.Z. Dilnesa, B. Lothenbach, G. Renaudin, A. Wichser, D. Kulik, Synthesis and characterization of hydrogarnet $Ca_3(Al_xFe_{1-x})_2(SiO_4)_y(OH)_{4(3-y)}$, Cement and Concrete Research 59 (2014) 96–111.

[28] T.G. Jappy, F.P. Glasser, Synthesis and stability of silica-substituted hydrogarnet $Ca_3Al_2Si_{3-x}O_{12-4x}(OH)_{4x}$, Advances in Cement Research 4 (1991) 1–8.

[29] E. L'Hôpital, B. Lothenbach, G. Le Saout, D. Kulik, K. Scrivener, Incorporation of aluminium in calcium-silicate-hydrates, Cement and Concrete Research 75 (2015) 91–103.

[30] G.K. Sun, J.F. Young, R.J. Kirkpatrick, The role of Al in C–S–H: NMR, XRD, and compositional results for precipitated samples: NMR, XRD, and compositional results for precipitated samples, Cement and Concrete Research 36 (2006) 18–29.

[31] X. Pardal, I. Pochard, A. Nonat, Experimental study of Si–Al substitution in calcium-silicate-hydrate (C-S-H) prepared under equilibrium conditions, Cement and Concrete Research 39 (2009) 637–643.

[32] D.S. Klimesch, A. Ray, Hydrogarnet formation during autoclaving at 180°C in unstirred metakaolin-lime-quartz slurries, Cement and Concrete Research 28 (1998) 1109–1117.

[33] M.U. Okoronkwo, F.P. Glasser, Compatibility of hydrogarnet, $Ca_3Al_2(SiO4)_x(OH)_{4(3-x)}$, with sulfate and carbonate-bearing cement phases: 5–85 °C, Cement and Concrete Research 83 (2016) 86–96.

[34] R.I. Harker, Scawtite and its synthesis, Mineralogical Magazine and Journal of the Mineralogical Society 34 (1965) 232–236.

[35] K. Kyritsis, C. Hall, D.P. Bentz, N. Meller, M.A. Wilson, Relationship between engineering properties, mineralogy, and microstructure in cement-based hydroceramic materials cured at 200°-350°C, Journal of the American Ceramic Society 92 (2009) 694–701.

[36] E.B. Nelson, D. Guillot, Well cementing, 2nd ed., Schlumberger, Sugar Land, Tex., 2006.

2.5 A commercial UHPC compound

In this section, a commercial UHPC product Nanodur® Compound 5941 is used to confirm the findings derived from the previous section. This compound comprises 59 wt. % CEM II/B-S 52.5 R and 41 wt. % quartz powder. A large amount of quartz powder is beneficial to maintain the poorly crystallized C-S-H with a low Ca/Si ratio under autoclaving, which favors microstructure densification.

2.5.1 Materials and methods

Nanodur® Compound 5941 is produced by Dyckerhoff GmbH for the simple production of UHPC. Different contents of fly ash are introduced to adjust the mixture compositions. The particle size distributions of the raw materials are shown in Fig. 2.13. Their chemical compositions are determined by X-ray fluorescence, as shown in Table 2.3. The mixture recipes are given in Table 2.4. According to the supplier's suggestion, the water/solid (Nanodur® Compound 5941 + fly ash) ratio is set as 0.16, which the water in the superplasticizer is not included. The dosage of the superplasticizer MasterGlenium ACE 430 (MBCC group) is 1.3% by weight of solid.
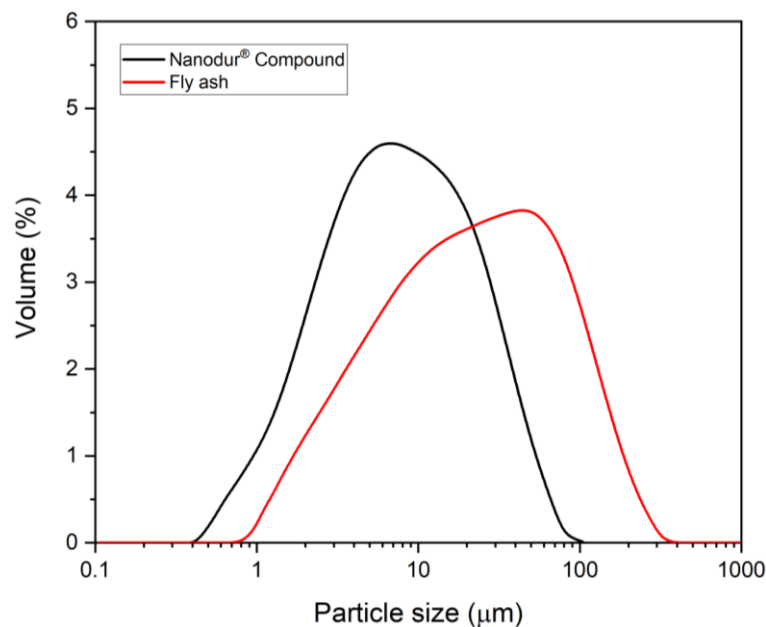

Fig. 2.13 Particle size distributions of the raw materials measured by laser diffraction.

Table 2.3 Recipes of the mixtures (wt. %).

	NC	NCF20	NCF40
Nanodur® Compound 5941	100	80	60
Fly ash	0	20	40

Table 2.4 Chemical compositions of the raw materials (wt. %).

	Nanodur® Compound 5941	Fly ash
SiO_2	55.35	53.26
CaO	34.29	5.40
Al_2O_3	3.60	20.61
K_2O	0.38	2.11
MgO	1.48	2.32
Mn_2O_3	0.06	0.07
Na_2O	0.23	0.88
P_2O_5	0.07	0.99
Fe_2O_3	0.68	7.68
SO_3	2.06	0.77
TiO_2	0.26	0.85
LOI	1.21	2.99
Sum	98.89	97.93

After thoroughly mixing, the pastes were cast into small cubic molds 2 x 2 x 2 cm^3. The autoclaving used in this section was the same as that in section 2.4. The characterization methods XRD and MIP were also used to analyze the evolution of hydrates assemblage and pore structures with autoclaving. In addition, TG analysis was performed to study the variation of bound water in autoclaved samples. The TG measurements were carried out using a TG 209 F3 Tarsus® (NETZSCH) in a nitrogen atmosphere with a 30 mL/min flow rate. 10 ± 1 mg of powder sample was used for each measurement. The temperature was increased from 20 °C to 850 °C at a rate of 10 °C/min.

2.5.2 Results and discussion

2.5.2.1 XRD analysis

The hydrates evolution of the pure cement compound (without fly ash) with autoclaving is shown in Fig. 2.14. For the reference sample NC-R, a significant amount of C_3S and C_2S are still unhydrated after 28 d of normal curing. The typical hydration products of amorphous C-S-H, ettringite, and portlandite are identified. However, once subjected to autoclaving, the hydration kinetics and hydrates are substantially changed. The peak intensities of clinkers in NC-1 are weaker than that in NC-R, indicating the accelerated hydration by autoclaving. Ettringite disappears in autoclaved samples due to its instability at high temperatures [1,2]. Instead, Si-poor hydrogarnet is identified. Hydroxyellestadite forms in autoclaved samples, which accumulates the released SO_4^{2-} by ettringite decomposition. Portlandite gradually decreases with autoclaving due to the pozzolanic reaction with quartz powder. Tobermorite, xonotlite, and scawtite form as the main crystalline C-S-H after 50 cycles of autoclaving due to the presence of a large amount of quartz powder. Tobermorite becomes unstable at temperatures above ~150 °C, and the insertion of Al can improve its thermal stability [3,4]. The initially formed Si-poor hydrogarnet gradually decreases with autoclaving, providing Al for the stabilization of tobermorite [5]. The diffuse peak at 2θ ~29.4° indicates the presence of poorly crystallized C-S-H, which is also reported in [5,6]. The persistence of such poorly crystallized C-S-H without conversation to crystalline phases is due to the formation of C-S-H precursor with a low Ca/Si ratio and the limited space in the matrix (high solid volume fraction), which is detailedly discussed in the previous section.
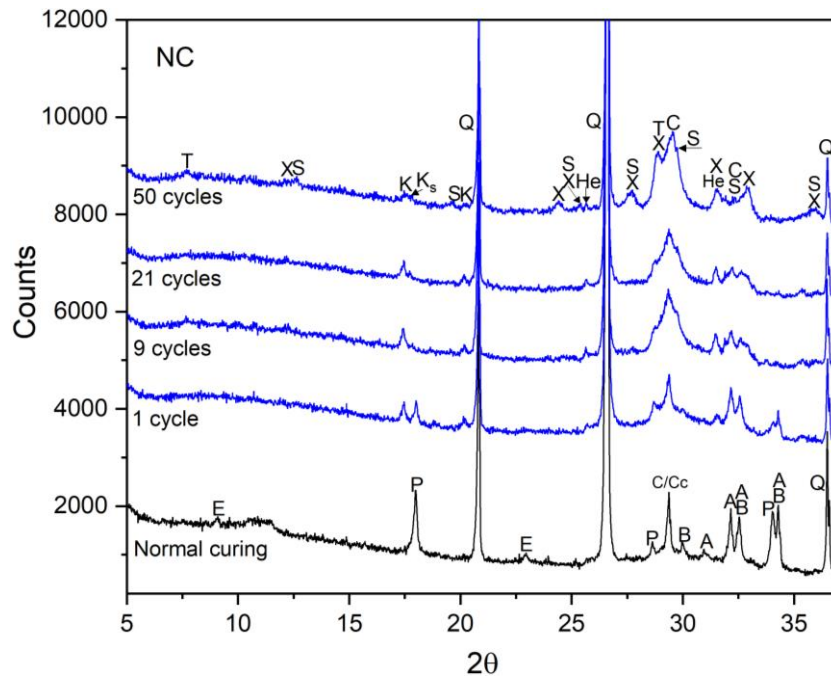
Fig. 2.14 XRD patterns of the pure cement compound (X: xonotlite, T: tobermorite, S: scawtite, He: hydroxylellestadite, K: Si-poor hydrogarnet, Ks: Si-rich hydrogarnet, C: C-S-H, P: portlandite, Q: quartz, E: ettringite, A: alite, B: belite, Cc: calcite).

The XRD results of the blended samples NCF20 and NCF40 are shown in Fig. 2.15. The incorporation of fly ash leads to the main hydrate of tobermorite. It is well reported that Al can accelerate the transformation of C-S-H precursor to tobermorite and improve its thermal stability under hydrothermal conditions [7,8]. In addition, the effective Ca/Si ratio of the matrix may also be changed by fly ash, which affects the tobermorite formation. However, it is difficult to determine whether the effective Ca/Si ratio increases or decreases, because the specific components of the Nanodur® Compound 5941 and their activities are unknown. Hydroxylellestadite first forms after one autoclaving cycle and decreases gradually with autoclaving (tobermorite increase), generating anhydrite.
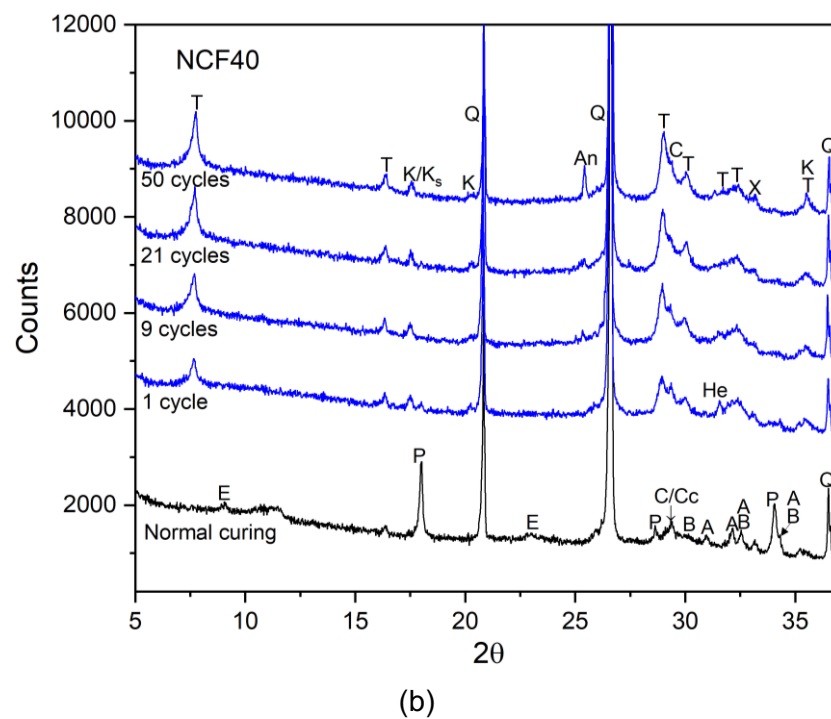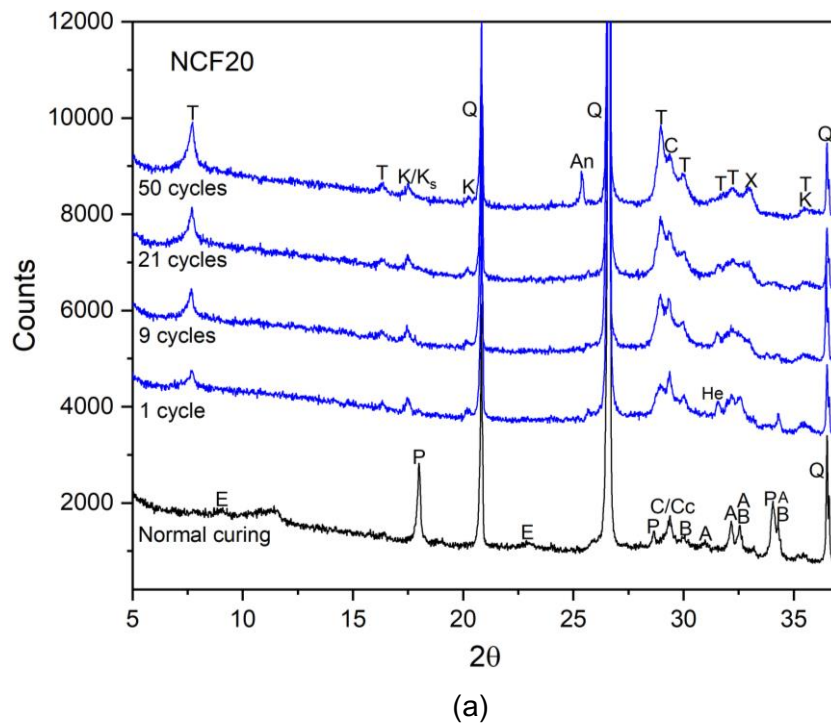
(a)

(b)

Fig. 2.15 XRD patterns of the blended samples: (a) NCF20 and (b) NCF40 (T: tobermorite, He: hydroxylellestadite, X: xonotlite, K: Si-poor hydrogarnet, K_s: Si-rich hydrogarnet, An: anhydrite, C: C-S-H, P: portlandite, Q: quartz, E: ettringite, A: alite, B: belite, Cc: calcite).

2.5.2.2 TG analysis

Thermogravimetric analysis of the pure cement compound is shown in Fig. 2.16. For the reference sample NC-R, four main mass loss peaks can be identified by the DTG curve. The first peak between around 50-250 °C is assigned to the decomposition of ettringite and the water loss in amorphous C-S-H [9,10]. The second sharp peak centered at ~430 °C corresponds to the portlandite dehydroxylation. The third peak at ~620 °C is contributed by the carbonates decomposition. The last shallow peak reflects the dehydroxylation of C-S-H [9,11].

The signals of the autoclaved samples are different. The evolution of water loss between 50-250 °C with autoclaving is plotted as shown in Fig. 2.17. Due to the decomposition of ettringite, the water loss between 50-250 °C is mainly contributed by the loss of loosely bound water in C-S-H. For NC-1, a large amount of C-S-H rapidly forms after one autoclaving cycle, and the decrease of water loss between 50-250 °C from NC-1 to NC-9 is owing to the transformation of amorphous C-S-H to more ordered phases, losing the excessive gel water. However, an increase from NC-9 to NC-20 is observed, probably because the cement is significantly decreased and the ratio of silica to cement thus increases in the late stage of autoclaving, leading to the formation of C-S-H with a low Ca/Si ratio which has low convertibility to crystalline phases. A similar result is also reported in the hydrothermally cured mixtures of cement, quartz, and lime, which the C-S-H with a high Ca/Si ratio tends to form rapidly and then reacts with the dissolved silica at the late stage of hydrothermal curing, resulting in the C-S-H with a lower Ca/Si ratio [12]. This phenomenon also exists in the mixture of cement and silica fume under room temperature: the initially formed C-S-H possesses a higher Ca/Si ratio than the later formed C-S-H, especially once the portlandite is consumed entirely [13]. From NC-20 to NC-50, the water loss between 50-250 °C shows a slight increase. The broad peak between 250–570 °C (Fig. 2.16) relates to the decomposition of hydrogarnet at above 260 °C [14] and scawtite to xonotlite and calcite at ~400 °C, losing one molecular water per formula unit [15]. The peak at ~620 °C corresponds to the carbonates decarbonation. The last peak at ~790 °C is owing to the dehydroxylation of C-S-H, recrystallizing into wollastonite $Ca_3Si_3O_9$ [16].
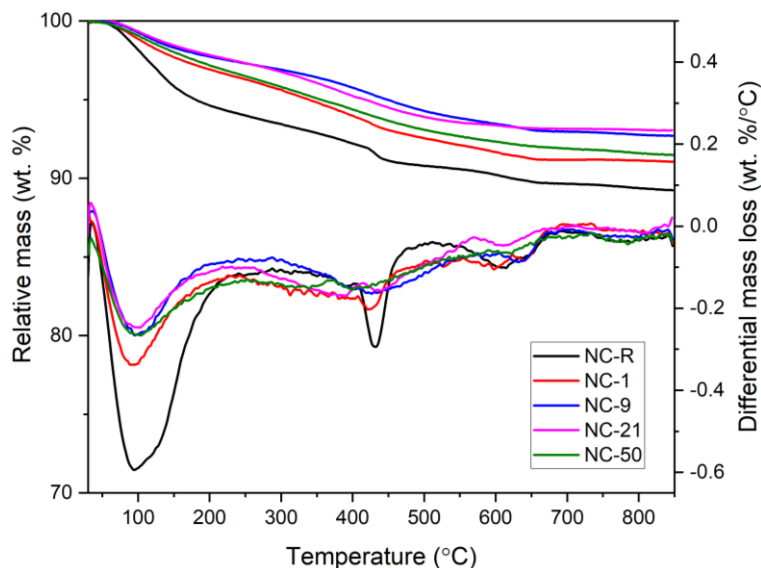
Fig. 2.16 TG and DTG diagrams of the pure cement compound.
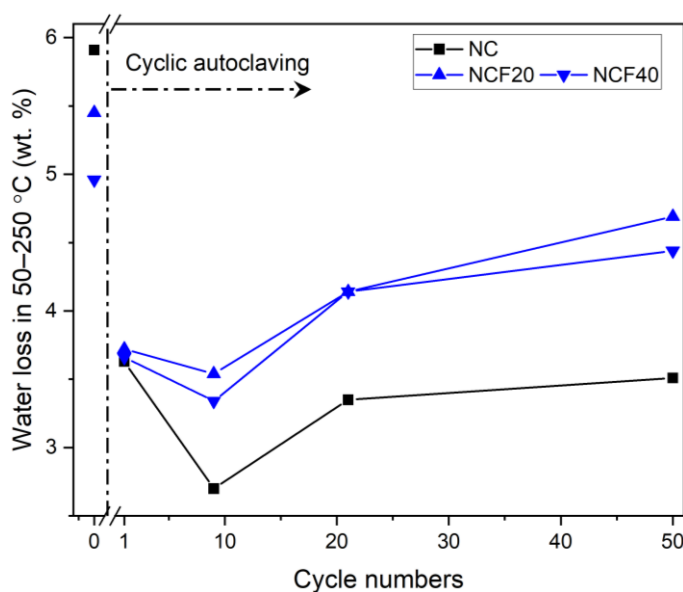
Fig. 2.17 The evolution of mass loss between 50-250 °C with autoclaving.

The TG and DTG diagrams of NCF20 and NCF40 are shown in Fig. 2.18. It is reported that tobermorite loses the four loosely bound molecular water per formula unit from 50 to 250 °C, and the remaining molecular water is lost between 250-750 °C [16,17]. Therefore, the first peak of mass loss between 50-250 °C corresponds to the water loss in poorly crystallized C-S-H and the partial dehydration of tobermorite. The evolution of water loss between 50-250 °C

with autoclaving of autoclaved NCF20 and NCF40 is shown in Fig. 2.17. The water loss between 50-250 °C first decreases from NCF20-1 to NCF20-9 due to the conversion of initially formed C-S-H to tobermorite, losing the excessive gel water. The further increase of tobermorite and the formation of C-S-H with a low Ca/Si ratio with autoclaving lead to the increase of water loss from NCF20-9 to NCF20-50. NCF40 shows a similar evolution of water loss between 50-250 °C with autoclaving.
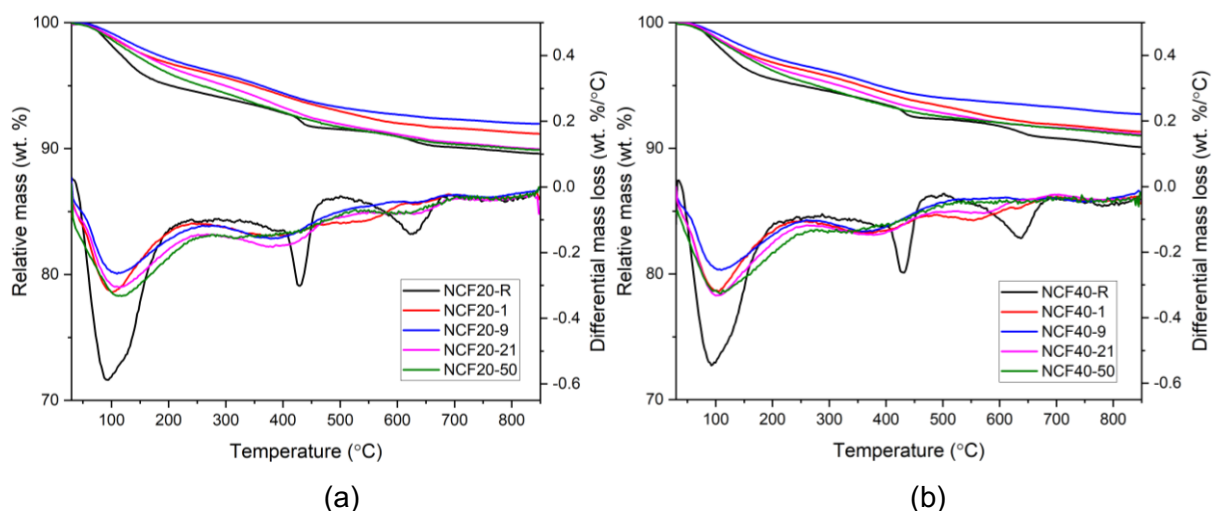

(a)   (b)

Fig. 2.18 TG and DTG diagrams of the blended samples: (a) NCF20 and (b) NCF40.

2.5.2.3 Pore structure analysis

The pore structures of NC and NCF40 are shown in Fig. 2.19. It can be seen that the porosity of NC-1 is decreased by one autoclaving cycle compared with that of NC-R. Meanwhile, the critical pore diameter of NC-1 is shifted to a lower value. This result coincides with the literature [18,19] which the microstructure of UHPC is significantly densified by several hours of autoclaving due to the accelerated hydrates formation. However, the porosity of NC-9 is greatly increased. As confirmed by XRD and TG analysis, the initially formed C-S-H gradually converts to more ordered phases with autoclaving, losing the excessive gel water and leading to a decreased solid volume. Thus, the porosity increases from NC-1 to NC-9, consistent with the decrease of water loss between 50-250 °C from NC-1 to NC-9 (Fig. 2.17). Nonetheless, the porosity of NC-50 is decreased as more hydrates are generated with autoclaving. Furthermore, the C-S-H formed in the late stage of autoclaving tends to have a low Ca/Si ratio, which is hard to convert to crystalline phases and benefits the microstructure densification.
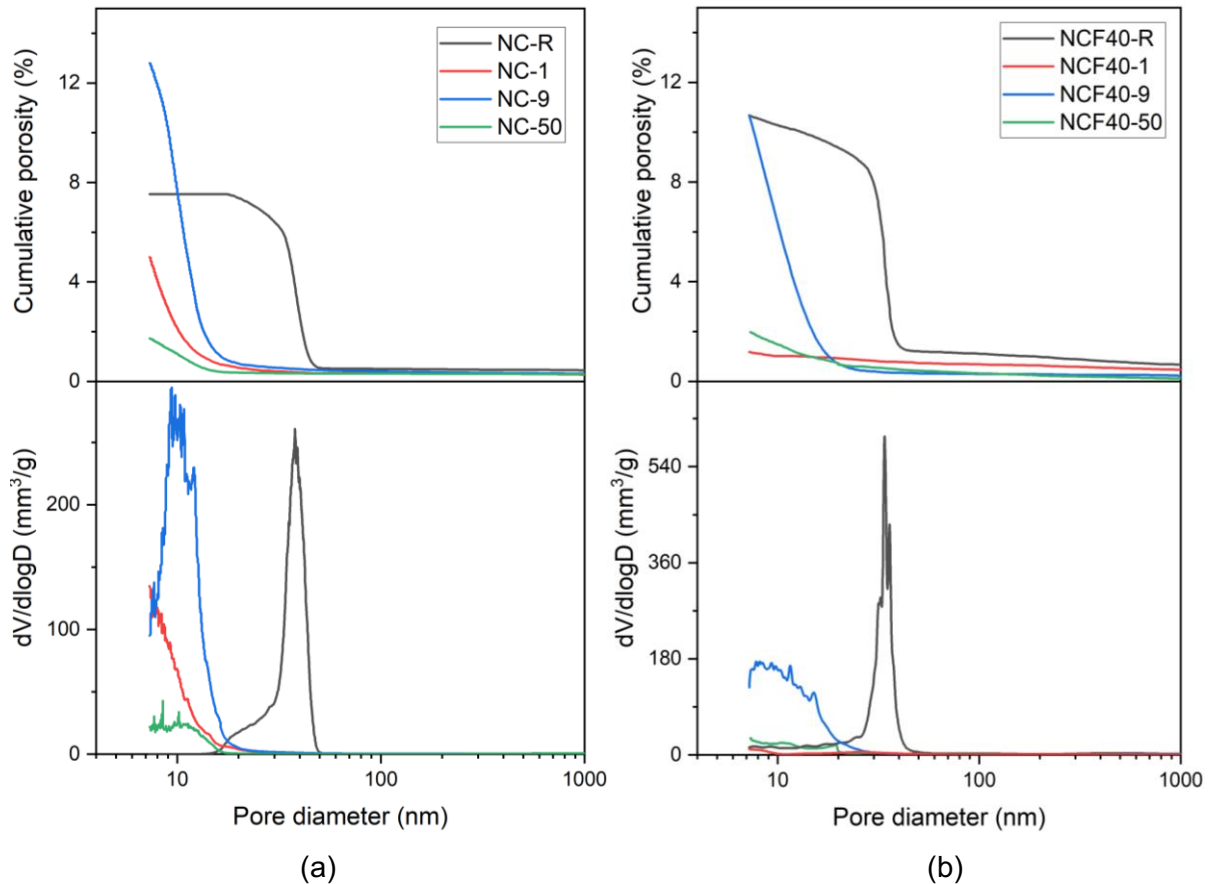
Fig. 2.19 Pore structures of the pure cement compound (a) and the blended cement compound with 40 wt. % fly ash (b).

NCF40 presents a similar evolution of pore structure with autoclaving: the porosity first decreases from NCF40-R to NCF40-1, then increases from NCF40-1 to NCF40-9, and finally decreases from NCF40-9 to NCF40-50. This evolution of porosity coincides with the variation of water loss between 50-250 °C with autoclaving (Fig. 2.17). Due to the presence of a large amount of silica, tobermorite and poorly crystallized C-S-H form as the main hydrates, preventing the formation of crystalline C-S-H with high density and ensuring the densified microstructure.

2.5.3 Conclusion

This section studies the performance of a commercial UHPC compound under autoclaving. Due to the presence of a large amount of quartz powder, the pure compound presents the main silicate hydrates of tobermorite, xonotlite, scawtite, and poorly crystallized C-S-H. Si-poor hydrogarnet is identified and gradually decreases with autoclaving, providing Al for tobermorite

stabilization. The addition of fly ash leads to tobermorite as the main hydrate. Hydroxylellestadite first forms after one autoclaving cycle and decomposes as an intermediate of tobermorite in the subsequent autoclaving, generating anhydrite.

Compared with normal curing, one autoclaving cycle decreases the porosity of the matrix. However, the porosity is then increased in the subsequent autoclaving due to the initially formed C-S-H gradually converts to more ordered phases. Nonetheless, the final porosity is decreased as more hydrates are generated with autoclaving. In addition, the C-S-H with a low Ca/Si ratio forms in the late stage of autoclaving, benefiting microstructure densification.

2.5.4 References

[1] N. Meller, K. Kyritsis, C. Hall, The hydrothermal decomposition of calcium monosulfoaluminate 14-hydrate to katoite hydrogarnet and β-anhydrite: An in-situ synchrotron X-ray diffraction study, Journal of Solid State Chemistry 182 (2009) 2743–2747.

[2] V. Satava, O. Veprek, Thermal decomposition of ettringite under hydrothermal conditions, Journal of the American Ceramic Society 58 (1975) 357–359.

[3] S.Y. Hong, F.P. Glasser, Phase relations in the $CaO\text{-}SiO_2\text{-}H_2O$ system to 200 °C at saturated steam pressure, Cement and Concrete Research 34 (2004) 1529–1534.

[4] S. Shaw, S. Clark, C. Henderson, Hydrothermal formation of the calcium silicate hydrates, tobermorite ($Ca_5Si_6O_{16}(OH)_2\cdot4H_2O$) and xonotlite ($Ca_6Si_6O_{17}(OH)_2$): an in situ synchrotron study, Chemical Geology 167 (2000) 129–140.

[5] K. Matsui, J. Kikuma, M. Tsunashima, T. Ishikawa, S.-Y. Matsuno, A. Ogawa, M. Sato, In situ time-resolved X-ray diffraction of tobermorite formation in autoclaved aerated concrete: Influence of silica source reactivity and Al addition, Cement and Concrete Research 41 (2011) 510–519.

[6] K.J. Krakowiak, J.J. Thomas, S. James, M. Abuhaikal, F.-J. Ulm, Development of silica-enriched cement-based materials with improved aging resistance for application in high-temperature environments, Cement and Concrete Research 105 (2018) 91–110.

[7] C. Rios, C. Williams, M. Fullen, Hydrothermal synthesis of hydrogarnet and tobermorite at 175 °C from kaolinite and metakaolinite in the $CaO\text{–}Al_2O_3\text{–}SiO_2\text{–}H_2O$ system: A comparative study, Applied Clay Science 43 (2009) 228–237.

[8] S. Eℓ-Hemaly, T. Mitsuda, H. Taylor, Synthesis of normal and anomalous tobermorites, Cement and Concrete Research 7 (1977) 429–438.

[9] R.J. Myers, E. L'Hôpital, J.L. Provis, B. Lothenbach, Effect of temperature and aluminium on calcium (alumino)silicate hydrate chemistry under equilibrium conditions, Cement and Concrete Research 68 (2015) 83–93.

[10] X. Guo, F. Meng, H. Shi, Microstructure and characterization of hydrothermal synthesis of Al-substituted tobermorite, Construction and Building Materials 133 (2017) 253–260.

[11] T. Maeshima, H. Noma, M. Sakiyama, T. Mitsuda, Natural 1.1 and 1.4 nm tobermorites from Fuka, Okayama, Japan: Chemical analysis, cell dimensions, 29Si NMR and thermal behavior, Cement and Concrete Research 33 (2003) 1515–1523.

[12] T. Mitsuda, K. Sasaki, H. Ishida, Phase evolution during autoclaving process of aerated concrete, Journal of the American Ceramic Society 75 (1992) 1858–1863.

[13] J.E. Rossen, B. Lothenbach, K.L. Scrivener, Composition of C–S–H in pastes with increasing levels of silica fume addition, Cement and Concrete Research 75 (2015) 14–22.

[14] J.M. Rivas-Mercury, P. Pena, A.H. de Aza, X. Turrillas, Dehydration of $Ca_3Al_2(SiO_4)_y(OH)_{4(3-y)}$ (0<y<0.176) studied by neutron thermodiffractometry, Journal of the European Ceramic Society 28 (2008) 1737–1748.

[15] S. Marincea, E. Bilal, J. Verkaeren, M.-L. Pascal, M. Fonteilles, Superposed parageneses in the spurrite-, tilleyite-and gehlenite-bearing skarns from Cornet Hill, Apuseni Mountains, Romania, The Canadian Mineralogist 39 (2001) 1435–1453.

[16] S. Shaw, C. Henderson, B. Komanschek, Dehydration/recrystallization mechanisms, energetics, and kinetics of hydrated calcium silicate minerals: an in situ TGA/DSC and synchrotron radiation SAXS/WAXS study, Chemical Geology 167 (2000) 141–159.

[17] C. Biagioni, E. Bonaccorsi, M. Lezzerini, S. Merlino, Thermal behaviour of Al-rich tobermorite, European Journal of Mineralogy 28 (2016) 23–32.

[18] H. Zhang, T. Ji, B. He, L. He, Performance of ultra-high performance concrete (UHPC) with cement partially replaced by ground granite powder (GGP) under different curing conditions, Construction and Building Materials 213 (2019) 469–482.

[19] H. Zhang, T. Ji, X. Lin, Pullout behavior of steel fibers with different shapes from ultra-high performance concrete (UHPC) prepared with granite powder under different curing conditions, Construction and Building Materials 211 (2019) 688–702.

3 Main results and discussion

3.1 Phase assemblage

According to the actual requirements of the project, the autoclaving temperature is set as 200 °C. The characterization of phase assemblage is carried out on small cubic samples (2 x 2 x 2 cm^3) without aggregate. After a pre-curing for one day, the samples are subjected to long-term autoclaving. In this section, the influence of mixture compositions and water/solid (w/s) ratio on the phase assemblage (clinkers and hydrates) under autoclaving is discussed. The mixture compositions are changed by adding quartz powder, fly ash or limestone powder, aiming to adjust the relative contents of the main elements Ca, Si, and Al in the matrix. Two w/s ratios are used to study the role of water in cement hydration and hydrates transformation under autoclaving.

Compared with normal curing, autoclaving accelerates the clinkers hydration. As confirmed by XRD in section 2.4, the peaks of C_3S and C_2S in the samples after one autoclaving cycle are even weaker than that in the reference samples after 28 d of normal curing. It is well known that cement usually cannot hydrate entirely in UHPC under normal conditions due to the low w/b ratio. However, according to the SEM images of the samples after 10 d of autoclaving, no sign of C_3S and C_2S is observed (sections 2.2 and 2.3). This is probably due to the transformation of amorphous C-S-H to more ordered phases, releasing the redundant gel water, and the hydration of C_3S and C_2S can thus achieve a higher degree under autoclaving. Besides, ettringite and AFm phases decompose under autoclaving, and hydrogarnet instead forms with lower water content, which releases more bound water and may also favor the hydration of C_3S and C_2S.

Nonetheless, a certain amount of C_4AF phase is partially unhydrated after the long-term autoclaving, which is confirmed by XRD and SEM analysis. The behavior of this phase under autoclaving is detailedly studied in section 2.2 by SEM. The areas around C_4AF are porous and loose, probably because the initially formed ettringite and AFm phases during pre-curing at room temperature decompose under autoclaving, leading to the formation of hydrogarnet and hydroxylellestadite with high densities and thus the unfilled cavity. It is observed that the partially unhydrated C_4AF particle is encased by a dense hydrate layer (or reaction rim). C_4AF phase generally hydrates fast once in contact with water, and calcium sulfates are usually added to suppress its hydration, probably by the adsorption of sulfate ion on active dissolution sites and forming sulfate-AFm gel around anhydrous particles [1,2]. However, sulfate-AFm gel

129

is unstable under autoclaving. According to the EDX element point analysis, the main elements in the hydrate layer are Ca, Si, Al, Fe, and S. The possible hydrate containing Ca, Si, Al, Fe, and S of Portland cement under autoclaving is Al intermixed siliceous hydrogarnet ($Ca_3(Al_xFe_{1-x})_2(SiO_4)_y(OH)_{4(3-y)}$; $0<x<1$, $0<y<3$) [3]. However, the element ratio of Ca/(Al + Fe) in the hydrate layer is much higher than that in the hydrogarnet, which rules out the possibility that the hydrate layer is exclusively constructed of hydrogarnet. Note that the Si/Ca ratio of the hydrate layer is slightly lower than that of the matrix. Al and S [4–6] have also been reported to insert into C-S-H under autoclaving (175 and 200 °C) by replacing Si, and Fe inserts into C-S-H by replacing Ca [7–9]. Thus, it is speculated that the dense hydrate layer is built by C-S-H or the combination of C-S-H and hydrogarnet, which hinders the hydration of C_4AF under autoclaving. The retardation of C_4AF phase after heat curing is also reported in the literature [10], and a higher temperature exerts a stronger retardation effect (20-100 °C).

In addition to cement clinkers, the hydrates assemblage is substantially changed by autoclaving, and the types of hydrates depends on the temperature and the composition of raw materials. The influence of mixture compositions, w/s ratios, and autoclaving time on the hydrates assemblage is briefly summarized in Table 3.1. The typical hydrates of Portland cement system at room temperature are amorphous C-S-H, portlandite, and ettringite. Due to the main components of C_3S, C_2S, C_3A, C_4AF, and $C\overline{S}H_x$, a pure Portland cement paste presents the environment with a high Ca/Si ratio. Therefore, jaffeite, reinhardbraunsite, and hydroxylellestadite are identified as the main crystalline silicate hydrates under autoclaving. Ettringite disappears and hydrogarnet instead forms which keeps constant under autoclaving. The sulfate released from the decomposition of ettringite precipitates in hydroxylellestadite and inserts into C-S-H. Due to the absence of additional silica, the pozzolanic reaction of portlandite in pure cement pastes is weak, but portlandite can also participate in hydrothermal reactions by the reaction with C-S-H, generating the C-S-H with a higher Ca/Si ratio, such as the transformation of hillebrandite to jaffeite.

The compositions of raw materials play a significant role in the hydrates formation under autoclaving. Quartz powder is used in section 2.4 to adjust the compositions of cement pastes, aiming to study the influence of Ca/Si ratio on the hydrates assemblage. It is proved that quartz powder can actively participate in hydrothermal reactions by providing Si. Due to the decreased Ca/Si ratio, xonotlite, scawtite, trabzonite and hydroxylellestadite are identified as the main crystalline silicate hydrates in the autoclaved samples with 20 wt. % quartz powder. Note that tobermorite and α-dicalcium silicate hydrate are identified at the early age of

autoclaving, but disappear in the subsequent autoclaving (LQ20-50), indicating that the formation kinetics of hydrates plays an important role in the hydrates assemblage during short-term autoclaving. However, the hydrates formed after long-term autoclaving depend more on their thermal stability and the availability of raw materials. The presence of quartz powder may lead to hydrates with a wide range of Ca/Si ratios. As observed in sections 2.2 and 2.3 by SEM, a reaction rim (or hydrate layer) occurs on the surface of quartz powder, which restricts the transportation of further dissolved ions. Therefore, a gradient difference of Ca/Si ratio may exist around quartz powder, and the hydrates formed around quartz powder thus tend to possess a relatively low Ca/Si ratio compared with the hydrates formed far away from quartz powder.

With the increase of quartz powder, poorly crystallized C-S-H is maintained under autoclaving. As mentioned in section 2.1, poorly crystallized C-S-H first forms from the rapid reaction of $Ca(OH)_2$ with SiO_2 [11] and then recrystallize into more stable and crystalline phases under hydrothermal conditions [12,13]. The transformation depends on the property of C-S-H precursor and the solid volume fraction of the matrix [14,15]. The C-S-H precursor with a low Ca/Si ratio tends to possess long and cross-linked chains of silicate tetrahedra, which is relatively hard to transform into crystalline phases as more bonds need to be reorganized compared with the C-S-H precursor with a high Ca/Si ratio [16–19]. The addition of a large amount of quartz powder greatly decreases the Ca/Si ratio of the matrix, leading to the formation of C-S-H precursor with a low Ca/Si ratio. Thus, the poorly crystallized C-S-H is identified by XRD even after long-term autoclaving. The influence of the solid volume fraction (w/s ratio) of the matrix on C-S-H transformation is discussed later. Besides, for the autoclaved samples with 40 wt. % quartz powder, only tobermorite is identified as the main crystalline silicate hydrate (section 2.4).

The addition of fly ash aims to study the influence of Al on the hydrates assemblage under autoclaving. It is proved that fly ash can provide active pozzolanic reaction under autoclaving, consuming portlandite. Compared with plain cement paste, the Ca/Si ratio of the blended matrix is effectively decreased, leading to the C-S-H with a lower Ca/Si ratio. In the samples with 20 wt. % fly ash (LF20-50), jaffeite, hydroxylellestadite, xonotlite, scawtite, and tobermorite form as the main crystalline silicate hydrates. As more fly ash is added (LF40), the Ca/Si ratio of the matrix is further decreased, and tobermorite thus generates massively. Besides, a large amount of hydrogarnet also exists in the samples with fly ash. The formation of tobermorite and hydrogarnet is highly sensible to the Al content in the matrix. At 200 °C, the formation of tobermorite is affected by the effective Ca/Si ratio and Al content in the matrix, because Al can

accelerate the transformation of C-S-H precursor to tobermorite and improve its thermal stability [15,20,21]. In the system with an appropriate Ca/Si ratio to tobermorite (LQ40 and HQ40 in section 2.4), the formation of tobermorite is accompanied by the decomposition of Si-poor hydrogarnet which releases Al for tobermorite stabilization. However, in the presence of excessive Al, Si-rich hydrogarnet massively forms, competing with tobermorite for the raw materials and thus retarding the tobermorite formation.

The two groups of Si-poor and Si-rich hydrogarnet can coexist. Their composition and persistence under autoclaving are controlled by the effective Si and Al contents in the matrix. Si-poor hydrogarnet can easily form in autoclaved samples, but its persistence is affected by the effective Si and Al contents. As mentioned above, in the system rich in Si and poor in Al, Si-poor hydrogarnet decomposes as the intermediate of tobermorite. However, Si-poor hydrogarnet can persist when the Ca/Si ratio in the matrix is adverse to tobermorite or there is enough Al which exceeds the upper limit of the incorporation of Al into tobermorite [22–25]. For Si-rich hydrogarnet, the composition is roughly calculated by plotting the Si content against the unit cell size, as shown in Fig. 2.8. Si-rich hydrogarnet can only form in the system rich in Al. The increase of Al and Si can increase the Si content of hydrogarnet. In the presence of enough Al, an exclusive increase of Si can also increase the Si content of hydrogarnet. The stabilizing effect of silica on hydrogarnet has been reported in [3,26]. This coincides with the persistence of Si-rich hydrogarnet under autoclaving.

Similar with Si-poor hydrogarnet, hydroxylellestadite can easily form in autoclaved samples, accumulating the released sulfate from the decomposition of ettringite. However, its persistence is highly related to the tobermorite formation. As it is reported that hydroxylellestadite can decompose as an intermediate of tobermorite [15], the formation of tobermorite is accompanied by the decrease of hydroxylellestadite in this study. Accordingly, anhydrite as a decomposition product of hydroxylellestadite can be identified. Two formation manners of hydroxylellestadite are observed. As discussed in section 2.2, hydroxylellestadite forms around the partially unhydrated C_4AF phase, probably due to the preferential formation of ettringite around the aluminous phase which provides raw materials for hydroxylellestadite by decomposition. However, such formation manner of hydroxylellestadite may lead to the unfilled cavity around the C_4AF phase due to the high density of hydroxylellestadite. In addition, hydroxylellestadite can form in the track of portlandite, filling up the area initially occupied by portlandite and presenting a leafy shape (pseudomorphic formation). This formation manner is also reported in [27].

The w/s ratio can exert a significant influence on the phase assemblage. The availability of raw materials for the hydrates formation is controlled by the w/s ratio. In the system with a low w/s ratio, the dissolution of the raw materials is incomplete, and a high w/s ratio can thus allow more dissolution of the raw materials. Therefore, the types and contents of the hydrates can be changed by the w/s ratio. As shown in section 2.4, HB-50 (high w/s ratio) has more portlandite and less jaffeite than LB-50, because the high water content accelerates clinkers (C_3S and C_2S) dissolution, generating more portlandite. The accelerated dissolution of C_2S thus decreases the Ca/Si ratio in HB-50, which is unfavorable for the formation of jaffeite. Trabzonite as a new crystalline C-S-H is observed in HQ20-50 (high w/s ratio), and the quartz powder is entirely consumed in HQ20-50. In contrast, there is no trabzonite in LQ20-50, and quartz powder still exists in LQ20-50. In addition, the solid volume fraction in the matrix varies with the w/s ratio, affecting the transformation of C-S-H precursor. As confirmed by XRD profile fitting, HQ40-50 (high w/s ratio) shows a higher ratio of tobermorite to poorly crystallized C-S-H compared with LQ40-50 due to the high solid volume fraction in LQ40 (low w/s ratio) and thus the limited space for crystallization. This effect is also reported in [15]. However, the influence of w/s ratio on the transformation of C-S-H precursor is not apparent in the autoclaved samples other than LQ40 and HQ40. This is probably because, in LQ40 and HQ40, the C-S-H precursor with a low Ca/Si ratio is hard to transform into crystalline phases and occupies more space due to the low density. Furthermore, tobermorite has a low density and needs more space for crystallization compared with other crystalline C-S-H phases, e.g., xonotlite, scawtite, and hydrogarnet. Thus, the inhibiting effect on the formation of tobermorite by high solid volume fraction of matrix is magnified in LQ40 and HQ40. In addition, the w/s ratio also influences the composition of hydrogarnet. For the samples with the same content of fly ash and/or quartz powder, a low w/s ratio gives the Si-rich hydrogarnet with a high Si content (more anhydrous, Fig. 2.8).

Due to the components silica fume and quartz powder, the C-S-H in autoclaved UHPC also present a low Ca/Si ratio confirmed by SEM element point analysis. Note that the particle size of quartz powder used in the UHPC mixtures (sections 2.2 and 2.3) is larger than that in the cement pastes (section 2.4). However, the formation of tobermorite in the UHPC with typical components (silica fume, cement, and quartz powder) is not apparent because of the deficiency of Al and the improper Ca/Si ratio of around 1.0-2.0 which is larger than that of tobermorite. The partial replacement of cement by fly ash increases the ratio of silica to cement and provides additional Al, as shown in section 2.3. Tobermorite is thus identified in the blended UHPC mixtures with fly ash (autoclaved C2). Besides, more poorly crystallized C-S-H is maintained in autoclaved C2 due to the decreased Ca/Si ratio. According to the SEM

element mapping, S mainly concentrates around aluminoferrite particles and the areas filled by hydroxylellestadite. Besides, it is reported that sulphate can be co-sorbed on the surface and interlayer of poorly crystallized C-S-H together with Ca^{2+} [28] and inserted into the structure of crystalline C-S-H under hydrothermal conditions [4]. Similarly, Al is also widely distributed in the matrix in addition to the part concentrated around aluminoferrite particles, originating from the formation of C-(A-)S-H and hydrogarnet.

The partial replacement of cement by a small amount of limestone powder leads to a comparable Ca/Si ratio in the hydrates between autoclaved L0 and L1. This is because the partial replacement of cement by limestone powder increases the ratio of silica to cement, while partially dissolved limestone powder can provide some Ca. However, due to the low solubility product, the presence of CO_3^{2-} in liquid, which can only be reduced by insertion into C-S-H, restricts the further dissolution of limestone powder, causing the limited participation of limestone powder in the hydrates formation. Therefore, the further increase of limestone powder, which cannot provide Ca as effectively as cement does, decreases the Ca/Si ratio in autoclaved L2 and L3, leading to more poorly crystallized C-S-H with a low Ca/Si ratio. Note that hydroxylellestadite can be decreased by addition of limestone powder or fly ash, as the content of sulfate, which is exclusively supplied by cement and essential to the formation of hydroxylellestadite, is decreased by the partial replacement of cement by limestone powder or fly ash.

Table 3.1 A brief summary for the influence of mixture compositions, w/s ratios, and autoclaving time on the hydrates assemblage.

	mixtures	main hydrates (after final autoclaving)	autoclaving time
cement pastes	C	portlandite[+], jaffeite[-], reinhardbraunsite, Si-poor hydrogarnet, hydroxylellestadite	hillebrandite + portlandite → jaffeite
	C+20 wt. % QP	xonotlite, scawtite, hydroxylellestadite, Si-poor hydrogarnet, trabzonite[1]	tobermorite and α-dicalcium silicate hydrate disappear with autoclaving; xonotlite forms faster than scawtite and trabzonite
	C+40 wt. % QP	tobermorite[+], C-S-H[-]	Si-poor hydrogarnet and hydroxylellestadite decompose with autoclaving
	C+20 wt. % FA	Si-rich hydrogarnet[2], Si-poor hydrogarnet, scawtite, hydroxylellestadite, xonotlite	
	C+40 wt. % FA	tobermorite[-], Si-rich hydrogarnet[+], Si-poor hydrogarnet, scawtite	hydroxylellestadite only decomposes in LF40 with autoclaving
	C+20 wt. % QP+20 wt. % FA	tobermorite, Si-rich hydrogarnet, scawtite	Si-poor hydrogarnet and hydroxylellestadite decompose with autoclaving
UHPC compounds	C+SF+QP[3]	C-S-H, hydroxylellestadite	
	C+SF+QP+10 wt. % LP	C-S-H[4], hydroxylellestadite	
	C+SF+QP+30 wt. % LP	C-S-H, hydroxylellestadite	
	C+SF+QP+50 wt. % LP	C-S-H, hydroxylellestadite	
	C+SF+QP+20 wt. % FA	C-S-H, tobermorite, hydroxylellestadite	
	a commercial UHPC	C-S-H, xonotlite, scawtite	
	a commercial UHPC+20 wt. % FA	C-S-H, tobermorite	
	a commercial UHPC+40 wt. % FA	C-S-H, tobermorite	

C: cement, QP: quartz powder, FA: fly ash, LP: limestone powder, SF: silica fume, C-S-H: poorly crystallized C-S-H. The proportions of QP, FA, and LP are represented by the replacement level of cement. For commercial UHPC compounds, the proportion of FA is represented by the replacement level of the compound.
[+] and [-] represent the formation is increased and decreased in the mixtures with a high w/s ratio, respectively.
[1] There is no quartz left in the mixtures with a high w/s ratio and the pozzolanic reaction is promoted by high water content. Trabzonite is only identified in the mixtures with a high w/s ratio.
[2] The composition of hydrogarnet depends on the relative contents of Ca, Si, and Al in the matrix.
[3] The particle size of the quartz powder used in UHPC compounds is larger than that in cement pastes.
[4] There is no apparent difference in Ca/Si ratio in autoclaved L0 and L1. Further increase of LP (autoclaved L2 and L3) decreases the Ca/Si ratio of the hydrates.

3.2 Pore structure

For the cement pastes with different contents of quartz powder and fly ash, the pore structures are analyzed after 50 cycles of autoclaving. The pore structures of the samples after autoclaving are significantly influenced by the mixture compositions. After long-term autoclaving, the plain cement paste shows a high porosity, and capillary pores dominate in the pore volume due to the absence of pozzolanic reaction and the formation of crystalline hydrates with high densities, e.g., reinhardbraunsite and jaffeite. Although the addition of fly ash induces active pozzolanic reaction, the porosities of the blended samples with a low w/s ratio are comparable with that of plain samples. At a high w/s ratio, the porosities of the blended samples with fly ash are even larger than that of plain samples. This is because the hydrogarnet with high density (low solid volume) massively forms in the samples with fly ash. In contrast, the samples with quartz powder show lower porosities due to formation of hydrates with lower densities than hydrogarnet. For example, the samples with 40 wt. % quartz powder present the lowest porosity due to the maintaining of poorly crystallized C-S-H. It is concluded that for a fixed w/s ratio, the formation of hydrates with low densities, e.g., tobermorite and poorly crystallized C-S-H, can provide high solid volume and thus densify microstructure, leading to a low porosity and finer texture. In contrast, the hydrates with high densities, e.g., trabzonite and Si-rich hydrogarnet, tend to give the matrix a large porosity. Under autoclaving, the sample with a low w/s ratio does not necessarily have a low porosity, such as that HB-50 (high w/s ratio) shows a slightly lower porosity than LB-50 (section 2.4).

The pore structure analysis of UHPC is carried out on the mixtures of cement, silica fume, and fine quartz powder. The pore structures of the samples are significantly affected by autoclaving. In section 2.2, compared with plain UHPC after normal curing, autoclaved plain UHPC shows a higher porosity and finer texture with a high proportion of gel pores. The newly formed hydrates under autoclaving tend to have high densities than the typical hydrates formed under normal condition. The accelerated formation of hydrates by autoclaving fills up capillary pores and generates more gel pores. The partial replacement of cement by limestone powder decreases hydrogarnet, hydroxylellestadite, and partially unhydrated ferrite phase, favoring microstructure densification. Furthermore, the addition of limestone powder decreases the Ca/Si ratio in the matrix and induces more poorly crystallized C-S-H, leading to a low porosity of UHPC. In section 2.3, the mixtures have a slightly higher w/b ratio than the mixtures in section 2.2. However, compared with plain UHPC after normal curing, autoclaved plain UHPC presents a lower porosity, probably because the high water content accelerates the pozzolanic

reaction, generating more hydrates. Besides, the partial replacement of cement by fly ash leads to a lower porosity of autoclaved C2. As confirmed by SEM, the partial replacement of cement by fly ash provides additional Si and increases the ratio of silica to cement, which results in more poorly crystallized C-S-H, providing more solid volume. Therefore, according to the pore size distribution curve, the pore volume of autoclaved C2 is dominated by gel pores, which mainly originates from the fine internal porosity of hydrates. However, compared with autoclaved C2, a larger fraction of the pores from 3 nm to 40 nm is shown in the differential curve of autoclaved C1. This part of pores contains gel and capillary pores, probably because more crystalline hydrates of scawtite, hydroxylellestadite, and hydrogarnet form in autoclaved C1, leading to the shrinkage of solid volume.

The evolution of pore structures with autoclaving is studied based on the commercial UHPC compound (section 2.5). This compound comprises 59 wt. % CEM II/B-S 52.5 R and 41 wt. % quartz powder. After the short-term autoclaving (NC-1 and NCF40-1), a low porosity and finer texture of the matrix are obtained, which coincides with the literature [29,30] that the microstructure of UHPC is significantly densified by several hours of autoclaving due to the accelerated hydrates formation. However, the porosity is then greatly increased in the subsequent autoclaving (NC-9 and NCF40-9), probably because the initially formed C-S-H gradually converts to more ordered phases with autoclaving, losing the excessive gel water and leading to a decreased solid volume (XRD and TG in section 2.5). Nonetheless, the final porosity (NC-50 and NCF40-50) after the long-term autoclaving is decreased, benefiting from the accelerated hydrates formation by autoclaving. Furthermore, the C-S-H formed in the late stage of autoclaving tends to have a low Ca/Si ratio, which is hard to convert to crystalline phases and benefits the microstructure densification.

3.3 Compressive and flexural strength

For autoclaved UHPC, the compressive strength can stay robust. It is confirmed that amorphous C-S-H can transform to more ordered phases after long-term autoclaving. Ettringite and AFm phases decompose and hydrogarnet instead forms under autoclaving. These hydrothermal reactions cause a decrease of solid volume, but the compressive strength is not affected. This is because the typical components of UHPC (silica fume and quartz powder) play a positive role in maintaining compressive strength, although their addition initially aims to compact the mixture packing density. The presence of a large amount of silica (silica fume and quartz powder) induces active pozzolanic reaction under autoclaving and leads to

tobermorite and poorly crystallized C-S-H as the main hydrates, preventing the strength degradation under long-term autoclaving.

However, the flexural strength is vulnerable to autoclaving. The transformation of amorphous C-S-H to more ordered phases leads to the degradation of bond strength and thus a low flexural strength. Limestone powder and fly ash are introduced to mitigate the detrimental effect caused by long-term autoclaving. In order to eliminate the effect caused by the variation of particle size distribution in the mixture, the contents of quartz powder and silica fume are not changed, and the particle sizes of limestone powder and fly ash are comparable to that of cement. Partially replacing cement with limestone powder or fly ash can change the relative contents of Ca, Si, and Al in the matrix, and thus the hydrates assemblage can be tailor-made under autoclaving.

After normal curing, the replacement of cement by limestone powder leads to a gradual decrease of compressive and flexural strength due to the dilution effect and the reduction of cementitious hydration products. However, the addition of limestone powder in autoclaved UHPC shows the different influence. The effective Ca/Si ratio in the matrix is decreased by partially replacing cement with a high amount of limestone powder (autoclaved L2), and more poorly crystallized C-S-H with a low Ca/Si ratio can be maintained, leading to the improved mechanical strength. Besides, foreign ions of Al and S which accelerate the C-S-H crystallization under autoclaving are also decreased by adding limestone. The poorly crystallized C-S-H thus shows low convertibility to more ordered phases under autoclaving. However, overmuch poorly crystallized C-S-H may lead to interstice in matrix-quartz powder interfaces and thus low mechanical strength (autoclaved L3). This is because the increase of poorly crystallized C-S-H increases the water content in matrix. The thermal mismatch between matrix and quartz powder/aggregate is thus magnified when the autoclaved samples cool to room temperature [31–33], leading to cracks around quartz particles.

The partial replacement of cement by fly ash (rich in Si and Al) also causes a slight decrease in compressive and flexural strength under normal curing. Nevertheless, appropriate addition of fly ash can improve the performance of UHPC under autoclaving. A clear interstice is observed in the interface between steel fibers and matrix of autoclaved plain UHPC. The addition of fly ash increases the Si and Al in the matrix, leading to the main hydrates of poorly crystallized C-S-H and tobermorite. The fiber-matrix interface is also densified, resulting in an improved bond strength. Tobermorite is a desirable hydrate for cement-based materials under autoclaving conditions, probably due to its low density, ensuring densified microstructure [34].

However, the content of fly ash should be restricted as fly ash (rich in Al) can effectively release Al, and excessive Al may result in the massive formation of hydrogarnet, which is detrimental to mechanical strength [35].

In addition, the mechanical strength of autoclaved samples is not strictly related to their porosity, and the effect of hydrate assemblage outweighs that of porosity concerning mechanical strength under autoclaving. The decrease of crystalline hydrates and increase of poorly crystallized C-S-H effectively decreases the porosity. However, due to the foregoing thermal mismatch between matrix and aggregate, a low porosity does not necessarily lead to high mechanical strength.

3.4 Supplementary cementitious materials

Quartz powder and fly ash are used in this research as the representatives of Si-rich and Al-rich SCMs, respectively. Unlike at room temperature, the addition of quartz powder can effectively decrease the matrix Ca/Si ratio under autoclaving, while fly ash can simultaneously increase the Si and Al content of the matrix. Limestone powder is also a practical SCM as a partial replacement of cement to adjust the Ca/Si ratio and tailor-make hydrates assemblage in UHPC under autoclaving. Appropriate addition of SCMs in UHPC can not only decrease the production cost and improve sustainability, but also intensify the performance of autoclaved UHPC. Note that the behavior of SCMs in autoclaved UHPC is highly affected by their availability which is controlled by the physicochemical properties, such as size and crystallinity. Inappropriate use of SCMs cannot effectively adjust the chemical compositions, leading to the undesired performance of UHPC. The impurities from SCMs can influence the formation of amorphous or poorly crystallized intermediates by accelerating or suppressing the dissolution of raw materials, induce the uptake of foreign ions in C-S-H, change the stability of crystalline phases, and result in additional phases. For example, alkalis and sulfate can accelerate the dissolution of silica-bearing raw materials, favoring the formation of amorphous intermediate C-S-H [4,5,36–38]. The uptake of Al, Mg, or Fe in C-S-H results in the preferential growth of tobermorite along the *b*-axis (silicate chains), forming a lath-like and needle-like morphology [39,40], while sulfate-substituted tobermorite crystals present larger leafy shapes [4]. The presence of excessive Na and Mg can generate pectolite and magnesium silicate hydrates, respectively [39,41,42]. Therefore, when SCMs are used under autoclaving, in addition to the physical parameters, the chemical and mineralogical compositions of the SCMs should be considered.

3.5 References

[1] D. Ectors, J. Neubauer, F. Goetz-Neunhoeffer, The hydration of synthetic brownmillerite in presence of low Ca-sulfate content and calcite monitored by quantitative in-situ-XRD and heat flow calorimetry, Cement and Concrete Research 54 (2013) 61–68.

[2] V. Morin, P. Termkhajornkit, B. Huet, G. Pham, Impact of quantity of anhydrite, water to binder ratio, fineness on kinetics and phase assemblage of belite-ye'elimite-ferrite cement, Cement and Concrete Research 99 (2017) 8–17.

[3] B.Z. Dilnesa, B. Lothenbach, G. Renaudin, A. Wichser, D. Kulik, Synthesis and characterization of hydrogarnet $Ca_3(Al_xFe_{1-x})_2(SiO_4)_y(OH)_{4(3-y)}$, Cement and Concrete Research 59 (2014) 96–111.

[4] N.Y. Mostafa, A.A. Shaltout, H. Omar, S.A. Abo-El-Enein, Hydrothermal synthesis and characterization of aluminium and sulfate substituted 1.1nm tobermorites, Journal of Alloys and Compounds 467 (2009) 332–337.

[5] K. Baltakys, R. Siauciunas, Influence of gypsum additive on the gyrolite formation process, Cement and Concrete Research 40 (2010) 376–383.

[6] K. Baltakys, Influence of gypsum additive on the formation of calcium silicate hydrates in mixtures with C/S = 0.83 or 1.0, Materials Science Poland Vol. 27, No. 4/1 (2009).

[7] G. Qian, D.D. Sun, J.H. Tay, Z. Lai, G. Xu, Autoclave properties of kirschsteinite-based steel slag, Cement and Concrete Research 32 (2002) 1377–1382.

[8] N.K. Labhasetwar, O.P. Shrivastava, Y.Y. Medikov, Mo¨ssbauer study on iron-exchanged calcium silicate hydrate: $Ca_{5-x}Fe_xSi_6O_{18}H_2 \cdot nH_2O$, Journal of Solid State Chemistry 93 (1991) 82–87.

[9] Sonja Haastrup, Donghong Yu, Yuanzheng Yue, Impact of minor iron content on crystal structure and properties of porous calcium silicates during synthesis, Materials Chemistry and Physics 205 (2018) 180–185.

[10] R. Yang, J.H. Sharp, Hydration characteristics of Portland cement after heat curing: I, Degree of hydration of the anhydrous cement phases, Journal of the American Ceramic Society 84 (2001) 608–614.

[11] G.O. Assarsson, Hydrothermal reactions between calcium hydroxide and amorphous silica: the reactions between 180 and 220°, The Journal of Physical Chemistry 61 (1957) 473–479.

[12] G.O. Assarsson, E. Rydberg, Hydrothermal reactions between calcium hydroxide and amorphous silica, The Journal of Physical Chemistry 60 (1956) 397–404.

[13] T. Mitsuda, H.F.W. Taylor, Influence of aluminium on the conversion of calcium silicate hydrate gels into 11 Å tobermorite at 90°C and 120°C, Cement and Concrete Research 5 (1975) 203–209.

[14] K.J. Krakowiak, J.J. Thomas, S. James, M. Abuhaikal, F.-J. Ulm, Development of silica-enriched cement-based materials with improved aging resistance for application in high-temperature environments, Cement and Concrete Research 105 (2018) 91–110.

[15] K. Matsui, J. Kikuma, M. Tsunashima, T. Ishikawa, S.-Y. Matsuno, A. Ogawa, M. Sato, In situ time-resolved X-ray diffraction of tobermorite formation in autoclaved aerated concrete: Influence of silica source reactivity and Al addition, Cement and Concrete Research 41 (2011) 510–519.

[16] 5 Hydration of the calcium silicate phases, in: H.F.W. Taylor (Ed.), Cement chemistry, Thomas Telford Ltd, London, 2009, pp. 113–156.

[17] J.J. Chen, J.J. Thomas, H.F.W. Taylor, H.M. Jennings, Solubility and structure of calcium silicate hydrate, Cement and Concrete Research 34 (2004) 1499–1519.

[18] I.G. Richardson, Tobermorite/jennite- and tobermorite/calcium hydroxide-based models for the structure of C-S-H: applicability to hardened pastes of tricalcium silicate, β-dicalcium silicate, Portland cement, and blends of Portland cement with blast-furnace slag, metakaolin, or silica fume, Cement and Concrete Research 34 (2004) 1733–1777.

[19] A. Nonat, The structure and stoichiometry of C-S-H, Cement and Concrete Research 34 (2004) 1521–1528.

[20] S.Y. Hong, F.P. Glasser, Phase relations in the CaO-SiO_2-H_2O system to 200 °C at saturated steam pressure, Cement and Concrete Research 34 (2004) 1529–1534.

[21] S. Shaw, S. Clark, C. Henderson, Hydrothermal formation of the calcium silicate hydrates, tobermorite ($Ca_5Si_6O_{16}(OH)_2 \cdot 4H_2O$) and xonotlite ($Ca_6Si_6O_{17}(OH)_2$): an in situ synchrotron study, Chemical Geology 167 (2000) 129–140.

[22] E. L'Hôpital, B. Lothenbach, G. Le Saout, D. Kulik, K. Scrivener, Incorporation of aluminium in calcium-silicate-hydrates, Cement and Concrete Research 75 (2015) 91–103.

[23] G.K. Sun, J.F. Young, R.J. Kirkpatrick, The role of Al in C–S–H: NMR, XRD, and compositional results for precipitated samples: NMR, XRD, and compositional results for precipitated samples, Cement and Concrete Research 36 (2006) 18–29.

[24] X. Pardal, I. Pochard, A. Nonat, Experimental study of Si–Al substitution in calcium-silicate-hydrate (C-S-H) prepared under equilibrium conditions, Cement and Concrete Research 39 (2009) 637–643.

[25] D.S. Klimesch, A. Ray, Hydrogarnet formation during autoclaving at 180°C in unstirred metakaolin-lime-quartz slurries, Cement and Concrete Research 28 (1998) 1109–1117.

[26] M.U. Okoronkwo, F.P. Glasser, Compatibility of hydrogarnet, $Ca_3Al_2(SiO_4)_x(OH)_{4(3-x)}$, with sulfate and carbonate-bearing cement phases: 5–85 °C, Cement and Concrete Research 83 (2016) 86–96.

[27] C. Lehmann, Neue Perspektiven für Ultra-Hochleistungsbeton durch gezielte Beeinflussung des Nanogefüges, Technische Universität Berlin, 2013.

[28] R. Barbarulo, H. Peycelon, S. Leclercq, Chemical equilibria between C–S–H and ettringite, at 20 and 85 °C, Cement and Concrete Research 37 (2007) 1176–1181.

[29] H. Zhang, T. Ji, B. He, L. He, Performance of ultra-high performance concrete (UHPC) with cement partially replaced by ground granite powder (GGP) under different curing conditions, Construction and Building Materials 213 (2019) 469–482.

[30] H. Zhang, T. Ji, X. Lin, Pullout behavior of steel fibers with different shapes from ultra-high performance concrete (UHPC) prepared with granite powder under different curing conditions, Construction and Building Materials 211 (2019) 688–702.

[31] M.H.H. Hettema, The thermo-mechanical behaviour of sedimentary rock: An experimental study, 1996.

[32] Y. El Bitouri, F. Jamin, C. Pélissou, M.S. El Youssoufi, Tensile and shear bond strength between cement paste and aggregate subjected to high temperature, Materials and Structures 50 (2017).

[33] H. Cagnon, T. Vidal, A. Sellier, C. Soula, X. Bourbon, G. Camps, Effects of water and temperature variations on deformation of limestone aggregates, cement paste, mortar and High Performance Concrete (HPC), Cement and Concrete Composites 71 (2016) 131–143.

[34] E.B. Nelson, D. Guillot, Well cementing, 2nd ed., Schlumberger, Sugar Land, Tex., 2006.

[35] K. Kyritsis, C. Hall, D.P. Bentz, N. Meller, M.A. Wilson, Relationship between engineering properties, mineralogy, and microstructure in cement-based hydroceramic materials cured at 200°-350°C, Journal of the American Ceramic Society 92 (2009) 694–701.

[36] W. NocuÒ-Wczelik, Effect of Na and Al on the phase composition and morphology of autoclaved calcium silicate hydrates, Cement and Concrete Research 29 (1999) 1759–1767.

[37] E.A. Blakeman, J.A. Gard, C.G. Ramsay, H.F.W. Taylor, Studies on the system sodium oxide-calcium oxide-silica-water, Journal of Applied Chemistry and Biotechnology 24 (1974) 239–245.

[38] R. Siauciunas, A. Bankauskaite, K. Baltakys, M. Stankeviciute, The impact of Na_2O on the synthesis of α-C_2SH with different mineral composition and the stability of intermediate and final products, Ceramics International 45 (2019) 2846–2851.

[39] N.Y. Mostafa, E.A. Kishar, S.A. Abo-El-Enein, FTIR study and cation exchange capacity of Fe^{3+}- and Mg^{2+}-substituted calcium silicate hydrates, Journal of Alloys and Compounds 473 (2009) 538–542.

[40] X. Qu, Z. Zhao, X. Zhao, Microstructure and characterization of aluminum-incorporated calcium silicate hydrates (C–S–H) under hydrothermal conditions, RSC Advances 8 (2018) 28198–28208.

[41] E.B. Nelson, G.L. Kalousek, Effects of Na_2O on calcium silicate hydrates at elevated temperatures, Cement and Concrete Research 7 (1977) 687–694.

[42] L. Fernandez, C. Alonso, C. Andrade, A. Hidalgo, The interaction of magnesium in hydration of C_3S and CSH formation using ^{29}Si MAS-NMR, Journal of Materials Science 43 (2008) 5772–5783.

4 Conclusion

The behavior of Portland cement-based materials under autoclaving (200 °C) is studied. Autoclaving substantially changes the cement hydration kinetics and the phase assemblage compared with normal curing. The hydration is significantly accelerated and achieves a higher degree due to the transformation of amorphous C-S-H to more ordered phases under autoclaving, releasing more water for hydration. However, some calcium aluminoferrite particles remain partially unhydrated, probably because the hydrate layer encases the calcium aluminoferrite particles, hindering further hydration. The hydrates assemblage highly depends on the composition of raw materials. Due to the main components of C_3S, C_2S, C_3A, C_4AF, and $C\bar{S}H_x$, a pure cement paste tends to generate the crystalline C-S-H with a high Ca/Si ratio. Quartz powder can effectively decrease the Ca/Si ratio, leading to the crystalline C-S-H with a relatively low Ca/Si ratio. Further increase of quartz powder results in the formation of poorly crystallized C-S-H which can persist under autoclaving. The addition of fly ash can concurrently increase the Si and Al contents, leading to the C-S-H with a low Ca/Si ratio and hydrogarnet. The composition of hydrogarnet depends on the contents of Si and Al in the matrix; the increase of Si and Al can increase the Si content of hydrogarnet. A high water/solid ratio can increase the availability of raw materials (more dissolution), leading to a different hydrates assemblage. Moreover, in the case with a low Ca/Si ratio, a high water/solid ratio favors the transformation of C-S-H precursor to tobermorite. For the samples with the same content of fly ash and/or quartz powder, a low water/solid ratio gives the hydrogarnet with a high Si content (more anhydrous).

The C-S-H in autoclaved UHPC also present a low Ca/Si ratio due to the components silica fume and quartz powder. Ettringite and AFm decompose, while hydrogarnet and hydroxylellestadite instead form under autoclaving. The partial replacement of cement by a small amount of limestone powder results in an unapparent change in the Ca/Si ratio of the hydrates, while the further increase of limestone powder decreases the Ca/Si ratio, leading to more poorly crystallized C-S-H with a low Ca/Si ratio in the autoclaved UHPC. The addition of fly ash can also decrease the Ca/Si ratio of the hydrates and increase the poorly crystallized C-S-H. However, the Al in the matrix is simultaneously increased, leading to the formation of tobermorite in the blended UHPC with fly ash. Besides, the elements S and Al widely distribute in the matrix, originating from the presence of hydroxylellestadite, C-(A-)S-H, and hydrogarnet.

The formation of hydrates with low densities ensures the matrix with low porosities. The sample with a low w/s ratio does not necessarily have a low porosity. In the case with a low Ca/Si ratio,

compared with normal curing, short-term autoclaving leads to a lower porosity due to the accelerated hydrates formation. However, the porosity is increased by the subsequent autoclaving because of the transformation of initially formed C-S-H to more ordered phases. Nonetheless, the final porosity after long-term autoclaving is decreased, benefiting from the increased hydrates and the C-S-H with a low Ca/Si ratio formed in the late stage of autoclaving which can persist and densify the microstructure.

The compressive strength of autoclaved UHPC can stay robust, because a large amount of silica (silica fume and quartz powder) prevents the formation of crystalline hydrates with high densities and leads to tobermorite and poorly crystallized C-S-H as the main hydrates. However, the flexural strength is vulnerable to autoclaving. The transformation of amorphous C-S-H to more ordered phases leads to the degradation of bond strength and thus a low flexural strength. The partial replacement of cement by limestone powder decreases the ratio of cement to silica, leading to more poorly crystallized C-S-H with a low Ca/Si ratio, which intensifies the mechanical strength. However, the excessive poorly crystallized C-S-H may magnify the thermal mismatch between matrix and quartz powder/aggregate, leading to cracks and low mechanical strength. The addition of fly ash increases the Si and Al contents and induces the formation of tobermorite and poorly crystallized C-S-H as the main hydrates, mitigating the detrimental effect caused by long-term autoclaving. The partial replacement of cement by limestone powder or fly ash also decreases hydroxylellestadite and calcium aluminoferrite phase which is usually accompanied by the unfilled cavities, benefiting microstructure densification and mechanical strength. Meanwhile, the content of fly ash (rich in Al) should also be restricted as excessive Al results in the massive formation of hydrogarnet. Furthermore, the mechanical strength is not strictly related to the porosity of UHPC under autoclaving. Due to the foregoing thermal mismatch, a low porosity does not necessarily lead to high mechanical strength.

The influence of autoclaving is highly related to the UHPC composition. Although the compressive strength can stay robust under long-term autoclaving, exceptional attention should be paid to the flexural strength. For designing UHPC working in autoclaving conditions, the accelerated chemical reactions by autoclaving should also be considered, as the traditional design rules are mainly based on the physical properties of the raw materials, aiming at a compact packing. Given the appropriate flowability, a low water/binder ratio or high solid volume fraction is preferred to restrict the C-S-H transformation to crystalline phases. Additional silica, probably silica-rich SCMs of silica fume and fly ash, may be needed to maintain the poorly crystallized C-S-H under autoclaving. Appropriate incorporation of SCMs

can effectively adjust the chemical compositions and thus tailor-make the hydrates assemblage in UHPC, ensuring a durable and sustainable UHPC structure.

Bibliographic information

- Hongwei Tian, Dietmar Stephan, Barbara Lothenbach, Christian Lehmann (2021): Influence of foreign ions on calcium silicate hydrate under hydrothermal conditions: A review. Construction and Building Materials, 301, 124071.
  Publisher's version added in section 2.1.
  DOI: https://doi.org/10.1016/j.conbuildmat.2021.124071.

- Hongwei Tian, Dietmar Stephan, Christian Lehmann (2022): Mechanical strength and microstructure of ultra-high performance concrete under long-term autoclaving. Journal of Materials in Civil Engineering, manuscript number MTENG-14374.
  Accepted version added in section 2.2.
  DOI: https://doi.org/10.1061/(ASCE)MT.1943-5533.0004588.

- Hongwei Tian, Tamino Hirsch, Dietmar Stephan, Christian Lehmann (2022): The influence of long-term autoclaving on the properties of ultra-high performance concrete. Frontiers in Materials, Volume 9, Article 844268.
  Publisher's version added in section 2.3.
  DOI: https://doi.org/10.3389/fmats.2022.844268.